ISSN 0911-5730
UVSOR-33
July 2006

UVSOR ACTIVITY REPORT 2005

UVSOR II
since 2003

UVSOR Facility
Institute for Molecular Science
National Institutes of Natural Sciences

UVSOR
ACTIVITY REPORT
2005

edited by

M.Hosaka, H.Hagiwara, Y.Hikosaka

Preface

This Activity Report covers the research activities carried out at the UVSOR facility in FY2005 (April 2005-March 2006). This is the third volume in the new series for the third decade of UVSOR, corresponding to the third year of the use of the low-emittance UVSOR-II storage ring. Through FY2005, the UVSOR-II ring has been stable in operation at the initial beam current of 350 mA for every 6-hour injection and the beam emittance of 27 nm-rad. One of the next upgrade plans is to increase the beam energy of the booster synchrotron from 0.6 GeV to 0.75 GeV, to realize the full energy injection in this year and the topping-up operation in the coming year. We have improved and enhanced radiation shields (walls) surrounding the storage ring; the users will be able to stay in the storage ring hall during the injection soon. The number of beamlines has been reduced from 21 to 13 for these four years. At present we have two injections (12-hour beamtime) per day from Tuesday to Friday; decrease of the total number of beamlines will be possibly compensated by the topping-up operation and the increase of beamtime per day and/or per week. Our final goal is to have 8 dipole lines for the 8 bending magnets and 6 undulator/free-electron laser (FEL) lines on the UVSOR-II ring, where ca. 40 % of the circumference is available for insertion devices.

The Ministry of Education, Culture, Sports, Science and Technology (MEXT) has been supporting SPring-8, Photon Factory, and UVSOR as three major facilities in Japan. To fill in the gap between Photon Factory and UVSOR and to enhance advanced study using high-brilliant VUV and soft X-rays, the synchrotron radiation community in Japan was eager to have the fourth major facility with a third generation VUV and soft X-ray storage ring, and finally decided to concentrate on the SuperSOR project of the University of Tokyo as the most promising proposal. Unfortunately, last year the University of Tokyo decided to withdraw the project. This means that UVSOR has been still exclusively responsible for the high-brilliant VUV light source in Japan. To enhance advanced VUV study, we will soon install the fourth undulator of 3m long at one of the 4 long straight sections BL7U and make possible high-resolution VUV photoemission study. The short in-vacuum undulator previously installed at BL7U will be moved to one of the 4 short straight sections BL6U for a new project covering surface chemistry and physics.

We look forward to more exciting activities in the coming years of UVSOR-II.

April, 2006

Nobuhiro Kosugi
Director of UVSOR

Dr. Takaki Hatsui won the JSSRR Young Scientist Award

Dr. Takaki Hatsui, a Research Associate, received the JSSRR Young Scientist Award from the Japanese Society for Synchrotron Radiation Research, for his contribution to "Development of a Novel Transmission-Grating Spectrometer for High-Resolution Soft X-Ray Emission Studies".

Dr. Hatsui (top center) with technicians

Novel Transmission-Grating Spectrometer for Soft X-Ray Emission Studies at BL3U

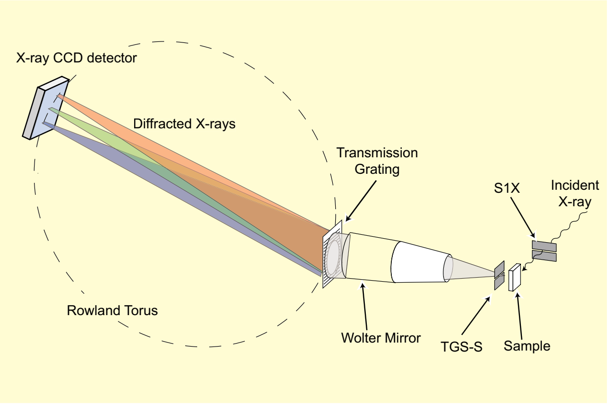

Schematic Layout of the Spectrometer

UVSOR Organization (2006/4/1)

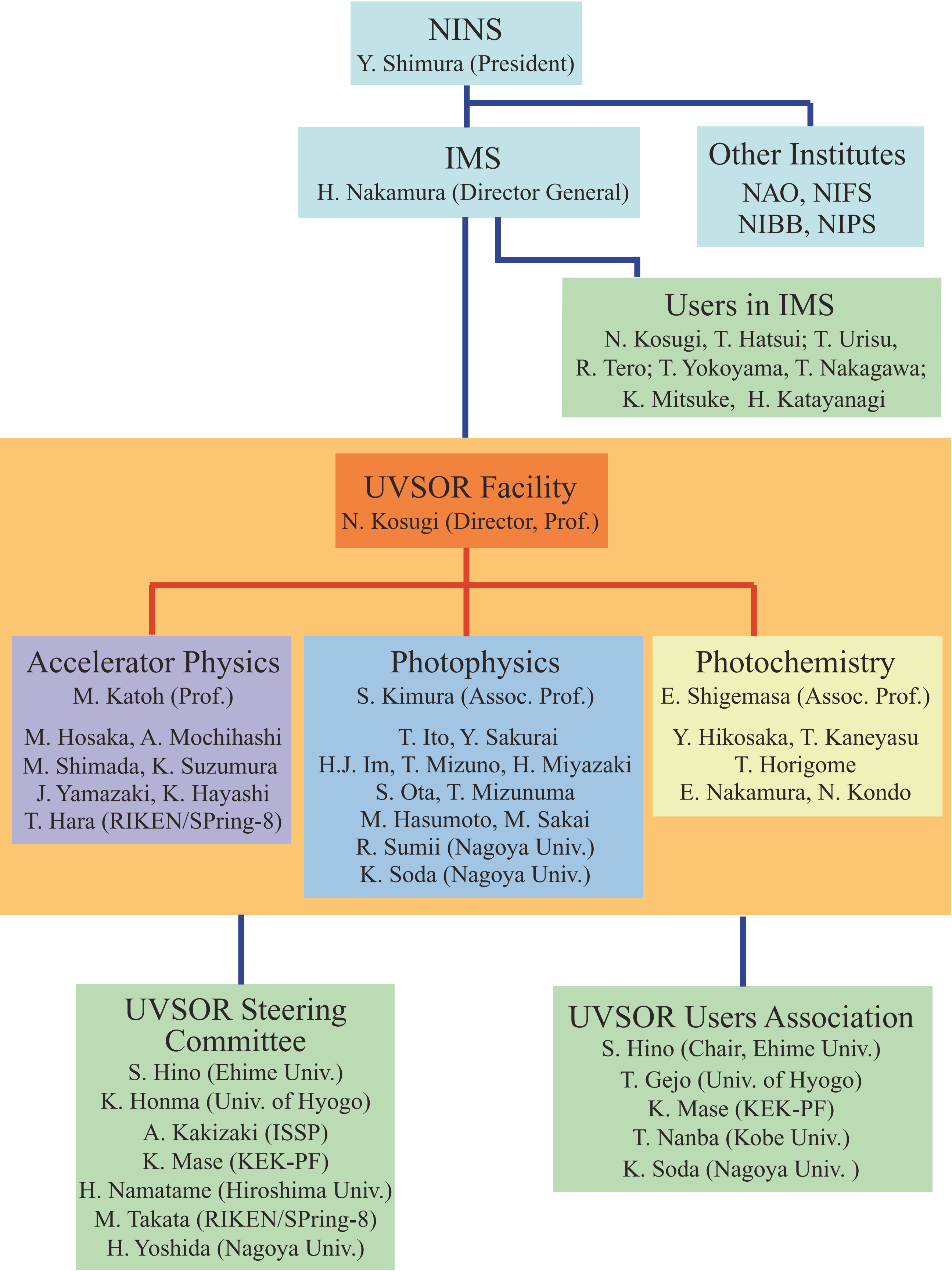

NINS
Y. Shimura (President)

IMS
H. Nakamura (Director General)

Other Institutes
NAO, NIFS
NIBB, NIPS

Users in IMS
N. Kosugi, T. Hatsui; T. Urisu,
R. Tero; T. Yokoyama, T. Nakagawa;
K. Mitsuke, H. Katayanagi

UVSOR Facility
N. Kosugi (Director, Prof.)

Accelerator Physics
M. Katoh (Prof.)

M. Hosaka, A. Mochihashi
M. Shimada, K. Suzumura
J. Yamazaki, K. Hayashi
T. Hara (RIKEN/SPring-8)

Photophysics
S. Kimura (Assoc. Prof.)

T. Ito, Y. Sakurai
H.J. Im, T. Mizuno, H. Miyazaki
S. Ota, T. Mizunuma
M. Hasumoto, M. Sakai
R. Sumii (Nagoya Univ.)
K. Soda (Nagoya Univ.)

Photochemistry
E. Shigemasa (Assoc. Prof.)

Y. Hikosaka, T. Kaneyasu
T. Horigome
E. Nakamura, N. Kondo

UVSOR Steering Committee
S. Hino (Ehime Univ.)
K. Honma (Univ. of Hyogo)
A. Kakizaki (ISSP)
K. Mase (KEK-PF)
H. Namatame (Hiroshima Univ.)
M. Takata (RIKEN/SPring-8)
H. Yoshida (Nagoya Univ.)

UVSOR Users Association
S. Hino (Chair, Ehime Univ.)
T. Gejo (Univ. of Hyogo)
K. Mase (KEK-PF)
T. Nanba (Kobe Univ.)
K. Soda (Nagoya Univ.)

UVSOR Staff

Director

KOSUGI, Nobuhiro	Professor	kosugi@ims.ac.jp	

Light Source Division (Accelerator Physics)

KATOH, Masahiro	Professor	mkatoh@ims.ac.jp	
HOSAKA, Masahito	Research Associate	hosaka@ims.ac.jp	
MOCHIHASHI, Akira	Research Associate	mochi@ims.ac.jp	
YAMAZAKI, Jun-ichiro	Unit Chief Engineer	yamazaki@ims.ac.jp	
HAYASHI, Kenji	Engineer	h-kenji@ims.ac.jp	
MATSUO, Suekichi	Supporting Engineer	matsuo@ims.ac.jp	(since May 2005)
HARA, Toru	Guest Associate Professor		(since Apr. 2005)
SHIMADA, Miho	Post-Doctoral Fellow	shimada@ims.ac.jp	(since Apr. 2006)

Beamline Division (Photophysics)

KIMURA, Shin-ichi	Associate Professor	kimura@ims.ac.jp	
ITO, Takahiro	Research Associate	tito@ims.ac.jp	
HASUMOTO, Masami	Unit Chief Engineer	hasumoto@ims.ac.jp	
SAKAI, Masahiro	Engineer	sakai@ims.ac.jp	
SAKURAI, Yoko	Post-Doctoral Fellow	sakurai@ims.ac.jp	
YOSHIMURA, Daisuke	Guest Researcher	daisukey@ims.ac.jp	(until Oct. 2005)
SUMII, Ryohei	Guest Researcher	sumii@ims.ac.jp	(since Sep. 2005)
SODA, Kazuo	Guest Professor		(since Apr. 2006)

Beamline Division (Photochemistry)

SHIGEMASA, Eiji	Associate Professor	sigemasa@ims.ac.jp	
HIKOSAKA, Yasumasa	Research Associate	hikosaka@ims.ac.jp	
HORIGOME, Toshio	Facility Chief Engineer	horigome@ims.ac.jp	
NAKAMURA, Eiken	Unit Chief Engineer	eiken@ims.ac.jp	
KONDO, Naonori	Engineer	nkondo@ims.ac.jp	
KANEYASU, Tatsuo	Post-Doctoral Fellow	kaneyasu@ims.ac.jp	(since Apr. 2005)

Secretary

HAGIWARA, Hisayo		hagiwara@ims.ac.jp	

Graduate Students

NISHI, Tatsuhiko	Grad. Univ. Adv. Studies	tnishi@ims.ac.jp	(until Mar. 2006)
IM, Hojun	Grad. Univ. Adv. Studies	hojun@ims.ac.jp	(since Oct. 2003)
MIZUNO, Takafumi	Grad. Univ. Adv. Studies	tmizuno@ims.ac.jp	(since Apr. 2005)
MIYAZAKI , Hidetoshi	Nagoya Univ.	hmiyasak@ims.ac.jp	(since Jun. 2005)
MIZUNUMA, Tatsuro	Meiji Univ.	mizunuma@ims.ac.jp	(since Apr. 2006)
OTA, Shunji	Nagoya Univ.	shunota@ims.ac.jp	(since Apr. 2006)
SUZUMURA, Kosuke	Nagoya Univ.	suzumura@ims.ac.jp	(since Apr. 2006)

Visiting Scientists

COUPRIE, Marie-Emmanuelle	CEA	(Jul.-Aug., Nov. 2005)
LAMBERT, Guillaume	CEA	(Jul. 2005)
LABAT, Marie	CEA	(Jul.-Aug. 2005)
XU, Hongliang	Univ. Sci. Tech. China	(Jul.-Aug. 2005)
WANG, Lin	Univ. Sci. Tech. China	(Jul.-Aug. 2005)
Huang, Guirong	Univ. Sci. Tech. China	(Jul.-Aug. 2005)
ZHANG, Shancai	Univ. Sci. Tech. China	(Jul.-Aug. 2005)
KWON, Yong-Seung	Sungkyunkwan Univ.	(Aug. 2005, Mar. 2006)
HONG, Jong Beom	Sungkyunkwan Univ.	(Aug. 2005)
KIM, Jeong Woo	Sungkyunkwan Univ.	(Aug. 2005)
KIM, Hyeong Do	PAL	(Aug., Sep. 2005)
RUEHL, Eckart	Wuerzburg Univ.	(Nov.-Dec. 2005)
PLENGE, Juergen	Wuerzburg Univ.	(Dec. 2005)
BIELAWSKI, Serge	Lill Univ.	(Nov.-Dec. 2005)
SZWAJ, Christophe	Lill Univ.	(Nov.-Dec. 2005)
STANKEVICH, Vladimir	Kurchatov Institute	(until Jul. 2005)
SIMON, Marc	CNRS	(Jan. 2006)
GUILLEMIN, Renand	CNRS	(Jan. 2006)
SHENG, Liusu	Univ. Sci. Tech. China	(Mar. 2006)
ZHANG, Guobin	Univ. Sci. Tech. China	(Mar. 2006)

UVSOR Steering Committee (FY2004-2005)

KOSUGI, Nobuhiro	UVSOR, IMS	Chair
KIMURA, Shin-ichi	UVSOR, IMS	
KATOH, Masahiro	UVSOR, IMS	
SHIGEMASA, Eiji	UVSOR, IMS	
HARA, Toru	UVSOR, IMS	(Guest Assocate Professor from RIKEN, since Apr. 2005)
YOKOYAMA, Toshihiko	IMS	
MATSUMOTO, Yoshiyasu	IMS	
OGAWA, Takuji	IMS	
MITSUKE, Koichiro	IMS	
KAKIZAKI, Akito	Univ. of Tokyo	
MASE, Kazuhiko	KEK-PF	
YOSHIDA, Hisao	Nagoya Univ.	
OSHIMA, Masaharu	Univ. of Tokyo	
SODA, Kazuo	Nagoya Univ.	
NAMBA, Hidetoshi	Ritsumeikan Univ.	
HIRAYA, Atsunari	Hiroshima Univ.	

Light Source in 2005

Masahiro KATOH

UVSOR Facility, Institute for Molecular Science

1. Status of UVSOR-II

In the fiscal year 2005, we have operated the UVSOR-II accelerators from May ’05 to March ’06. We had two shut-down periods, in April ’05 and March ’06. The former was to install a new RF cavity [1]. The latter was to reinforce radiation shield of the storage ring. The new cavity has capability of producing the accelerating field three times stronger than before. We also stopped the operation for one week in September for maintenance works and for two weeks around the New Years day.

We had a few troubles on the accelerators during FY2005. The most serious one happened on the power supply of the booster-synchrotron magnets, which has been working for more than 20 years. Fortunately, the power supply was soon recovered by replacing the broken electronic device. The users operation was canceled only for one day and a half. Same trouble happened last year. This power supply will be replaced in summer, 2006. The new one will have capability of increasing the maximum beam energy of the booster synchrotron from 600 MeV to 750 MeV, to realize the full-energy injection into the storage ring. We also had some minor troubles on the magnet power supplies of the storage ring, the RF amplifier of the linear accelerator and the power supply of the extraction kicker of the booster synchrotron. Fortunately, all of them could be recovered within several hours.

We had totally 38 weeks for the users operation, 36 weeks in multi-bunch mode and two weeks in single bunch mode. We had two weeks dedicated for machine studies. The monthly statistics of the operation time and the integrated beam current are shown in Figures 1. The normal operation pattern in a week is as follows. From Tuesday to Friday, the machine is operated for users. The beam injection is twice a day, at 9:00 and 15:00. The initial beam current of each run is 350 mA in multi-bunch mode and 100 mA in single bunch mode. On Monday and Saturday, the machine is operated for machine studies.

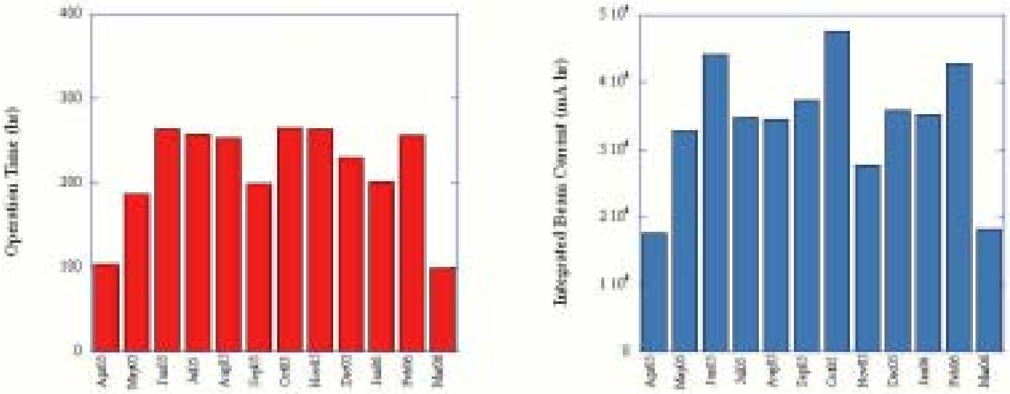

Fig. 1 Monthly statistics of the operation time (left) and of the integrated beam current (right).

2. Improvements

Operation with New RF Accelerating Cavity

The new RF accelerating cavity was installed in the ring, in March 2005. The cavity was successfully commissioned and the users operation with the new cavity was started in May. During the commissioning, it was proved that the new cavity could produce 150 kV accelerating voltage, which was the design goal [2]. However, it was also observed that the vacuum pressure started to rise when the accelerating voltage came closer to around 150 kV. Thus, we have decided to start the users operation with the accelerating voltage of 100 kV, which is still twice higher than before. Thanks to this higher voltage, the Touschek lifetime was improved. It was found that, even with the low emittance of 27 nm-rad, we could operate the storage ring with a sufficiently long lifetime, almost as long as that with the old cavity and with the moderately high emittance of 60 nm-rad.

Progress in Orbit Stabilization

The electron orbit of UVSOR-II shows drift motion of a few hundred microns with a time scale of hours. The orbit moves both in the horizontal and vertical planes. The origin of these motions is considered to be the temperature changes of the accelerator components and of the storage building itself. The machine is operated only for 12 hours a day. It was observed that the temperature of the accelerator components and the building were not stable. During night time, they are falling and, during day time, they are rising.

To suppress the orbit drift, a feedback system is under development. As the first step, a system has been constructed to correct the orbit displacement in the horizontal plane automatically by controlling the RF frequency [3]. This system has been successfully commissioned and the orbit drift in the horizontal plane is reduced significantly. The feedback system is now being upgraded to correct the orbit in both planes more precisely by using the correction magnets.

Replacement of Accelerator Control System

A control system based on the VAX computers and the CAMAC interfaces had been used for many years for the UVSOR accelerators [4]. The system itself was still reliable, however, it had been getting difficult to maintain the hardware, year by year. A few years ago, we started to replace the system, step by step, with more simple one based on PC’s. Until the end of FY2005, all the system has been replaced.

Control of Undulators

A simple and reliable system based on PC was developed for controlling the undulators [5]. The system can correct the orbit displacement caused by the pole-gap changes automatically. The system was first introduced to the in-vacuum undulator (U07) and then to the second in-vacuum one (U03). This year, the system was introduced to the helical undulator/optical klystron (U05). This device produces significant betatron tune shift when the pole gap is narrow. The system corrects the tune shift as well as the orbit displacement. The users can change the pole gap anytime, although the polarization change is still limited to be done during the beam-injection time.

3. Researches and Developments

Design and Construction of a new Variably Polarized Undulator

A design work on the new undulator, which will be installed in the straight section between B6 and B7, has been finished. This undulator will provide VUV light of linear polarization in both horizontal and vertical planes. It can also provide circular polarized VUV light. The configuration of the magnet array is of APPLE-II type [6]. The main parameters are shown in Table 1. The undulator is now under construction and will be installed in the ring in autumn, 2006.

Table 1 Main parameters of the new undulator.

Configuration	APPLE-II
Polarization	Hor/Ver/Helical
Number of periods	38
Period length	76 mm
Total Length	2945 mm
Magnetic gap	24–200 mm
Deflection parameter (Horizontal mode)	max. 5.4 K
Deflection parameter (Vertical mode)	max. 3.6 K
Deflection parameter (Helical mode)	max. 3.0 K

Free Electron Laser

The shortest wavelength of the free electron laser at UVSOR had been 239 nm for many years, which was once the world record [7]. However, thanks to the smaller emittance realized by the upgrade of the accelerators in 2003 and to the higher peak current of the electron beam realized by the new RF cavity, it has come to be possible to oscillate the FEL in shorter wavelength with higher out-coupled power. We have succeeded in oscillating in deep UV region around 215 nm with an average power of a few hundred mW [8].

The UVSOR-FEL had been driven by the electron beam of 600 MeV for many years. The lower beam energy itself gives a higher FEL gain. In addition, the smaller emittance at the lower energy also contributes to the higher gain. However, thanks to the recent improvements in the quality of the electron beam as described above, even with the electron beam of 750 MeV, we can obtain a sufficient FEL gain for realizing oscillation. The laser oscillation at 215 nm was successfully demonstrated for the beam energy of 750 MeV [8]. We have found that the out-coupled power was higher than the case of 600 MeV. In addition, the beam lifetime was longer.

Laser Bunch Slicing

A TiSa laser, which can be synchronized with the RF system of the UVSOR-II accelerators, was installed in spring, 2005. The repetition rate is 1 kHz and the pulse energy is 2.5 mJ. This system can be used for laser bunch slicing for short SR pulses or for coherent terahertz pulses, and for coherent harmonic generation. A laser beam transport line was constructed in summer, 2005, under an international collaboration program, which involved a French group leaded by Dr. M. E. Couprie.

The laser pulses injected in the ring interact with the electron pulse in the undulator, whose fundamental wavelength is tuned to the laser wavelength. By the interaction, an energy modulation is created on the electron bunch. The laser system has a capability to produce an energy modulation on the electron beam, whose amplitude is comparable to the RF bucket height. During a series of the experiments in 2005, we have already obtained some preliminary results which clearly indicated the occurrence of the bunch slicing.

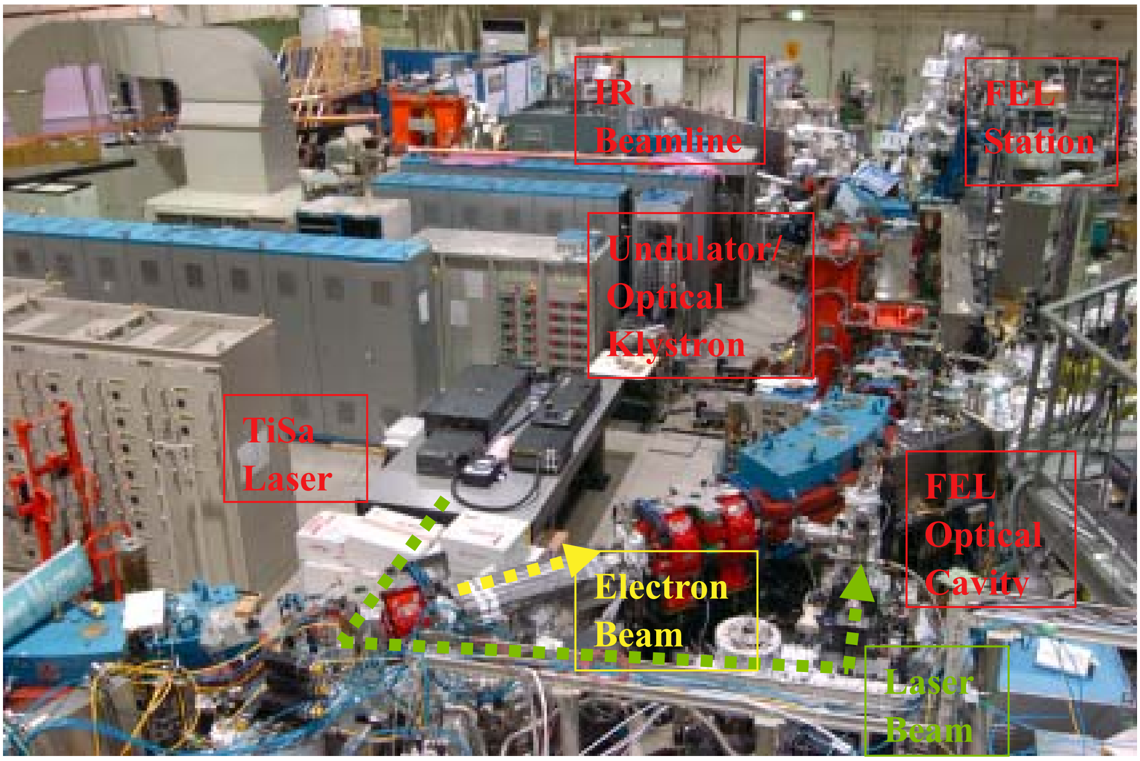

Fig. 2 Configuration of Laser Bunch Slicing Experiment.

[1] A. Mochihashi *et al.*, UVSOR Activity Report 2004 (2005) 35.

[2] A. Mochihashi *et al.*, in this report.

[3] Y. Suzumura *et al.*, in this report.

[4] N. Kanaya *et al.*, Nucl. Intr. Meth. A **352** (1994) 166.

[5] K. Hayashi *et al.*, UVSOR Activity Report 2002 (2003) 50.

[6] S. Sasaki, Nucl. Instr. Meth. A**347** (1994) 83.

[7] H. Hama *et al.*, Proc. the 3rd Asian Free Electron Lasers and 5th Symp. on FEL Appl. (Hirakata, Osaka, 1997) 17.

[8] M. Hosaka, in this report.

UVSOR Accelerator Complex

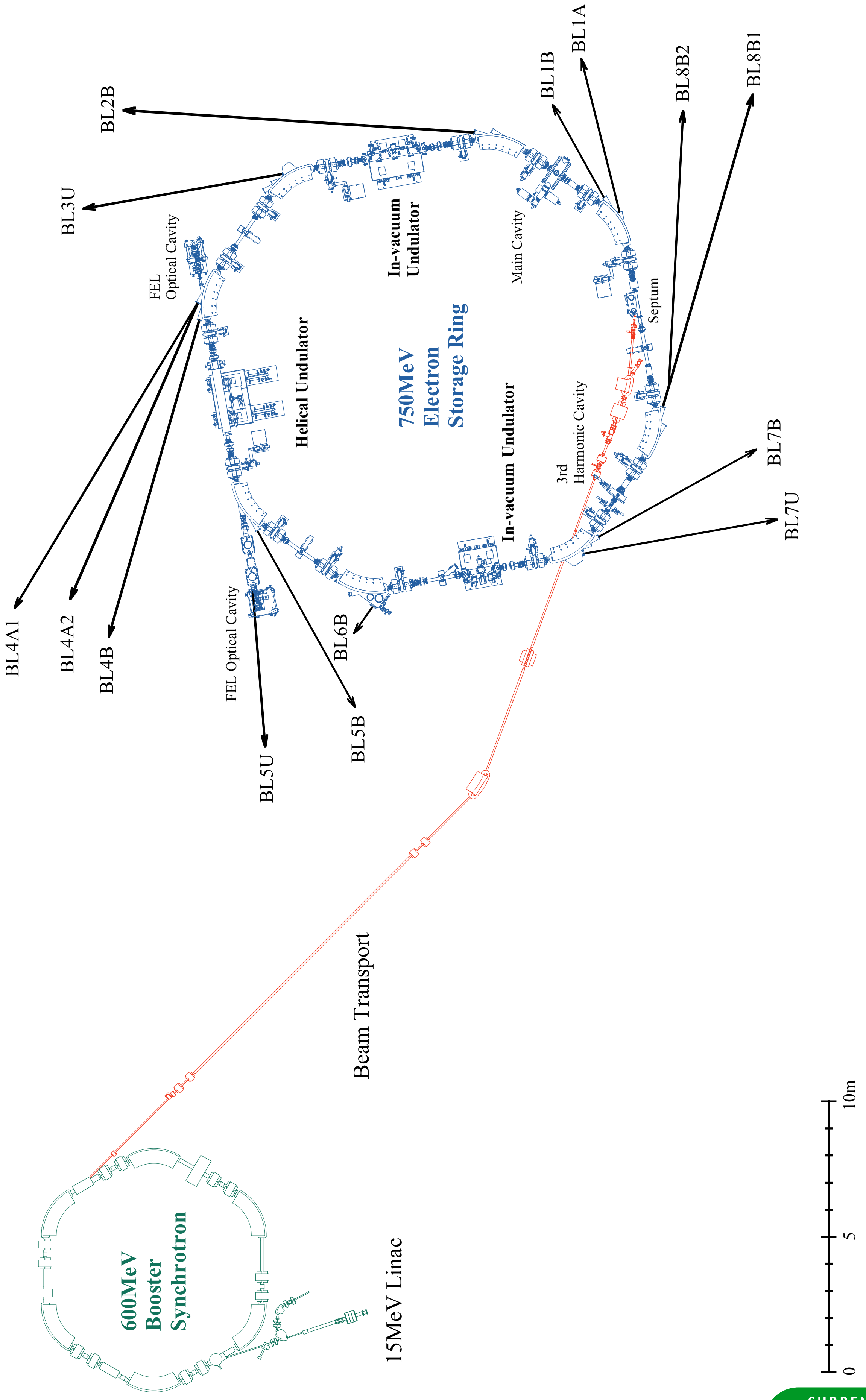

Parameters of Injection Linear Accelerator

Energy	15 MeV
Length	2.5 m
Frequency	2856 MHz
Accelerating RF Field	2π/3 Traveling Wave
Klystron Power	1.8 MW
Energy Spread	~ 1.6 MeV
Repetition Rate	2.6 Hz

Parameters of Booster Synchrotron

Energy	600 MeV
Injection Energy	15 MeV
Beam Current	32 mA (uniform filling)
Circumference	26.6 m
RF Frequency	90.1 MHz
Harmonic Number	8
Bending Radius	1.8 m
Lattice	FODO × 8
Betatron Tune	
Horizontal	2.25
Vertical	1.25
Momentum Compaction	0.138
Repetition Rate	2.6 Hz

Parameters of UVSOR-II Storage Ring

Energy	750 MeV
Injection Energy	600 MeV
Maximum Stored Current	500 mA (multi bunch) 100 mA (single bunch)
Natural Emittance	27.4 nm-rad
Circumference	53.2 m
RF Frequency	90.1 MHz
Harmonic Number	16
Bending Radius	2.2 m
Lattice	Extended DBA × 4
Straight Section	(4 m × 4) + (1.5 m × 4)
RF Voltage	100 kV
Betatron Tune	
Horizontal	3.75
Vertical	3.20
Momentum Compaction	0.028
Natural Chromaticity	
Horizontal	-8.1
Vertical	-7.3
Energy Spread	4.2×10^{-4}
Natural Bunch Length	108 ps

Electron Beam Optics of UVSOR-II Storage Ring

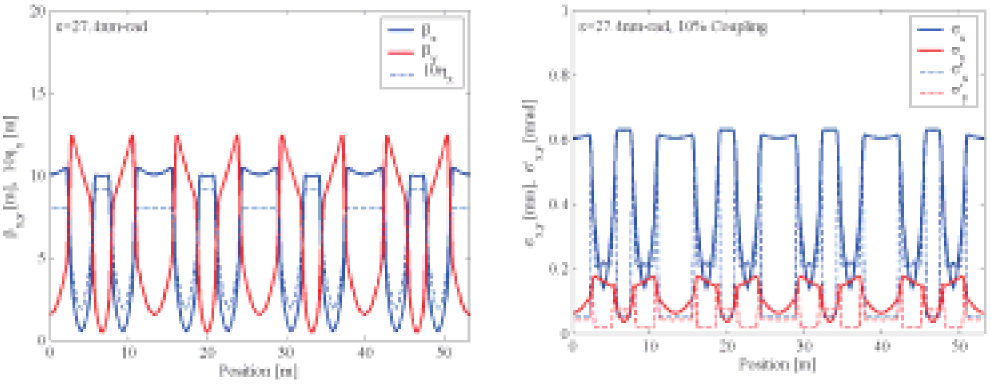

Horizontal/vertical betatron functions and dispersion function (left), and horizontal/vertical electron beam sizes and beam divergences (right) of UVSOR-II

Parameters of Insertion Devices

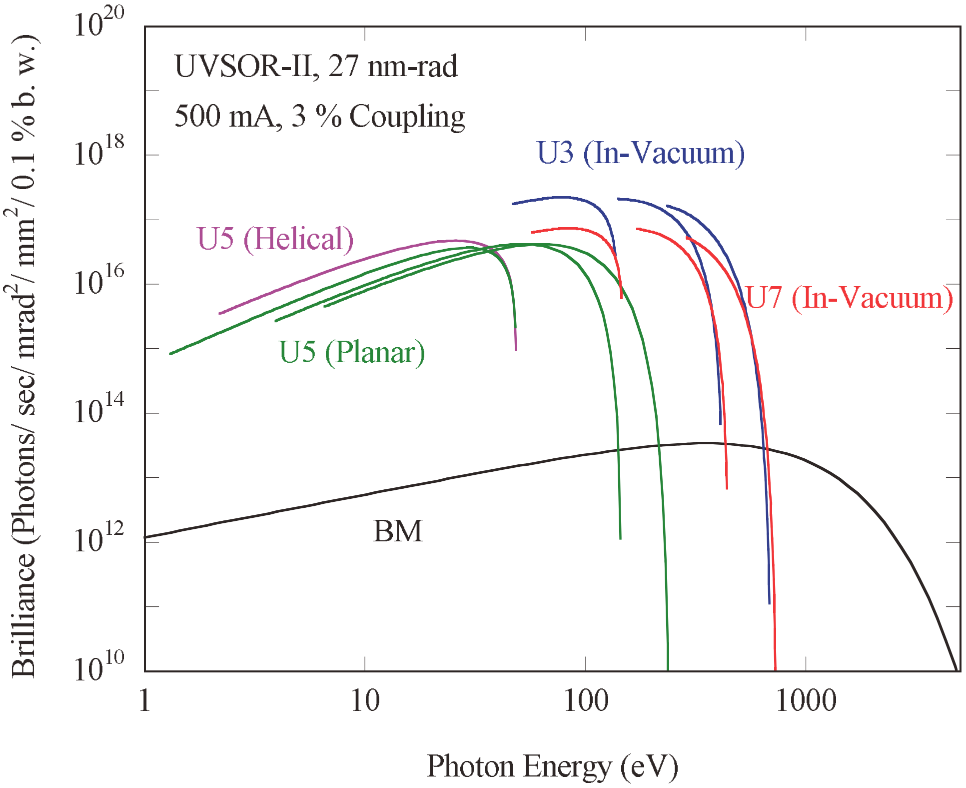

Brilliance of radiation from the insertion devices (U3, U5 and U7) and a bending magnet of UVSOR-II

BL3U In-vacuum Undulator

Number of Periods	50
Period Length	38 mm
Pole Length	1.9 m
Pole Gap	15~40mm
Deflection Parameter	2.00~0.24

BL5U Helical Undulator / Optical Klystron

Number of Periods	21 / 9+9(Opt. Kly.)
Period Length	110mm
Pole Length	2.35 m
Pole Gap	30~150 mm
Deflection Parameter	4.6~0.07(Helical) 8.5~0.15(Linear)

BL7U In-vacuum Undulator

Number of Periods	26
Period Length	36 mm
Pole Length	0.94 m
Pole Gap	15~40 mm
Deflection Parameter	1.78~0.19

Bending Magnets

Bending Radius	2.2 m
Critical Energy	425 eV

Beamlines in 2005

Eiji SHIGEMASA
UVSOR Facility, Institute for Molecular Science

Eight bending magnets and three insertion devices are available for utilizing synchrotron radiation at UVSOR. There is a total of sixteen operational beamlines in 2005, which are classified into two categories. Nine of them are so-called "Open beamlines", which are open to scientists of universities and research institutes belonging to the government, public organizations, private enterprises and those of foreign countries. The rest of the seven beamlines are so-called "In-house beamlines", and are dedicated to the use of research groups within IMS. We have one soft X-rays station equipped with a double-crystal monochromator, seven extreme ultraviolet and soft X-rays stations with a grazing incidence monochromator, three vacuum ultraviolet stations with a normal incidence monochromator, one infrared (IR) station equipped with Fourier-Transform interferometers, one station with a multi-layer monochromator, and three non-monochromatized stations for irradiation of white-light, as shown in the appended table for all available beamlines at UVSOR.

The upgrade project of the UVSOR storage ring, in which the creation of four new straight sections and the achievement of much smaller emittance (27 nm-rad) were planned, has been approved in the fiscal year of 2002 and has been accomplished on schedule. The new RF cavity has been installed to the short straight section between B01 and B02 before the end of March 2005. Keeping pace with the upgrade project, improvements and upgrades of the beamlines at UVSOR have been continuously discussed with users in a series of UVSOR workshops. From the viewpoint regarding radiation safety, the experiments carried out at the experimental stations on the second floor such as BL3B and BL7B, and the fine tunings of the laser system installed inside the shield walls during the machine study, seem to have become quite risky after introducing the so-called top-up operation of the UVSOR storage ring. Accordingly we have decided to put two old beamlines, BL8A and BL3B, out of service until the middle of March 2006. The experimental station for BL7B will be constructed at the vacant space after removing BL8A. All the beamline components have been completely removed from BL3B before the third week of March 2006, thanks to the efforts by Mitsuke’s group in Dep. VUV photoscience. The laser system will be moved to the corresponding empty lot of BL3B by the machine group. Regarding the utilization for the long straight section between B06 and B07, a UVSOR workshop has been held in March 2005. On the basis of the review and evaluation report on the present status of UVSOR in 2004, a high resolution and high flux variable polarization beamline for spectroscopy in the VUV range has been proposed and possible scientific cases performed on this beamline have been discussed there. The new beamline is planned to be constructed during the summer shutdown in 2006, and the beamline commissioning will be started after the installation of a new APPLE-II type undulator at the end of October 2006. Further serious discussion toward utilizing the available straight sections most effectively and formulating a basic plan on the beamline construction, will be continued.

All users are required to refer to the beamline manuals and the UVSOR guidebook (latest revision in 1999), on the occasion of conducting the actual experimental procedures. Those wishing to use the open and in-house beamlines are recommended to contact the stationmaster/supervisor and the representative, respectively. For updated information of UVSOR, http://www.uvsor.ims.ac.jp/.

Station Masters and Supervisors of Open Beamlines in FY2005

Beamline	Station Master	Sub Master	Supervisor
1A	N. Kondo	E. Shigemasa	E. Shigemasa
1B	M. Hasumoto	S. Kimura	S. Kimura
5U	T. Ito	S. Kimura	S. Kimura
5B	M. Hasumoto	E. Nakamura	E. Shigemasa
6B	S. Kimura	E. Nakamura	S. Kimura
7B	M. Hasumoto	S. Kimura	S. Kimura
8A	E. Nakamura	Y. Hikosaka	E. Shigemasa
8B1	Y. Hikosaka	E. Nakamura	E. Shigemasa
8B2	R. Sumii	E. Nakamura	S. Kimura

Representatives of In-House Beamlines in FY2005

Beamline	Representative	Affiliation
2B	K. Mitsuke	Dep. VUV Photoscience
3U	N. Kosugi	Dep. VUV Photoscience
4A1, 2	T. Urisu	Dep. VUV Photoscience
4B	E. Shigemasa	UVSOR

Beamlines at UVSOR-II

Beam-line	Monochromator, Spectrometer	Energy Region (eV)	Experiments	Beamline master
1A	Double-Crystal	600 eV 4 keV	Solid (Absorption)	N. Kondo nkondo@ims.ac.jp
1B	1m Seya-Namioka	1.9 eV 40 eV	Solid (Reflection, Absorption)	M. Hasumoto hasumoto@ims.ac.jp
2B	18m Spherical Grating (Dragon)	20 eV 200 eV	Gas (Photoionization, Photodissociation)	K. Mitsuke mitsuke@ims.ac.jp
3U	Varied-Line-Spacing Plane Grating (Monk-Gillieson)	40 eV 600 eV	Gas (Photoionization, Photodissociation) Solid (Photoemission)	T. Hatsui hatsui@ims.ac.jp
4A1	Multi-Layered-Mirror	50 eV 95 eV	Irradiation	T. Urisu urisu@ims.ac.jp
4A2	None		Irradiation	T. Urisu urisu@ims.ac.jp
4B	Varied-Line-Spacing Plane Grating (Monk-Gillieson)	25 eV 800 eV	Gas (Photoionization, Photodissociation) Solid (Photoemission)	E. Shigemasa sigemasa@ims.ac.jp
5U (FEL)	None (Optical Klystron)		Free Electron Laser	J. Yamazaki yamazaki@ims.ac.jp
5U	Spherical Grating (SGM-TRAIN*)	5 eV 250 eV	Solid (Photoemission)	T. Ito tito@ims.ac.jp
5B	Plane Grating	5 eV 600 eV	Calibration Solid (Absorption)	M. Hasumoto hasumoto@ims.ac.jp
6B (IR)	Martin-Puplett FT-FIR Michelson FT-IR	2.5 eV 0.25 meV	Solid (Reflection, Absorption)	S. Kimura kimura@ims.ac.jp
7U**	10m Normal Incidence (Modified Wadsworth)	6 eV 40 eV	Solid (Photoemission)	S. Kimura kimura@ims.ac.jp
7B	3m Normal Incidence	1.2 eV 30 eV	Solid (Reflection, Absorption)	M. Hasumoto hasumoto@ims.ac.jp
8B1	15m Constant Deviation Grazing Incidence	30 eV 600 eV	Solid (Absorption)	Y. Hikosaka hikosaka@ims.ac.jp
8B2	Plane Grating	1.9 eV 150 eV	Solid (Photoemission)	R. Sumii sumii@ims.ac.jp

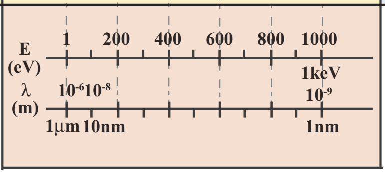

* Spherical Grating Monochromator with Translating and Rotating Assembly Including Normal incidence mount

** Under construction

BL1A

Soft X-Ray Beamline for Photoabsorption Spectroscopy

BL1A is a soft X-ray beamline for photoabsorption spectroscopy. The beamline is equipped with a focusing premirror and a double crystal monochromator [1]. The monochromator serves soft X-rays in the energy region from 585 to 4000 eV by using several kinds of single crystals such as β-Al_2O_3, beryl, KTP ($KTiOPO_4$), quartz, InSb, and Ge. The throughput spectra measured by a Si photodiode (AXUV-100, IRD Inc.) are shown in Fig. 1. Typical energy resolution (E/ΔE) of the monochromator is about 1500 for beryl and InSb. There are no experimental setups specific of this beamline, except for a small vacuum chamber equipped with an electron multiplier (EM) detector. Photoabsorption spectra for powdery samples are usually measured in a total electron yield mode, with the use of the EM detector.

[1] Hiraya *at al*, Rev. Sci. Instrum. **63** (1992) 1264.

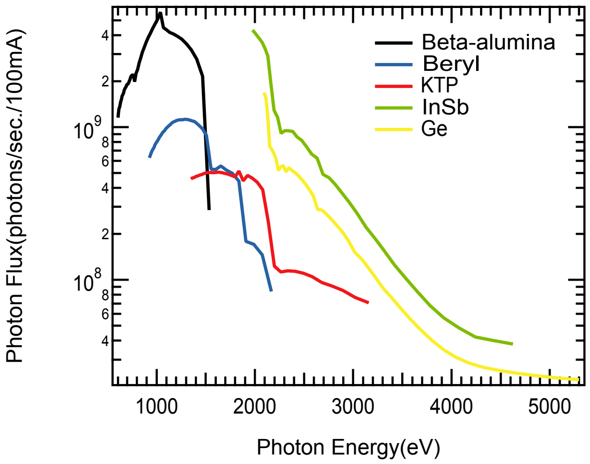

Fig. 1 Throughput spectra of the double crystal monochromator at BL1A.

Fig. 2 A side view of BL1A.

Beamline Specifications

Monochromator	Double crystal monochromator
Monochromator crystals: (2d value, energy range)	β-Al_2O_3 (22.53 Å, 585-1609 eV), beryl (15.965 Å, 826-2271 eV), KTP (10.95 Å, 1205-3310 eV), quartz (8.512 Å, 1550-4000 eV), InSb (7.481 Å, 1764-4000 eV), Ge (6.532 Å, 2094-4000 eV)
Resolution	E/ΔE = 1500 for beryl and InSb
Experiments	Photoabsorption spectroscopy

BL1B

Seya-Namioka Monochromator for General Purposes

BL1B has been constructed to perform various spectroscopic investigations such as absorption, reflectivity, and luminescence in condensed matters. This beamline consists of a pre-focusing mirror, a 1-m Seya-Namioka type monochromator, and post-focusing mirrors with different focal lengths. Three gratings of 600, 1200, and 2400 l/mm can cover the wavelength region ranging from 40 to 650 nm ($h\nu = 2 - 30$ eV). The post mirror with a longer focal length is usually used with an LiF window to separate the vacuum condition of the monochromator from a main experimental station, which make experiments for liquids and bio-specimens possible, while the other is mainly utilized for solid-state spectroscopy. The output flux from this monochromator is about 10^{10} photons/sec. around 200 nm with 0.1 mm slit openings. The spectral distributions for two gratings measured by a conventional photomultiplyer are shown in Fig. 1. A second monochromator (Spex 270M) and a LN-cooled CCD detector (Princeton Inc.) are available for luminescence measurements, together with a liquid helium-flow type cryostat. To perform time-resolved experiments, a TAC system is also available.

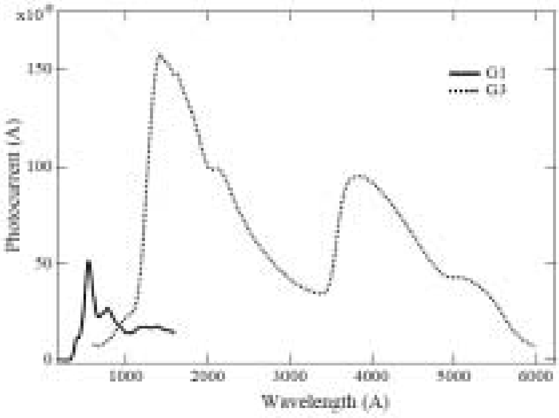

Fig. 1 Photocurrent at the sample position at BL1B.

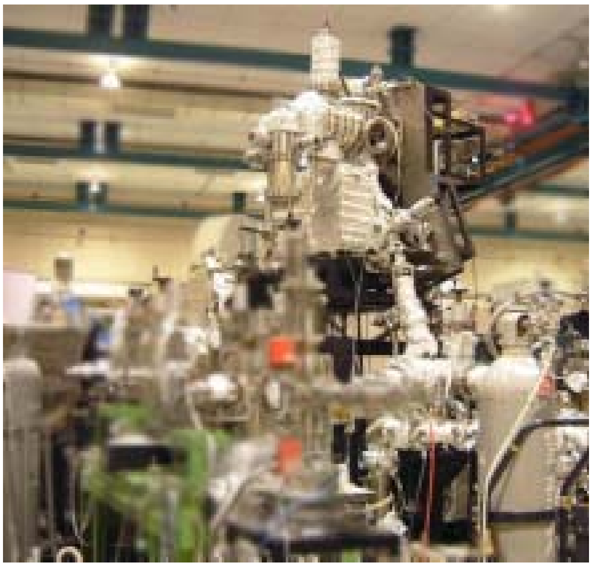

Fig. 2 Photo of BL1B.

Beamline Specifications

Monochromator	1-m Seya-Namioka type
Wavelength Range	40 to 600 nm (2-30 eV)
Resolution	E/ΔE~1000 at 100 nm (10 eV)
Experiment	Absorption, reflection, luminescence spectroscopy for solids

BL2B

Beamline for Gas Phase Photoionization and Reaction Dynamics

This beamline has been developed for the purpose of studying ionization, excitation and decay dynamics involving inner-valence electrons, 2*p* electrons of the third row atoms, and 4d electrons of the lanthanides. The monochromator is a spherical grating Dragon-type with 18-m focal length. High throughput (1×10^{10} photons s^{-1}) and high resolution ($E/\Delta E = 2000 - 8000$) are achieved simultaneously under the condition of the ring current of 100 mA [1]. A second-order light of 7 % is contained at a photon energy of 45.6 eV (G3). The optical system consists of two prefocusing mirrors, an entrance slit, three spherical gratings (G1 - G3), two folding mirrors, a movable exit slit and a refocusing mirror [2]. The monochromator is designed to cover the energy range of 23 - 205 eV with the three gratings: G1 (2400 lines mm^{-1}, $R = 18$ m) at 80 - 205 eV; G2 (1200 lines mm^{-1}, $R = 18$ m) at 40 - 100 eV; G3 (2400 lines mm^{-1}, $R = 9.25$ m) at 23 - 50 eV.

We have been taking photoion yield curves of various fullerenes. Geometrical structures and electronic properties of fullerenes have attracted widespread attention because of their novel structures, novel reactivity, and novel catalytic behaviors as typical nanometer-size materials. However, spectroscopic information is very limited in the extreme UV region, which has been probably due to difficulties in acquiring enough amount of sample. This situation has been rapidly changed in these few years, since the techniques of syntheses, isolation, and purification have been advanced so rapidly that appreciable amount of fullerenes can be readily obtained.

[1] M. Ono *et al.*, Nucl. Instrum. Meth. Phys. Res. A **467-468** (2001) 577.

[2] H. Yoshida and K. Mitsuke, J. Synchrotron Radiat. **5** (1998) 774.

Beamline Specifications

Monochromator	18-m spherical grating Dragon-type
Wavelength Range	6 – 55 nm
Resolution	2000-8000
Experiment	Mass spectrometry; Photoelectron spectroscopy

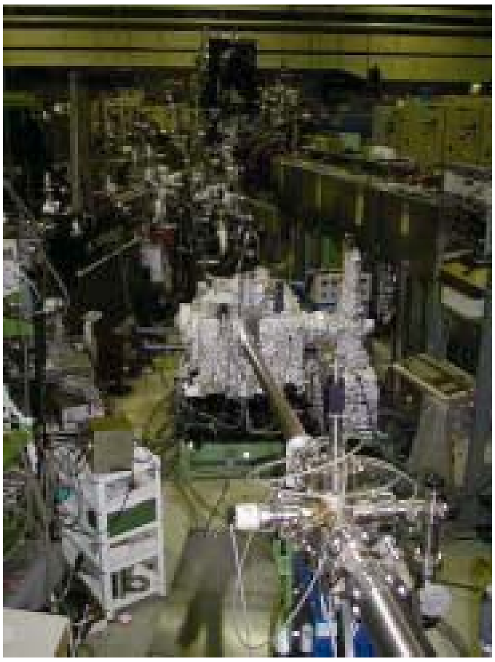

Fig. 1 18-m spherical grating monochromator installed at the Beamline 2B.

BL3U

Varied-Line-Spacing Plane Grating Monochromator for Molecular Soft X-Ray Spectroscopy

The beamline BL3U is equipped with an in-vaccum undulator composed of 50 periods of 3.8 cm period length. The emitted photons are monochromatized by the varied-line-spacing plane grating monochromator (VLS-PGM) designed for various spectroscopic investigations in the soft x-ray range including soft x-ray emission studies. Three holographically ruled laminar profile plane gratings are designed to cover the photon energy range from 60 eV to 800 eV. The beamline has two endstations, namely XES setup and Multi-purpose setup. The XES setup is used for soft x-ray emission spectroscopy. The beam is horizontally focused onto the sample position by plane-elliptical mirror, M2X. In the Multi-purpose setup, the beam is focused by the toroidal mirror M2. Between the sample position and M2, the differential pumping is placed.

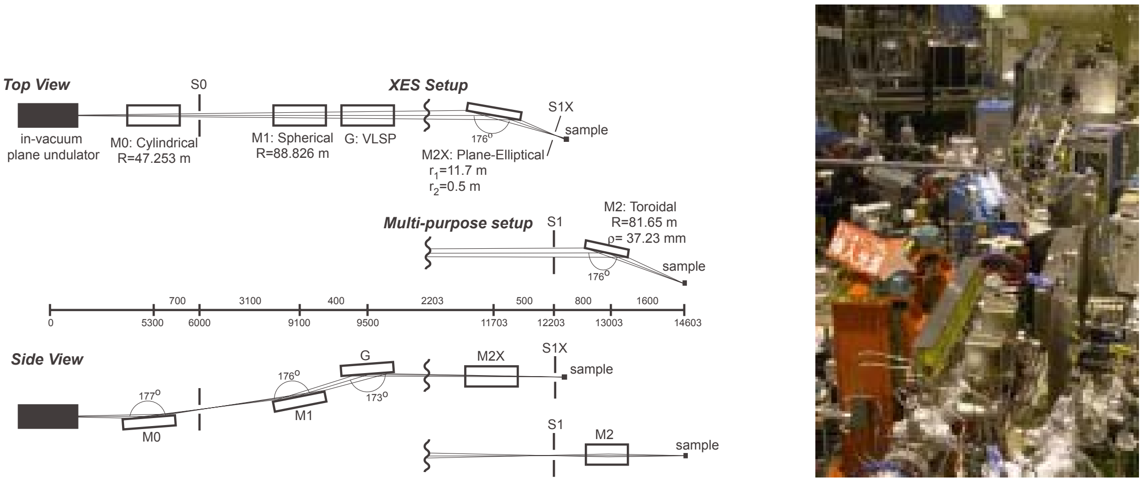

Fig. 1 Schematic layout (left) and the photography (right) of the BL3U. The distances along the beam from the center of the in-vacuum plane undulator are shown in mm. S1X and M2X can be replaced with the other exit slit S1 so that experiments can be carried out at either the XES or multi-purpose endstation. In the XES setup, the sample is placed at 5-10 mm downstream of S1X.

Beamline Specifications

Monochromator	Varied-line-spacing plane grating monochromator
Energy Range	60-800 eV
Resolution	E/ΔE > 7000
Experiment	Soft X-ray spectroscopy (XPS, XES, XAS)
Beam Size (XES Endstation)	Gaussian shape Vertical 5-20 μm; Horizontal 68 μm (FWHM)

BL4A1

SR-Induced XeF_2 Etching Beamline

This beamline is used for synchrotron radiation (SR)-induced XeF_2 etching on SiO_2/Si substrates (Fig. 1). XeF2 is used for a high-rate and anisotropic etching, since XeF2 has high-etching rate of 600 nm/min even in a dry-etching condition.

A XeF_2-flow chamber with LiF window is installed in the beamline chamber (Fig. 2). The XeF_2-flow chamber is independently evacuated in order to avoid the damage to the chambers and evacuation instruments in the beamline. The beam line has multilayered-mirror (MLM) monochromator. The beam line optics is optimized to obtain a high photon flux. Optimization concerning the reduction of the low energy background due to the total reflection has been made for the combination of the Mo/Si MLMs and the C filter. Mo/Si MLMs have a (normal incident) reflectivity of over 60% can be made for the energy region around 100 eV, which contains the core electron binding energies of Al and Si.[1] Pt-coated plane mirrors will be installed to reduce the intensity of higher energy region, which will be absorbed to the LiF window.

[1] H. Mekaru *et al.*, Rev. Sci. Instrum. **70** (1999) 2601.

Fig. 1 XeF_2 etching chamber in BL4A1.

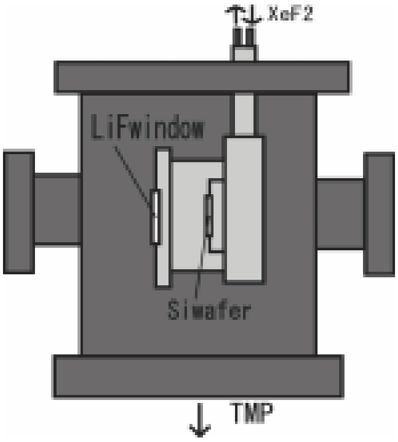

Fig. 2 Schematic drawing of the XeF_2 etching chamber.

Specifications

Monochromator	Multilayered-mirror monochromator
Wavelength range	13.3-22.5 nm
Resolution	5 - 9 eV (FWHM)

BL4A2

SR-Induced Photo Etching and CVD Beamline

This beam line is used for synchrotron radiation chemical vapor deposition (SR-CVD) and photo-etching experiments. The beam line has no monochromator for high photon flux to irradiate and consists of only two mirrors. One is for focusing and the other is for branching. At the beam line, the gas supply and extinction system is equipped for using legally controlled high pressure gasses such as SiH_4, Si_2H_6 and GeH_4. They are commonly used to CVD of semiconductor crystals.

The SR-CVD and photo-etching chambers are connected to the beam line as shown in Fig. 1. In those chambers, infrared reflection absorption spectroscopy (IRRAS) system is installed to study the surface photochemistry on Si surfaces modified with various kinds of molecules.

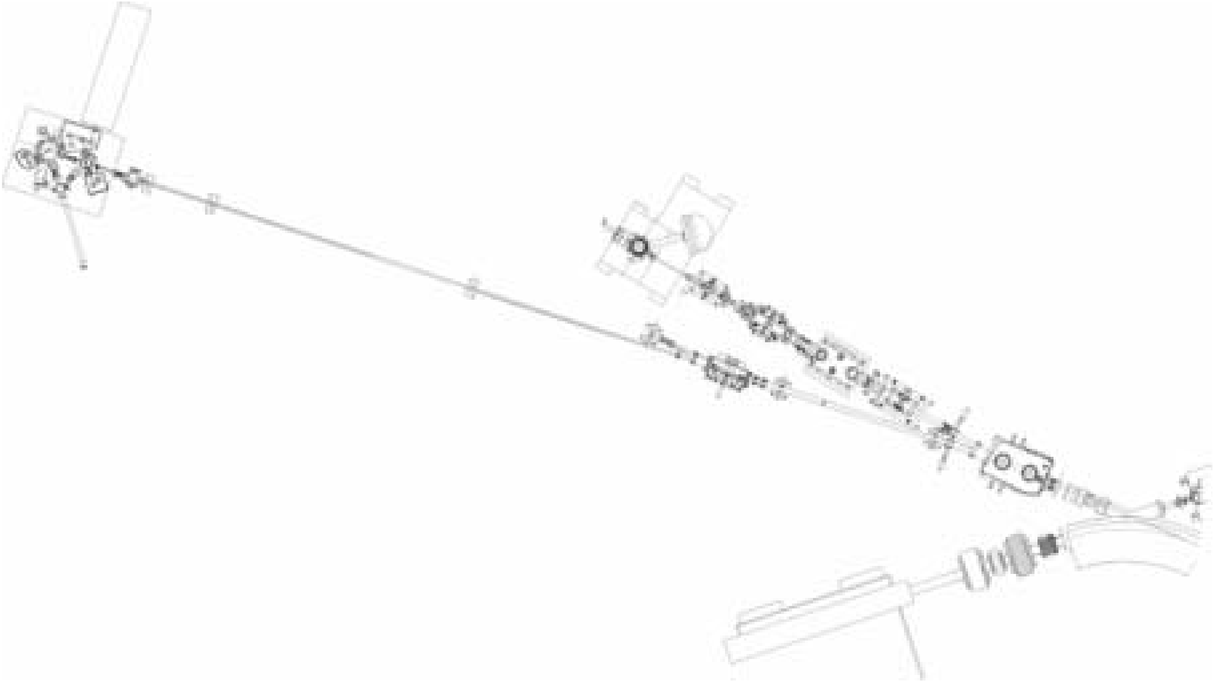

Fig. 1 Top view of BL4A2.

Beamline Specifications

Monochromator	None
Energy Range	The whole energy range of the synchrotron radiation
Resolution	—
Experiments	Synchrotron radiation chemical vapor deposition, and photo-etching experiments

BL4B

Varied-line-spacing Plane Grating Monochromator for Molecular Soft X-ray Spectroscopy

The beamline BL4B equipped with a varied-line-spacing plane grating monochromator (VLS-PGM) was constructed for various spectroscopic investigations in a gas phase and/or on solids in the soft X-ray range. Three holographically ruled laminar profile plane gratings with SiO_2 substrates are designed to cover the photon energy range from 25 eV to 800 eV. The gratings with the groove densities of 100, 267, and 800 l/mm cover the spectral ranges of 25-100, 60-300, and 200-1000 eV, respectively, and are interchangeable without breaking the vacuum. Fig. 1 shows the absolute photon flux for each grating measured by a Si photodiode (IRD Inc.), with the entrance- and exit-slit openings set at 50 and 50 µm, respectively. The maximum resolving power (E/ΔE) achieved for each grating is more than 5000.

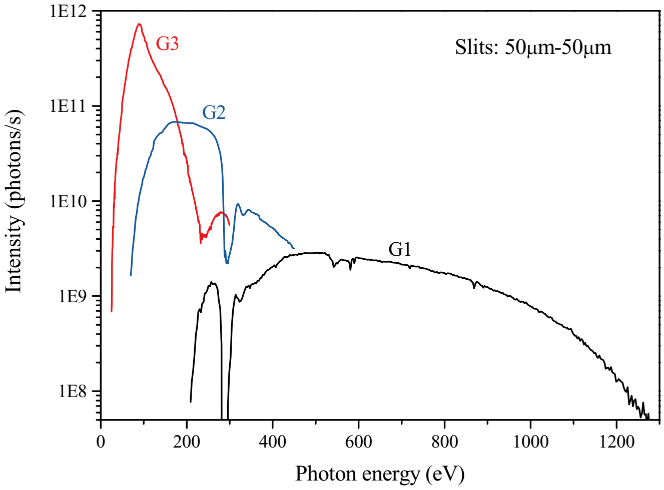

Fig. 1 Throughput from the VLS-PGM monochromator on BL4B.

Fig. 2 A photo of BL4B taken from the upper platform of BL3B.

Beamline Specifications

Monochromator	Varied-line-spacing Plane Grating Monochromator
Energy range	25-1000 eV
Resolution	E/ΔE > 5000 (at maximum)
Experiments	Soft X-ray spectroscopy (mainly, angle-resolved photoion spectroscopy for gaseous targets and photoelectron spectroscopy for gaseous and solid targets)

BL5U

Photoemission Spectroscopy of Solids and Surfaces

This beamline is designed for high-resolution angle-resolved photoemission study on solids and surfaces with the horizontal and circularly (CW, CCW) polarized synchrotron radiation from a helical undulator. The beamline consists of a Spherical Grating Monochromator with Translational and Rotational Assembly Including a Normal incidence mount (SGM-TRAIN), and a high-resolution angle-resolved photoemission spectrometer.

The SGM-TRAIN is an improved version of a constant-length SGM to aim the following points; (1) wide energy range of 5-250 eV, (2) high resolving power, (3) use of linearly and circularly polarized light, (4) reduction of second-order light, and (5) two driving modes by a computer control. The second-order light is well suppressed by using laminar profile gratings and combinations of mirrors and gratings.

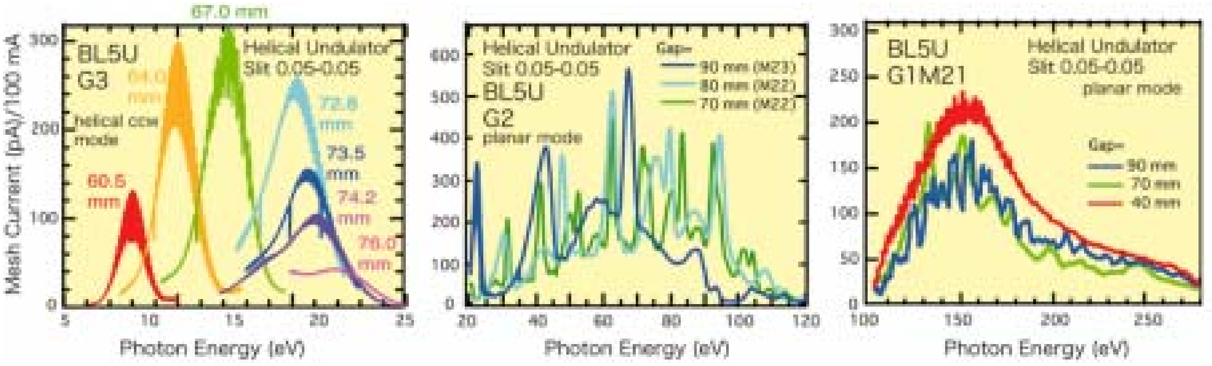

Fig. 1 Throughput from the SGM-TRAIN monochromator on BL5U.

Beamline Specifications

Monochromator	SGM-TRAIN
Energy Range	5-250 eV
Resolution	hν/ΔE >1000 for < 50μm slits
Experiment	ARPES, AIPES, XAS
Flux	<10^{11} photons/s for < 50μm slits (at the sample position)
Main Instruments	Hemispherical photoelectron analyzer (MBS-Toyama 'Peter' A-1), LEED of reverse type (OMICRON), Liq-He flow cryostat (5 – 400 K)

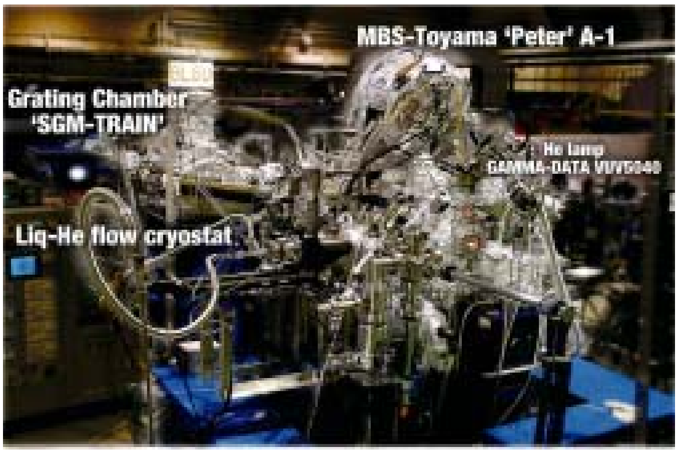

Fig. 2 High-resolution angle-resolved photoemission apparatus at BL5U.

BL5B

Calibration Apparatus for Optical Elements and Detectors

BL5B has been constructed to perform calibration measurements for optical elements and detectors. This beamline is composed of a plane grating monochromator (PGM) and three end stations in tandem. The most upstream station is used for calibration measurements of optical elements, the middle one for optical measurements for solids and the last for photo-stimulated desorption experiments. The experimental chamber at the most downstream station is sometimes changed to a chamber for photoemission spectroscopy.

The calibration chamber shown in Fig. 2 is equipped with a goniometer for the characterization of optical elements, which has six-degree-of-freedom; X-Y translation of a sample, and interchange of samples and filters. These are driven by pulse motors in vacuum. Since the polarization of synchrotron radiation is essential for such measurements, the rotation axis can be made in either horizontal or vertical direction (s- or p-polarization).

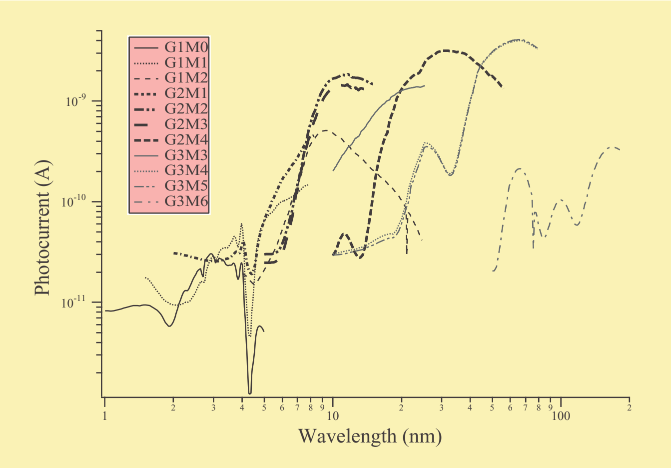

Fig. 1 Throughput spectra for possible combinations of gratings and mirrors at BL5B measured by a gold mesh.

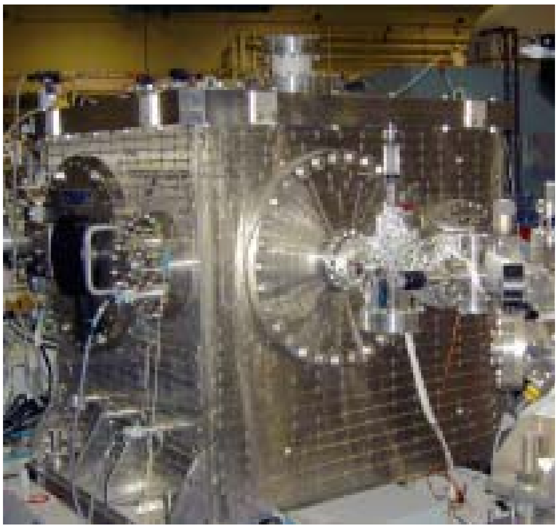

Fig. 2 A side view of the experimental chamber for calibration measurements.

Beamline Specifications

Monochromator	Plane Grating Monochromator
Energy range	6-600 eV (2-200 nm)
Resolution	E/ΔE ~ 500
Experiments	Calibration of optical elements, absorption of solids, photo-stimulated desorption from rare gas solids

BL6B (IR)

Infrared and Terahertz Spectroscopy of Solids

SR has a good performance (high brilliance and high flux) not only in VUV and SX regions but also in IR and terahertz regions. This beamline covers in the IR and terahertz regions. The previous beamline BL6A1 that has been constructed in 1985 is the pioneer of the infrared SR research. The beamline was upgraded in the spring of 2004 and the name was changed to be BL6B (IR). The front-end part including the bending duct #6 was replaced to a new one with higher acceptance angle using a magic mirror as shown in Fig. 1.

The beamline is equipped with two interferometers, one is Michelson-type (Bruker IFS-66v) and the other Martin-Puplett-type (JASCO FARIS-1), for the wide spectral region from several to 20,000 cm^{-1} ($h\nu$ = several 100 μeV – 2.5 eV) as shown in Fig. 2. The experimental chamber in which users bring can be equipped at the free port. In the near future, an IR microscope covering down to terahertz region will be set up.

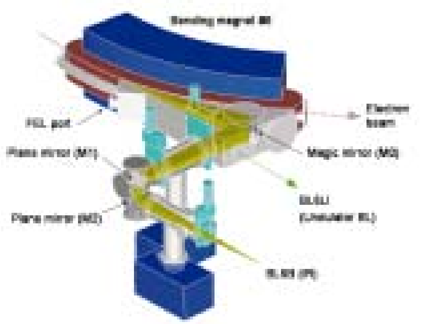

Fig. 1 The design of optics and front end of BL6B.

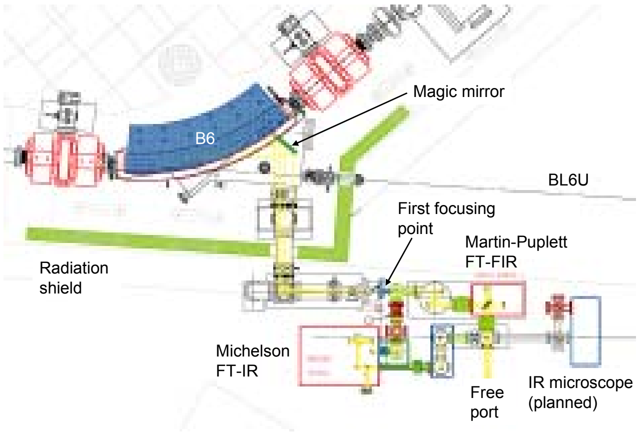

Fig. 2 Schematic figure of top view of BL6B.

Beamline Specifications

Interferometer	Michelson (Bruker IFS66v), Martin-Puplett (JASCO FARIS-1)
Wavenumber Range (Energy range)	several – 20,000 cm^{-1}, (several 100 μeV – 2.5 eV)
Resolution in cm^{-1}	0.1cm^{-1} for IFS66v, 0.25cm^{-1} for FARIS-1
Experiments	Reflectivity and transmission, Magneto-optics (Microspectroscopy)
Miscellaneous	Users can bring their experimental system in this beamline.

BL7U

High-Resolution Angle-Resolved Photoemission of Solids in VUV

The beamline BL7U is constructed to provide the photon flux with high energy resolution and high flux mainly for high-resolution angle-resolved photoemission spectroscopy of solids. The light source is an APPLE-II-type variable polarization undulator. The undulator light is monochromatized by the modified Wadsworth-type monochromator with three gratings (R=10 m; 1200, 2400 and 3600 lines/mm optimized at 10, 20, and 33 eV) is equipped. The monochromator has two normal-incident optics, one is a grating (G) and the other is a plane mirror (M1). The photon flux is strongly reduced at higher energy region. Then some multilayer coating mirrors with high reflection at special photon energies are equipped to M1. The beam size at the exit slit (S) position is reduced to 1/3 by the monochromator. After S, the light is focused on a sample by a troidal mirror (M3). The beam size is reduced to 1/2 by M3, then the beam size on the sample is 1/6 of the source size.

The beamline will be dedicated to users in 2007 autumn.

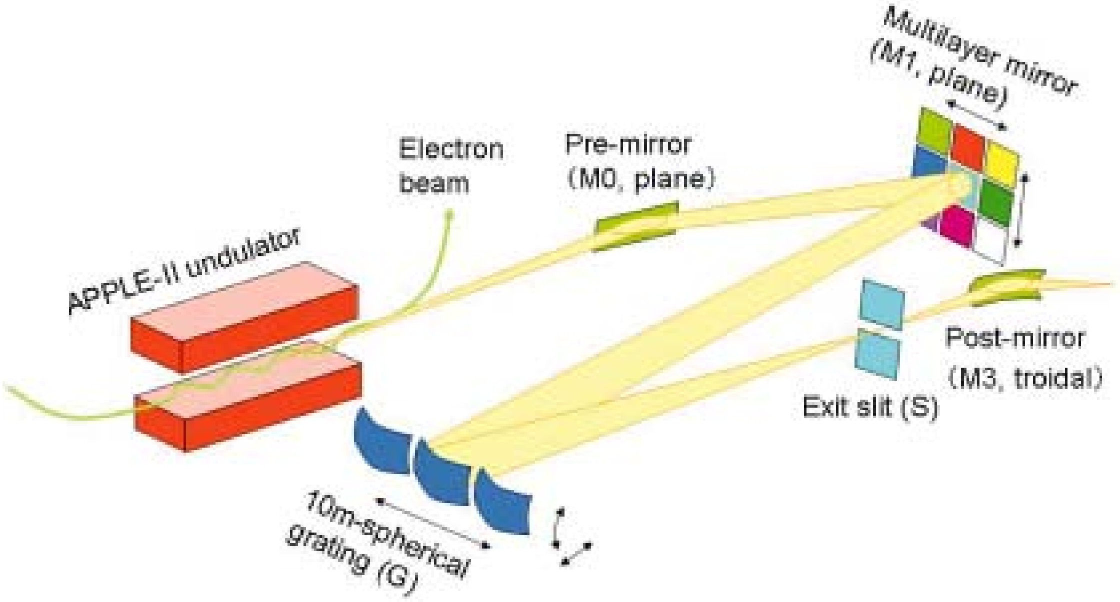

Fig. 1 Schematic figure of BL7U.

Beamline Specifications

Monochromator	10-m Normal Incidence Monochromator (modified Wadsworth-type)
Photon energy range	6 to 40 eV (λ = 30 - 200 nm)
Resolution	$E/\Delta E = 1\times10^4 \sim 5\times10^4$ (Expected)
Photon flux on sample	$\geq 10^{12}$ ph/s (Expected)
Beam size on sample	100(H)×10(V) μm^2 (Expected)
Experiments	Angle-resolved photoemission of solids, photo-chemistry, VUV microscopy

BL7B

3-m Normal Incidence Monochromator for Solid-State Spectroscopy

BL7B has been constructed to provide sufficiently high resolution for conventional solid-state spectroscopy, enough intensity for luminescence measurements, a wide wavelength coverage for Kramers-Kronig analyses, and the minimum deformation to the polarization characteristic of the incident synchrotron radiation. This beamline consists of a 3-m normal incidence monochromator which covers the vacuum ultraviolet, ultraviolet, visible and infrared, *i.e.* the wavelength region of 40 -1000 nm, with three gratings (1200, 600, and 300 l/mm). Two interchangeable refocusing mirrors provide two different focusing positions. For the mirror with the longer focal length, an LiF or a MgF2 window valve can be installed in between the end valve of the beamline and the focusing position. Figure 1 shows absolute photon intensity for each grating with the entrance and exit slit openings of 0.5 mm. A silicon photodiode (AXUV-100, IRD Inc.) was utilized for measuring the photon intensity and the absolute photon flux was estimated, taking the quantum efficiency of the photodiode into account.

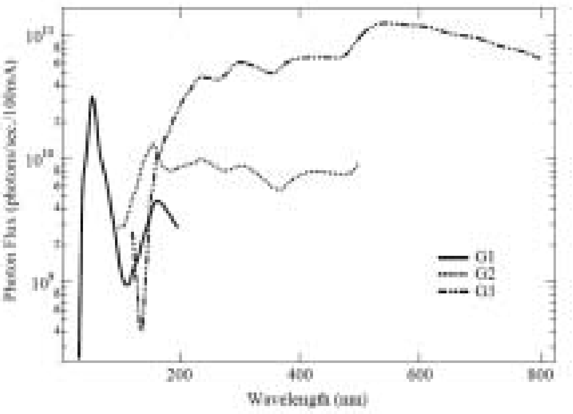

Fig. 1 Throughput spectra of BL7B measured by a silicon photodiode.

Fig. 2 Photo of BL7B.

Beamline Specifications

Monochromator	3-m Normal Incidence Monochromator
Wavelength Range	50 to 1000 nm (1.2 - 25 eV)
Resolution	$E/\Delta E$ = 4000 – 8000 for 0.01 mm slits
Experiment	absorption, reflection, fluorescence spectroscopy, mainly for solids

BL8B1

Spherical Grating Monochromator for Soft X-Ray Spectroscopic Studies on Solids and Surfaces

The beamline BL8B1 equipped with a constant-deviation constant-length spherical grating monochromator [1] provides soft X-ray photons in the energy range 30-800 eV with medium energy resolution. The photon energy range is covered by using three gratings (R=15 m; 1080 l/mm, R=15 m; 540l/m, and R=7.5m; 360 l/mm) which are interchangeable in vacuum. Figure 1 shows a throughput spectrum measured with the entrance- and exit-slit openings of 10 μm. Under this condition, the achievable resolving power is about 4000 at 400 eV and 3000 at 245 eV, respectively.

An experimental chamber is equipped for conventional measurements of electron yield spectra, or pseudo-photoabsorption spectra, under a ~1×10^{-6} Torr vacuum condition.

[1] Hiraya *et al.*, Rev. Sci. Instrum. **66** (1995) 2104.

Fig. 1 Photo of the monochromator at BL8B1.

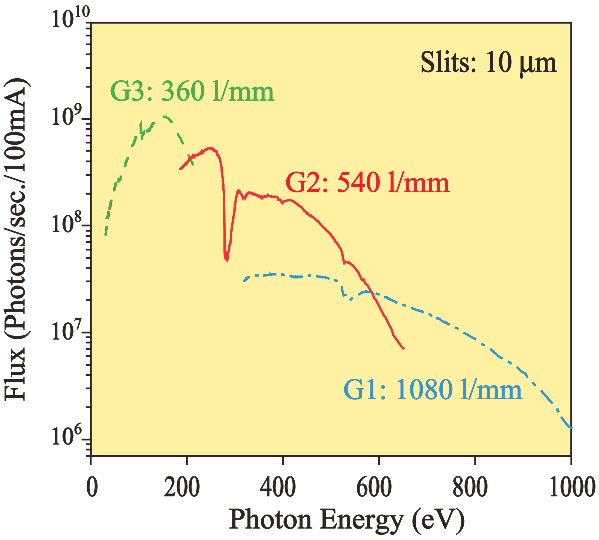

Fig. 2 Throughput of the monochromator at BL8B1.

Beamline Specifications

Monochromator	Constant-deviation constant-length spherical grating type
Energy range	30-800 eV
Resolution	E/ΔE = 4000 at 400 eV and 3000 at 245 eV
Experiments	Photoabsorption spectroscopy, electron spectroscopy and electron-ion coincidence spectroscopy for solids and surfaces

BL8B2

Angle-Resolved Ultraviolet Photoelectron Spectrometer for Solids

BL8B2 is a beamline for angle-resolved ultraviolet photoemission spectroscopy (ARUPS) system which is designed for measuring various organic solids such as molecular crystals, organic semiconductors, and conducting polymers. This beamline consists of a plane-grating monochromator (PGM), a sample preparation chamber with a fast entry Load-Lock chamber, a measurement chamber with an accurate for temperature dependence (base pressure 1×10^{-10} Torr), a cleaning chamber (base pressure 1×10^{-10} Torr), and a sample evaporation chamber (base pressure 3×10^{-10} Torr). The cleaning chamber is equipped with a back-view LEED/AUGER, an ion gun for Ar^+ sputtering, and an infrared heating unit. The PGM consists of premirrors, a plane grating, focusing mirror, and a post-mirror, with an exit slit. It covers the wide range from 2 to 130eV with exchanging two gratings (G1: 1200 l/mm, G2: 450 l/mm) and five cylindrical mirrors. The toroidal mirror focuses the divergent radiation onto the sample in the measurement chamber. The spot size of the zeroth-order visible light at the sample surface is about $1\times1\text{mm}^2$. Figure 1 shows the throughput spectra of PGM (slit=100 μm). The energy resolution at a slit width of 100 μm was found to be $E/\Delta E = 1000$ in the wavelength range from 2 to 130 eV. A hemi-spherical electron energy analyzer of 75 mm mean radius with an angular resolution less than 2° can be rotated around vertical and horizontal axes. The sample mounted on a manipulator can be also rotated around two axes.

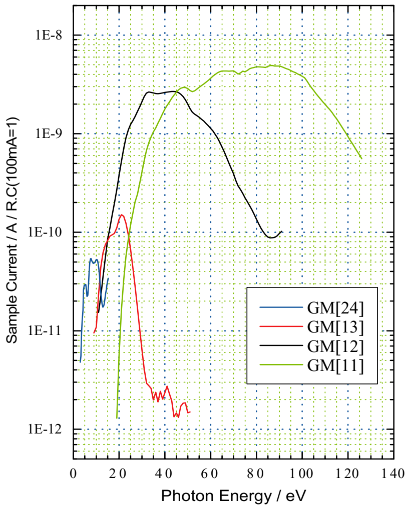

Fig. 1 Throughput spectra of plane-grating monochromator at BL8B2 (slit=100 μm).

Fig. 2 A photo of BL8B2.

Beamline Specifications

Monochromator	Plane-grating monochromator
Wavelength Range	9- 600 nm
Resolution	$E/\Delta E = 1000$
Experiment	Angle-resolved ultraviolet photoemission spectroscopy

Present Status of Main RF Cavity in UVSOR-II

A. Mochihashi[1], M. Katoh[1], M. Hosaka[1], K. Hayashi[1], J. Yamazaki[1], Y. Takashima[2],
H. Suzuki[3]
[1]*UVSOR Facility, Institute for Molecular Science, Okazaki 444-8585 Japan*
[2]*Graduate School of Engineering, Nagoya University, Furo-cho, Chikusa-ku, Nagoya 464-8603 Japan*
[3]*Toshiba Corporation, Tsurumi-ku, Yokohama, Kanagawa 230-0045 Japan*

As we have reported in the previous activity report[1] we have renewed main RF cavity in UVSOR-II electron storage ring in the last spring. Because of the renewal we have obtained the RF accelerating voltage up to 150kV that is about 3 times higher than the previous cavity voltage (55kV). Table 1 shows basic specifications of previous/present RF cavities. Compared to the previous cavity, basic design of the present cavity has no drastic change, however, unloaded-Q and shunt impedance (Rs) have improved extremely. Because of the performance, the RF accelerating voltage up to 150kV has been obtained by only changing the RF cavity itself: not changing RF transmitter.

Table 1 Specifications of previous/present cavities.

	Previous	Present
Frequency	90.1 MHz	90.1 MHz
Cavity voltage	55 kV	150 kV
Rs	1 MΩ	2.45 MΩ
Unloaded Q	8370	20300
Material	SUS + Cu	Cu (OFHC)
Cells	Re-entrant×1	Re-entrant×1
Inner diameter	1000mm	964mm
Bore radius	50mm	55mm

Until last spring UVSOR-II has been operated in 60nm-rad (achromatic) mode for daily users run, whereas immediate shift of the operating condition from 60nm-rad to 27nm-rad (chromatic) mode has also been strongly requested. In such a low-emittance condition, however, it was difficult to keep sufficient Touschek beam lifetime unless momentum acceptance was improved. Because the acceptance in UVSOR-II is mainly determined by the RF accelerating voltage, it is possible to improve Touschek beam lifetime by increasing the RF voltage. Fig. 1 shows the change in Iτ product on the RF voltage in the chromatic condition. In 750MeV, the product at 100/150kV has improved about twice/three times as much as that in the previous voltage of 55kV. Because of the improvement, the operating condition for users runs has been shifted from 60nm-rad to 27nm-rad mode after the installation of the present RF cavity. At present, typical Iτ product in daily users run (multi bunch, 27nm-rad) is about 1200 mA-Hour that is almost the same as that in previous operating condition (60nm-rad, 55kV). Beam-development study for obtaining much better beam lifetime still continues today.

Because of the improvement of the RF voltage, not only the improvement of the beam lifetime but also decrease in bunch length is expected. Fig. 2 shows experimental results and calculation of natural bunch length in 600/750 MeV under single-bunch operation in UVSOR-II. The natural bunch length has become 63/90 ps in 600/750 MeV when the RF voltage is 150kV; that corresponds to less than 70% in the previous cavity operation (55kV). The compression of the longitudinal bunch size can contribute short pulse SR experiment in single-bunch operation and improvement of laser gain in free electron laser[2].

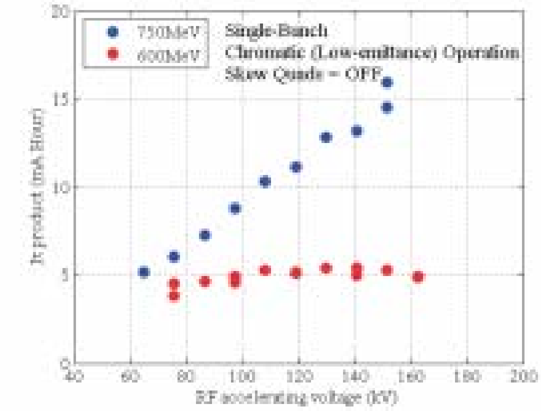

Fig. 1 Change in Iτ product on RF voltage.

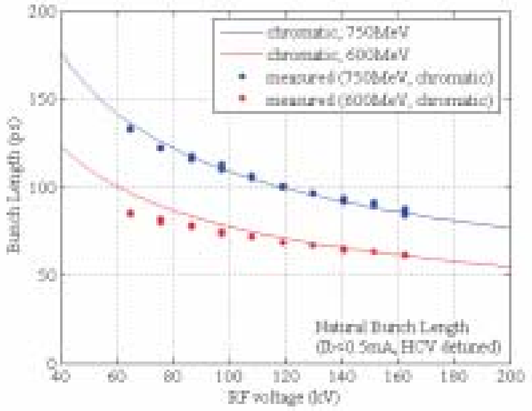

Fig. 2 Natural bunch length in various RF voltages.

[1] A. Mochihashi *et. al.,* UVSOR Act. Rep. 2004 (2005) 35.
[2] M. Hosaka *et. al.,* in this report.

Synchronization System of Mode-Locked Femto-Second Pulse Laser for Beam-Laser Experiment

A. Mochihashi[1], M. Hosaka[1], M. Katoh[1], Y. Takashima[2]
[1]*UVSOR Facility, Institute for Molecular Science, Okazaki 444-8585 Japan*
[2] *Graduate School of Engineering, Nagoya University, Furo-cho, Chikusa-ku, Nagoya 464-8603 Japan*

In previous activity reports [1,2,3] we have discussed feasibility of generation of ultra-short pulse synchrotron radiation and coherent synchrotron radiation by 'bunch slicing' method with ultra-short laser pulse. In 2005 March, we have installed a mode-locked femto-second pulse laser system whose wavelength is 800nm. With the system we have started to perform beam-laser experiment just after successful installation and tuning of the laser system. Here, we make a brief report of the system, especially for timing system that we have developed; with the timing system we have obtained sufficient synchronization between the laser pulse and the electron beam. Figure 1 shows a schematic diagram of the ultra-short pulse laser system. The laser system is mainly composed of mode-locked titanium-sapphire (Ti:Sa) laser (Coherent, Mira 900-F) that generates laser pulses that synchronize with the RF signal (f_{rf} =90.1MHz) of UVSOR-II and a regenerative amplifier (Coherent, Legend HE) that generates high intense femto-second pulse laser. Typical pulse duration and averaged power from Ti:Sa laser are 130fs and 1W. To make sufficient synchronization between the laser pulse and the electron beam, RF signal that comes from a pick-up coupler of RF accelerating cavity is used for the mode-locking signal. Typical frequency resolution of the cavity length actuator in the mode-locked laser is f_{rf}±100Hz. The seed laser pulses from the Ti:Sa laser are injected into the regenerative amplifier that makes high intense laser pulse whose power is typically 2.5mJ/pulse. The regenerative amplifier is driven by Q-switched pump laser whose averaged power is 30W. The repetition of the Q-switched laser f_Q is based on sub-harmonics of revolution frequency f_{rev} ($=f_{rf}/16$=5.6MHz), namely, $f_Q=f_{rev}/5632$=1kHz. Because of the synchronization with the sub-harmonics of the beam revolution, the regenerative amplifier can be driven in sufficient synchronization with the beam revolution despite the repetition rate. To select and fix the electron bunch which the laser pulse cuts, an RF bucket selector that can change the timing of the beam revolution signal with a unit of bunch spacing time is used for making the Q-switching trigger signal. To adjust the timing of the laser pulse within the bunch spacing time precisely, a phase of the RF signal from the RF cavity can be changed with a phase shifter. Typical timing jitter for the Q-switching trigger signal is less than 20ps that is negligible compared to the bunch spacing time of UVSOR-II. The high-intense pulse laser is transported from a laser room to a viewing port that is usually used for extraction port of storage ring free electron laser (SR-FEL) [4] through into pipes in the atmosphere. The laser pulses pass through a long straight section in which a helical/linear undulator is settled, and they interact with the electron beam in the undulator section. Because both spontaneous undulator radiation from the electron bunch and the pulse laser can be observed from another viewing port that is settled in the opposite side of the extraction port of the SR-FEL, the condition of the synchronization between the beam and the laser pulse can be verified easily.

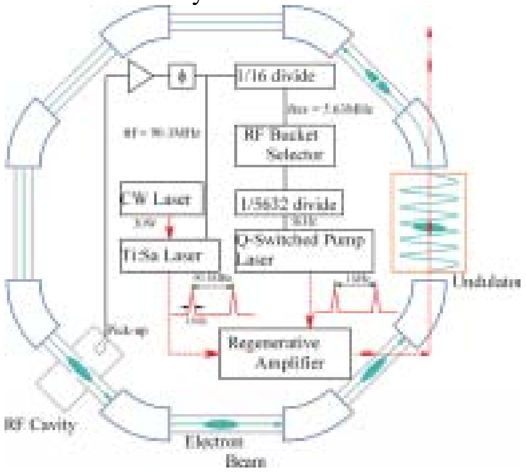

Fig. 1 Schematic diagram of the ultra-short pulse laser system.

Just after the installation of the laser system, we have started beam-laser experiment based on 'bunch slicing' scheme, especially for generation of infra-red coherent synchrotron radiation [5] and coherent harmonic generation experiment [6]. In parallel with the experiments we still continue estimation of basic performance of the pulse laser system; especially for the timing jitter and stability between the laser pulse and the electron bunch that are key issues of the beam-laser experiment.

[1] Y. Takashima *et. al.,* UVSOR Act. Rep. 2001 (2002) 43.

[2] Y. Takashima *et. al.,* UVSOR Act. Rep. 2002 (2003) 56.

[3] Y. Takashima *et. al.,* UVSOR Act. Rep. 2003 (2004) 33.

[4] M. Hosaka *et. al.,* in this report.

[5] M. Katoh *et. al.,* in proc. of European Particle Accelerator Conference 2006 (to be presented).

[6] M. Labat *et. al.,* in proc. of European Particle Accelerator Conference 2006 (to be presented).

Development of an Orbit Feedback System at UVSOR-II

K. Suzumura[1], M. Katoh[2], Y. Takashima[1], K. Hayashi[2], A. Mochihashi[2], J. Yamazaki[2], M. Hosaka[2]

[1]*Graduate School of Engineering, Nagoya University, Chikusa-ku Nagoya 464-8603 Japan*

[2]*UVSOR Facility, Institute for Molecular Science, Okazaki 444-8585 Japan*

Abstract

The drift of the electron orbit on a synchrotron light source causes a drift of the light source position, which makes harmful effects on the users experiments. To minimize the effect, we have developed a feedback system correcting automatically the drift of electron orbit by controlling RF frequency. The system is routinely operating now, and the drift of electron orbit is suppressed.

Feedback System

We have developed a feedback system to correct the electron orbit. The following is the principle of the correction. If we make the RF frequency of the storage ring smaller, the electron orbit should extend outward to keep the synchronization with RF acceleration. If we do opposite operation, it should be on the inside. The feedback system corrects the electron orbit by the use of this mechanism.

Fig.1 shows the flow chart of the feedback system. First, the displacements of electron orbit from a standard orbit is obtained by a BPM(Beam Position Monitor) system, which measures the beam position at 24 points in the ring. Second, a program calculates RF frequency “ δf_{RF} ” which is pertinent to the correction with the use of a formula as follows;

$$\delta f_{RF} = \frac{\alpha \cdot f_{RF}}{\sum^{24} \eta_i} \sum^{24} \delta X_i$$

At the last, the program transfers the value of RF frequency to the master oscillator of the RF system. The program continues doing a set of these actions every 10 seconds. The program has a checking function to prevention of transferring abnormal value of RF frequency calculated by some unexpected reason. We can previously set allowable range of RF frequency and beam current in the system. If the value of RF frequency calculated at second step is out of the range we have set, the transferring should be cancel. The same goes for beam current.

Result and Discussion

Fig.2 shows the orbit drift in the horizontal plane of a day before introduction of the feedback system, and Fig.3 shows that of after introduction. It is clear that the displacement of each point has been closer to the standard orbit. The two lines being distant from standard orbit, the yellow and green line, are exceptions. The BPMs of these lines are installed on a vacuum duct which has some trouble on the water cooling system. It is highly possible that the apparent orbit displacement is caused by the thermal deformation. These two points are removed in the calculation of the RF frequency.

Conclusion

We have developed an orbit feedback system. The system was successfully commissioned. The orbit drift in the horizontal plane has been suppressed at some level.

Future, we aim more accurate correction by using the correction electrical magnets, and we should correct the orbit drift in the vertical plane.

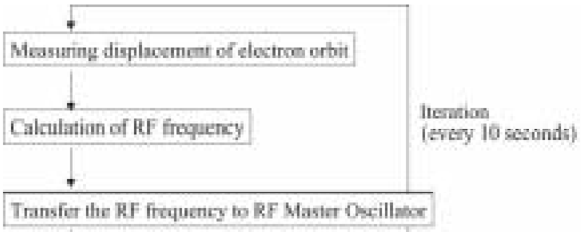

Fig. 1 Block diagram of the feedback system.

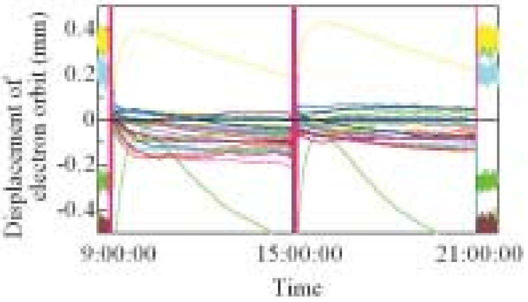

Fig. 2 Displacement of a day before introduction of the feedback system.

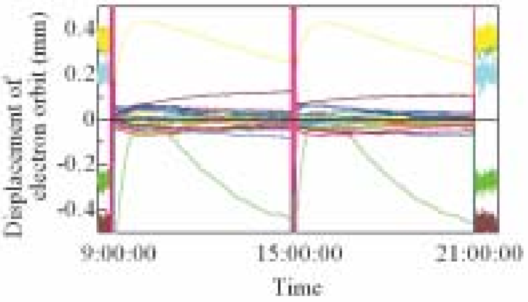

Fig. 3 Displacement of a day after introduction of the feedback system.

Correlation of Terahertz Bursts with Bunch Motion at UVSOR-II

Y. Takashima[1], M. Katoh[2], M. Hosaka[2], A. Mochihashi[2], S. Kimura[2], T. Takahashi[3]
[1]*Graduate School of Engineering, Nagoya University, Chikusa-ku Nagoya 464-8603 Japan*
[2]*UVSOR Facility, Institute for Molecular Science, Okazaki 444-8585 Japan*
[3]*Research Reactor Institute, Kyoto University, Kumatori-cho, Osaka, 590-0494 Japan*

We have observed intense far-infrared synchrotron radiation at the beam line BL6B of UVSOR-II storage ring operated in single bunch modes.[1] The peak intensity of the bursts is about 10000 times larger than the intensity of synchrotron radiations in the same wavelength region observed in normal multi-bunch modes. The duration and the period of the bursts are about 200 μsec and 10 - 15 msec, respectively. Each burst consists of several quasi-periodic micro-bursts whose periods are about 30 μsec. The period is close to the half of the synchrotron period and the bunch length is changed for the same period of the bursts.

Experiments and Results

We measured the bursts of far-infrared synchrotron radiation at the beam line, BL6B(IR) constructed for using the synchrotron radiation of infrared region.[2] During the experiments, the UVSOR-II storage ring was operated in single bunch mode and the electron beam energy was 600 MeV.

We used a liquid-helium-cooled InSb hot electron bolometer to detect the terahertz radiations. The detector was sensitive to the wavelength region between 0.2 mm and 3 mm. The response of the detector was several microseconds.

Fig. 1 shows typical time structure of individual burst at 201 mA. The each burst contains several peaks which appear quasi-periodically. The period time is about 30 μs. The period of the micro-bursts of about 30 μs is close to the half value of the inverse of the synchrotron frequency of 14.4 kHz. We changed the RF accelerating voltage from 55 to 28 kV and observed the change of the periodic microstructure of the bursts. In this condition, the synchrotron frequency was changed to 10.3 kHz. As shown in the Fig. 2, the period of the micro structure was changed to about 45 μs and is also close to the half value of the inverse of the synchrotron frequency of 10.3 kHz in this condition.

Fig. 3 shows the terahertz bursts and the electron bunch length. The bunch length is derived by the measurement of synchrotron radiation by using a streak camera and the measurement was performed at the same time as the measurement of terahertz bursts. The bunch length is changed periodically and the period is the same as that of the terahertz bursts. There is strong correlation between the generation of the bursts and the bunch motion.

Summary

We observed bursts of far-infrared synchrotron radiation in the wave length region between 0.2 mm and 3.0 mm at BL6B of UVSOR-II. Each bursts contains many peaks whose period is close to the half of the synchrotron period. We measured the bunch length at the same time as the measurement of the bursts and the bunch length is changed in the same period as the generation of the bursts. These may suggest that the bursts are generated by longitudinal density modulations and their evolutions in the bunches.

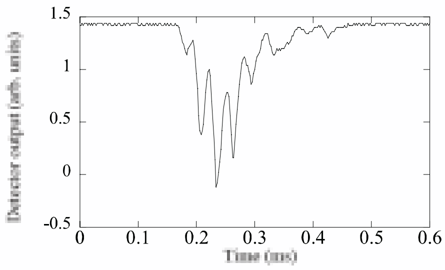

Fig. 1 Time structure of a burst (Ib=201mA).

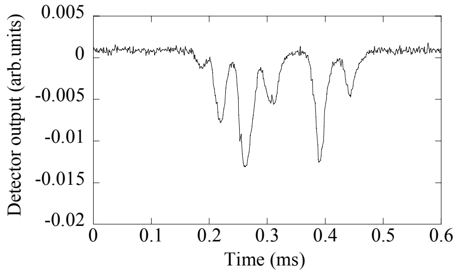

Fig. 2 Time structure of a burst (Ib=197mA,Vrf=28kV).

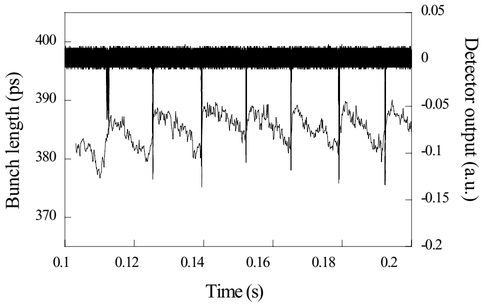

Fig. 3 Terahertz bursts and bunch length (Ib=183mA).

[1] Y. Takashima *et al.*, Jpn. J. Appl. Phys., **44** (2005) L1131.
[2] S. Kimura *et al.*, AIP Conf. Proc. **705** (2004) 416.

BL5U(FEL)

Deep UV Lasing around 215 nm on the UVSOR-II FEL

M. Hosaka[1], M. Katoh[1], A. Mochihashi[1], K. Hayashi[1], J. Yamazaki[1], Y. Takashima[2]
[1]UVSOR Facility, Institute for Molecular Science, Okazaki 444-8585 Japan
[2]Graduate School of Engineering, Nagoya University, Furo-cho, Chikusa-ku, Nagoya 464-8603 Japan

On a storage ring free electron laser (FEL), quality of the electron beam is a critical issue for lasing in a short wavelength region. At UVSOR-II, we have continued to improve the performance of the electron beam since 2002. We replaced an accelerating rf cavity in early 2005 and can operate it in higher voltage by factor 3 [1]. Since the FEL gain is proportional to the bunch length, this upgrade is very effective to the FEL. With the electron beam of upgraded performance, we succeeded in lasing around the wavelength of 215 nm that is the shortest wavelength in the UVSOR. In this article, we report on the lasing experiment.

So far the shortest wavelength of the UVSOR-FEL had been 239 nm. In order to meet the recent demand from users, we tried lasing in shorter wavelength region around 215 nm. In the former experiment, multi–layers of HfO_2/SiO_2 were employed as cavity mirrors. The oxide can not be employed for the lasing of 215 nm because the band-gap of HfO_2 is about 5.6 eV (220 nm). Then multi-layers of Al_2O_3/SiO_2 were chosen for the lasing: the band-gap of Al_2O_3 is about 7 eV (180 nm). Since refraction index of Al_2O_3 is smaller than that of HfO_2 , the number of layers of the mirrors should be increased. On the other side, we need high transmission to extract high out-coupled power for users' experiment. Compromising reflectivity and transmission, we chose numbers of layer of 49 for forward mirror and of 37 for backward mirror, from which an FEL power is extracted. The expected round-trip reflectivity of the mirrors is 99.3 % and the transmission of the backward mirror is 0.5 %.

Preparatory to a lasing experiment, we measured the round-trip reflectivity of the mirrors by ring-down method with a low electron beam current. The measured value was round 97.8 %, which was much smaller than expected one. We suppose that a degradation due to synchrotron radiation from the undulator is serious in case of Al_2O_3/SiO_2 mirror. The first lasing experiment was made with an electron energy of 600 MeV, which is ordinal energy for the FEL experiment. Fig. 1 shows a measured FEL spectra using a spectroscope. The measured spectral line width (0.075 nm) is limited by the resolution of the spectroscope. Although the reflectivity of the mirrors is not so high, the lasing continued at the threshold beam current of 11 mA/bunch because of the high FEL gain (Fig. 2). As a next step of the experiment, we increased the electron energy from 600 MeV to 750 MeV. Storing a high beam current in the storage ring, we obtained successful lasing. As seen in Fig.2, the measured threshold current for lasing at 750 MeV is about two time higher than at 600 MeV, however, we obtained much higher power at a beam current of higher than 50 mA/bunch. Moreover, the measured lifetime of the electron beam was about 3 times longer. These characteristics are very favorable for application experiments. Hereafter, we are going to employ the 750 MeV operation for users experiment

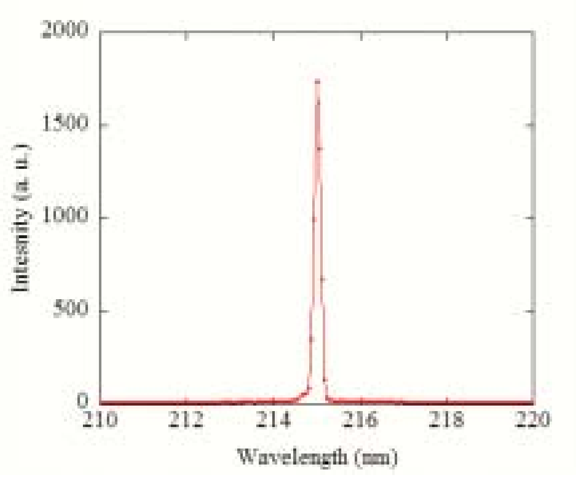

Fig. 1 Measured FEL spectrum at 215 nm.

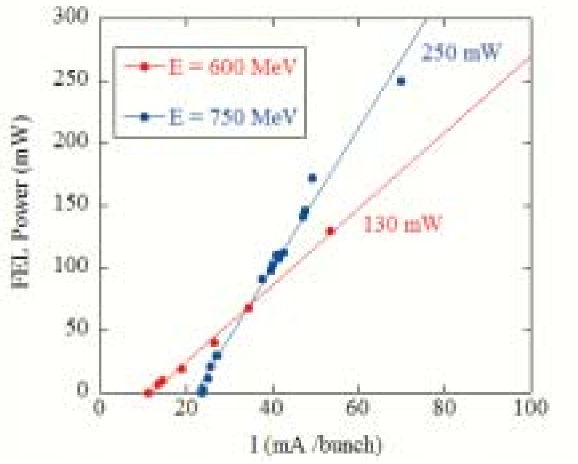

.

Fig. 2 Measured FEL out-coupled power around λ = 215 nm at electron energies of 600 MeV and 750 MeV.

[1] A. Mochihashi *et. al.,* in this report.

BL2B

Photofragment Imaging Apparatus for Measuring Momentum Distributions in Dissociative Photoionization of Fullerenes

B. P. Kafle[1], H. Katayanagi[1, 2], K. Mitsuke[1, 2]

[1]*Department of Vacuum UV Photo-Science, Institute for Molecular Science,*
Okazaki 444-8585 Japan

[2]*Graduate University for Advanced Studies, Okazaki 444-8585 Japan*

In dissociative photoionization of solitary fullerenes (C_{60}, C_{70}), we have measured the fragment ($C_{60-2n}{}^{z+}$, $C_{70-2n}{}^{z+}$) yield curves in the photon energy range of 45-150 eV [1,2]. From the results it is concluded that the excess energy is statistically distributed among the internal degrees of freedom of the parent ions ($C_{60-2n}{}^{z+}$, $C_{70-2n}{}^{z+}$) and C_2 units are ejected sequentially. Moreover, the results imply that the dissociation has no potential barrier and that no resonant state participates in the dissociation. To clarify these implications, we designed the photofragment imaging apparatus based on the time-of-flight mass spectrometer that we had constructed. From the photofragment images, we will be able to extract the kinetic energy and angular distributions of the fragments. These distributions reveal clearly whether there exist a barrier and/ or resonance.

We adopted the Eppink-Parker type velocity focusing electrodes [3] to achieve the kinetic energy resolution of ca. 0.01 eV on the photofragment images. To select a bunch of fragments having the same mass-to-charge ratio m/z from neighboring bunches (m±24)/z, for example, separating $C_{58}{}^{+}$ from $C_{60}{}^{+}$ and $C_{56}{}^{+}$, we designed a mass gate which consists of a cylindrical potential switch and retarding electrodes. In order to optimize the dimensions of the setup, we performed ion trajectory simulations utilizing SIMION version 7.0 [4]. The most suitable dimensions were achieved already as depicted in the Fig. 1.

The operation principle of this setup is as follows: As long as the tube of the potential switch is kept grounded, all fragments are reflected back by the retarding electrode and do not impinge an imaging detector. When an entire bunch of fragments having a desired mass enters inside the tube, the pulsed voltage is applied to the tube. The potential felt by the bunch are suddenly elevated and the bunch passes through the retarding electrode and thus can reach the 2D detector.

Parts of this setup are being fabricated at the machine shop in the Institute for Molecular Science. The parts will be installed in the end-station at the BL2B in the UVSOR facility, where the synchrotron radiation from bending magnet is dispersed by the 18-m spherical grating grazing incidence monochromator of dragon type. We are planning to examine the performance of the apparatus using SF_6 as a standard sample.

[1] J. Kou *et al.*, Phys. Chem. Chem. Phys. **7** (2005) 119.

[2] K. Mitsuke *et al.*, Am. Inst. Phys. CP **811** (2006) 161.

[3] A.T.J.B. Eppink and D.H. Parker, Rev. Sci. Instrum. **68** (1997) 3477.

[4] D.A. Dahl, SIMION 3D 7.0, Scientific Instrument Services Inc., Boise Idaho, 2000.

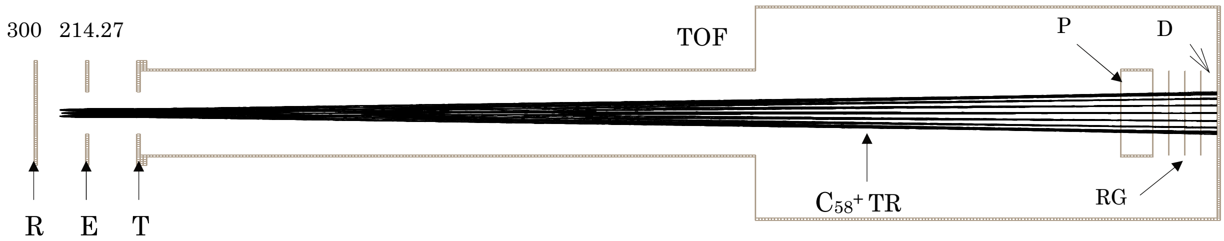

Fig. 1 Schematic 2D view of the imaging lens setup in combination with potential switch and kinetic energy analyzer. Trajectories of $C_{58}{}^{+}$ fragment ions having initial KE of 0.1 eV are drawn. R: Repeller; E: Extractor; T: Tube Electrode (grounded); TOF: TOF Tube; P: Potential switch; RG: Retarding grid; D: Detector.

BL2B

Development of an Apparatus for Coincidence Measurements of Threshold Electrons and Ions Produced by Dissociative Photoionization of Fullerenes

H. Katayanagi[1,2], B. P. Kafle[2], S. I. Prodhan[2], K. Mitsuke[1,2]
[1]*Department of Vacuum UV Photo-Science, Institute for Molecular Science,*
Okazaki 444-8585 Japan
[2]*Graduate University for Advanced Studies, Okazaki 444-8585 Japan*

We developed an apparatus for threshold electron – photoion coincidence (TEPICO) measurement to make clear the photodissociation mechanism of gaseous fullerenes (C_{60}, C_{70}).

We had measured yield curves of photoions which were produced by dissociative photoionization of the fullerenes with the synchrotron radiation in the photon energy range of 45 – 150 eV [1,2]. We found that the fullerenes lose C_2 units sequentially. As a result, we concluded that the photodissociation mechanism can be described by statistical energy redistribution. We derived this conclusion from the comparison between the experimental yield curves and results of the RRKM calculation performed by us. In this comparison, in order to evaluate internal energies of parent fullerene ions, we assumed that the energy of the photoelectrons is zero. This assumption, however, is valid only at onsets of yield curves. At the onsets, it is appropriate that all the excess energy change to the internal energy of parent ions and zero kinetic energy (threshold) electrons be emitted. We thus could make the comparison only close to the onsets. Once high-energy electrons begin to be emitted, we cannot convert the photon energy directly to the internal energies of the parent ions because a portion of excess energy is transmitted to a kinetic energy of emitted electrons.

A photoelectron – photofragment coincidence measurement allows us to regulate the internal energies of the parent ions. Using the TEPICO technique, the internal energies are directly related to the energy of the synchrotron radiation. Development of a TEPICO apparatus enables us to discuss the dissociation mechanism beyond the onsets.

We designed a set of electrodes to perform the TEPICO measurement. The set was produced at the machine shop in IMS and installed in an endstation at the beamline 2B in UVSOR. Figure 1 shows sectional view of an assembly of the electrodes. The operation principle is as follows. We utilized "dark gaps" in which electron bunches were thinned out in a temporal profile of the synchrotron radiation. No ionization takes place during the dark gap. While the threshold electrons can linger at the ionization region even in the dark gap, high-energy electrons escape immediately. Only the threshold electron signals are detected by an application of a pulsed voltage to an electron repeller (b) after escaping of the high-energy electrons. Using the electron signal as a trigger to apply a pulsed voltage to an ion repeller (c), photofragments produced simultaneously with threshold electrons can be detected.

Prior to an application to fullerenes, we examined the efficiency of our apparatus to select threshold electrons using helium and oxygen as samples. Figure 2 shows threshold electron spectrum of oxygen. A peak was observed at 24.56 eV and its energy corresponded to a transition to the c ($^4\Sigma_u^-$) state. The spectra, however, suffer from intense background. The background consists of high-energy electrons emitted by transitions to lower energy states than c ($^4\Sigma_u^-$) and electrons generated by stray light.

Although we succeeded in observing threshold electrons from gaseous samples, the background needs to be reduced to the utmost in order to perform the TEPICO measurement. It is necessary that we improve the efficiency to collect threshold electrons. Electron trajectory simulations to seek for the best design of the electrodes are under way.

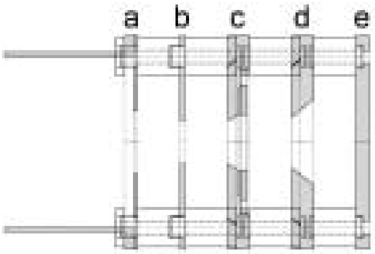

Fig. 1 Sectional view of the TEPICO electrode assembly. Symbols in the figure stand for a: entrance of ion TOF tube, b: electron repeller, c: ion repeller, d: ground plate, e: MCP support plate (made of Teflon). Ionization region is between b and c. Metal mesh is put at each hole.

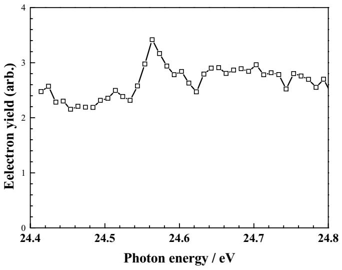

Fig. 2 Threshold electron spectrum of oxygen.

[1] J. Kou *et al.*, Phys. Chem. Chem. Phys. **7** (2005) 119.

[2] K. Mitsuke *et al.*, AIP Conference Proceedings **811** (2006) 161.

BL3U

Improvement of the Horizontal Beam Size at the XES Endstation of BL3U

T. Hatsui[1], T. Horigome[2], N. Kosugi[1]
[1]*Dept. of Vacuum UV photoscience, Institute for Molecular Science, Okazaki 444-8585 Japan*
[2]*UVSOR Facility, Institute for Molecular Science, Okazaki 444-8585 Japan*

Last year we constructed an XES (x-ray emission spectroscopy) endstation of the undulator beamline BL3U. High-resolution soft-x-ray emission spectroscopy generally requires small beam size at the sample position, because a smaller opening of the spectrometer entrance slit is needed to achieve higher energy resolution. At the XES endstation of BL3U, we have installed a transmission-grating spectrometer for high-energy resolution XES. In order to get the maximum energy resolution, the spectrometer demands a beam size of 1 µm in the energy dispersion direction, which is achieved by an entrance slit with an opening of 1-30 µm. In contrast to the conventional Rowland spectrometer, the present spectrometer demands a beam size less than 200 µm in the non-dispersion direction as well. This is because the spectrometer is equipped with an Wolter type I pre-mirror with a collection angle as high as 1.5 x 10^{-3} sr at the expense of a considerable aberration [1]. In the case of solid samples, where small grazing angle of 20 ° is used in order to avoid self absorption, horizontal beam size of less than 68 µm (=200*sin 20°) is required.

Since April 2005, the beam emittance of the operation mode of the UVSOR-II ring has been upgraded from 60 nm-rad to 27.4 nm-rad. The horizontal electron beam size at the BL3U undulator has been improved from 890 to 602 µm (σ), accordingly. As depicted in Fig. 1, the horizontal beam profile at the sample position is an image of the horizontal electron source profile demagnified by the M2X mirror (1/23.4). Thus, the horizontal beam size is expected to be smaller since April 2005 owing to the upgraded operation mode.

The horizontal beam size has been measured by using a knife-edge method. By fitting with an error function, we have obtained a full width half maximum FWHM for the horizontal direction of 41.2 µm at 115 eV as shown in Fig. 2, where the beam profile obtained in October 2005 is compared with the one taken in Dec. 2004. The results clearly show that the smaller emittance offered smaller beam size in the horizontal direction. The current horizontal beam size is 57 % of the one in 2004 in accord with the reduction of the electron beam size.

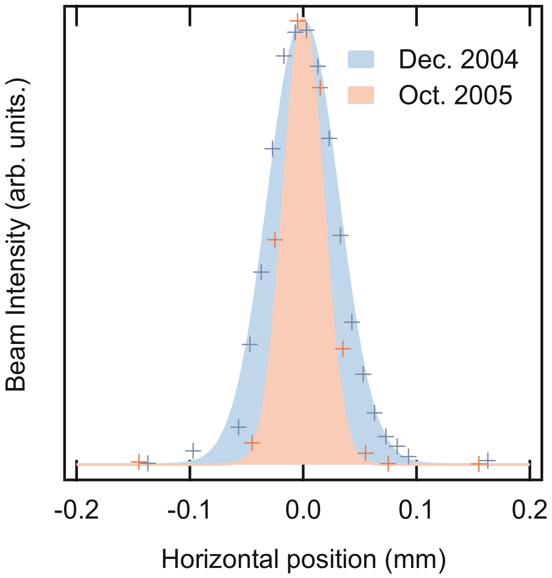

Fig. 2 Horizontal Beam Profile at the sample position ($h\nu$= 115 eve) measured in Dec. 2004 and October 2005 with FWHM of 72.1±1.3 µm and 41.2±1.46 µm, respectively.

[1] T. Hatsui, H. Setoyama, E. Shigemasa and N. Kosugi, J. Electron Spectrosc. Relat. Phenom. **144** (2005) 1059.

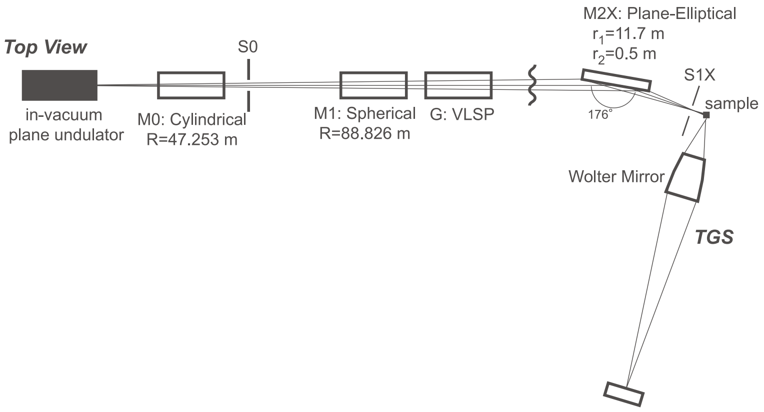

Fig. 1 Schematic Optical Layout of BL3U in XES mode.

BL3U

Development of a Transmission-Grating Spectrometer for High-Resolution Soft X-Ray Emission Studies

T. Hatsui[1], T. Horigome[2], N. Kosugi[1,2]

[1]*Dept. of Vacuum UV photoscience, Institute for Molecular Science, Okazaki 444-8585 Japan*

[2]*UVSOR Facility, Institute for Molecular Science, Okazaki 444-8585 Japan*

High resolution soft x-ray emission spectroscopy (XES) in combination with synchrotron radiation as incident soft x-rays has been extensively are used to study valence states of solid, liquid, and gas phase systems. The design of their grazing-incidence spectrometer is based on the Rowland circle mount. In this case, the horizontal acceptance angle is mainly limited by the detector size. In order to achieve higher resolution, the Rowland radius, R, or the spectrometer size, should be larger due to the relationship of $\lambda/\Delta\lambda \propto R$. The detector size is however limited. It is therefore desirable to design a novel optical system which can focus the emitted x-rays not only in the (vertical) dispersion direction but also in the other (horizontal) direction. In addition, recent advances make the charge-coupled devices (CCD) a promising soft-x-ray detector. It is however not a trivial problem to adopt it in the high resolution Rowland spectrometer, since the CCD detectors have low quantum efficiency at the small grazing-incidence angle.

In order to overcome these difficulties, we have developed a transmission-grating spectrometer (TGS). This spectrometer is designed to realize a resolution E/ΔE up to 5000 in the energy region of 50-600 eV with high throughput (Fig. 1) [1]. The spectrometer has a Wolter type I premirror, a free-standing transmission grating (TG), and a back-illuminated CCD. The Wolter mirror with a high collection angle of 1.5×10^{-3} sr shows a slope error better than 0.4 arcsec [2]. A self-standing TG made of silicon carbide with a groove density of 6250 lines/mm has been developed [3]. The UHV compatible back-illuminated CCD has been developed [4]. By measuring the center of the electron charge cloud generated in depletion layer [4], the spatial resolution of the CCD was found to be less than 2 μm for photon energy larger than 500 eV. The CCD detector is mounted at 1.472 m downstream of the grating on a Rowland torus mount. Diffracted x-rays are detected in the normal incidence geometry, resulting in high detection efficiency. Ray-trace simulations using TGSGUI code [5] indicate that aberrations do not practically degrade the energy resolution as high as 5000 [1]. The energy resolution was examined by measuring the diffuse scattering of 114 eV photons. Without the entrance slit, TGS shows an energy resolving power of 3000 with high count rate, where the resolution is limited by the source size. Further evaluation of the performance by introducing the entrance slit has been carried out with a slit opening of 1 μm. The results indicated that the energy resolution is better than 4500 at 114 eV (Fig. 2).

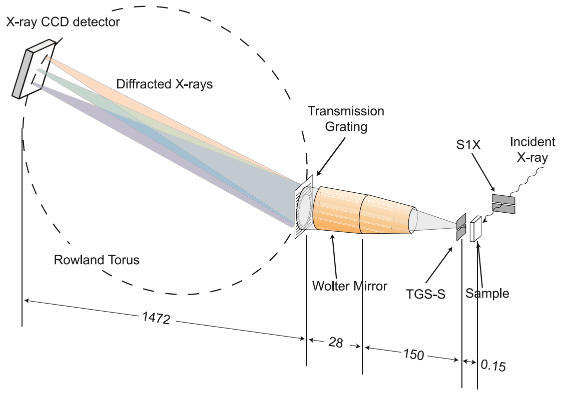

Fig. 1 Schematic Layout of the transmission grating spectrometer The distances between the optical elements are shown in mm (not to scale).

[1] T. Hatsui *et al.*, J. of Electron Spectrosc. Relat. Phenom. **144** (2005) 1059.
[2] Manufactured by A. Ohba, S. Onoda, and Y. Sugiyama (Hamamatsu Photonics).
[3] Manufactured by NTT-ATN.
[4] J. Hiraga *et al.*, Jpn. J. Appl. Phys. **40** (2001) 1493.
[5] T. Hatsui, http://www.uvsor.ims.ac.jp/TgsguiHatsui/index.html

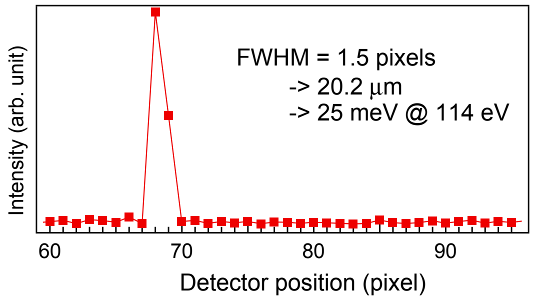

Fig. 2 Intensity profile of 114 eV x-rays on the CCD detector along the dispersion direction.

BL4A2

Beamline BL4A2 for Synchrotron Radiation Etching Using XeF_2 as Reaction Gas

N. Nakai[1], H. Uno[2], R. Tero[1,2], K. Suzui[2], T. Makimura[3], K. Murakami[3], T. Urisu[1,2]
[1]*The Graduate University for Advanced Studies, Okazaki 444-8585 Japan*
[2]*Dept. Vacuum UV Photoscience, Institute for Molecular Science, Okazaki 444-8585 Japan*
[3]*Institute of applied physics, Tsukuba Univ., Tsukuba 305-8577 Japan*

Synchrotron radiation etching has unique characteristics such as low damage, beam induced (spatially localized) process, and unique material selectivity. However, the etching rate, order of 10 Å/min, obtained by using the conventional etching gas such as SF_6 is too low to apply it to the micro-fabrication of MEMS devices, which require the etching rate of the order of 1 μm/min. So we have constructed an etching beam line using XeF_2 as an etching gas, which is known to give a rate of order of 1μm/min in the fabrication of MEMS devices [1]. A unique anisotropicity and material selectivity between SiO_2 and Si are expected to appear by carrying out XeF_2 etching under the SR irradiation. Since XeF_2 is an extremely corrosion, the SR beam is introduced into the reaction chamber through the LiF window as shown in Fig. 1.

Furthermore, to reduce the damage of LiF window by the SR irradiations, the high energy part of the SR beam, which corresponds to the absorption region of LiF, is attenuated by reflecting (θ= 25 degree in Fig.2) the beam using a pair of Al coated plane mirrors attached to the mirror holders of the double crystal monochromater in BL4A2 (Fig.2). The spectrum distribution of the incident SR beam to the LiF window was calculated. Etching rates for Si and SiO_2, and the SR irradiation effects are going to be measured in the 2006 year beam time.

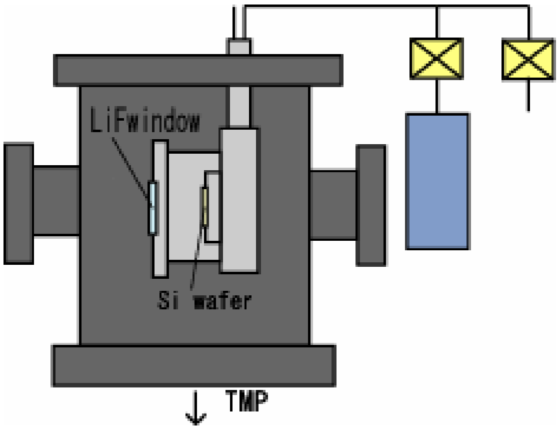

Fig. 1 Chamber for XeF_2 etching.

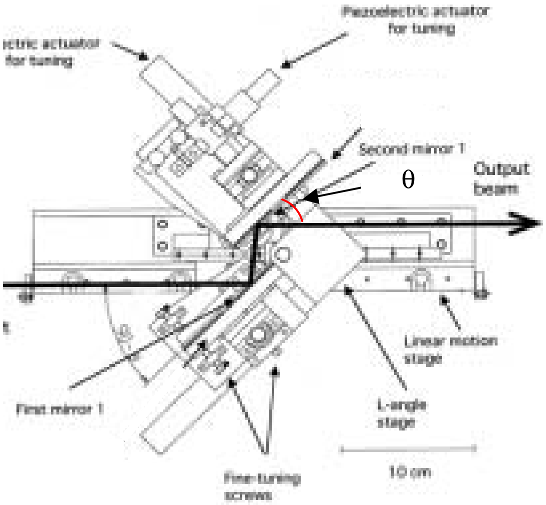

Fig. 2 Double crystal monochromater of BL4A2.

[1] B. Li, U. Streller, H.-P. Krause, I. Twesten and N. Schwentner, J. Appt. Phys. **77** (1995) 1.
.

BL4B

Development of Electron–Ion Coincidence Spectrometer for Studies on Decay Dynamics of Core Excited Molecules

T. Kaneyasu, Y. Hikosaka, E. Shigemasa
UVSOR Facility, Institute for Molecular Science, Okazaki 444-8585 Japan

A new electron-ion coincidence spectrometer for studies on decay dynamics of core excited/ionized molecules has been developed. Energy and ejection angle of electrons, and momentum vectors of fragment ions are simultaneously measured in each event by means of a multi-coincidence technique. The coincidence spectrometer consists of a double toroidal electron analyzer (DTA), a three-dimensional ion momentum spectrometer which are followed by time- and position-sensitive detectors (PSD) as schematically illustrated in Fig. 1. The present system is based on the Auger electron–ion coincidence setup using the original DTA combined with an ion mass spectrometer [1].

The Auger electron is energy analyzed by DTA, while the ions are extracted from the interaction region by a pulsed electric field triggered by the detection signal of the electron, and the time-of-flight (TOF) of the ions and their position information on the ion PSD are obtained. The information gained enables the reconstruction of initial momentum vectors of fragments. In order to achieve high resolution for ion momentum measurements, we have newly designed the electrostatic lenses for ion trajectory focusing. The time focusing as well as space focusing conditions for the ions are satisfied by introducing the lens system, even in the pulsed electric field. A high performance pulse generator is the key to realizing the present experiments. We introduce a new high voltage pulse generator with the electronic time delay of 160 ns and rise time of 20 ns.

We have carried out photoelectron–ion coincidence measurements for the Ar 2*p* photoionization of Ar, as a performance test of the spectrometer. The TOF spectrum and two dimensional image of the Ar ions detected with the Ar 2*p* photoelectrons are shown in Fig. 2. Mulitply charged Ar ions, which are produced through the Auger decay of the 2*p* hole states, are clearly resolved in the TOF spectrum. The narrow TOF peaks and the small spot on the image clearly indicate that the time and space focussing for the ions are well satisfied. So far the time focussig less than 17 ns (FWHM), and the space resolution of 2.8 mm (FWHM) have been achieved. The relative intensitities of the prduct ions in this measurement are 84%, 14% and 2% for Ar^{2+}, Ar^{3+} and Ar^{4+}, respectively. The charge state ratio well agrees with the experimental result obtained by the photoelectron-ion coincidence spectroscopy [2]. This result suggests that the transmission of the momentum spectrometer and the detection efficiency of the ion PSD for various Ar ions are almost constant without any calibrations.

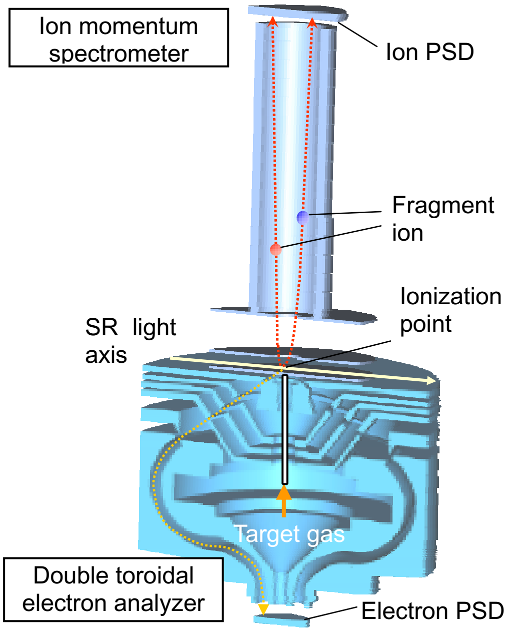

Fig. 1 Three-dimensional view of the electron-ion coincidence spectrometer.

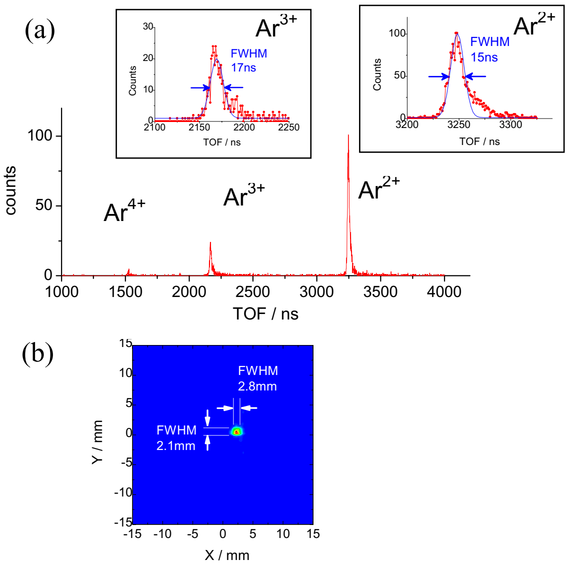

Fig. 2 (a) Time-of-flight spectrum of product Ar ions through the Ar 2*p* Auger transitions. The ions are extracted from the interaction region by pulsed electric field triggered by the detection of Ar 2*p* photoelectron. (b) Image of Ar ions on PSD.

[1] D. Céolin *et al.,* J. Electron. Spectrosc. Relat. Phenom. **141** (2004) 171.

[2] S. Brünken *et al.,*Phys. Rev. A **65** (2002) 042708.

BL6B(IR)

Spatial Resolution of the THz Microscope

S. Kimura[1,2], T. Mizuno[2]
[1]*UVSOR Facility, Institute for Molecular Science, Okazaki 444-8585 Japan*
[2]*School of Physical Sciences, The Graduate University for Advanced Studies, Okazaki 444-8585 Japan*

Infrared synchrotron radiation (IR-SR) is a powerful tool for microspectroscopy and imaging not only in the IR but also in the terahertz (THz) regions because of its high brilliance. Then almost all IR-SR beamlines in the world equip commercial IR microscopes that are available only in the IR region. The commercial IR microscope has an advantage of the conventional apparatus but it is not suitable for the THz region. Then we install a newly designed IR microscope that covers down to the THz region.

The design concept is as follows; 1) Large working distance because some special experiments including at very low temperature, under high pressure, a near-field spectroscopy and so on are planned, 2) Covering down to the THz region because quasiparticle states of correlated materials and finger print vibration mode of proteins appear in the THz region. Then we employed a large-size schwarzschild mirrors (140 mm in diameter, NA = 0.5, working distance = 106 mm) for covering the THz region [1].

After installation of the THz microscope, we checked the spatial resolution in the different wavenumber ranges in which the microscope covers as shown in Fig. 1. The THz microscope in conjunction with UVSOR-II covers down to 40 cm^{-1} in contrast that with a globar lamp covers above 500 cm^{-1}. The spatial resolution and the intensity using UVSOR-II is much higher than that using a globar lamp in the whole wavenumber range. This indicates that the THz microscope using UVSOR-II is a very efficient means of microspectroscopy in the IR and THz regions.

[1] S. Kimura *et al.*, Infrared Sci. Tech. (2006) in press.

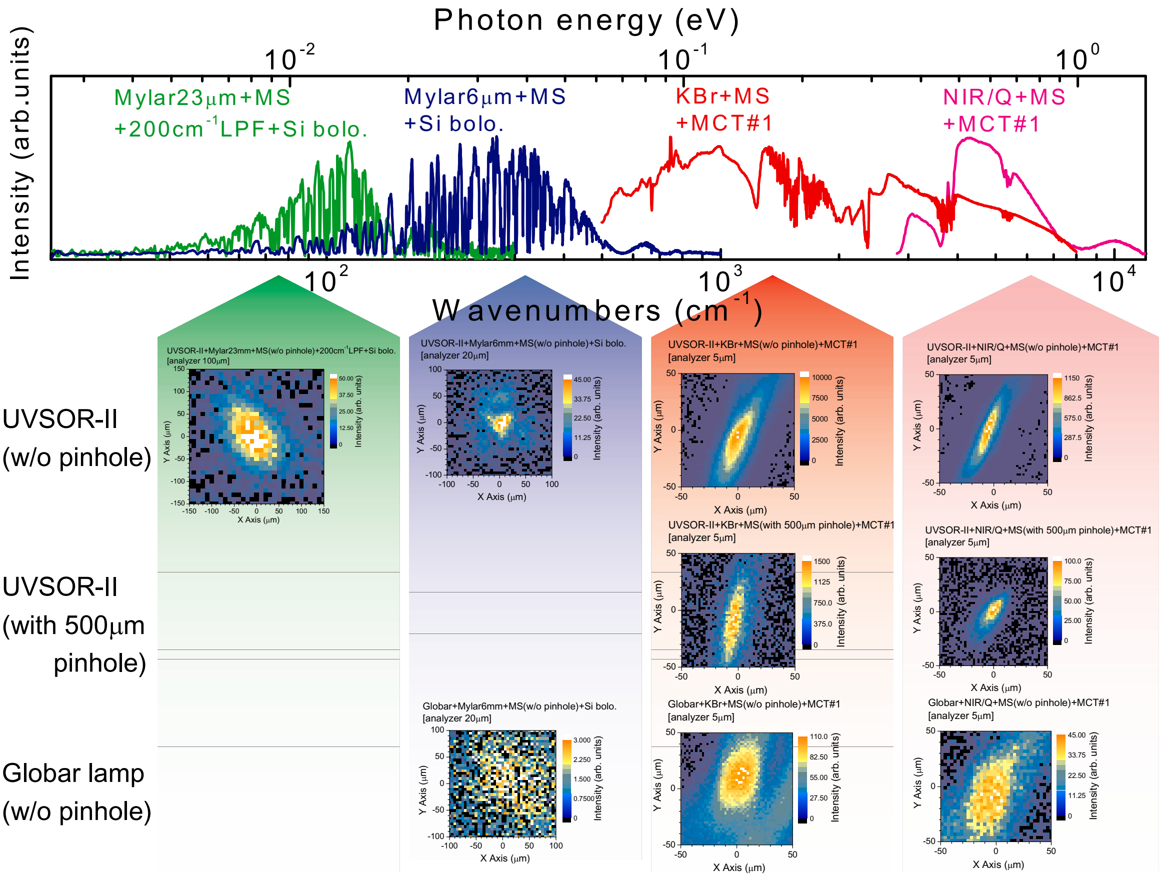

Fig. 1 Spectral shape and spatial resolution of THz microscope at different wavenumber regions using UVSOR-II compared with a globar lamp. Fine structures in the spectral shapes are due to the absorption of water vapor.

BL2B

Evaluation of Absolute Photoabsorption Cross Sections of an Endohedral Metallofullerene, Pr@C_{82}

H. Katayanagi[1,2], B. P. Kafle[2], T. Mori[1], J. Kou[1], Y. Takabayashi[3], E. Kuwahara[3], Y. Kubozono[3], K. Mitsuke[1,2]
[1]*Department of Vacuum UV Photo-Science, Institute for Molecular Science, Okazaki 444-8585 Japan*
[2]*Graduate University for Advanced Studies, Okazaki 444-8585 Japan*
[3]*Department of Chemistry, Okayama University, Okayama 700-8530 Japan*

We measured yield curves of photoions produced by the photoionization of an endohedral metallofullerene, Pr@C_{82}, and reported the result last year [1]. Figure 1 shows the yield curves of doubly (a) and singly (b) charged photoions. In Fig. 1, a peak accompanied by an oscillatory structure is discernible at around 130 eV. In [1], we concluded that the peak originated from the giant resonance of encapsulated Pr atoms and that the oscillatory structure implies an interference effect by the fullerene cage. To make clear these phenomena more quantitatively, we evaluated absolute photoabsorption cross sections of Pr@C_{82} from the photoion yield curves.

The experimental technique to obtain the yield curves was described in detail elsewhere [2]. Briefly, a Pr@C_{82} beam was generated by sublimation in vacuum and ionized by the synchrotron radiation in the photon energy range of 100 – 150 eV; photoions were observed by time-of-flight mass spectrometer.

The photoabsorption cross sections to produce singly and doubly charged ions can be expressed by the formula [3]:

$$\sigma(\mathrm{Pr@C_{82}}^{z+}) = R(\mathrm{Pr@C_{82}}^{z+})\,\Phi\, n\, L\, \eta\, f\, \tau \qquad (1)$$

$R(\mathrm{Pr@C_{82}}^{z+})$ is the count rate of the ion signals of $\mathrm{Pr@C_{82}}^{z+}$, Φ is the photon flux of synchrotron radiation, n is the number density of Pr@C_{82} in the ionization region, L is the length of the ionization volume along the light path, η is the overall detection efficiency of the apparatus, f is the repetition rate of the pulsed electric field applied to the ionization region and τ is the average residence time of the ions in the ionization volume. We can obtain the above values directly from the experiment except the detection efficiency, η. We used C_{60} as a standard sample to estimate η. We evaluated total photoabsorption cross sections by summing up the cross sections to produce singly and doubly charged ions since signal intensities of triply and higher charged ions were found to be very low. Here we assumed that the quantum yield for photoionization is equal to unity in the photon energy range used.

The values of the cross sections at on- and off-resonance energies are listed in Table 1. Lengthy discussion on the validity of an evaluation method used and the accuracy of the cross sections is omitted here and can be found elsewhere [4]. The difference between the cross sections at 110 and 130 eV is 16.5 Mb. This value corresponds to an enhancement by the giant resonance. The value agrees well with that of Ce@C_{82} (14.3Mb). Since a typical value of cross sections of the lanthanide atom is 40 – 50 Mb, the giant resonance was found to be suppressed by the fullerene cage in Pr@C_{82} as well as in Ce@C_{82} [2].

From the present study on Pr@C_{82}, we found that the existence (and the suppression) of the giant resonance is not just a characteristic of Ce@C_{82} sample and can be a tendency of metallofullerenes. Furthermore, we are designing a more intense fullerene beam source to obtain the oscillatory structure with higher reproducibility. Such spectra will allow us to apply an analysis method similar to that used in XAFS spectroscopy to make clear local structures and charge distributions around interior metal atoms. The analysis will complement results obtained by the X-ray powder diffraction.

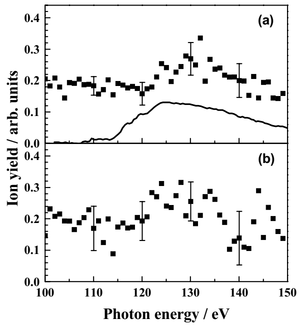

Fig. 1 Ion yield curves of (a) $\mathrm{Pr@C_{82}}^{2+}$ and (b) $\mathrm{Pr@C_{82}}^{+}$. Error bars correspond to 1σ of five experimental runs. Solid curve in (a) is the absorption spectrum of Pr atoms.

Table 1 Cross sections of Pr@C_{82} at the photon energy of 110 and 130 eV. All cross sections are in Mb. Numbers in parentheses show estimated errors.

Photon energy	cross section		
	$\mathrm{Pr@C_{82}}^{+}$	$\mathrm{Pr@C_{82}}^{2+}$	Total
110 eV (off-resonance)	5.8 (2.6)	14.1 (6.1)	19.8 (7.3)
130 eV (on-resonance)	10.6 (3.2)	25.6 (6.4)	36.3 (9.2)

[1] H. Katayanagi *et al.*, UVSOR Activity Report **2004** (2005) 51.

[2] K. Mitsuke *et al.*, J. Chem. Phys. **122** (2005) 064304.

[3] T. Mori *et al.*, J. Electron Spectrosc. Relat. Phenom. **144 – 147** (2005) 243.

[4] H. Katayanagi *et al.*, in preparation.

BL3U

Orbital-Dependent Stabilization in the Valence Ionization of CS_2 Cluster

T. Hatsui[1], J. Plenge[2], E. Rühl[2], N. Kosugi[1]
[1]*Dept. of Vacuum UV photoscience, Institute for Molecular Science, Okazaki 444-8585 Japan*
[2]*Physical and Theoretical Chemistry, Freie Universität Berlin, Takustr. 3, 14195 Berlin*

Van der Waals clusters have been interested since they give opportunities to investigate the connection between isolated and condensed phases. Cluster formation is known to give the decrease in adiabatic binding energy, which is commonly interpreted in terms of final state polarization stabilization, where the created hole upon ionization polarizes the surrounding atom/molecules. The polarization stabilization is dependent on the distance to the surrounding atoms/molecules and their polarizability. In the case of valence ionization of molecular clusters, valence holes are generally delocalized within the molecule, where the shape of the hole is characteristic of the valence molecular orbital (MO). In this study, we have investigated the stabilization effect in CS_2 cluster in order to observe MO dependent stabilization of the valence ionized states.

CS_2 cluster was produced by a continuous supersonic jet expansion with seeding He gas. The jet is intersected with a beam of linearly polarized soft X-rays from the in-vacuum undulator beam line BL3U with an energy resolving power E/ΔE better than 1000 at 65 eV photon energy. Electrons are analyzed at 55° to the electric vector of the incident x-rays by a Scienta SES-200 hemispherical analyzer and an MBS A-1 control system (A1_200_#86) with path energy of 20 V.

The photoelectron spectra of CS_2 molecule and the mixture of CS_2 molecule and cluster are presented in Fig. 1. The mixture spectrum clearly shows broad bands at the binding energy lower than the bare molecule bands. The cluster spectrum is obtained by subtracting the molecular spectrum. The cluster spectrum arises from clusters with different sizes. In the case of larger mean size with increased stagnation pressure, the peaks of the cluster bands are shifted toward the lower binding energy. The band profile indicates the abundance of the cluster in terms of their size. The peak position of each band can be regarded as the vertical binding energy at certain cluster size. In order to observe the dependence of the energy shift on the ionized states, higher resolution photoelectron spectra are measured by using He I source. The obtained spectrum is similarly subtracted to obtain the cluster spectrum, and plotted in relative energy scale, where zero energy is chosen to be the vertical energy of each ionized states for molecule (Fig. 2). X band has the peak maximum around relative binding energy of -0.6 eV. The relative binding energies are increased in order of X, A, B, and C. It is probable that vibrational progression of each ionized states does not change upon the cluster formation because the progressions are mainly determined by the potentials associated with the intra-molecular vibrational modes. The results therefore indicate that ionized state with lower binding energy has smaller stabilization effect. The polarization for low-lying ionized states with a delocalized valence hole is expected to give smaller stabilization. This trend is consistent with the present observation. In summary, the energies of the valence ionized states in CS_2 cluster are determined by the polarization stabilization, which is dependent on the MO character of the holes.

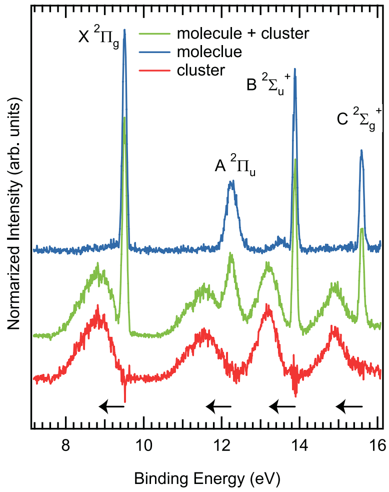

Fig. 1 Photoelectron spectra of CS_2 molecule, the mixture of molecule and cluster, and the cluster. Arrows indicate the decrease of the binding energy upon cluster formations.

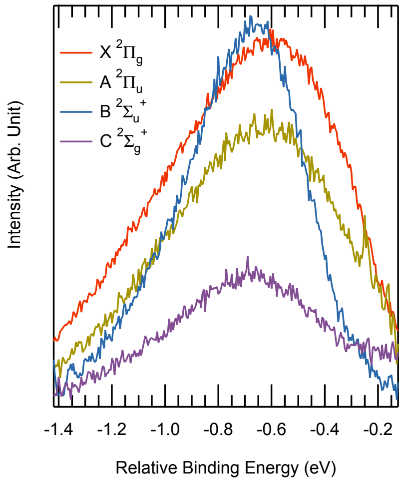

Fig. 2 Valence bands for cluster relative to the vertical binding energy of the corresponding states in molecule.

BL3U&4B

Efficient Production of Metastable Fragments around the 1s Ionization Threshold in N_2

Y. Hikosaka[1], P. Lablanquie[2], E. Shigemasa[1]
[1]*UVSOR Facility, Institute for Molecular Science, Okazaki 444-8585 Japan*
[2]*Laboratoire de Chimie Physique-Matière et Rayonnement, 75231 Paris Cedex 05 France*

Photoionization dynamics at small excess energy from the inner-shell threshold of an atom or a molecule, closely relates to post-collision interaction (PCI), *i.e.* the interaction between photoelectron, Auger electron and the atomic field which changes during the process. The PCI effect is exhibited on both the energy distributions of photoelectrons and Auger electrons. When the photon energy is tuned close to the inner-shell threshold, PCI can lead the photoelectron to be recaptured into a Rydberg orbital. The photoelectron recapture results in singly-charged ions in high-n Rydberg states. This phenomenon has been relatively well studied for atoms but rarely for molecules. In this work, we have measured the yields of neutral species, in the vicinity of the 1s ionization threshold of N_2 [1]. The present work demonstrates the neutral particle observation can be a new probe for investigating the dynamics on the photoelectron recapture in molecules.

The neutral particle yield spectrum in hν=405.8-412 eV of N_2 is displayed in Fig. 1, in comparison with an ion yield spectrum. Below the 1s threshold, the structures corresponding to Rydberg excitations are seen on both spectra. An intriguing characteristic of the neutral particle yield spectrum is the large peak around the 1s threshold, which is absent from the ion yield spectrum. The large peak lies at hν=410.0 eV, just above the 1s ionization threshold, which results from the detection of metastable fragments N* [1].

For the N* formation below the 1s threshold, we propose the following mechanism whose reaction sequence is illustrated in Fig. 2. A high-n Rydberg state converging to $N_2^+(1s)^{-1}$ is populated by photoexcitation (Reaction 1). The subsequent resonant Auger decay from this high-n Rydberg state results in an N_2^+ state, where spectator Auger decay is more favored due to the weak interference between the core hole and the high-n Rydberg electron (Reaction 2). After the spectator Auger decay, the Auger final state is a singly-charged high-n Rydberg state converging to an N_2^{2+} state. Since most N_2^{2+} states are dissociative, it is very likely that the high-n Rydberg N_2^+ state dissociates into N^+ + N* (Reaction 3), due to the parallelism between the potential energy curves of the high-n Rydberg N_2^+ state and the N_2^{2+} state. The resulting N* should be in a high-n Rydberg state, and can be detected by our neutral particle detector.

The large peak on the neutral particle yield spectrum clearly shows a tail to the higher photon energy side. The tail is interpreted in terms of the PCI effect. The reaction sequence of the N* formation due to PCI is also illustrated in Fig. 2. At the 1s threshold, and above, a slow photoelectron is emitted (Reaction 1'). The formed 1s core-hole usually decays non-radiatively and emits a fast Auger electron. The fast Auger electron overtakes the slow photoelectron, which results in a decrease of the kinetic energy of the photoelectron. The shift of the photoelectron energy can exceed the initial energy given at the photoionization, and the photoelectron can be recaptured into a high-n Rydberg orbital (Reaction 2'). The resultant N_2^+ in a high-n Rydberg state may produce an N* fragment (Reaction 3). This process appears as the tail seen on the neutral particle yield spectrum

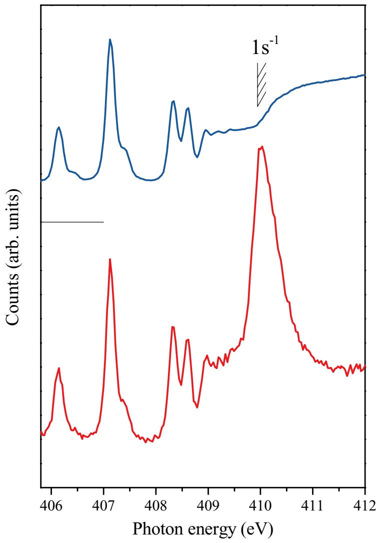

Fig. 1 Ion yield (blue) and neutral particle yield (red) in N_2.

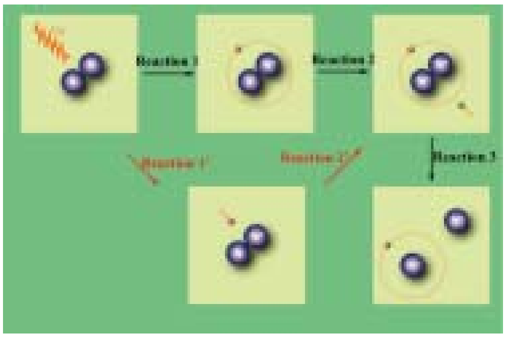

Fig. 2 Reaction sequence for the N* formation.

[1] Y. Hikosaka *et al.*, J. Phys. B **38** (2005) 3597.

Coster-Kronig Decay of HCl Studied by the Threshold Photoelectron-Auger Electron Coincindence Spectroscopy

T. Kaneyasu[1], T. Aoto[2], Y. Hikosaka[1], E. Shigemasa[1], K. Ito[2]
[1]*UVSOR Facility, Institute for Molecular Science, Okazaki 444-8585 Japan*
[2]*Photon Factory, Institute of Materials Structure Science, Tsukuba 305-0801 Japan*

Inner-shell ionization and its subsequent Auger decay produce doubly ionized states. Auger electron spectroscopy has been one of the useful experimental methods to investigate the doubly ionized states of atoms and molecules, because the kinetic energy of the Auger electron corresponds to the transition energy from the initial core-hole state to the final doubly ionized state. The interpretation of the Auger spectrum often becomes, however, difficult in the conventional Auger spectroscopy, mainly due to the following two reasons. The first one is the so-called lifetime broadening of the Auger peaks, resulting from the life time of the initial core-hole state due to the uncertainty principle (ΔE=100 meV ⇔ ΔT=6.5 fs). Secondly, it is difficult to observe the individual Auger lines separately, when the Auger lines associated with various core-hole states and their satellites are superimposed.

In order to overcome such difficulties, coincidence Auger spectroscopy has been emerged where an Auger electron and a photoelectron are detected simultaneously. The coincidence detection enables to select the initial core-hole state associated with the Auger lines. Furthermore, the natural linewidth of the core-hole state does not affect the spectral resolution of the coincidence Auger spectrum, which can be better than the natural linewidth of the initial core-hole state. The spectral resolution is determined only by the experimental condition when the kinetic energies of both the Auger electron and the photoelectron are measured.

So far we have applied the coincidence Auger spectroscopy to rare gases and an H_2S molecule (see *e.g.* [1] and references therein) by detecting a threshold photoelectron as a counter part of Auger electrons. The experimental procedure of the threshold photoelectron-Auger electron coincidence spectroscopy has already been described in the paper [2]. In this work, we have firstly measured weak Cl 2*s* Coster-Kronig Auger lines of HCl. Figure 1 shows the yield of threshold photoelectrons against the photon energy measured in the vicinity of the Cl 2*s* threshold. The spectral structures in Fig. 1 are corresponding to the excitation and ionization processes of the Cl 2*s* electron. The first peak at 271.5 eV is attributed to the excitation to the 3$p\sigma$* orbital. The second one around 276 eV is owing to the unresolved Rydberg states. The threshold electron yield reaches its maximum at 279.5 eV, which should relate to the Cl 2s photoionization. The ionization energy of the Cl 2*s* is however determined to be 278.0 eV. Such difference can be explained by the post-collision interaction effect, namely, the slower photoelectron is overtaken by the Auger electron.

The Cl 2*s* coincidence/normal Auger spectra are presented in Fig. 2. It is obvious that the Auger lines are clearly resolved in the coincidence spectrum, in contrast to the normal Auger spectrum. The spectral resolution is expected to be 0.5 eV in the coincidence spectrum, which is well below the natural linewidth of the Cl 2s core-hole state (1.8 eV). However, any sharp structures can hardly be seen in the coincidence spectrum. This may indicate that many doubly ionized states with (Cl 2p)$^{-1}$(V)$^{-1}$ configurations lie in the energy region of Fig. 2, and are overlapped. The two major structures at 233 eV and 237 eV are probably due to the formation of HCl^{2+} [(Cl 2p)$^{-1}$(V)$^{-1}$] sates with 2π and 5σ valence holes, respectively.

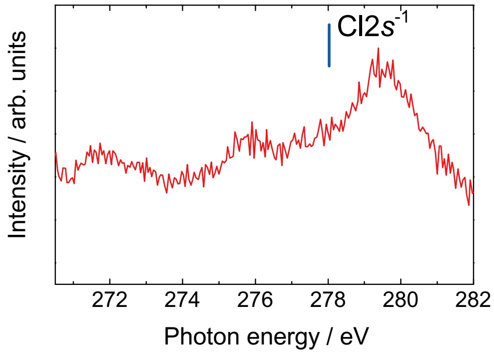

Fig. 1 Threshold photoelectron spectrum of HCl measured in vicinity of the Cl 2*s* threshold.

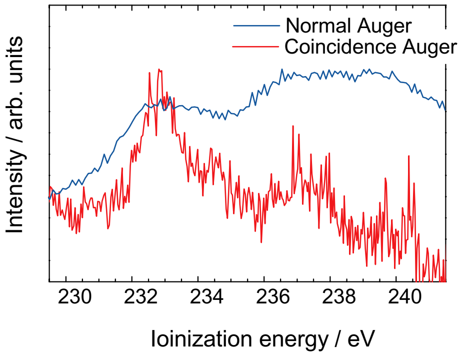

Fig. 2 Cl 2*s* Coster-Kronig Auger spectra of HCl measured at $h\nu$=357.5 eV for normal Auger, and at $h\nu$=279.5 eV for coincidence Auger spectrum.

[1] Y. Hikosaka *et al.,* J. Electron Spectrosc. Relt. Phenom. **133-140** (2004) 287.

[2] Y. Hikosaka *et al.,* Meas. Sci. Tech. **11** (2000) 1697.

BL4B&8B1

Doulbe Toroidal Electron Anlyzer for Auger Electron-Ion Coincidence Experiments

T. Kaneyasu, Y. Hikosaka, E. Shigemasa
UVSOR Facility, Institute for Molecular Science, Okazaki 444-8585 Japan

A double toroidal type electron analyzer (DTA) has been constructed for studies on anisotropic electron emission following molecular inner-shell photoionization. The analyzer, which is based on the high luminosity electron spectrometer originally developed by the French group [1], allows simultaneous measurements of angular distributions and energy distributions of electrons utilizing a two-dimensional position sensitive detector (PSD). The acceptance solid angle is 5% of 4π sr and electrons within the energy range 10% of the pass energy can be observed. A three-dimensional view of our DTA is shown in Fig. 1, which consists of a four element conical electrostatic lens, two toroidal shaped deflectors and PSD. The conical symmetry of the lens system defines the detection angle of 54.7° with respect to the analyzer symmetrical axis. The ejected electrons are focused by the four element lens system and energy dispersed by the toroidal deflectors. The electrons are finally detected by PSD. The pass energy of DTA is adjusted by the potential applied to the entrance slit and the energy resolution is expected to be smaller than 1% of the pass energy. The angular resolution is estimated to be 5-7 degrees.

A typical image for observing the Kr MNN Auger electrons following the Kr 3*d* photoionization is presented in Fig. 2. In this measurement, the Auger electrons in the energy range of 48-58 eV are measured. At first glance, four coaxial circles which correspond to individual Auger lines are clearly separated. The intervals of the Auger lines are almost 1 eV. The Auger electron spectrum is deduced from the image, by summing the intensity along the radial direction. From Fig. 2, it is safe to say that the spectral resolution is better than 1 eV at the pass energy of 80 eV. In angular distributions, the concentric circles in Fig. 2 are far from isotropic. This anisotropy is resulted from the analyzer transmission efficiency and the detection efficiency of PSD. The three insensitive regions are apparent on the image. They are induced by three supporting struts in the lens system. To measure angular distribution of ejected electrons, the transmission and the detection efficiency of the analyzer should be calibrated by observing the Auger/photoelectron which shows isotropic angular distribution.

Our next plan is to develop an electron-ion coincidence spectrometer by combining DTA with an ion momentum spectrometer [2]. The coincidence spectrometer is under construction and will be applied to observe anisotropic electron emissions in a molecular frame.

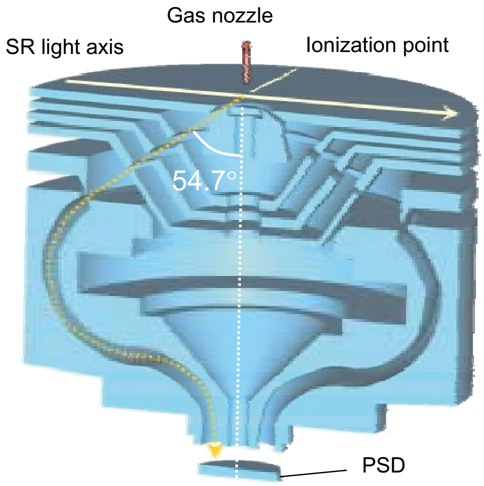

Fig. 1 Schematic drawing of DTA. DTA is equipped with the two-dimensional PSD, which provides energy and angular distributions of electrons.

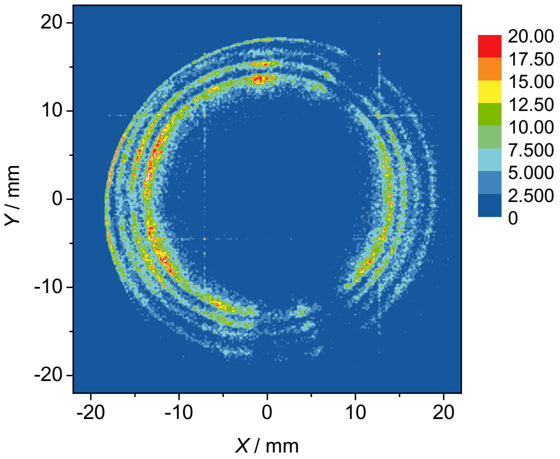

Fig. 2 Two-dimensional image of Kr *MNN* Auger electrons following Kr 3*d* photoionization. DTA was operated with the electron pass energy of 80 eV. Four concentric circles on the image are attributed to the Auger lines and their energy intervals are almost 1 eV.

[1] C. Miron *et al.,* Rev. Sci. Insturm. **68** (1997) 3728.
[2] T. Kaneyasu *et al.,* in this report.

BL4B

Efficient Production of Metastable Hydrogen Fragments around the Cl 2p Ionization Thresholds of HCl

E. Shigemasa[1], M. Simon[2], R. Guillemin[2], T. Kaneyasu[1], Y. Hikosaka[1]
[1]*UVSOR Facility, Institute for Molecular Science, Okazaki 444-8585, Japan*
[2]*Laboratoire de Chimie Physique - Matière et Rayonnement (LCPMR), Université Pierre et Marie Curie, 11 rue Pierre et Marie Curie, 75231 PARIS Cedex 05, France*

Multielectron processes, in which more than two electrons are promoted by the absorption of a single photon, have long drawn special attention in the research field of atomic and molecular inner-shell physics. The multielectron processes are known to happen not only in the primary inner-shell hole creation processes, but also in their relaxation processes.

Recently some trial experiments have been made for observing minor products, such as highly excited neutral species and anions after the molecular inner-shell excitations, in order to find a direct probe for investigating the multielectron processes. A strong enhancement due to the N* formation has been observed around the 1s threshold of N_2 molecules [1]. It has been found that the highly excited N_2^{+*} states leading to the N* formation are populated by spectator Auger decay from the core-excited states, as well as by the recapture of slow photoelectrons into the Rydberg orbitals. It turns out that the metastable observation is a new and sensitive probe to study the decay dynamics of core-excited states and the photoelectron recapture due to the post-collision interaction. Neutral particle formation in the K-shell excitation regions of O_2, CO, and NO has also been investigated and similar enhancements of the neutral particle yields around all the thresholds have been observed. Metastable fragment emission seems to be a common process on the decay of high-n Rydberg states in molecular inner-shell regions.

Here, preliminary results on the neutral fragment formation near the Cl 2p ionization thresholds of HCl molecules are presented. The experiment was carried out on BL4B, by using a simple MCP detector with retarding grids. Figure 1 shows the neutral and ion yield curves in the vicinity of the Cl 2p ionization thresholds. The peak structures in the lower photon energy region correspond to the Rydberg states. The clear differences between the two curves are detected around the thresholds; two broad features are observed only in the neutral yield curve. A direct evidence for producing metastable fragments can be gained by performing the coincidence detection between metastable and ionic fragments, which can also lower the fluorescence contribution in the neutral yield curve considerably. It has turned out that only the H^*/Cl^{n+} coincidence signals are detectable. The H^*/Cl^{n+} coincidence yield curve near the Cl 2p ionization region of HCl is exhibited in Fig. 2. In comparison to the red curve in Fig. 1 and the blue one in Fig. 2, the sufficient reduction of the fluorescence contribution is evident. It is nicely demonstrated that the H* fragments are efficiently produced mainly just around the Cl 2p ionization thresholds. The HCl^{+*} states produced by the spectator Auger decay from the core-excited states, as well as by the recapture of the slow photoelectrons into the Rydberg orbitals play an important role for the efficient H* formation near the thresholds. Similar investigation for the Cl 1s ionization region has been attempted on BL1A, but no practical result has been obtained, due to the low photon intensity around 2.8 keV.

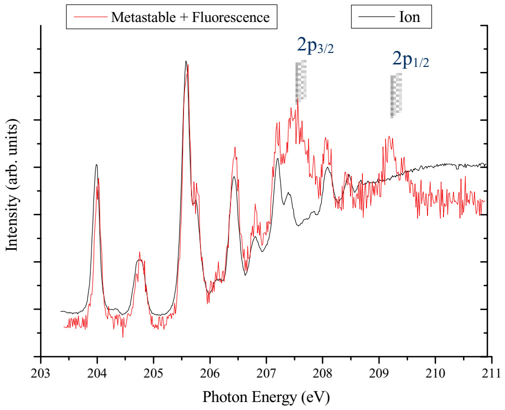

Fig. 1 Neutral and ion yield curves near the Cl 2p ionization region of HCl.

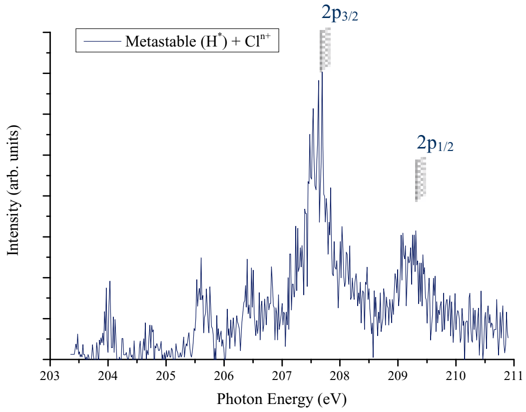

Fig. 2 H^*/Cl^{n+} coincidence yield curve near the Cl 2p ionization region of HCl.

[1] Y. Hikosaka, P. Lablanquie, and E. Shigemasa, J. Phys. B **38**, (2005) 3597.

BL7B

Optical Pseudogap from Iron States in AFe$_4$Sb$_{12}$ (A=Yb, Ca, Ba)

J. Sichelschmidt[1], H.J. Im[2,3], S. Kimura[2,3], V. Voevodin[1], H. Rosner[1], W. Schnelle[1],
A. Leithe-Jasper[1], J.A. Mydosh[1,4], Yu. Grin[1], F. Steglich[1]
[1]*Max Planck Institute for Chemical Physics of Solids, 01187 Dresden, Germany*
[2]*School of Physical Sciences, The Graduate University for Advanced Studies, Okazaki 444-8585 Japan*
[3]*UVSOR Facility, Institute for Molecular Science, Okazaki 444-8585 Japan*
[4]*II. Physikalisches Institut, Universität zu Köln, 50937 Köln, Germany*

Introduction

The class of compounds known as "skutterudites" exhibits a wealth of topical behaviors. A variety of properties have been observed – mainly for rare-earth filled skutterudites – ranging from metal-insulator transitions to magnetic and quadrupole orderings, conventional and unconventional superconductivity, heavy-fermion/non-Fermi-liquid behavior, and fluctuating/intermediate valency. Many studies suggest that the physics of filled skutterudites with rare-earth metals is governed by a subtle interplay of the filler ions and their surrounding transition-metal pnictogen host structure.

The skutterudites AFe$_4$Sb$_{12}$ filled by nonmagnetic ions of alkali and alkaline-earth metals show remarkable properties which indicate the importance of magnetism originating in the polyanionic host [1,2]. These compounds either show ferromagnetic ordering (A = Na, K) or are close to a ferromagnetic instability (A = Ca, Ba). Strong ferromagnetic spin fluctuations, a high density of states (DOS) at the Fermi level E_F and, therefore, an enhanced electronic specific heat coefficient $\gamma \approx$ 100-140 mJ mol^{-1}K^{-2} are found [2,3]. Thus, with respect to these new findings the size of the contribution of the 4f-conduction electron hybridization to the creation of an enhanced/heavy effective electronic mass in some rare-earth filled iron skutterudites becomes questionable. In YbFe$_4$Sb$_{12}$ the Yb is non-magnetic and stable divalent as recently proven experimentally [3,4]. In contrast, previous optical investigations of YbFe$_4$Sb$_{12}$ claim 4f -related heavy fermion properties reflected in a hybridization induced far-infrared (FIR) pseudogap [5]. We clarified the nature of this pseudogap by comparing the optical properties of YbFe$_4$Sb$_{12}$ with those of (Ca/Ba)Fe$_4$Sb$_{12}$. We found a low-energy pseudogap structure, very similar for each compound. It reflects the fine details of the band structure near E_F which can be understood in a single particle picture without including explicitly electron-electron correlations [6]. The Fe-3d states generate the observed pseudogap whose characteristics appears to be very similar to the so-called hybridization gap found in some strongly correlated 4f electron systems.

Experiment

We have measured the near normal incidence optical reflectivity $R(\omega)$ of polycrystalline samples of AFe$_4$Sb$_{12}$ (A = Yb, Ca, Ba). Their preparation and structure as well as their transport, thermodynamic, and magnetic properties were reported previously [1-3]. For the optical experiments the sample surfaces were well polished.

A rapid-scan Fourier spectrometer of Michelson and Martin-Puplett type was used for energies $\hbar\omega$ between 3 meV and 3 eV (2 K< T < 300 K) and for higher energies at T = 300 K only. Synchrotron radiation (UVSOR, BL7B) extended the energy range from 1.2 eV up to 30 eV [7]. As high accuracy for the reflection data was required, the polycrystalline samples were coated *in-situ* with gold and then used for measuring the reference spectra. Using Kramers-Kronig relations, we calculated the dissipative part $\sigma_1(\omega)$ of the optical conductivity from $R(\omega)$. Above energies of 30 eV, where an eventual small temperature dependence of $R(\omega)$ has negligible influence on $\sigma_1(\omega \approx 10$ meV), a free-electron approximation of the form $R(\omega) \propto \omega^{-4}$ was used. We fitted the low-energy end $\sigma_1(\omega \leq 30$ meV) to the electrical conductivity σ_{DC} ($\omega \rightarrow 0$) by a Drude-Lorentz function such that σ_{DC} values were described within ±20%. Uncertainties of the $\sigma_1(\omega)$ spectra due to variations of the low-energy extrapolation of $R(\omega)$ are negligible for energies > 6 meV.

Results

The measured reflectivity spectra $R(\omega,T)$ data are shown in Fig. 1 at selected temperatures. A sharp drop of $R(\omega)$ around 0.5 eV separates a Drude-like charge carrier contribution at low energies from electronic interband transitions dominating the high-energy region (see inset). Below $T \approx$ 90 K $R(\omega)$ shows a pronounced suppression of up to ≈ 4% (T = 4 K) with a minimum located at about the same energy (12 meV) for CaFe$_4$Sb$_{12}$ and YbFe$_4$Sb$_{12}$, and at ≈ 15 meV for BaFe$_4$Sb$_{12}$. The compounds show conventional metallic behavior in the optical conductivity $\sigma_1(\omega,T)$ above $T \approx$90 K whereas for T < 90 K it is continuously suppressed until it reaches a minimum value at the lowest temperature. This behavior of $\sigma_1(\omega,T)$ and its enhancement for energies between 17 and 60 meV indicates the formation of a pseudogap in the electronic charge excitations below ≅ 17 meV (see Fig. 2).

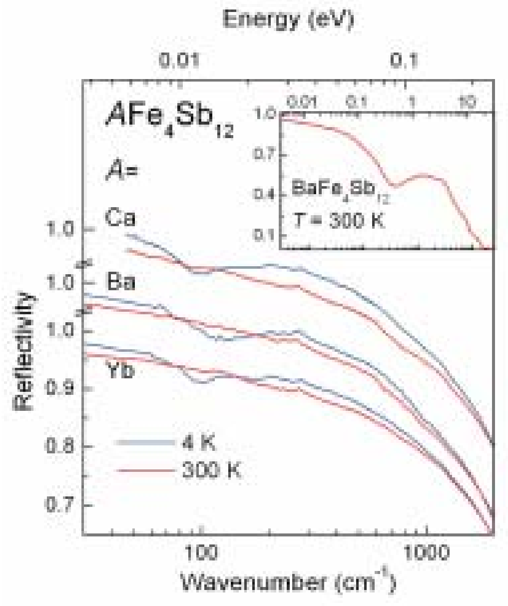

Fig. 1 Reflectivity spectra displaying for all compounds at $T = 4$ K a pronounced dip around 100 cm^{-1}. Inset: the complete accessible spectral range shown for one compound.

Remarkably, all investigated compounds AFe_4Sb_{12} (A = Yb, Ba, Ca) show a very similar pseudogap behavior of their optical conductivities, pointing towards a very similar electronic band-structure. Indeed, the optical pseudogap and its different appearances in $BaFe_4Sb_{12}$ and $CaFe_4Sb_{12}$ as well as the sharp features (for example close to 200 cm^{-1}) are very well reproduced by our high-resolution LDA band-structure calculations [6]. Therefore, at least for AFe_4Sb_{12} with A = Yb, Ca, Ba only weak electronic correlations within the Fe 3*d* – Sb 5*p* bands seem to be present. This is a completely different mechanism than the Kondo-insulator gap scenario for 4*f* heavy-fermion compounds leading, surprisingly however, to similar optical spectra.

Keeping in mind the relevance claimed for the hybridization gap picture in other filled skutterudites [5,8] our results, with unexpected clearness, demonstrate that FIR optical pseudogaps can originate from the single particle electronic band structure of these systems.

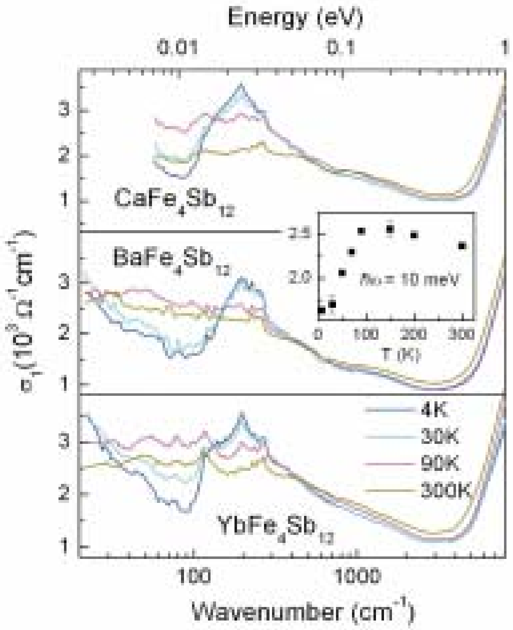

Fig. 2 Spectra of the optical conductivity $\sigma_1(\omega,T)$ at selected temperatures below and above $T \approx 90$ K, where a pseudogap forms below 17 meV. For $BaFe_4Sb_{12}$ the inset shows $\sigma_1(\omega,T)$ at $\hbar\omega = 10$ meV, demonstrating the evolution of the pseudogap.

This work was partially supported from the international collaboration program of IMS (2004).

[1] A. Leithe-Jasper *et al.*, Phys. Rev. Lett. **91** (2003) 037208.
[2] A. Leithe-Jasper *et al.*, Phys. Rev. B **70** (2004) 214418.
[3] W. Schnelle *et al.*, Phys. Rev. B **72** (2005) 020402(R).
[4] D. Bérardan *et al.*, J. Alloys Compd. **351** (2003) 18; *ibid.* J. Magn. Magn. Mater. **285** (2005) 245.
[5] S. Dordevic *et al.*, Phys. Rev. Lett. **86** (2001) 684.
[6] J. Sichelschmidt *et al.*, Phys. Rev. Lett **96** (2006) 037406.
[7] K. Fukui *et al.*, Nucl. Instrum. Methods Phys. Res. Sect. A **467-468** (2001) 601.
[8] M. Matsunami *et al.*, J. Phys. Soc. Jpn. **72** (2003) 2722.

BL1A, 5B, 7B&8B1

Photo Luminescence Spectra and Time Resolved Decay Curves of UV Emission Bands in AlGaN Alloys Using High Energy Excitation

S. Naoe[1], N. Nakagawa[2], K. Fukui[2], H. Miyake[3], K. Hiramatsu[3]
[1]*Faculty of Engineering, Kanazawa University, Ishikawa 920-1192, Japan*
[2]*Research Center for Development of Far-Infrared Region, Fukui 910-8562, Japan*
[3]*Faculty of Engineering, Mie University, Mie 514-8507, Japan*

AlGaN is becoming an important optical material which gives UV emission band with variable energy position from 3.4 to 6.25 eV, therefore the study of mechanism of UV emission in the photoluminescence measurements by using SR in wide energy range of exciting photon is expected.

All samples are made by MOCVD (MOVPE) methods. The thicknesses of AlGaN thin film are about 1 μm on 1 μm AlN single crystal films with sapphire substrates. The measurements were carried out at BL1A, under single bunch operation to take of time resolved decay (TRD) curves.

TRD curves have three components (fast < 1 ns, middle ~18 ns, slow ~60 ns) by analyzing based on the three single exponential components linear combination model. Previous works revealed that the rate of the fast component among them increases with increasing excitation photon energy up to 1.5 keV in TRD curves of AlGaN [1]. This time, TRD measurements were done for sliced parts of UV emission band with the precision of receiving light monochromator resolving power (0.02 eV), using various energy ranges of excitation photon (BL7B, BL5B, BL8B1, BL1A). Thus, it gives life time resolved PL spectra.

In the case of band-to-band excitation (BL7B), the rates of three components of TRD have shown to vary with changing the detected photon energy value of the sliced parts among the UV emission band (this result will be reported elsewhere in this article).

In the case of high energy excitation (BL1A), where the fast component was known to become dominant in TRD curve for the whole of UV emission band, the behavior of the rate of three components in the life time resolved PL spectra is interesting , varying the energy of detecting photon among the UV emission band.

The results of TRD measurements at low temperature are shown in Fig. 1 and Fig. 2. Fig.1 shows UV emission band and the inserted color points show the position of detecting photon energy in TRD measurement. Fig.2 shows TRD curves at several energy position of photon detected. There is no considerable difference at the energy values (corresponding to the color points in Fig. 2) among the UV emission band, in contrast to the case of band-to-band excitation (BL7B).

These TRD results will be interpreted by the relaxation process of some holes and electrons produced by the high energy excitations, on the UV emission. The fast component will be considered to originate from an intrinsic exciton process (overlapping between electron and hole wave functions), then it will be suggested as a schematic view that many holes which were produced by relaxation process of inner core holes are gathering around the element initially excited and recombining with nearby electrons rapidly, before making some relaxation state.

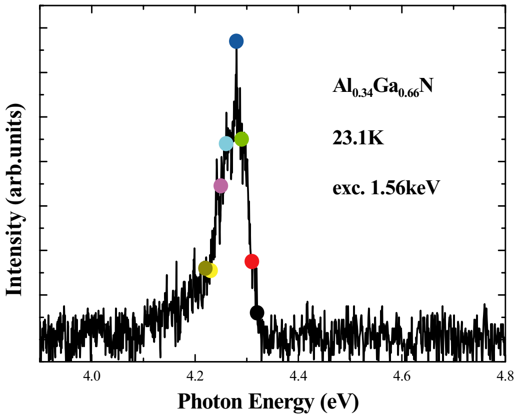

Fig. 1 UV emission band of $Al_{0.34}Ga_{0.66}N$ at 23.1K.

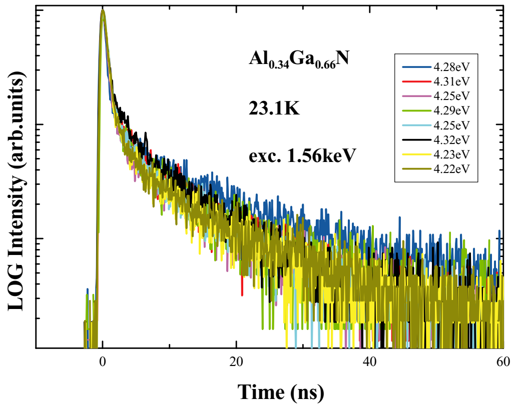

Fig. 2 Time resolved decay curves of $Al_{0.34}Ga_{0.66}N$ at 23.1K.

[1] S. Naoe *et al.,* UVSOR Activity Report 2004, (2005) 78.

Luminescence Properties of $NaYF_4:Bi^{3+}$

K. Chong[1], T. Hirai[1], T. Kawai[2], N. Ohno[1]
[1]Division of Electronics and Applied Physics, Graduate School of Engineering,
Osaka Electro-Communication University, Neyagawa, Osaka 572-8530, Japan
[2]Graduate School of Science, Osaka Prefecture University, Sakai 590-0035, Japan

Xe dimer (Xe_2) discharge fluorescent lamp is one of the candidates for alternative lighting sources to a conventional Hg discharge fluorescent lamp. New phosphors suitable for the conversion of vacuum ultraviolet (VUV) light into visible light are quite desired at present. In the Xe_2 discharge florescent lamps, phosphors are excited by VUV light at 7.2 eV. Most fluoride hosts are transparent up to ~ 10 eV, so that the VUV light can directly excite impurity activators in fluoride hosts.

Metal ions with s^2 electronic configurations doped in wide-gap materials such as alkali halides, which are called Tl^+-type ions, show several absorption bands due to $s^2 \rightarrow sp$ transitions. Since the optical transitions are dipole-allowed, the absorption is expected to be much stronger than that due to the dipole- forbidden *f-f* transitions in rare-earth ions. The strong absorption would give efficient conversion of the VUV light from the Xe_2 discharge fluorescent lamps.

$NaYF_4:Bi^{3+}$ samples were prepared by amounts of the appropriate starting compound powders of NaF and YF_3 adding BiF_3 (~ 1 mol %), mixing and firing in a carbon crucible at 850ºC in argon atmosphere. X-ray diffraction patterns showed that obtained crystals were of a hexagonal structure. Impurity Bi^{3+} ions are trivalent Tl^+-type ions, so that they would be substituted for Y^{3+} ions in the host lattices.

Figure 1 shows PL (blue curve) and PLE (red curve) spectra of $NaYF_4:Bi^{3+}$ measured at 10 K. A broad luminescence band peaking at 2.75 eV is observed for the excitation of VUV light. The 2.75 eV band is excited with photons of 5.0 eV in the UV region, and ~ 6.2 eV in the VUV region. These excitation peaks are located at lower energies than the absorption edge of the host $NaYF_4$ (~ 8 eV). Therefore, the 2.75 eV luminescence band is responsible for intra-ionic transitions in impurity Bi^{3+} ions.

Tl^+-type ions doped in alkali halide crystals with a high symmetry crystal structure exhibit three characteristic absorption bands arising from the $s^2 \rightarrow sp$ transitions, namely, A, B and C bands [1]. These absorption bands have been attributed to the optical transition from the $^1S_0$ ground state to $^3P_1$, $^3P_2$, and $^1P_1$ states, respectively. Kang *et al.* have reported that the A and C bands appear at 3.7 and ~ 6.0 eV, respectively, in the absorption spectrum of $KCl:Bi^{3+}$ at low temperatures [2].

In Bi^{3+} ions doped in fluoride hosts, the absorption bands would shift to the higher energy side, as compared to those in chloride hosts. In fact, in $CaF_2:Bi^{3+}$ and $SrF_2:Bi^{3+}$ crystals, the A band appears at ~ 5.8 eV and the C band at ~ 8.2 eV [3]. In $NaYF_4:Bi^{3+}$ crystals, the excitation band appearing at 5.0 eV is tentatively assigned as the A band nature due to $^1S_0 \rightarrow {}^3P_1$ transition in Bi^{3+} ions, although the transition energy is somewhat smaller compared with that of Bi^{3+} ions in other fluoride compounds. The excitation bands at 5.6 – 7.1 eV show composite structures, which is a common feature of the C band of Tl^+-type ions. Therefore, these structures in the VUV region is ascribed to the C band nature due to $^1S_0 \rightarrow {}^1P_1$ transitions in Bi^{3+} ions.

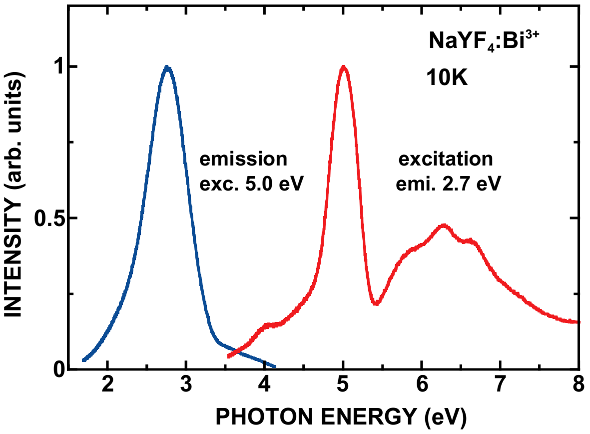

Fig. 1 Luminescence (blue curve) and excitation spectra (red curve) of $NaYF_3:Bi^{3+}$ at 10 K.

[1] W.B. Fowler, Physics of Color Centers, Academic Press Inc., New York, 1968.
[2] J.G. Kang, H.M. Yoon, G.M. Chun, Y.D. Kim and T. Tsuboi, J. Phys.: Condens. Matter **6** (1994) 2101.
[3] K.P. Oboth, F.J. Lohmeier and F. Fisher, phys. stat. sol. (b) **154** (1989) 789.

BL1B

Optical Anisotropy at the Absorption Edge in CaMoO$_4$ and CaWO$_4$

M. Fujita[1], M. Itoh[2], S. Takagi[2], T. Shimizu[2], N. Fujita[2]
[1]*Japan Coast Guard Academy, Wakaba, Kure 737-8512*
[2]*Department of Electrical and Electronic Engineering, Shinshu University, Nagano 380-8553*

Calcium tungstate is well known as intrinsic scintillation material. The crystal belongs to scheelite structure of tetragonal space group. The lowest absorption band of CaWO$_4$ was regarded as due to the transition to the 1*s* exciton state. Recent two-photon excitation experiment, however, suggests that the band is ascribed to the band-to-band transition [1].

In the present study, optical anisotropy of CaMoO$_4$ and CaWO$_4$ has been studied in order to clarify the nature of the lowest band as well as the structures at higher energy region.

Experiment

Single crystals of CaMoO$_4$ and CaWO$_4$ grown by the Czochralski method were used for the experiment. Reflectivity spectra were measured at 10 K for the polarization ***E***//***a*** and ***E***//***c*** using the polished surfaces of (010) plane. The optical constants such as dielectric functions were calculated from the reflectivity spectra using a Kramers-Kronig analysis.

Results and discussion

The solid curves in Fig. 1 show the spectra of imaginary part of dielectric functions (ε_2) of CaMoO$_4$ and CaWO$_4$ in the lowest band region. The broadness of these bands compared with the exciton band of PbWO$_4$ indicates that they are attributed to the band-to-band transition [1]. The width of the band for ***E***//***a*** is larger than that for ***E***//***c*** for both materials. In order to examine the band shape in detail, the spectra of the second-energy-derivative of ε_2 ($d^2\varepsilon_2/dE^2$) were calculated. The derivative spectra shown by the dotted curves in Fig. 1 indicate that the band consists of two components for ***E***//***a*** and a single component for ***E***//***c*** for both materials. Figure 2 shows the energy diagram of a MoO$_4^{2-}$ (WO$_4^{2-}$) oxyanion molecule. In a free molecule of T$_d$ symmetry, the highest occupied orbital is of t_1 symmetry of O2*p* character, and the lowest unoccupied orbital is of *e* symmetry of mainly Mo4*d* (W5*d)* character. In the scheelite crystal, the symmetry of the molecule is lowered to D$_{2d}$ and both the t_1 and *e* orbitals split into two sublevels. The dichroism of the band in Fig. 1 can be explained well in terms of the assignment given in Fig. 2. Thus the optical excitation at the absorption edge in CaMoO$_4$ and CaWO$_4$ can be ascribed to the transition from the valence band of t_1 orbital to the conduction band made of *e* orbital in the oxyanion molecule.

Figure 3 shows the ε_2 spectra up to 30 eV. A clear correspondence between the structures in CaMoO$_4$ and CaWO$_4$ is seen with respect to the spectral shape and polarization dependence, as numbered in Fig. 3. The structures 2-4 are assigned to the transition from the valence band to the next higher conduction band of t_2 orbital of mainly Mo4*d* (W5*d)* character, and the structures 5-8 to the transition to the conduction band of the Ca state.

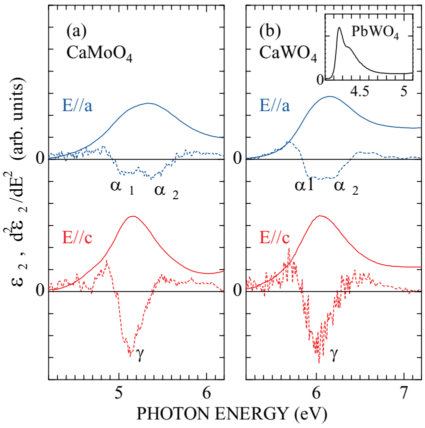

Fig. 1 The spectra of ε_2 (solid curves) and $d^2\varepsilon_2/dE^2$ (dotted curves) of (a) CaMoO$_4$ and (b) CaWO$_4$. The ε_2 spectrum of PbWO$_4$ [2] is shown in the inset of (b).

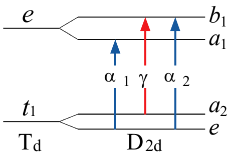

Fig. 2 Energy diagram of a MoO$_4^{2-}$ (WO$_4^{2-}$) molecule of T$_d$ and D$_{2d}$ symmetry. Blue and red arrows indicate the allowed transitions for ***E***//***a*** and ***E***//***c***, respectively.

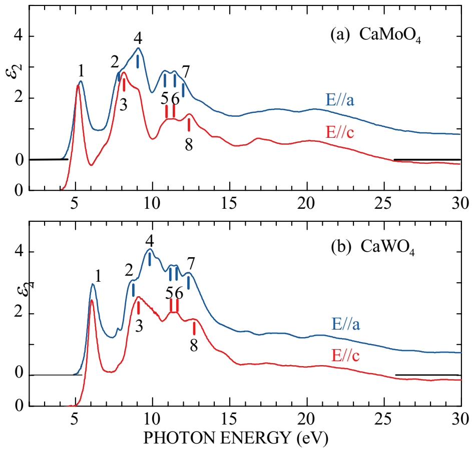

Fig. 3 The spectra of ε_2 of (a) CaMoO$_4$ and (b) CaWO$_4$ up to 30 eV.

[1] V. B. Mikhailik *et al.*, Phys. Rev. B **69** (2004) 205110.
[2] M. Fujita *et al.*, Phys. Rev. B **65** (2002) 195105.

BL1B

Photoluminescence in Polyamide-6/Mica Nanocomposite

N. Fuse[1], M. Okada[1], T. Tanaka[2], Y. Ohki[1]
[1]*Department of EEBS, Waseda University, Shinjuku 169-8555 Japan*
[2]*Graduate School of IPS, Waseda University, Kita-Kyushu 808-0135 Japan*

Dielectric properties of polymer nanocomposites (NCs) have been reported actively in recent years because of their wide potential application fields [1]. The present article reports photoluminescence (PL) and PL decay characteristics of polyamide-6, focusing on the effect of addition of mica nanofillers.

Experimental

The samples investigated are three kinds of polyamide-6 NCs with 2, 4 and 5 wt% addition of mica nanofillers. Mica was exfoliated to 1 nm thick layers, which were then uniformly dispersed in polyamide-6 resin by *in situ* polymerization [2]. As a reference, polyamide-6 without mica nanofillers was also used. The samples are called PA-0, PA-2, PA-4 and PA-5 according to their mica contents. Using synchrotron radiation (SR) under multi-bunch operation at the BL1B line of UVSOR Facility (Institute of Molecular Science, Okazaki, Japan, beam energy: 750 MeV) as a photon source, PL spectra from the samples were measured. The PL decay profiles were measured by a single photon counting method using SR under single-bunch operation (SR duration: 0.55 ns, interval: 176 ns). All the measurements were done at room temperature.

Results and Discussion

Fig. 1 shows a two-dimensional map that shows the PL intensity distribution observed for PA-0 by changing the excitation photon energy. The PL intensity is normalized by the maximum intensity of PL A that has an excitation peak around 3.6 eV and an emission peak around 3.0 eV. Another PL called PL B, which has an excitation peak around 4.8 eV and an emission peak around 2.9 eV, is also observed. Note that Band 1 is the excitation light, and that Band 2 is a fake replica of Band 1 that goes through the monochromator at the wavelength twice the designated value. Moreover, Bands 3 and 4 are originated from interference for the excitation light with the monochromator gratings. Therefore, only PLs A and B are the true PL spectra related to the samples.

Fig. 2 shows decay profiles of PLs A and B. For both PLs A and B, no change in the decay profile was induced by the addition of nanofillers. Namely, it is confirmed that the same two PLs, A and B, appear in all the samples irrelevantly to the nanofiller loading.

Further results show that neither the emission energies nor excitation energies of two PL bands change by the addition of nanofillers. Moreover, no new PLs are induced in the range from 2.0 eV to 6.0 eV. These are negative results for the appearance of new localized states in the forbidden band at least as long as luminous ones, while it has been reported that shallow traps are introduced in the forbidden band by the addition of nanofillers [3].

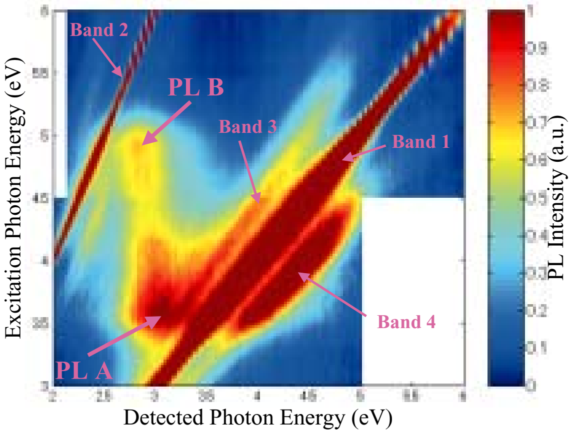

Fig. 1 Two-dimensional distribution of PL intensity induced by SR photons in PA-0.

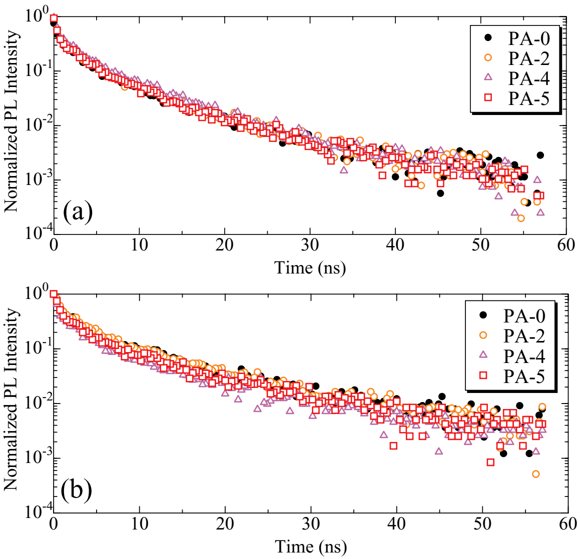

Fig. 2 Decay profiles of PLs A (a) and B (b).

[1] T. Tanaka *et al.*, IEEE Trans. Dielectr. Electr. Insul. **11** (2004) 763.

[2] S. Katahira *et al.*, Kobunshi Ronbunshu **55** (1998) 83 [in Japanese].

[3] G.C. Montanari *et al.*, IEEE Trans. Dielectr. Electr. Insul. **11** (2004) 754.

BL1B

Temperature Dependence of Absorption and Luminescence Spectra of $BaMgF_4:Ce^{3+}$ Crystals

E. Hayashi[1], Y. Ohsumi[1], T. Hasegawa[1], M. Yoshida[1], M. Yamaga[1], S. Ono[2], N. Sarukura[2]
[1]*Department of Electric and Electronic Engineering, Gifu University, Gifu 501-1193, Japan*
[2]*Institute for Molecular Science, Okazaki 444-8585, Japan*

Recently, laser materials operating in the vacuum ultraviolet (VUV) region below 200 nm is required. In order to satisfy this requirement, a frequency doubling method using a nonlinear effect is useful. Ce^{3+}-doped $BaMgF_4$ (BMF) crystals attract attention as laser materials with a nonlinear effect. In this report, we discuss temperature dependence of absorption and luminescence spectra of Ce^{3+} in BMF.

Figure 1 shows temperature dependence of absorption spectra of BMF:Ce^{3+}. The absorption spectra consist of four intense VUV bands at 115, 127, 144, and 157 nm, and five VUV/UV bands at 174, 199, 232, 246, and 258 nm. The latter is assigned as optical transitions from the $^2F_{5/2}$ ground state to five non-degenerated 5d excited states of Ce^{3+}. Shapes of three bands around 250 nm do not change below 100 K. However, in increasing a temperature above 100 K, the widths are broadened and the peaks are shifted to longer wavelengths with an amount of about 2 nm. The intense VUV bands may be due to complexes composed of color centre (two electrons trapped at an F^- vacancy) and Ce^{3+} impurity [1,2].

Figure 2 shows temperature dependence of luminescence spectra with different excitation wavelengths. Three luminescence bands denoted by A, B, and C are shifted to longer wavelengths in alphabetical order. Broadening and peak-shift of the absorption bands occur with an increase of temperature as shown in Fig. 1. Taking account of these effects, intensities of A and C luminescence bands are independent of temperature except those of A and B bands with 196-nm and 156-nm excitation. The A-band luminescence is due to Ce^{3+} ions substituting for Ba^{2+} ions. The B-band luminescence is due to Ce^{3+} ions perturbed by charge compensators. The C-band luminescence is assigned to a complex composed of Ce^{3+} and color centre [1,2].

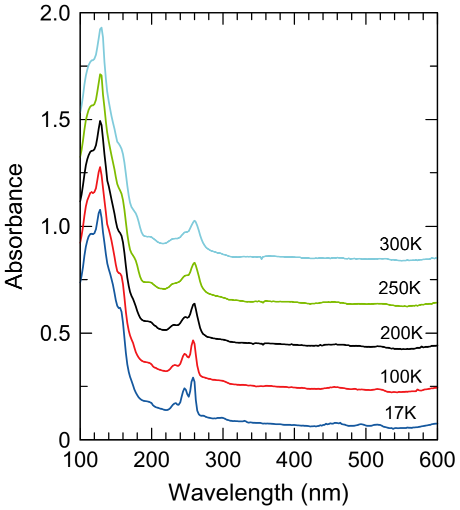

Fig. 1 Temperature dependence of absorption spectra of $BaMgF_4:Ce^{3+}$.

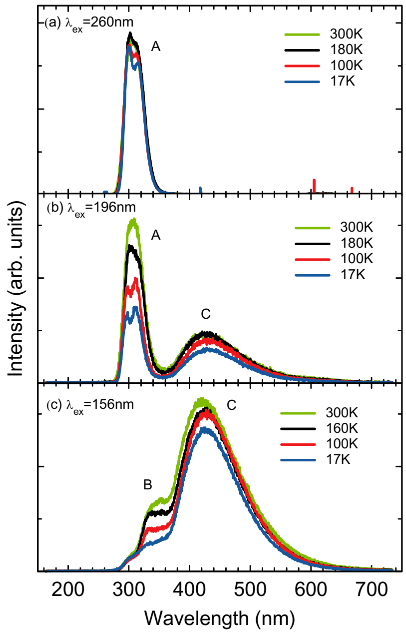

Fig. 2 Temperature dependence of luminescence spectra of $BaMgF_4:Ce^{3+}$.

[1] E. Hayashi, K. Itoh, S. Yabashi, M. Yamaga, N. Kodama, S. Ono and N. Sarukura, J. Alloys and Compounds **408-412** (2006) 883.

[2] E. Hayashi, K. Itoh, S. Yabashi, M. Yamaga, N. Kodama, S. Ono and N. Sarukura, J. Lumin. (2006) in press.

BL1B

Effect of Alkyl Chain Length on Photoionization at the Water Surface

T. Ishioka, A. Harata

Department of Molecular and Material Sciences, Kyushu University, Kasugakoen 6-1,
Kasuga-shi, Fukuoka 816-8680, Japan

Photocurrent has been measured from anthra-quinone derivatives at the water surface by synchrotron radiation. Photoionization threshold did not change by elonging alkyl chains bound to the molecule but its intensity increased from C_2 to C_8 and then drastically decreased at C_{12}. It is suggested that solvation of anthraquinone by water is not largely influenced by alkyl chains but electrons emitted are remarkably scattered when alkyl chains are long enough to form self-assembled layers.

Introduction

Photoionization at the water surface give useful information on electric states and structures of adsorbed species and SR light has been used for measuring precise threshold energy by its inherent tunability in photon energy. However, photoionizing behavior of adsorbed molecules at an aqueous solution surface has not fully studied even though there are a wide variety of surface-active molecules and their adsorption behavior has a great importance in physical chemistry, biochemistry, environmental chemistry, and technology.

We have analyzed photoionizing behavior of dye molecules with surfactant layers over the adsorbed dye [1]. From the measurement, aggregation of dye molecules, self-assembled layer formation of surfactamts, and charge interactions between dye and surfactant molecules had a large effect on measured photoionization current. However, it was too difficult to distinguish each contribution from others because of complex surface constructions.

In this report, anthraquinone derivatives with alkyl chains were synthesized for simplifying the surface construction. Photoionization behavior on water surface is analyzed using this simple system and effects of alkyl chains are discussed.

Experimental

The monochromated synchrotron light (4-8 eV) was obtained from BL1B at the UVSOR facility and emitted from the chamber to a He-purged cell through an MgF_2 window. The emitted light was reflected on an Al mirror and vertically irradiated on the aqueous solution surface through a Cu-mesh electrode. The electrode was set at 5 mm high above the liquid surface and high voltage (400 V) was applied. The photocurrent (~100 fA) was measured by a picoammeter.

Anthraquinone derivatives modified with alkyl chains via thiourea (Fig. 1) were synthesized from 1-aminoanthraquinone and dissolved in benzene at 0.2 mM. The benzene solution was spread by 10 μL on the pure water surface.

Results and Discussion

In all cases, photoionization current increased above approximately the same threshold energies around 6.2 eV (Fig. 2). Since the threshold energy of molecule on the water surface is lowered by polarization energy of solvation, the difference of measured threshold from gas-phase ionization potential reflects the state of solvation. Unchaged threshold energy by elongation of alkyl chain length shows that the solvation state of water around anthraquinone ring is not largely distorted by the presence of hydrophobic functional groups.

However, photoionization intensity itself largely depends on the length of alkyl chains. For the shorter case, the small intensity can be explained by a loss of surface molecule to the bulk phase by its slight solubility to water. While C_{12} case, the decrease should arise from another reason. The observation of increased fluctuation of current at C_8 would suggest the presence of aggregated species on the surface. Thus it is considered that self-assembled layer is formed at C_{12} and electrons emitted are scattered by alkyl layers formed on the water surface.

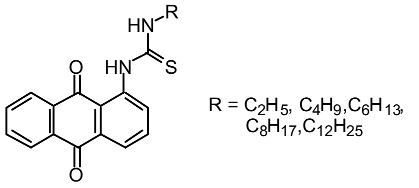

Fig. 1 Structure of synthesized anthraquinone derivatives.

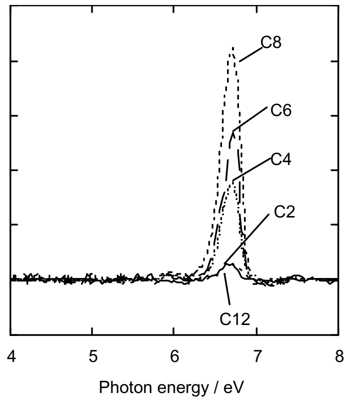

Fig. 2 Measured photoionization current from anthraquinone derivatives on the water surface.

[1] T. Ishioka and A. Harata, UVSOR Activity Report 2003 (2004) 62.

Optical Properties of Tl^+ Centers Doped in CsH_2PO_4

T. Kawai[1], T. Hirai[2], N. Ohno[2,3]
[1]*Graduate School of Science, Osaka Prefecture University, Sakai 590-0035, Japan*
[2]*Academic Frontier Promotion Center, Osaka Electro-Communication University*
[3]*Graduate School of Engineering, Osaka Electro-Communication University,*
Neyagawa 572-8530, Japan

Tl^+ centers doped in alkali halide crystals with the NaCl-type crystal structure exhibit three absorption bands called A, B and C in an energy region below the absorption edge of host crystals [1,2]. The absorption bands are attributed to the intraionic transitions corresponding to $^1S_0 \rightarrow {}^3P_1$ (spin-orbit allowed), $^1S_0 \rightarrow {}^3P_2$ (vibration induced), $^1S_0 \rightarrow {}^1P_1$ (dipole allowed), respectively. On the other hand, the Tl^+ centers doped in cesium halide crystals with the CsCl-type crystal structure exhibit remarkably different absorption bands from those doped in the NaCl-type alkali halides. Though the Tl^+ ions doped in NaCl- and CsCl-type alkali halide crystals are situated under the highest symmetry O_h , these ion arrangements around the Tl^+ ions are different in both the crystals. Optical properties of an impurity center are strongly affected by ion arrangements and the symmetry around the center. Therefore, it is of great interest to study the optical properties of the Tl^+ center doped in host crystals with lower symmetries.

In the present study, we have investigated optical properties of the Tl^+ center doped in CsH_2PO_4 (CDP), which belongs to a family of ferroelectric materials of the KH_2PO_4 (KDP) type. The crystal structures of KDP and CDP are orthorhombic and monoclinic at low temperature, respectively. Therefore, the Tl^+ ions doped in both crystal are situated under the lower symmetry. It is known that the Tl^+ center doped in KDP exhibits five characteristic polarized absorption bands [3,4]. On the other hand, there are few studies on optical properties of the Tl^+ center doped in CDP.

The CDP compound was synthesized by mixing stoichiometric amounts of Cs_2CO_3 and H_3PO_4. After several times of recrystallization, TlH_2PO_4 (TDP) compound was added to the aqueous solution of the purified crystals. Crystals of CDP:Tl^+ were grown by an ordinary evaporation method from the CDP saturated aqueous solution doped with about 10^{-3} mol% TDP. Absorption, luminescence and excitation spectra of CDP:Tl^+ have been measured at the BL-1B beam line of UVSOR.

Figure 1 shows absorption (blue curve), luminescence (green curve), excitation (red curve) spectra of CDP:Tl^+ at 10 K. The absorption bands are observed at 5.86 and 7.54 eV. Their energy values are almost equal to those of the A and C absorption bands in KDP:Tl^+, respectively [3,4]. Therefore, the 5.86 and 7.54 eV bands in CDP:Tl^+ would be attributed to the A and C absorption bands.

When the A band at 5.86 eV is photo-excited, a broad luminescence band with a large Stokes shift is observed at 4.13 eV. The 4.13 eV luminescence band exhibits non-Gaussian bandshape and the lower energy tail. The fact implies that the 4.13 eV band is composed of several luminescence bands. The excitation spectrum for the 4.13 eV band exhibits the strong response on 5.86 eV light. The fact indicates that the 4.13 eV band is related with the Tl^+ center doped in CDP. Since there is a response on the lowest A absorption band in the excitation spectrum, the 4.13 eV luminescence band should be ascribed to a radiative transition from the relaxed excited states of $^3P_1$.

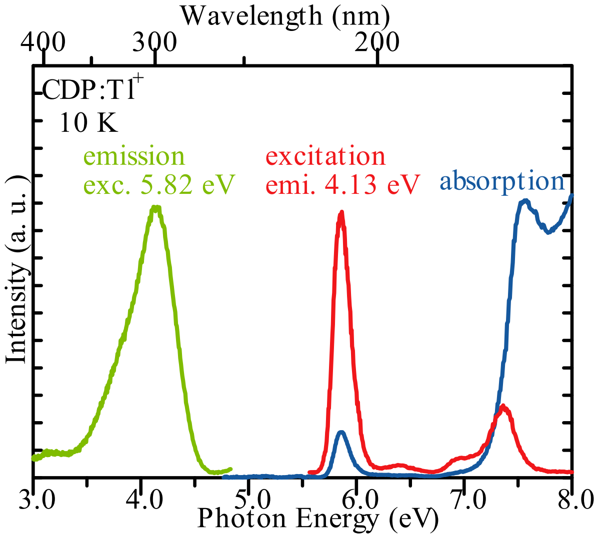

Fig. 1 Absorption (blue curve) and luminescence (green curve) and excitation (red curve) spectra of CDP:Tl^+ at 10K.

[1] A. Ranfagni *et al*., Adv. Phys. **32** (1983) 8253.
[2] P.W.M. Jacobs, J. Phys. Chem. Solids **52** (1991) 35.
[3] I. Fujita, Phys. Rev. B **49** (1994) 6462.
[4] T. Fuyuki and N. Ohno, UVSOR Activity Report 2004 (2005) 69.

BL1B

Vacuum-Ultraviolet Reflectance Spectroscopy of 3d Transition-Metal Oxides

I. Kezsmarki[1], S. Miyasaka[1] Y. Tomioka[2], Y. Tokura[1,2,3]
[1]*Department of Applied Physics, University of Tokyo, Tokyo 113-8656 Japan*
[2]*Correleted Electron Research Center (CERC), National Institute of Advanced Industrial Science and Technology (AIST), Tsukuba 305-8562 Japan*
[3]*Spin Superstructure Project (SSS), ERATO, Japan Science and Technology Agency (JST), Tsukuba 305-8562 Japan*

One of the most important characteristics for the strongly correlated electron systems is the drastic re-construction of electronic structure over an energy scale of eV with changes of temperature, doping concentration and so on. In this beam time, we measured the reflectivity spectra for single crystals of perovskite-type $R_{1-x}A_x$MnO$_3$ (R=trivalent rare-earth elements, A=divalent alkaline-earth ones) with the hole concentration of x=0.45, for an energy range of 4 eV < E < 35 eV using the beam line BL1B. The measured reflectivity data, together with that below 4 eV, were used to derive the optical conductivity spectra via the Kramers-Kronig analysis.

It is well known that the magnetic and electronic characters are controlled by the doping concentration and the effective one electron band-width in $R_{1-x}A_x$MnO$_3$. Recent studies have indicated that the bicritical feature caused by the competition between the ferromagnetic metal (FM) and charge/orbital ordering (CO/OO) insulator plays an important role in the colossal magnetoresistance effect. In addition, it has been revealed that the effect of quenched disorder due to the random chemical replacement of the perovskite A site is one of controllable parameters [1]. In $R_{0.55}$Sr$_{0.45}$MnO$_3$, the transition temperature of the ferromagnetic ordering (T_C) decreases from ~ 280 K to ~ 50 K, as R changes from Nd to Eu, i.e., as the effective one electron band-width decreases. In R=Gd compound, the ferromagnetic state becomes further unstable, and then the FM is taken over by a spin glass-like insulator below T_G= ~ 50 K. In the Pr$_{0.55}$(Ca$_{1-y}$Sr$_y$)$_{0.45}$MnO$_3$ system, by contrast, the reduction in T_C is not so remarkable as in the $R_{0.55}$Sr$_{0.45}$MnO$_3$ system. Moreover, the phase change from a FM to a CO/OO (long range) insulator is typically bicritical with T_C=T_{CO} ~ 200 K. That is, the phase diagram of the $R_{0.55}$Sr$_{0.45}$MnO$_3$ system is different from the bicritical feature in spite of the common hole-doping level and even when the average radius of the perovskite A site is taken as the same value. The dramatic modification of the FM vs CO/OO phase diagrams is quite analogous to the case of the A-site order versus disorder of $R_{0.5}$Ba$_{0.5}$MnO$_3$, where the perfect R/Ba ordering along the c axis alters the phase diagram of the R/Ba solid solution (similar to that of the R/Sr solid solution) to the typical bicritical phase diagram (similar to that of Pr$_{0.55}$(Ca$_{1-y}$Sr$_y$)$_{0.45}$MnO$_3$) [2]. Therefore, the large modification of the phase diagram in $R_{0.55}$Sr$_{0.45}$MnO$_3$ case is likely to arise from the random potential affecting on the FM vs CO/OO bicritical feature. The source of the random potential may be the local lattice distortion arising from the larger mismatch of the ionic size of R/Sr ions than Pr/(Ca, Sr) ones.

We present the optical conductivity spectra for $R_{0.55}$Sr$_{0.45}$MnO$_3$ (R=Nd and Eu) in Fig. 1. In the spectra at high temperatures, the lowest optical transition around 1 eV can be assigned to the optical transition across the Mott-type gap. Above the Mott gap, a much more intense optical transition is clearly discerned. The position and intensity suggest that the transition be assigned to the charge transfer excitation from O 2p to Mn 3d upper Hubbard state. In the temperature region of T<T_C, the Mott gap disappears and the spectral weight around 1 eV is transferred to the lower energy region. Resultantly, the Drude-like structure appears below T_C. The spectral change takes place at about room temperature in Nd$_{0.55}$Sr$_{0.45}$MnO$_3$, while that occurs below 50 K in Eu$_{0.55}$Sr$_{0.45}$MnO$_3$.

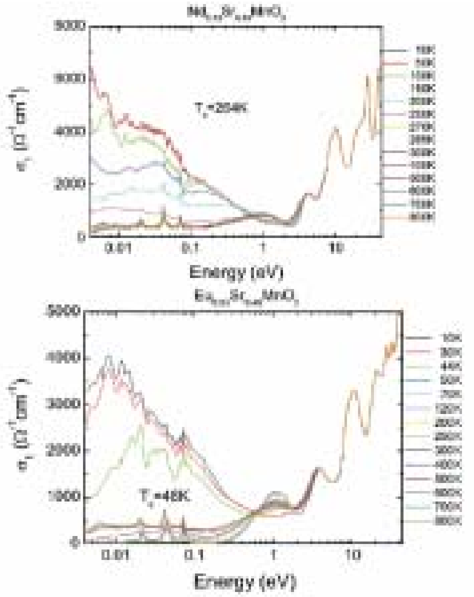

Fig. 1 The optical conductivity spectra (σ_1) for $R_{0.55}$Sr$_{0.45}$MnO$_3$ (R=Nd and Eu) at various temperatures.

[1] Y. Tomioka *et al.*, Phys. Rev. B **68** (2005) 094417.
[2] D. Akahoshi *et al.*, Phys. Rev. Lett. **90** (2003) 177203.

BL1B

Photoluminescence of Hydroxyapatite Irradiated by Ultraviolet Synchrotron Orbital Radiation Light (2)

M. Ohta

Department of Material Science and Technology, Faculty of Engineering, Niigata University, 8050 Ikarashi 2-no-cho, Niigata 950-2181, Japan

It was known that rare earth ions dosed for oral administration to mouse and rat are transferred to blood vessel through the ileum and deposited its teeth and bone, which mainly consists of hydroxyapatite (HAp; $Ca_{10}(PO_4)_6(OH)_2$) [1-2]. We have found that Eu ion substituted Ba ion in Eu doped $Ba_{10}(PO_4)_6Cl_2$ phosphor, which matrix is apatite structure [3]. In this study, rare earth ion-doped HAp samples were prepared in order to make clear the segregation mechanism of rare earth ion on teeth and bone. Their characteristics were investigated by photoluminescent (PL) property of rare earth ion-doped HAp excited by ultraviolet synchrotron orbital radiation light.

Eu-doped HAp and Gd-doped HAp were prepared as follows: HAp was soaked at 310K in $EuCl_3$ or $GdCl_3$ aqueous solution. After 72 hr, Eu-doped or Gd-doped HAp was separated from $EuCl_3$ or $GdCl_3$ aqueous solution by filtation and then dried by using with infrared ray (unfired samples). Fired samples were prepared by firing the unfired samples at 1373K for 1 hr in air.

The PL property of each sample exited by ultraviolet synchrotron orbital radiation light (BL1B) was detected by using with a multi-channel analyzer.

Figure 1 shows PL spectra of unfied and fired Eu-doped HAp samples excited by BL1B. The PL spectra of both Eu-doped HAp samples exited by 120 nm or 160 nm had many peaks which were not ascribed to Eu ion. These facts indicate the inner shell excitation in host crystals and traps of electron and/or hole due to the defects of host crystal structure exits in both Eu-doped HAp samples, since the PL property is similar to that of self doped phosphors. The PL spectra of both Eu-doped HAp samples exited by 200 nm or 240 nm had the peaks due to the f-f electronic transitions of trivalent Eu ion as from $^5D_0$ to $^7F_1$ (595 nm), from $^5D_0$ to $^7F_2$ (612 nm), from $^5D_0$ to $^7F_3$ (654 nm) and from $^5D_0$ to $^7F_6$ (700 nm). These PL peaks height of fired sample was higher than that of unfired sample.

Figure 2 shows PL spectra of unfired and fired Gd-doped HAp samples excited by BL1B. The PL spectra of unfired Gd-doped HAp sample had many peaks which were not ascribed to Gd ion, even if exited by 120-240nm. While the PL spectra of fired Gd-doped HAp sample exited by 120-240nm had the peaks due to the f-f electronic transition of trivalent Gd ion as from $^6P_{7/2}$ to ^8S (316 nm), especially, the peak height of the sample exited by 160 nm was remarkably large.

These facts indicate that Eu and Gd ions deposit in the surface of HAp and Eu ion substitute for Ca ion in HAp according to ion exchange reaction at 310K. The fired samples are higher crystallinity and exhibit brighter PL due to the f-f-electronic transition of trivalent Eu and Gd ion.

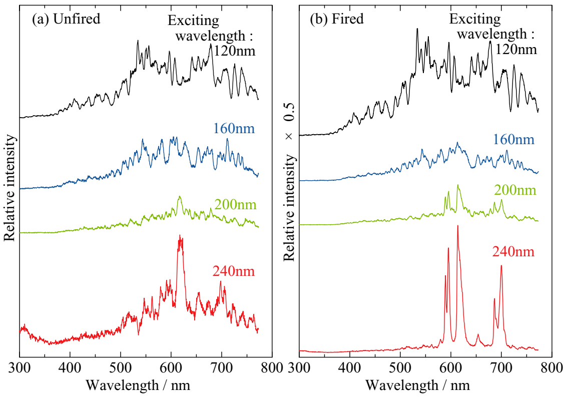

Fig. 1 Photoluminescence spactra of Eu-doped HAp sample excited by ultraviolet synchrotron orbital radiation light.

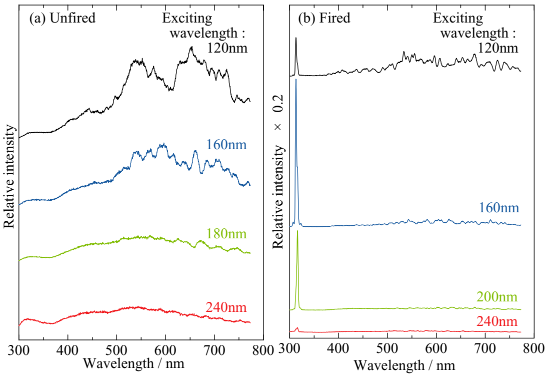

Fig. 2 Photoluminescence spactra of Gd-doped HAp sample excited by ultraviolet synchrotron orbital radiation light.

[1] S. Hirano, K. T. Suzuki, Environ. Health Perspect. **104** (Supplement 1) (1996) 85.

[2] K. Kostial, B. Kargacin, M. Lendeka, Int. J. Radiat. Biol. Relat. Stud. Phys. Chem. Med. **51** (1987) 139.

[3] M. Sato, T. Tanaka, M. Ohta, J. Electrochem. Soc., **141** (1994) 1851.

BL1B

Photoluminescence from Langasite $La_3Ga_5SiO_{14}$ Crystals

S. Takagi[1], T. Shimizu[1], M. Itoh[1], M. Fujita[2], M. Kitaura[3]
[1]*Faculty of Engineering, Shinshu University, Wakasato, Nagano 380-8553*
[2]*Japan Coast Guard Academy, Wakaba, Kure 737-8512*
[3]*Fukui National College of Technology, Sabae 916-8507*

Lanthanum gallium silicate (langasite; $La_3Ga_5SiO_{14}$) is a new piezoelectric crystal and is abbreviated to LGS. The absence of structural phase transitions between the melting point (1470°C) and room temperature makes the application of this material at elevated temperatures feasible [1]. The crystal of LGS consists of tetrahedral layers, perpendicular to the crystalline *c*-axis, between which there are layers formed by cations in distorted cubes coordinated by eight O atoms and in octahedral by six O atoms.

Because of the strong exciton-phonon interaction in LGS, it is very interesting to investigate whether a self-trapped exciton (STE) exists or not. Bearing this in mind, we performed luminescence measurements of LGS at low temperatures.

Experiment

The single crystals of LGS used in this work were obtained from Mitsubishi Materials, Japan. They were grown by the Czochralski method, and annealed at 1000–1300°C for 24 h in reduced atmosphere. Three-dimensional (3-D) emission-excitation spectra were measured using an Acton SpectraPro-3000i monochromator equipped with an LN/CCD camera.

Results and Discussion

Figure 1 shows the 3-D spectrum of LGS measured at 5 K under the condition that the electric vector of the incident light is parallel to the *Y*-axis of a sample. The lower part corresponds to the contour plot of the upper spectrum. One may see two emission bands at 420 and 500 nm. The intensity of the 420 nm band increases at 220 nm, and reaches the maximum around 205 nm, followed by the decrease in the short wavelength region. The 500 nm band is strongly excited with UV light at around 245 nm. The 3-D spectrum for the polarization parallel to the *Z*-axis was almost the same as Fig. 1, indicating that there is no appreciable polarization characteristic of two emission bands at 420 and 500 nm.

The electronic structure of LGS has been studied experimentally and theoretically [2]. The valence band is mainly formed by the O 2*p* states, and the lower part of the conduction band is dominated by the La 5*d* states. The excitation threshold of the 420 nm band coincides with the fundamental absorption edge at ≈ 235 nm. Such a coincidence suggests that this band is of intrinsic origin. It is likely that a hole is self-trapped at an oxygen ion because of the strong coupling with phonons. As a result, an STE is formed through the capture of a conduction electron by the self-trapped hole. We suppose that the 420 nm band is ascribed to the radiative annihilation of STEs. On the other hand, the 500 nm band is due to the decay of localized excitons perturbed by some lattice imperfection, because it is induced in the energy region below the fundamental absorption edge.

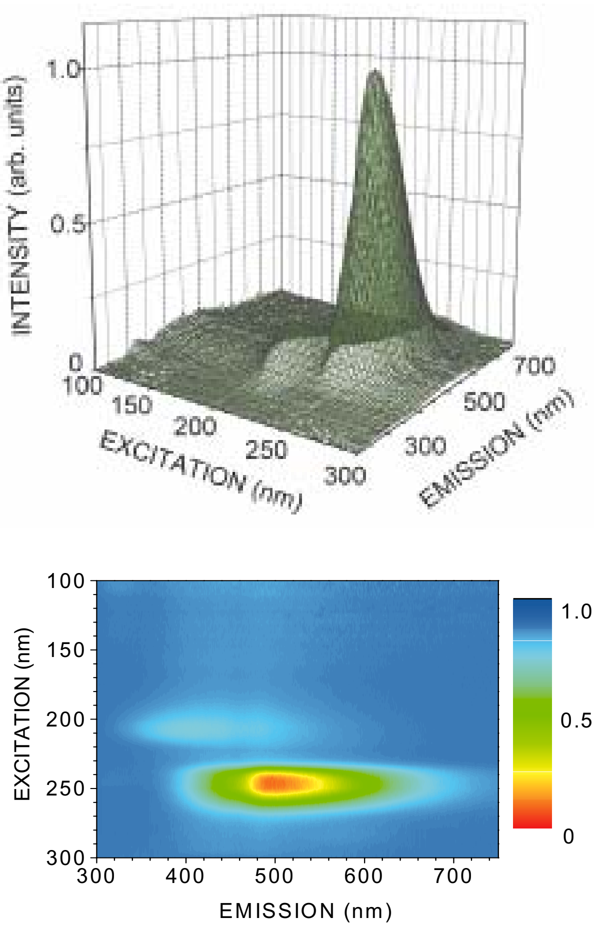

Fig. 1 3-D emission-excitation spectrum of LGS measured for the polarization parallel to the *Y*-axis, together with the contour plot of the upper spectrum.

[1] K. Shimamura, H. Takeda, T. Kohno and T. Fukuda, J. Cryst. Growth **163** (1996) 388.
[2] M. Kitaura, K. Mochizuki, Y. Inabe, M. Itoh, H. Nakagawa and S. Oishi, Phys. Rev. B **69** (2004) 115120.

BL1B

Luminescence Properties of $YAl_3(BO_3)_4$ Substituted with Sc^{3+} Ions

H. Yoshida[1,2], K. Fujikawa[1], H. Toyoshima[1], S. Watanabe[1], K. Ogasawara[1]

[1]*Department of Chemistry, Kwansei Gakuin University, 2-1 Gakuen, Sanda, 669-1337, Japan*
[2]*Research and Development Division, NEC Lighting, Ltd., 3-1 Nichiden, Minakuchi-cho, Koka, 528-8501, Japan*

Introduction

The $YAl_3(BO_3)_4:Gd^{3+}$ (YAB:Gd) phosphor has a strong ultraviolet (UV) emission line at 3.96 eV, which is effectively stimulated under the vacuum ultraviolet excitation. Its crystal structure (space group *R*32) is isostructural with the mineral huntite, $CaMg_3(CO_3)_4$. One of the interesting points is that there are two kinds of BO_3 atomic groups within an unit cell of $YAl_3(BO_3)_4$ (YAB) crystal. Recently, we successfully explained the origin of the excitation spectrum of YAB:Gd phosphor by the first-principles method [1]. Moreover, as we expected, it was confirmed that the luminescence peak intensity of $Y_{0.65}Gd_{0.25}Sc_{0.1}Al_3(BO_3)_4$ was about 1.4 times that of YAB:Gd phosphor [2]. However, the mechanisms of the excitation processes with the presence of Sc^{3+} ions are not fully understood. To clarify the origin of this luminescence enhancement, luminescence and excitation spectra of YAB and $Y_{0.9}Sc_{0.1}Al_3(BO_3)_4$ (YSAB) have been measured at low temperature.

Sample Preparation Method

YAB and YSAB samples were synthesized with a solid-state reaction using Y_2O_3 (4N), H_3BO_3(2N) Al_2O_3(5N) and Sc_2O_3(3N) as the starting materials. The powder samples were obtained by firing in air for 20 hours at 1450 K.

Results and Discussion

Yokosawa *et al.* reported that UV emission band at about 310 nm is obserbed for YAB under VUV excitatuon [3]. Figure 1 shows the excitation spectra of YAB and YSAB detected at the emisson peak position. In the YAB, the valence band of our calculations is mainly build of O 2*p* state and the conduction band is composed of mixing state of the B 2*p* and Y 4*d* [1]. Therefore, a clear structure peaking at 7.8eV corresponds to transitions from O 2*p* state to the mixed state of B 2*p* and Y 4*d*. As we can see, the absorption edge of YSAB is lower energy side than that of YAB. It is concluded that the origin of additional structure at about 7 eV is due to the Sc 3*d* states according to the electronic state calculation by DV-Xα method.

In fig. 2, the luminescence spectra of YAB and YSAB are shown. As we can see, it is found that these emission peek position were different. In YAB, two emission bands peaking at 3.2 and 3.9 eV are observed. On the other hand, there appear two emission bands at 3.2 and 4.1 eV in YSAB. The origins of these emission bands are ascribed to BO_3 atomic groups [3], and we suppose that the shift of the peak around 3.9-eV emission bands is deeply related to the fact that one kind of BO_3 atomic groups of YSAB are significantly distorted compared to that of YAB. It is still a question as to how 3.9-eV band shifts toward higher energy side by Sc^{3+} substitution. The obtained results suggested the need for further experiments and theoretical considerations.

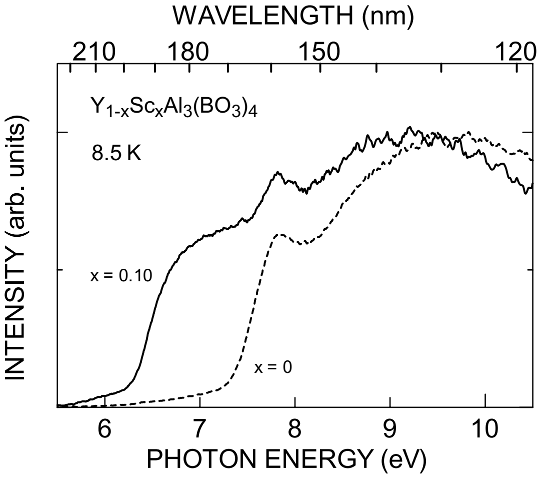

Fig. 1 Excitation spectra of $YAl_3(BO_3)_4$ (solid line) and $Y_{0.9}Sc_{0.1}Al_3(BO_3)_4$ (dash line) at 8.5 K.

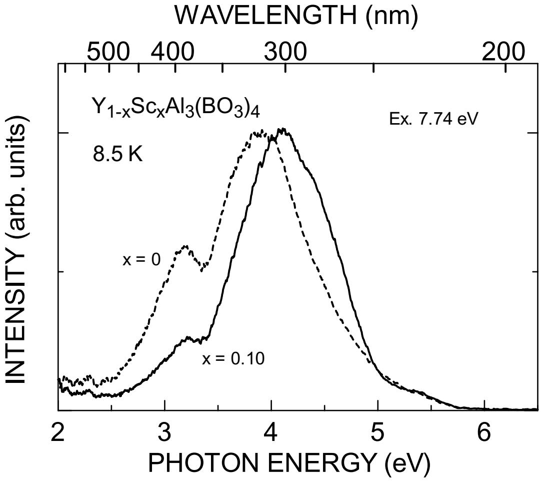

Fig. 2 Luminescence spectra of $YAl_3(BO_3)_4$ (solid line) and $Y_{0.9}Sc_{0.1}Al_3(BO_3)_4$ (dash line) at 8.5 K.

[1] H. Yoshida, R. Yoshimatsu, S. Watanabe and K. Ogasawara, Jpn. J. Appl. Phys. **45** (2006) 146.
[2] H. Yoshida, R. Yoshimatsu and K. Ogasawara, J. Lumin. to be published.
[3] N. Yokosawa and E. Nakazawa, Jpn. J. Appl. Phys. **42** (2003) 5656.

Luminescence Properties of (Y,Gd)$Al_3(BO_3)_4$:Tb^{3+} Phosphors Substituted with Sc^{3+} Ions

H. Yoshida[1,2], K. Fujikawa[1], H. Toyoshima[1], S. Watanabe[1], K. Ogasawara[1]

[1] *Department of Chemistry, Kwansei Gakuin University, 2-1 Gakuen, Sanda, 669-1337, Japan*

[2] *Research and Development Division, NEC Lighting, Ltd., 3-1 Nichiden, Minakuchi-cho, Koka, 528-8501, Japan*

Introduction

Plasma display panels (PDPs) and new mercury-free lamps using xenon discharge have been developed and required new phosphors with high efficiency. Especially, a green phosphor is deeply related to the luminous intensity. Tanimizu *et al.* [1] and Yokosawa *et al.* [2] reported that the efficiency of luminescence for Tb^{3+} activated $YAl_3(BO_3)_4$ phosphor under vacuum ultraviolet (VUV) excitation is almost the same as that of Zn_2SiO_4:Mn which is a green phosphor of typical PDPs. However, the efficiency is not enough and more improvement of luminescence properties are demanded. Recently, we reported the luminescence properties of $YAl_3(BO_3)_4$:Gd substituted with Sc^{3+} ions that has a higher efficiency of luminescence than that of $YAl_3(BO_3)_4$:Gd. In this study, we have been investigated the luminescence and excitation spectra of (Y,Gd)$Al_3(BO_3)_4$:Tb^{3+} phosphors substituted with Sc^{3+} ions at low temperature.

Results and Discussion

Figure 1 shows the luminescence spectrum of $Y_{0.55}Gd_{0.25}Tb_{0.2}Al_3(BO_3)_4$ phosphor under the excitation light at 7.74 eV. As we can see, the several strong emission lines are observed. The 2.29-eV emission line is useful as a green emission, which orginates from the $^5D_4 \rightarrow {}^7F_5$ transitions in Tb^{3+} ions.
In Fig. 2, excitation spectra of $Y_{0.55-x}Gd_{0.25}Tb_{0.2}Sc_xAl_3(BO_3)_4$ (x = 0, 0.05, 0.10, 0.15, 0.20, 0.25) detected at 2.29-eV emission line are shown. A clear structure peaking at 7.8 eV corresponding to transitions from O 2*p* state to mixture state of B 2*p* and Y 4*d* orbitals [3]. The structure in the range from about 4.5 eV to 7 eV is assigned to $4f^9$-$4f^85d^1$ transitions in Tb^{3+} ions. It is clearly found that the intensity of excitation band at about 6.8 eV increases with increasing Sc concentration. We suppose that this additional excitation band is due to the Sc 3*d* state, which is a good agreement with our calculation results of the electronic state by the first principles DV-Xα method [4]. We have also confirmed that the luminescence peak intensity and luminance of $Y_{0.55-x}Gd_{0.25}Tb_{0.2}Sc_xAl_3(BO_3)_4$ (x = 0.10) at room temperature is stronger by a factor of about 1.3 compared with $Y_{0.55}Gd_{0.25}Tb_{0.2}Al_3(BO_3)_4$ under the VUV excitation light (peak wavelength:172 nm) using a xenon excimer lamp.

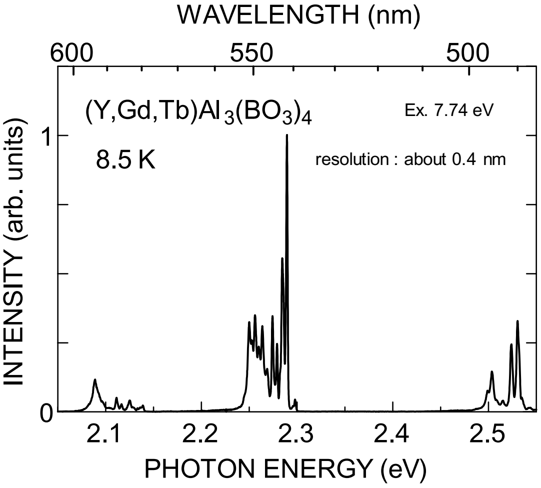

Fig. 1 Luminescence spectrum of $Y_{0.55}Gd_{0.25}Tb_{0.2}Al_3(BO_3)_4$ at 8.5 K.

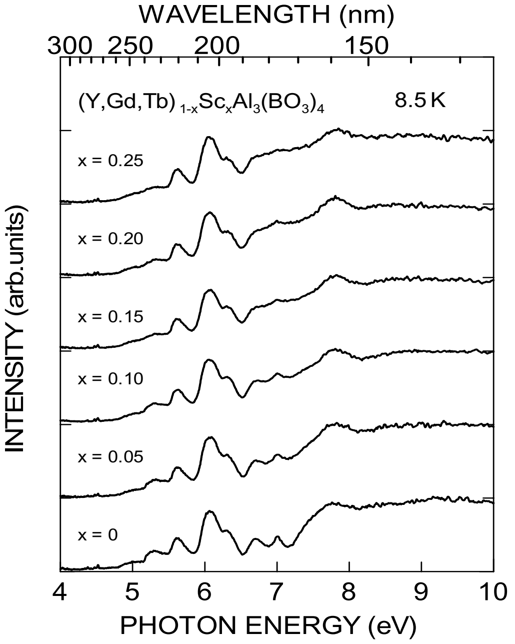

Fig. 2 Excitation spectra of $Y_{0.55-x}Gd_{0.25}Tb_{0.2}Sc_xAl_3(BO_3)_4$(x = 0, 0.05, 0.10, 0.15, 0.20, 0.25) at 8.5 K.

[1] S. Tanimizu, T. Suzuki, M. Shiiki and C. Okazaki, Proc. 9th Int. Symp. Sci. Tec. Light Sci. (2001) 393.
[2] N. Yokosawa, K. Suzuki and E. Nakazawa, Jpn. J. Appl. Phys. **42** (2003) 5656.
[3] H. Yoshida, R. Yoshimatsu, S. Watanabe and K. Ogasawara, Jpn. J. Appl. Phys. **45** (2006) 146.
[4] H. Yoshida, R. Yoshimatsu and K. Ogasawara, J. Lumin. to be published.

BL5B

Photoinduced Change in Vacuum Ultraviolet Transmission Spectra of Amorphous Chalcogenide Films Induced by Bandgap Light

K. Hayashi
Department of Electrical and Electronic Engineering, Gifu University, Gifu 501-1193, Japan

Introduction

It is well known that amorphous chalcogenide semiconductor materials, such as amorphous As_2S_3 (a-As_2S_3) and amorphous As_2Se_3 (a-As_2Se_3), show a variety of photoinduced phenomena [1-3]. The most prominent photoinduced phenomenon is the so-called photodarkening arising from the shift of the absorption edge. The absorption edge shifts to lower energy side by irradiation of light with the energy corresponding to the optical bandgap. For well annealed sample, the darkened state is removed by annealing near the glass-transition temperature. The X-ray diffraction and the volume change before and after irradiation suggest that the photodarkening is due to a change of local structure of the amorphous network [2]. Although a large number of studies have been done on the photodarkening induced by irradiation of bandgap (BG) light, the details of the mechanism is still unknown. To our knowledge, little attention has been given to the change of other energy structure induced by irradiation of BG light. To obtain a wide knowledge of the photoinduced phenomena, it is necessary to investigate photoinduced phenomena over a wide energy range. In previous reports, we reported photoinduced change in spectra of the vacuum ultraviolet (VUV) reflection and the total photoelectric yield by irradiation of BG light [4]. In this report, we investigate photoinduced change in VUV transmission spectra of amorphous chalcogenide films induced by irradiation of BG light.

Experimental

Thin films of amorphous chalcogenide semiconductor (a-As_2S_3 and a-As_2Se_3) were prepared onto ultrathin collodion films by conventional evaporation technique. A typical thickness of an amorphous film was around 160 nm. The ultrathin collodion films were prepared onto stainless steel metal plates in which two pinholes of the 1.5 mm diameter opened. A xenon arc lamp with IR-cut-off filter was used as a BG light source. Before the measurement of the VUV transmission spectrum, the unilateral of the sample was irradiated with the BG light in a vacuum to the degree in which the sample sufficiently produced the photodarkening. The measurement of the VUV transmission spectra were carried out at room temperature at the BL5B beam line of the UVSOR facility of the Institute for Molecular Science. And the spectrum was measured by using the silicon photodiode as a detector. To eliminate the higher order light from the monochromator, an aluminum thin film was inserted between the monochromator and sample. We also monitored the spectrum of the light source by measuring the photoelectric yield of a gold mesh.

Results and Discussion

Figure 1 shows the VUV transmission spectra of a-As_2S_3 film at room temperature in the photon energy region between 41 and 49 eV. One main absorption peak was observed in this energy region. This absorption peak around 44 eV corresponds to the 3d core level of As atom. As shown in Fig. 1, after irradiation with BG light, the absorption peak slightly shifts to higher energy side and the width of the spectrum becomes narrow. The similar change is also observed in the VUV reflection spectrum and a-As_2Se_3 films. As for the origins of the changes, it is not clear. I think that these changes are related to a change of the local structure of the amorphous network by irradiation of BG light. The detailed experiments and analysis will be done in the next step.

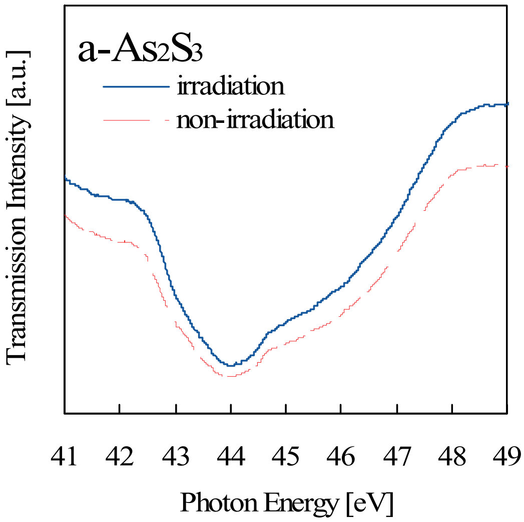

Fig. 1 The VUV transmission spectra of a-As_2S_3 film in non-irradiation part (broken line) and irradiation part (solid line) of BG light.

[1] Ke. Tanaka, Rev. Solid State Sci. **4** (1990) 641.
[2] K. Shimakawa, A.Kolobov, and S. R. Elliott, Adv. Phys. **44** (1995) 475.
[3] Ke. Tanaka, Encyclopedia of Nanoscience and Nanotechnology **7** (2004) 629.
[4] K. Hayashi, UVSOR Activity Report 2001 (2002) 126.

BL6B(IR)

Electronic Structure Analysis of Pt Clusters with Far-IR

Y.-T. Kim, K. Ohshima, A. Fujiwara, T. Mitani
School of Materials Science, Japan Advanced Institute of Science and Technology,
Ishikawa 923-1292 Japan

It is well-known that the band structure for bulk materials is changed into the discrete electronic structure with size decreasing. This phenomenon can be understood with a quantum size effect (QSE) due to the confined electronic wave in clusters size. The changed electronic structure by QSE have resulted in a number of interesting physicochemical properties, such as single electron tunneling in conductivity, considerable odd-even effect in magnetism, changed color due to surface plasmon and high activity in catalysis. Among them, the effect of electronic structure due to QSE on catalytic activity is unclear yet, because it is very difficult to form finely size-controlled clusters on supports as an essential premise to investigate QSE.

Two main chemical routes have been suggested for the formation of highly dispersed and size-controlled Pt clusters on carbon supports: the colloidal method and impregnation. Several outstanding studies have shown that the colloidal method is a successful way to control the size and shape of clusters. However, eliminating the surface ligands or protectors should be applied to electrocatalysts since the ligands act as surface poisons in electrocatalytic reactions. In contrast, the impregnation method, characterized by the deposition of a precursor followed by a gas or liquid-phase reduction, is simpler and cheaper than the colloidal method. However, with this method it is quite difficult to control the size and dispersity of clusters on the carbon supports, especially those having an inert surface nature, since the affinity of the carbon surface for the precursor solution exerts the dominant effect on dispersity in the deposition step.

To solve such problems, we have recently developed a new cluster formation route based on the fundamental bottom-up approach, namely, SAC (Single Atom to Cluster) approach composed of following two steps, as shown in Figure 1: [1]

1. Form monolayer of single Pt atoms by reducing the Pt precursor (H_2PtCl_6) with $NaBH_4$ on thiolated multi-walled carbon nanotubes (S-MWNT), in which the prepared samples are represented by Pt-S-MWNT.
2. Form Pt clusters from single atoms by eliminating thiol groups with heat treatments at various T_h (Temperature of heat treatment), followed by slow quenching to R.T., in which the prepared samples are represented by Pt_{h-q}/MWNT.

The electronic structure, especially discrete gap of size-controlled Pt clusters formed by SAC approach was investigated with terahertz spectroscopy of BL6B, UVSOR. As can be seen in Figure 2, we have recorded the spectra for Pt clusters supported on MWNT. Pt-S-MWNT is in the state of single Pt atom and the size of Pt_{h-q}/MWNT (T_h=523K) and Pt_{h-q}/MWNT (T_h=873K) is around 1 nm and 4 nm, respectively. The difference of absorption edge around 6 cm^{-1} is clearly shown for Pt-S-MWNT reflecting the fairly different electronic structure from two other samples, although there is little difference between Pt_{h-q}/MWNT (T_h=523K) and Pt_{h-q}/MWNT (T_h=873K). This absorption edge is attributable to the discrete energy level for single Pt atom. However, no discrete level for clusters was observed, because the measurement was conducted room temperature causing thermal excitation. Hence, the experiment at extremely low temperature is required to obtain a clear absorption peak for clusters.

[1] Y.-T. Kim, K. Ohshima, K. Higashimine, T. Uruga, M. Takata, H. Suematsu and T. Mitani, “Fine Size Control of Platinum on Carbon Nanotubes: from Single Atom to Cluster,” *Angew. Chem. Int. Ed.*, DOI: 10.1002/anie.200501792, In Press (2005).

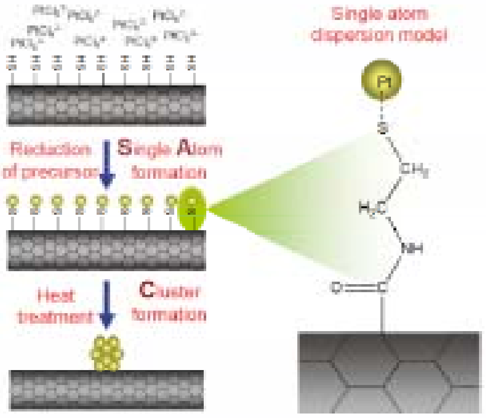

Fig. 1 Scheme of SAC approach.

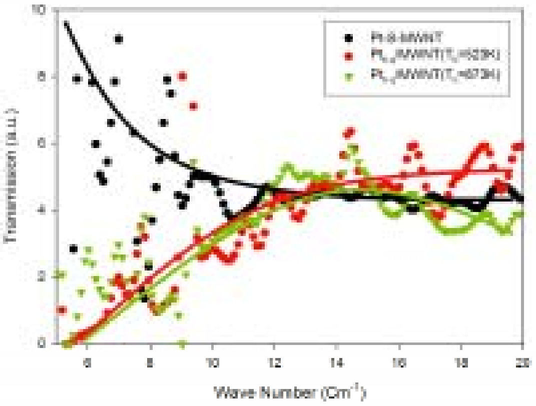

Fig. 2 Terahertz spectroscopy of Pt particles.

Collapse of the Heavy Quasiparticles of $SrFe_4Sb_{12}$ under Magnetic Fields

S. Kimura[1,2], T. Mizuno[2], K. Hayashi[3], E. Matsuoka[3], T. Takabatake[3,4]
[1]*UVSOR Facility, Institute for Molecular Science, Okazaki 444-8585 Japan*
[2]*School of Physical Sciences, The Graduate University for Advanced Studies, Okazaki 444-8585 Japan*
[3]*Department of Quantum Matter, ADSM, Hiroshima University, Higashi-Hiroshima 739-8530, Japan*
[4]*Institute for Advanced Materials Research, Hiroshima University, Higashi-Hiroshima 739-8530, Japan*

Alkaline-earth-filled iron-antimony skutterudites ($A^{2+}Fe_4Sb_{12}$) including $SrFe_4Sb_{12}$ are almost ferromagnetic systems with a paramagnetic Curie temperature (T_C) of 53 K [1]. The origin has been concluded to be the Fe 3*d* spin fluctuation because the thermodynamical properties can be fundamentally explained by the self-consistent renormalization (SCR) theory [2]. However the spin fluctuation is suppressed below 100 K. The origin is considered to be the hybridization between the charge carriers and Fe 3d spins, so-called “Kondo Effect”. To clarify it, we measured the magnetic field dependence of optical conductivity spectrum [$\sigma(\omega)$] and derived the effective mass [m^*] and the scattering rate [$1/\tau$] by using the extended Drude model [3].

Obtained magnetic field dependence of $\sigma(\omega)$ at T = 5 K is shown in Fig. 1. $\sigma(\omega)$ shows the pseudogap structure originating from the Fe states [4]. Below the energy gap, the $\sigma(\omega)$ shows the strong magnetic field dependence. This indicates that the Fe 3*d* spins strongly relates to the in-gap state.

The combination of the decreasing direct current conductivity and the change in $\sigma(\omega)$ implies that the heavy-fermion-like electronic structure collapse in the presence of a magnetic field. Due to the extended Drude analysis, m^* of the quasiparticles decreases with increasing magnetic field strength in spite that $1/\tau$ at the accessible lowest photon energy of 2.5 meV does not change as shown in Fig. 2. This is direct evidence of the creation of heavy quasiparticles due to the hybridization between charge carriers and the Fe 3d spins at low temperatures in $SrFe_4Sb_{12}$ and it is suppressed by the magnetic fields.

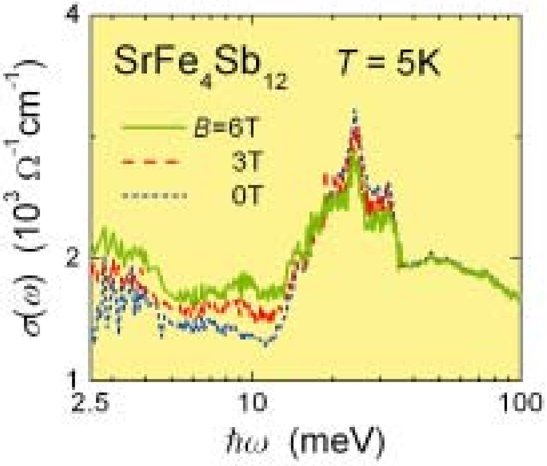

Fig. 1 The magnetic field dependence of optical conductivity spectrum [$\sigma(\omega)$] of $SrFe_4Sb_{12}$.

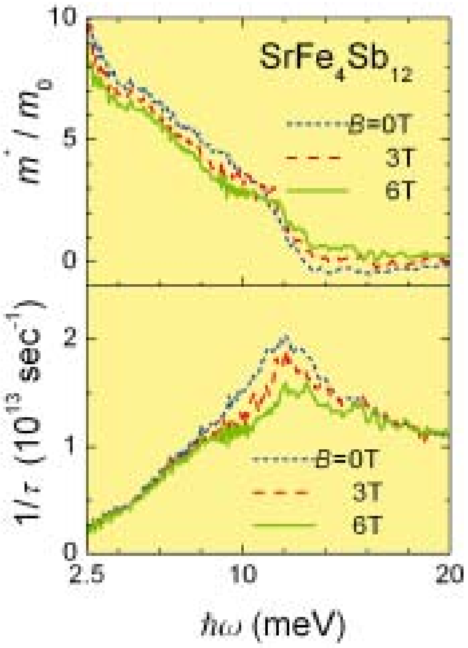

Fig. 2 The magnetic field dependent effective mass relative to the electron rest mass (m^* = m_0) and scattering rate ($1/\tau$) as a function of photon energy.

[1] E. Matsuoka *et al.*, J. Phys. Soc. Jpn. **74** (2005) 1382.
[2] K. Ueda and T. Moriya, J. Phys. Soc. Jpn. **39** (1975) 6687.
[3] M. Dressel and G. Grüner, *Electrodynamics of Solids* (Cambridge Univ. Press, Cambridge, 2002).
[4] J. Sichelschmidt *et al.*, Phys. Rev. Lett. **96** (2006) 037406.

BL6B(IR)&7B

Optical response of $CuRh_2S_4$ & $CuRh_2S_{e4}$

M. Kobayashi[1], K.Satoh[1], A.Irizawa[1], T. Nanba[1], L.Chen[2], M. Ito[3], T. Suzuki[3]
[1]*Kobe University, nada-ku, Kobe 657-8501, Japan*
[2]*ISSP University of Tokyo, 5-1-5 Kashiwanoha, Kashiwa, 277-8581, Japan*
[3]*Hiroshima University,Higashi-Hiroshima 739-8530,Japna*

Introduction

The spinel compound $CuRh_2S_4$ & $CuRh_2S_4$ at atmospheric pressure is a metal of wide temperature range, but undergoes a continuous cross-over change in the electronic states from the metal phase to the insulating phase at high pressures above 5 GPa and 8 GPa, respectively [1]. To study its fundamental electronic states close to the Fermi level ambient pressure, we measured the temperature dependence of optical reflectivity spectra $R(\omega)$ of polycrystalline $CuRh_2S_4$ & $CuRh_2S_4$.

Experimental

The optical reflectivity spectra $R(\omega)$ at ambient pressure was measured in the wide photon energy range from 7 meV to 30 eV in the temperature range of 8-300 K. The measurements were performed using a Fourier-transform interferometer combined with a thermal light source and synchrotron radiation source at the beam line BL6B & 7B of UVSOR. The optical conductivity $\sigma_1(\omega)$and complex dielectric function $\varepsilon_1(\omega)$ were obtained from a standard Kramers-Kronig (K-K) transformation of the measured reflectivity spectrum. $\sigma_1(\omega)$ connected with the absorption spectra by $\sigma_1 = \omega \bullet \varepsilon_2/4\pi$.

Results and discussion

Figure 1 shows the temperature dependences (8 to 300 K) of the σ-spectra of $CuRh_2S_4$ which were obtained from a K-K analysis of the measured $R(\omega)$. In the low energy part of the σ-spectra, two distinct peaks corresponding to electronic interband transitions were resolved at around 0.3 and 0.7eV in addition to the higher energy peaks, together with the small Drude component given by conduction electrons below 0.1 eV. The Drude component still survived even at 8 K.

Figure 2 shows the temperature dependences (8 to 300 K) of the σ-spectra of $CuRh_2S_{e4}$. $CuRh_2Se_4$ exhibits a similar structure with $CuRh_2S_4$ but more clear double peak structure around 0.3 and 0.8 eV (downward arrows). The peak structure becomes distinct accompanying with the growth of the Drude component with cooling at atmospheric pressure.

The weaker temperature dependence and the unresolved broad double peak structure around 0.2-0.8 eV in the σ-spectra of $CuRh_2S_4$ means that the hybridization of the electronic states close to the E_F level is weaker than $CuRh_2S_{e4}$.

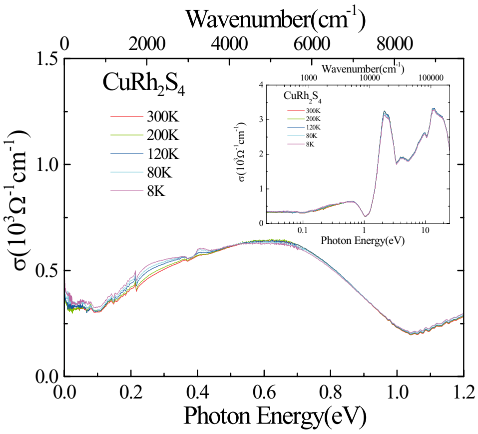

Fig. 1 Temperature dependence of σ-spectra of $CuRh_2S_4$ below 1.2 eV. Insertion indicates the whole spectra up to 30 eV.

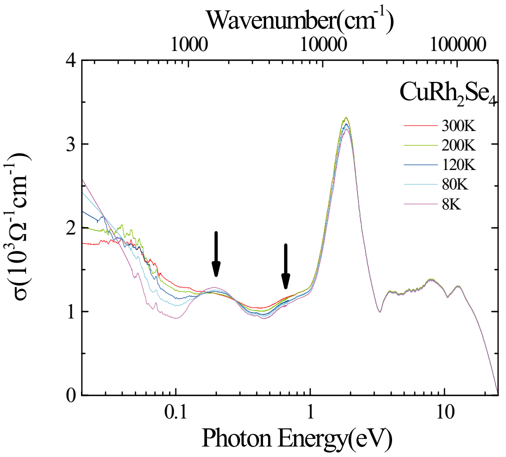

Fig. 2 Temperature dependence of σ-spectra of $CuRh_2S_{e4}$.

[1] M. Ito *et al.*, Phys. Rev. Lett. **91** (2004) 077001.

BL6B(IR)

Infrared Reflection-Absorption Spectroscopy of Alkali-Metal-Doped Alq$_3$ Thin Films Using Synchrotron Radiation

Y. Sakurai[1], S. Kimura[1], K. Seki[2]
[1]*Institute for Molecular Science, Okazaki 444-8585 Japan*
[2]*Department of Chemistry, Graduate School of Science, Nagoya University 464-8602 Japan*

Tris-(8-hydroxyquinoline) aluminum (Alq$_3$), which chemical structure and two possible geometrical isomers, meridional (C$_1$ symmetry) and facial (C$_3$ symmetry) forms are shown in Figure 1, is most widely used as an electron transport/light emitting layer in organic light emitting diodes (OLEDs). A typical OLED consists of indium tin oxide (ITO) as the anode, on which organic thin films are sequentially deposited, with low work function metals finally deposited as the cathode. Since the OLED's performance is affected by the interface, it is important to investigate the interface between the organic thin film and cathode.

Infrared Reflection Absorption Spectroscopy (IRAS) is a powerful probe for the structure and chemistry of a surface and interface. Though IR spectrum below 1000 cm^{-1} (Far infrared region) is expected to significantly change by the interaction between metal substrate and Alq$_3$ molecules, it is difficult to obtain the IRAS spectrum in this region using a typical laboratorial system with a globar source. Then we performed the IRAS measurement using synchrotron radiation. In this paper, we report the IRAS spectra of pristine and alkali-metal-doped Alq$_3$ in the FIR region.

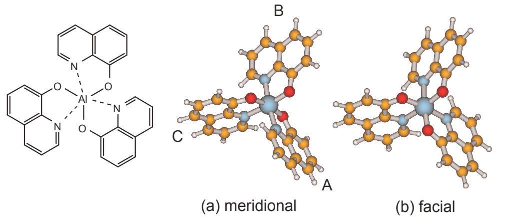

(a) meridional (b) facial

Fig. 1 The chemical structure and geometrical isomers of Alq$_3$.

Experiments including the sample preparation and measurement were performed in an ultrahigh vacuum chamber. Alq$_3$ films were prepared by vacuum evaporation onto Ag films deposited on Si substrates. Alkali metals (K, Na, Li) were evaporated from SAES getter sources. IRAS spectra were obtained with the SR light through KBr or CsI windows at the incident angle of 80° relative to the surface normal. The reflected light was detected with a liquid-helium-cooled Si bolometer.

Figure 2 shows the IRAS spectra as a function of the thickness of Alq$_3$ film in the wavenumber region of 300-500 cm^{-1}. In the spectrum of 1 nm thickness, a peak at 420 cm^{-1} assigned to the Al-N stretching mode was observed. This peak was shifted to 423 cm^{-1}. In addition, a peak at 460 cm^{-1} assigned to the pyramidalization mode was observed in the spectrum of 20 nm thickness. The frequencies of these modes correspond to those of meridional isomer [1]. The lower frequency shift of Al-N stretching mode in the spectrum of 1 nm thickness compared to that of 20 nm thickness is due to the interaction between Alq$_3$ and Ag surface.

Figure 3 shows potassium doping dependence of the IRAS spectra of an Alq$_3$ film of 20 nm thickness. The intensity of the peaks at 423 and 460 cm^{-1} gradually decrease and three peaks additionally appear at 435, 441 and 448 cm^{-1} with increasing evaporation amount. The similar behavior was also observed in sodium doping. Considering these behavior, the change is believed to be caused by the charge transfer to the Alq$_3$ molecule from the alkali atoms. However the additional peaks did not appear in lithium doping. This suggests that the interaction between Li and Alq$_3$ is different from those of K and Alq$_3$ and Na and Alq$_3$.

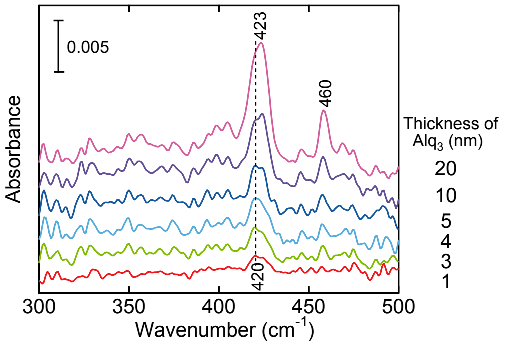

Fig. 2 IRAS spectra as a function of thickness of Alq$_3$ film.

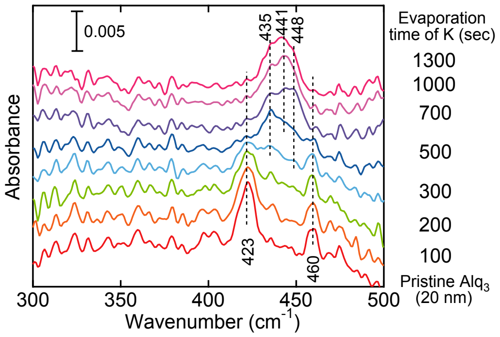

Fig. 3 Changes in IRAS spectra of an Alq$_3$ film with increasing potassium doping.

[1] M. Cölle, S. Forero-Lenger, J. Gmeiner and W. Brütting, Phys. Chem. Chem. Phys. **5** (2003) 2958.

BL6B(IR)

Metal-Nonmetal Transition of Bismuth Clusters

S. Yoshida, A. Asai, H. Ikemoto
Faculty of Science, University of Toyama, Gofuku 3190, Toyama 930-8555, Japan

A phase transition from Bi nanocrystalline to amorphouslike clusters with decreasing the size is suggested by Raman-scattering measurements [1]. It is very important to investigate the optical property directly to reveal the phase transition. In the present study we report results of optical absorption coefficients for Bi clusters.

Experimental

Bismuth of 99.999 % purity was slowly deposited onto the substrates from a tungsten boat. Then, KBr of 99.99 % purity was deposited to cover the Bi islands. The size of the islands was adjusted by controlling the thickness deposited on the substrates. As mentioned above the Bi clusters are formed in thin films, and samples are represented by their average thickness of the Bi thin films in this paper.

Measurements of optical absorption coefficients were performed in the energy range of 0.05~0.95 eV with the rapid-scan Michelson interferometer (Bruker, IFS-66V) at the IR beam line, BL6B.

Analysis

Figure 1 shows transmittance of the 70 nm-thick film which was on a thick KBr pelette and covered with a 100 nm-thick KBr film. In this report the reference of the transmission is defined by the intensities passed through the KBr pellet.

In the system the transmission is given by

$$T_{calculation} = T_1 \cdot T_2$$

$$= \frac{A}{B \cdot C} \exp(-\alpha_2 d_2)$$

$$A = (1 - R_{12})^2 + 4R_{12} \sin^2 \phi_{12}$$

$$B = 1 + R_{10}R_{12} + \sqrt{R_{10}R_{12}} \cos(\phi_{12} - 2\frac{2\pi n_1 d_1}{\lambda})$$

$$C = (1 - R_{12}e^{-\alpha_2 d_2})^2 + 4R_{12}e^{-\alpha_2 d_2} \sin^2(\phi_{12} - \frac{2\pi n_2 d_2}{\lambda}) .$$

Blue line in the Figure 1 shows transmittance calculated by optical constants of crystalline Bi []. The calculated values are in accordance with the experimental values. So we evaluated the absorption coefficients from the experimental data by using the equation 1, where values of A, B and C are calculated by the optical constants of the crystalline Bi. The result is represented by black dots in Figure 2.

Results and Discussion

Figure 2 presents a representative set of curves for the optical absorption coefficients of various thickness films. Several of the characteristics can be seen by examining the absorption data by itself. The absorption coefficients of the 100 nm and 70 nm thick films are close to those of crystalline Bi, suggesting that these films are semimetallic. The absorption coefficients of the 2 nm and 0.5 nm thick films are close to zero around 0.6 eV, and increase linearly with photon energy.

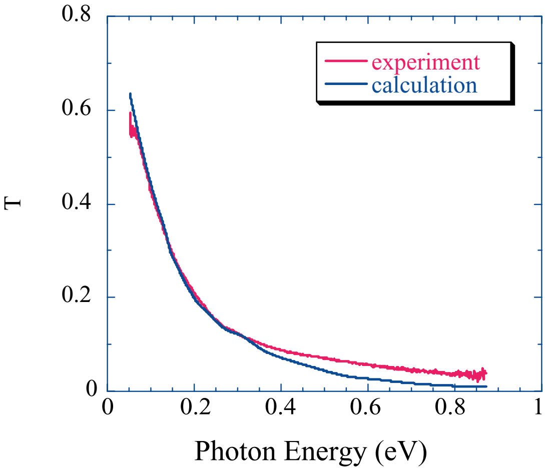

Fig. 1 Transmittance of the 70 nm-thick film.

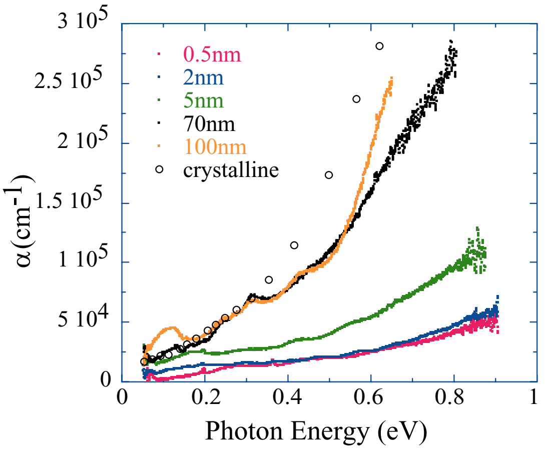

Fig. 2 Variations in optical absorption coefficients of the as-deposited Bi clusters for different thickness. Open circles denote those of polycrystalline [2].

[1] M.G. Mitch, S.J.Chase, J Fortner, R.Q. Yu and J. S. Lannin, Phys. Rev. Lett. **67** (1991) 875.

[2] A.D. Lenham *et al.* J. Opt. Soc. Am. **55** (1965) 1072.

Creation Process of Long-Lasting Afterglow in $SrAl_2O_4$:Eu and $SrAl_2O_4$:Eu,Ln (Ln=Dy, Gd, La) Phosphors

M. Kitaura
Fukui National College of Technology, Sabae, 916-8507, Japan

The $SrAl_2O_4$:Eu,Dy phosphor shows an intensive afterglow which lasts for several hours. The function of Dy^{3+} ions has been connected to the formation of photocarrier traps in host $SrAl_2O_4$ [1]. However, it is difficult with only the previous idea to explain the question why the afterglow is enhanced by such co-doping. Thus, the role of Dy^{3+} ions on the afterglow processes still remain unresolved. Since the intensity of afterglow is increased with the concentration of photo-created electrons and holes, the incorporation of Dy^{3+} may influence not only the formation of photocarrier traps but also the change in the absorption feature. In this connection, it is worth while to note the experimental result that the afterglow is efficiently caused with photons in the energy region lower than the fundamental absorption edge of $SrAl_2O_4$ [2]. This suggests the existence of absorption bands resulting from Dy^{3+} co-doping. The origin of the absorption bands has not yet been cleared.

In the present study, we have investigated the creation spectra of afterglow in the phosphors of $SrAl_2O_4$:Eu and $SrAl_2O_4$:Eu co-doped with Dy^{3+}, Gd^{3+} or La^{3+} ions. In order to obtain the creation spectrum of afterglow in each sample, the afterglow spectra were measured at various excitation photon energies by using a grating monochromator with a CCD detector. The creation spectra were corrected for the energy distribution of excitation light source.

The afterglow spectra are dominated by the 2.3 eV band from Eu^{2+} ions. The creation spectra of it in $SrAl_2O_4$:Eu and $SrAl_2O_4$:Eu,Ln (Ln = Dy, Gd, La) are shown in Fig. 1. The spectra were measured at the temperature that the afterglow intensity has the maximum in each sample. The temperatures were 270 K for $SrAl_2O_4$:Eu,Dy and 200 K for others. They exhibit a prominent peak at 6.3 eV. This result indicates that the 6.3 eV peak is not be related to the $4f \rightarrow 5d$ absorption of trivalent Ln ions. In addition, the possibility of the $4f \rightarrow 5d$ absorption band at Eu^{2+} ion is also excluded because the energy position of it does not coincide with that of the 6.3 eV peak. We suppose that the 6.3 eV peak is due to some lattice imperfection. According to Ref. 3, Dy^{3+} ions substitute Sr^{2+} sites. In this case, Sr^{2+} vacancies are necessarily introduced owing to charge compensation. In addition to the Sr^{2+} vacancies, a lot of O^{2-} vacancies should be also produced because all of samples were sintered in a reduced atmosphere. Such vacancies modulate the electronic states of host material, so that the perturbed absorption bands appear in the low energy tail of the fundamental edge. This situation can be seen in the present result.

The cluster calculation has been carried out using the discrete variational $X\alpha$ (DV-$X\alpha$) method [4] to clarify the influence of lattice imperfections on the energy level structure of host $SrAl_2O_4$. From the result of calculations, the intrinsic absorption edge was determined to be 7.73 eV. The agreement between experiment and calculation is good. Now, calculations are proceeding for the cluster introducing a Sr^{2+} or a O^{2-} vacancy.

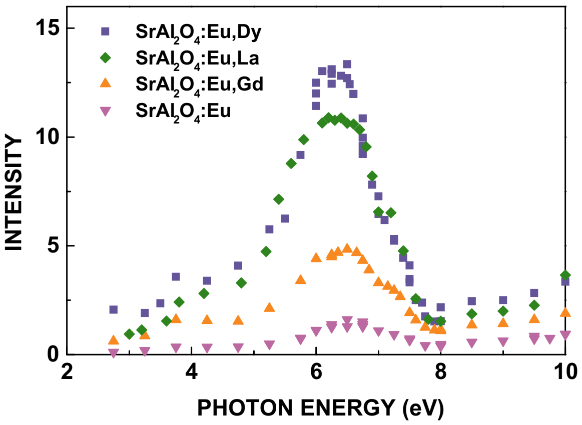

Fig. 1 Creation spectra of the afterglow at 2.3 eV $SrAl_2O_4$:Eu and $SrAl_2O_4$:Eu,Ln (Ln=Dy, Gd, La). The spectra were measured at 270 K for $SrAl_2O_4$:Eu,Dy and at 200 K for others.

[1] T. Matsuzawa, Y. Aoki, N. Takeuchi and Y. Murayama, J. Electrochem. Soc. **143** (1996) 2670.

[2] M. Kamada, J. Murakami and N. Ohno, J. Lumi. **87-89** (2000) 1042.

[3] T. Nakamura, K. Kaiya, N. Takahashi, T. Matsuzawa, C.C. Rowlands, V. Beltran-Lopez, G.M. Smith and P.C. Riedi, J. Mater. Chem. **87-89** (2000) 1073.

[4] H. Adachi, M. Tsukada and C. Satoko, J. Phys. Soc. Jpn. **45** (1978) 875.

BL7B

Vacuum UV Reflectivity Spectroscopy of PZT - Revisited

J. Mistrik[1], M. Aoyama[1], T. Yamaguchi[1], N. Dai[2]
[1]*Research Institute of Electronics, Shizuoka University, Hamamatsu 432-8013 Japan*
[2]*National Laboratory of Infrared Physics, Shanghai Institute of Technical Physics, Chinese Academy of Sciences, Shanghai 200083 China*

The work presented in this report follows up on our ellipsometric and reflectance study performed on Pb($Zr_{0.5}Ti_{0.5}$)O_3 (PZT) film in visible and near UV spectral ranges [1]. It also further refines our previously measured vacuum UV reflectivity data [2], that is important for determination of reliable optical constants of PZT. Forthcoming effort is focused on the development of new dispertion model for this material based on parametrization of the joint density of electronic states in the vicinity of the valence and conduction bands [3, 4].

Experimental

Polycrystalline PZT film was deposited by sol-gel technique on $LaNiO_3/Pt/Ti/SiO_2/Si$ substrate. The thickness of PZT and $LaNiO_3$ layers determined by spectroscopic ellipsometry was 217 nm and 100 nm, respectively. UVSOR facility was used for reflectivity measurements. Selected spectral range from 3eV to 30 eV of synchrotron radiation was scanned by 3-m normal incidence monochromator (beam line 7B). Three monochromator gratings G1 (1200 l/mm), G2 (600 l/mm), G3 (300 l/mm) and LiF and quartz filters were used to cover the studied spectral range. Incident and reflected light intensity was measured in room temperature by a Si photodiode. Angle of incidence was less then 15 deg. Reflectivity spectra recorded in step mode with dwelt time approximately 0.2 s, presented here, gave more reliable results with respect to the continuous scan configuration (our spectra presented in Ref. [2]).

Results and Discussions

In the visible range, reflectivity of the sample shows interference fringes due to combined effect of limited thickness and low absorption of PZT film. Knowledge of PZT optical constants determined in the visible range by spectroscopic ellipsometry enabled us to correct the reflectivity data for interference effect. Thus reflectivity of PZT bulk-like sample in vide spectral range (from 1 to 30 eV) was obtained (*c.f.* Fig 1).

Phase of reflectivity coefficient was calculated by Kramers-Kronig relations following numerical procedure reported by Wooten [5]. Extrapolation of reflectivity in low and high photon energy regions was adjusted to obtain best fit between complex refractive index determined from dispersion relations and ellipsometry in visible range. Resulting refractive index and extinction coefficient of PZT film are presented in Fig. 2. Slight deviation of extinction coefficient from zero value in PZT transparence region (1-3 eV) may be due to supplementary reflectance spectral feature located behind 30 eV and therefore unresolved by our experiment.

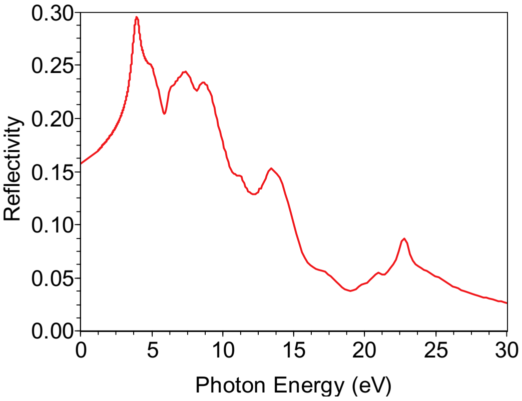

Fig. 1 Reflectivity of PZT.

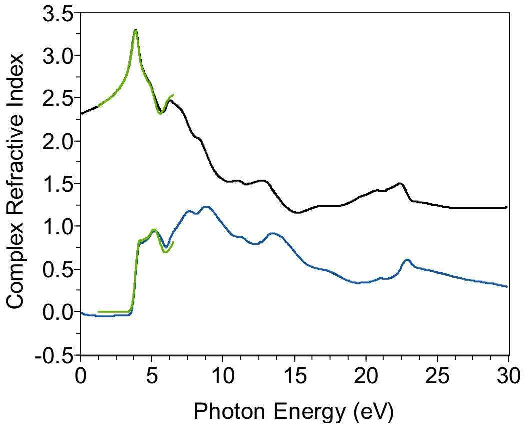

Fig. 2 Refractive index (black line) and extinction coefficient (blue line) of PZT derived from KK analyses of PZT reflectivity spectrum. Corresponding data obtained from ellipsometry are also displayed (green lines).

[1] D. Franta, I. Ohlidal, J. Mistrik, T. Yamaguchi, G. J. Hu, and N. Dai, App. Surf. Sci. **244** (2005) 338.
[2] J. Mistrik, T. Yamaguchi, N. Dai, and M. Shimizu, UVSOR Activity Report 2004 (2005) 87.
[3] D. Franta *et al.* App. Surf. Sci. **244** (2005) 426.
[4] D. Franta, I. Ohlidal, M. Frumar, J. Jedelsky, App. Surf. Sci. **212-213** (2003) 116.
[5] Wooten, Optical Properties of Solids, Academic Press, 1972.

BL7B

Life Time Resolved Photo Luminescence Spectra of UV Emission Bands in AlGaN Alloys

N. Nakagawa[1], K. Fukui[1], S. Naoe[2], H. Miyake[3], K. Hiramatsu[3]

[1]Research Center for Development of Far-Infrared Region, Fukui University, Fukui910-8507, Japan

[2]Faculty of Engineering, Kanazawa University, Kanazawa 920-1192, Japan

[3]Faculty of Engineering, Mie University, Mie 514-8507, Japan

The group III-V nitride semiconductors (AlN, GaN and InN) are promising materials for applications in opt-electronic devices. For ultraviolet LEDs and LDs, the ternary AlGaN alloys are promising semiconductors. We have been performed measurements of visible (VIS)-ultraviolet (UV) photo luminescence (PL) and their excitation spectra (PLE) to investigate PL mechanism of this alloy system [1]. In this report, we present the time resolved decay (TRD) curves profiles for studying the dynamics of this PL.

PL spectra and TRD curves measurements of $Al_xGa_{1-x}N$ (x=0.34~0.76) have been performed under band-to-band excitation region. AlGaN samples were made by MOVPE method at Mie University. The thickness of AlGaN thin films are about 1 μm on 1 μm AlN single crystal film with sapphire substrates. The measurements were carried out at BL7B under single bunch operation in the energy range from 3.4 to 25 eV. Conventional 30 cm VIS-UV monochromator with liquid N_2 cooled CCD detector is used for PL measurements of all samples.

PL spectra of AlGaN are composed of two bands. One is so-called B emission band (UV) which is located near bandedge and corresponding to exciton luminescence, the other is Y emission band (VIS) caused by lattice defects or impurities. Figure 1 shows the time resolved decay curve at each PL energy of UV emission band. Measurement temperature is 9.7 K. TRD curves showed different form at each PL energy position, although all TRD curves are resolved to similar three single exponential components. It suggests that UV emission band consists of three decay components (fast, middle and slow), and each component has different PL energy dependence.

Figure 2 shows PL intensities of three decay components, which are derived from the deconvolutions of all TRD curves in Fig. 1, as functions of PL energies.

These curves give the life time resolved PL spectra. Arrows in Fig.2 indicate the peak energy of each component, and suggest that these three decay components which constitute UV emission band emit with slightly different energies. According to the order of decay times of three components (fast < ns, middle ~ 18ns, slow ~ 80ns), we present consider the fast component as an intrinsic exciton luminescence and the other two components as defect derived ones.

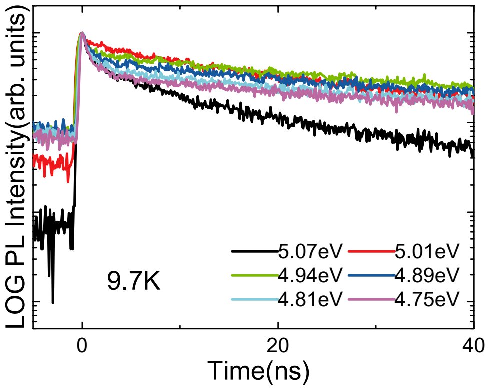

Fig. 1 Time resolved decay curves of $Al_{0.67}Ga_{0.33}N$ at 9.7K.

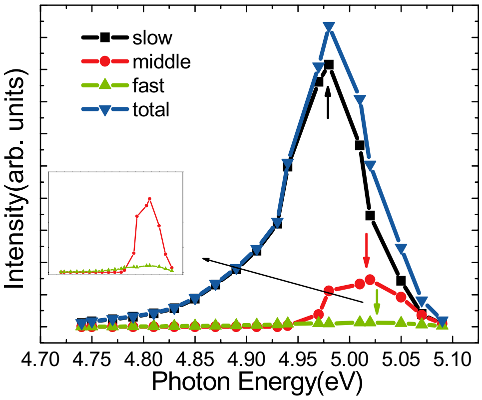

Fig. 2 Life time resolved photo luminescence spectra of $Al_{0.67}Ga_{0.33}N$ at 9.7K.

[1] K. Fukui *et al.*, UVSOR Activity Report 2004 (2005) 78.

VUV Reflection Spectroscopy of SiO_2 and SiO_{2-x} Thin Films

K. Nakagawa, T. Tsuda, T. Iwai, Y. Shiraishi, Y. Iwai,
SL. Chang, T. Mizunuma, S. Matsumoto, H. Matsumoto
School of Science & Technology, Meiji University, Kawasaki 214-8571 Japan

Silicon oxide is important material that is used as electronic devices and optical applications. Fundamental studies of silicon oxide are still performed [1]. As optical properties, reflection spectrum of bulk SiO_2 had been report by Philipp *et al.* [2], however those of the thin film of SiO_2 has not been studied. We report the reflection spectra of the thin films of SiO_2 and SiO_{2-x} that are considered as a state with defects of oxygen in the VUV region with synchrotron radiation.

Experimental

SiO_2 and SiO_{2-x} thin films were prepared by RF reactive sputtering. The Si plate with 99.999 % purity was used as a target and the sputtering was carried out in different mixtures of argon and oxygen, under a total pressure of 0.2 Pa. The films were sputtered onto MgF_2 substrate at 573 K. Film thicknesses were about 300 nm. Composition ratio and chemical bonding states of the prepared thin films were investigated by RBS and XPS.

Reflection spectra of SiO_2 and SiO_{2-x} thin films were measured in the vacuum ultraviolet region up to 25.0 eV with the 3-m normal incident monochromator (grating: G1 and G2) at BL-7B of UVSOR-II. And a silicon photodiode sensor was used as a detector for the reflection light.

Results and Discussion

From analyses by RBS and XPS, it was found that the value of x is about 0.5, SiO_2 state and middle state between Si and SiO_2 exist in SiO_{2-x} thin films.

Figure 1 shows the reflection spectra of SiO_2 and SiO_{2-x} thin films at room temperature. Peaks are named as indicated in the figures for convenience. In the spectrum of SiO_2 thin film, five peaks named as A, B, C, D and E were observed at 10.2 eV, 11.8 eV, 14.1 eV, 17.6 eV and 21.7 eV, respectively. This result corresponded with those of absorption spectrum of SiO_2 thin film [3] and reflection spectrum of bulk [2]. In the spectrum of SiO_{2-x}, the peaks corresponding to A~D in the reflection spectrum of SiO_2 thin films could observe, but the peaks became broad in comparison with these of SiO_2 thin film. To clear the structure of the spectra, they were analyzed by secondary derivative method. Figure 2 shows the results. These spectra were normalized as the peak intensity of A accorded with SiO_2 and SiO_{2-x}. From comparison of SiO_2 and SiO_{2-x}, the peak energy of A, C, D, E were shifted about 0.1~0.3 eV, and the peak energy of B was shifted 1.0 eV. Therefore, it seems that the band of the origin of the peak B was influenced by oxygen. From the results of the DV-Xa molecular orbital calculation, the conduction band is consists of the mixed orbital of Si-3s, Si-3p and Si-3d in this region. The band, which is the origin of the reflection peak B may be that the mixed states differ from these of other bands of the origin of the peak A, C, D and E. We expect that the effect of defects of oxygen on electronic structure will be apparent if the cause of the peak shift becomes clear.

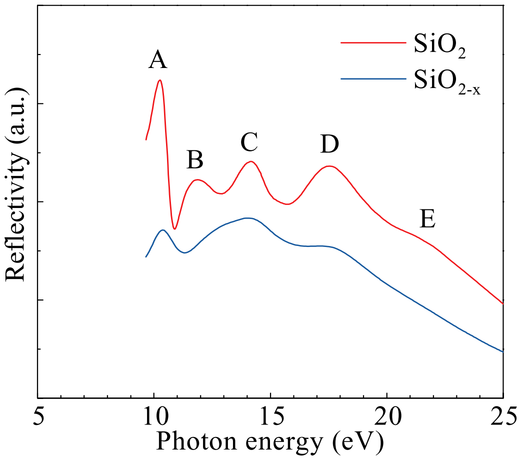

Fig. 1 Reflection spectra of SiO_2 and SiO_{2-x} thin films in the region from 9.5 to 25.0 eV at room temperature.

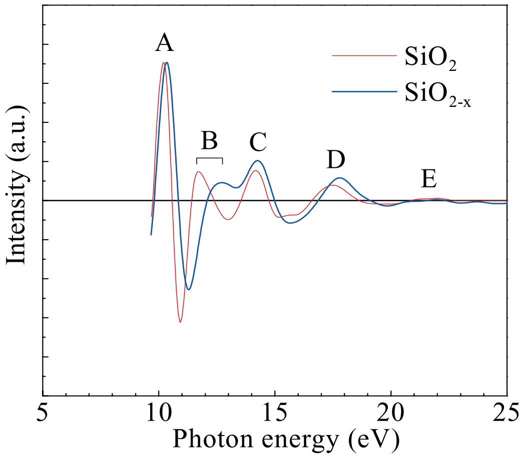

Fig. 2 Normalized secondary derivative spectra of reflection spectra (Fig. 1).

[1] M.P. Seah *et al.*, Surf. Interface Anal. **36** (2004) 1269.
[2] H.R. Philipp, Solid. State. Commun. **4** (1966) 73.
[3] K. Nakagawa *et al.*, UVSOR Activity Report 2004 (2005) 88.

BL7B

Luminescence Properties of YPO_4:Mn Codoped with Zr Ions

Y. Nakajima[1], M. Kitaura[2], M. Kaneyoshi[3], H. Nakagawa[1]
[1]*Dep. of Electrical & Electronics Engineering, Fukui University, Fukui, 910-8507*
[2]*Fukui National College of Technology, Sabae, 916-8507*
[3]*Shin-Etsu Chemical Company, Limited, Takefu Plant, Takefu, 915-8515*

The YPO_4:Mn shows a photoluminescence band peaking at 2.5 eV under excitation with photons in the vacuum ultraviolet (VUV) region at room temeprature. The 2.5 eV emission is enhenced remarkably by co-doping of Zr^{4+} ions.[1] Thus, YPO_4:Zr,Mn is a promising material as functional phosphors for Plasma Display Panels (PDPs) and Hg-free rare-gas discharge lamps. In the present study, photoluminescence properties of YPO_4:Mn, YPO_4:Zr, and YPO_4:Zr,Mn have been investigated at 9.4 and 300 K in order to make clear the role of Zr^{4+} ions on the enhancement in the 2.5 eV emission of YPO_4:Zr,Mn.

The host material YPO_4 was precipitated at 350 K by mixing an aqueous solution of yttrium chloride into a solution of phosphoric acid. The precipitate was filtrate, dried, and calcined in air at 1073K. The YPO_4 powder thus obtained were mixed in a molar together with ZrO_2, MnC_2O_4 and $(NH_4)_2HPO_4$. The mixture was fired in nitrogen flow at 1473K for 3 hours. The concentration of Zr and Mn ions was 2.5 mol% in preparations.

The mesurements of emission and excitation spectra were carried out at BL7B using a 3-m normal incidence monochromator. Photoluminescence from samples was guided into the incident slit of a grating monochromator by a optical fiber, and was detected by a CCD system. The emission spectra presented here were not corrected for the spectral response of detecting system. The excitation spectra were corrected for the spectral distribution of excitation light source.

Figure 1 shows emission spectra of YPO_4:Mn, YPO_4:Zr, and YPO_4:Zr, Mn at 9.4 K (black line) and 300 K (red line). The excitation energy is 7.2eV, which corresponds to the energy of Excimer luminescence by a Xe discharge. In YPO_4:Mn, the emission spectrum at 9.4 K is composed of two band at 2.5 and 1.9eV. This 1.9 eV band is not seen at 300K. The 2.5 eV band is observed at 300 K, though it is very weak. We suppose that the 2.5 and 1.9 eV bands originate in Mn^{2+} ions replacing the Y^{3+} site of YPO_4 lattce, because they are excited in the absorption bands due to the *d-d* transitions of Mn^{2+} ions.

In YPO_4:Zr, two emission bands appear at 4.0 and 3.0 eV. It was found that the 4.0eV band is stimulated with VUV photons in the absorption due to the transitions from O 2*p* states to Zr 4*d* states. Therefore, the 4.0 eV band is most likely assigned to be an emission band associated with Zr^{4+} ions. The 3.0 eV band is observed in YPO_4, so that it may be due to lattice imperfections in host YPO_4.

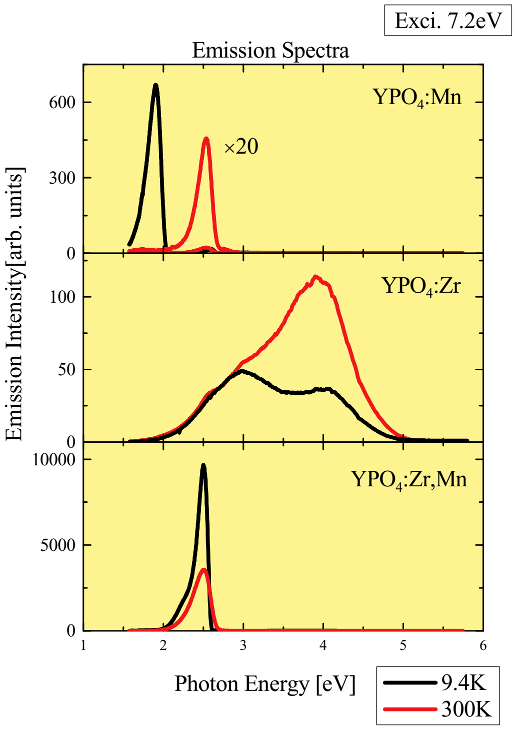

Fig. 1 Emission Spectra of YPO_4:Mn, YPO_4:Zr,and YPO_4:Zr,Mn at 9.4 (black line) and 300 (red line) K.

The 2.5 eV band dominates the emission spectra of YPO_4:Zr,Mn. The 1.9 eV band of YPO_4:Mn is not seen in the spectra. This result suggests that the electronic states of Mn is influenced by the incorporation of Zr^{4+} ions. Considering the ionic radii of Mn^{2+}, Y^{3+} and P^{5+} ions, Mn^{2+} ions can substitute Y^{3+} ions. On the other hand, since the ionic charge of Mn^{2+} is different from that of Y^{3+}, charge compensation requires to cancel the inconsistency of it between Mn^{2+} and Y^{3+} ions. This effect will introduce vacancies or interstices around Mn^{2+} ions substituting Y^{3+} ions, resulting in an additional perturbation for the electronic states of Mn^{2+}. Such a perturbation should be suppressed by co-doping of Zr^{4+} ions, because the lack of +1 at a Mn^{2+} ion can compensates with the excess of +1 at a Zr^{4+} ion. In this situation, why is the 2.5 eV band enhanced ? This is an open question at present.

[1] M. Kaneyoshi and E. Nakazawa, J. Electrochem. Soc. **152** (2005) H80.

BL7B

Reflectivity of Yb Metal in the Visible, UV and VUV Regions

H. Okamura, K. Senoo, T. Nanba

Graduate School of Science and Technology, Kobe University, Kobe 657-8501, Japan.

The 4*f* electron configuration of Yb in Yb metal is $(4f)^{14}$, hence the valence of Yb is 2+. It has been shown that Yb metal undergoes structural phase transitions with increasing external pressure [1]. At room temperature, the structure changes from fcc at ambient pressure to bcc at about 4 GPa, and to hcp at 26-30 GPa. Below the first transition at 4 GPa, the electrical resistivity of Yb increases with increasing pressure [1]. In addition, the valence of Yb, as probed by X-ray absorption spectroscopy, gradually increases to about 2.7 at 30 GPa [2,3]. When the valence of an Yb ion is 3+, it has a hole within the 4*f* shell; hence it possesses a localized magnetic moment. Namely, as the applied pressure is increased, the number of localized 4*f* holes increases. This can be viewed as a pressure-induced crossover from itinerant to localized character of the 4*f* electrons through the electron-hole symmetry. Associated with this crossover, there should be also changes in the strength of the hybridization between the conduction and 4f electron (*c-f* hybridization). Such characteristics may be viewed as a model system of the so-called ``heavy fermion compounds'', whose pressure-induced physical properties and electronic structures have been under intense research in recent years.

We have recently started infrared studies of Yb metal under external pressure, to probe how the microscopic electronic structures of Yb near the Fermi level evolve with external pressure. To do so, it is also important to study the higher energy optical spectrum, since a wide range of spectrum is required to obtain optical conductivity through the Kramers-Kronig relations. We have measured the reflectivity spectra of Yb metal at room temperature from visible to vuv ranges at BL7B. Since Yb is easily oxidized in air, the sample of Yb metal was prepared by depositing a film of Yb *in situ* on a glass plate by evaporation. A 4N (99.99 %) purity wire of Yb was evaporated with a tungsten filament under a pressure of 4 x 10^{-9} Torr in the sample chamber.

Figure 1 shows the overall reflectivity spectrum as a function of photon energy. At first, the Yb was deposited onto the glass plate so that we could not see through the glass any more. The reflectivity was first measured at this point, but the spectrum showed a periodic pattern as shown by the red curve. This is due to the interference of the light rays reflected off the front and rear surfaces of the film. This observation demonstrates very well the transparency of metal above the plasma frequency. By analyzing the periodicity of the interference pattern, *nd* ~ 50 nm was obtained (*n* is the refractive index, *d* is the thickness). When more Yb was deposited to make the film thickness larger, the interference pattern disappeared (blue curve in Fig. 1). We plan to use this reflectivity data in conjunction with the infrared data taken at Kobe University, to analyze the electronic structures of Yb in the future study.

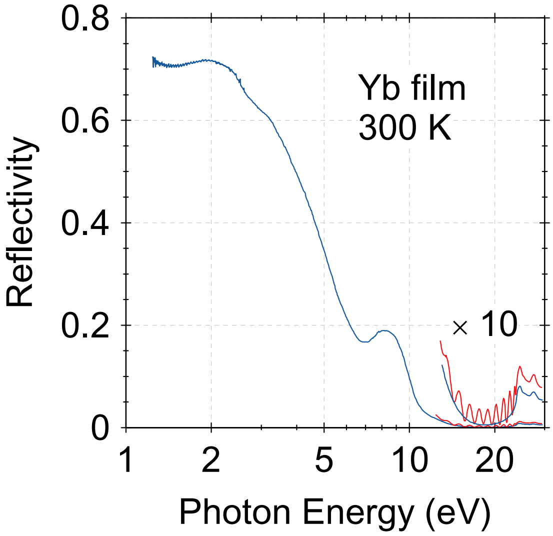

Fig. 1 Reflectivity spectrum of Yb metal at room temperature. The red curve shows the spectrum obtained for a thin film, which shows a periodic pattern due to internal reflection and interference. The blue curve shows the data for a thicker film, which has no interference pattern.

[1] McWhan *et al.*, Phys. Rev. **177** (1969) 1063.
[2] Syassen *et al.*, Phys. Rev. B **26** (1982) 4745.
[3] Fuse *et al.*, J. Alloys Compounds **376** (2004) 34.

BL1A

Si K-Edge XANES Study of Fe- and/or Ga-Substituted MFI Metallosilicates

H. Aritani[1], S. Koyama[1], K. Otsuki[1], A. Nakahira[2], H. Matsuhashi[3]
[1]*Faculty of Engineering, Saitama Institute of Technology, Fukaya 369-0293, Japan*
[2]*Graduate School of Engineering, Osaka Prefecture Universitty, Sakai*
[3]*Faculty of Education, Hokkaido University of Education, Hakodate 040-8567, Japan*

Zeolites are well known as microporous materials, and have been applied widely to several engineering processes because of peculiar surface activity based on acidity. They are open framework aluminosilicates consisting of SiO_4 and AlO_4, interconnected *via* oxygen atoms. Both Si and Al are present with T_d symmetry in zeolite framework. But distortion is often brought about by application of several thermal processes or reactions. MFI-type zeolite is one of a typical material for application of catalysts with unique activity. In particular, Cu^{2+} ion-exchanged H-MFI shows high deNO_x activity with hydrocarbons. But an important problem due to hydrothermal stability cannot be avoided in the case of modified MFI. On the other hand, metallosilicates are one of the appropriate materials because active cations (trivalent transition metal ions mainly) are incorporated onto zeolite framework. For example, Fe^{3+}-substituted MOR zeolites show high NO-SCR activity with methane.[1] But deactivation proceeds during the reaction, as a major subject. We synthesized Fe- and Ga-MFI with various metal ratios by hydrothermal synthesis. Fe^{3+}- and Ga^{3+}-co-substituted MFI (FeGaMFI) can be obtained. These materials show unique reactivity for NO_x-SCR; FeMFI with high Fe ratio shows high NO-SCR activity but no activity for NO_x-SCR (in coexistence of O_2). In contrast, GaMFI with high Ga ratio shows high activity for NO_x-SCR. In order to clarify the structural stability of zeolite framework over Fe- and/or Ga-substituted MFI metallosilicates, Si K-edge XAFS study is applied to characterize the local symmetry of Si atoms. KTP(011) monochromator gave more emission of soft X-ray source in the region of 1.2 - 2.1 keV,[2] and thus, accurate XANES can be obtained. In recent studies, Si K-edge XANES can give an information about the local symmetry of SiO_4 structure, reported by Tanaka et al.[3] and other workers. In our study, XANES at Si K-edge was applied to characterize the several types of zeolites in order to evaluate the possibility of characterization around Si atom. Fe- and/or Ga-substituted MFI (FeMFI, GaMFI, FeGaMFI) materials were obtained by hydrothermal synthesis, and followed by calcination at 873 K. Molecular ratio of Si/Al_2 is 72 in each materials, and Al^{3+} site is substituted to Fe^{3+} and/or Ga^{3+}. The XANES spectra at Si K-edges were measured in BL1A of UVSOR in a total electron yield mode at ambient temperature by using KTP(011) monochromator.

Fig. 1 shows the XANES spectra of FeMFI (100% of substituted Fe ratio), FeGaMFI (Fe 75%, Ga 25%), and GaMFI (Ga 100%) before/after the reaction. For FeMFI, white line due to SiO_4 tetrahedra in MFI framework can clearly be seen. The intensity of the peak is larger than that of H-MFI (consist of SiO_2-Al_2O_3), indicating highly symmetric T_d sites are formed. In contrast, the intensity in Ga-substituted MFI is slightly smaller than that of H-MFI, as well as that of FeGaMFI. These results suggest that Fe substitution brings about structural change of MFI framework, and Ga co-substitution inhibit the structural change. It is likely that Fe sites in FeMFI are less stable than Ga sites in MFI structure, supporting the results of Fe and Ga K-edge XAFS. After the reaction, the intensity in FeMFI becomes larger. It suggests the structural change due to separation of Fe site by hydration. But Ga site is almost stable for the reaction. It can be expected that the FeGa co-substituted MFI is appropriate for NO-SCR catalyst because of structural stability of active Fe sites with Ga sites. Detailed study is now in progress.

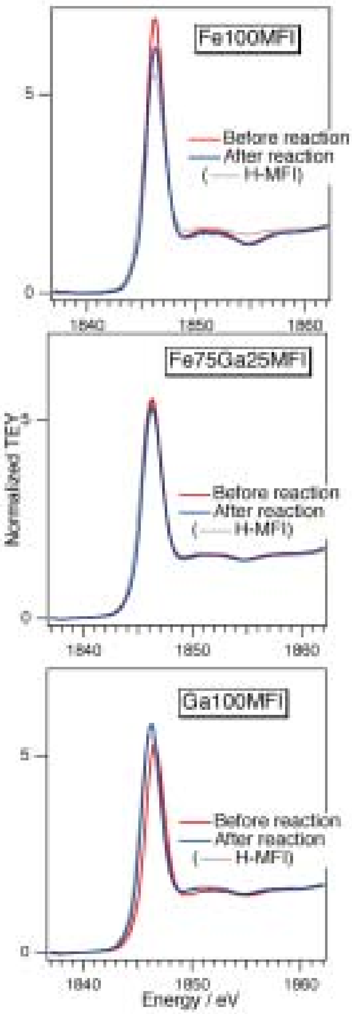

Fig. 1 Si K-edge XANES of FeMFI, FeGaMFI, and GaMFI before/after MOx-SCR with methane at 873 K for 3 h.

[1] H. Aritani *et al.*, Chem. Mater. **14** (2002) 562.
[2] Y. Takata *et al.*, J. Synchrotron Rad. **8** (2001) 351.
[3] T. Tanaka *et al.*, J. Phys. **IV** (Colloq. C2) (1997) 913.

BL1A

Evaluation of Catalytically Active Mo Species on H-MFI for Methane Dehydroaromatization

H. Aritani[1], S. Shinohara[1], S. Koyama[1], K. Otsuki[1], K. Saito[1], T. Kubo[2], A. Nakahira[2]
[1]*Faculty of Engineering, Saitama Institute of Technology, Fukaya 369-0293, Japan*
[2]*Graduate School of Engineering, Osaka Prefecture Universitty, Sakai 599-8531, Japan*

Many workers have focused on this catalyst system as a novel GTL process from natural gas to petroleum products since Wang et al. reported the methane dehydroaromatization over MoO_3/H-MFI catalysts in absence of oxygen. It has been revealed that reduction of Mo^{6+} ions is brought about in contact with methane in the initial step, and then Mo ions react methane to form carbide species, Mo_2C, in the next step. It is thus accepted that active Mo species are consist of reduced ions, Mo^{2+}, with Mo-carbide and/or oxycarbide species on H-MFI. On the other hand, molybdena catalysts supported on silica-alumina-based supports also show the dehydroaromatization activity. The activity for converting methane and its deactivation rate depend on the property of silica-alumina supports. In fact, molybdena supported on amorphous silica-alumina also shows dehydroaromatization activity, while it is lower than that on H-MFI. Relation between the silica-alumina support (with surface acidity) and active Mo species formed in the reaction is thus important to clarify the formation process of highly active Mo. In this study, Mo L_{III}-edge XANES is applied to characterize the Mo species on H-MFI and silica-alumina supports.

All the catalysts were prepared by impregnation of each silica-alumina support with ammonium heptamolybdate solution (7.5wt% loading as MoO_3), and followed by drying and calcination at 773 K for 3 h. Amorphous SiO_2-Al_2O_3 (containing 28.6 wt% Al_2O_3; denoted as SAH-1) and H-MFI (Si/Al_2=40, 90, 1880) supports were employed. Mo L_{III}-edge XANES spectra were measured in BL1A of UVSOR-IMS in total-electron yield mode.

Figure 1 shows the L_{III}-edge XANES spectra of reference samples. It is clear that edge energy values of XANES spectra in MoO_2, α-Mo_2C and Mo metal are different from each other. To clarify the difference, second derivatives of XANES spectra are also shown. The difference of energy value is significantly between Mo_2C (at 2525.3 eV) and Mo metal (at 2524.7 eV). This assignment can be applied to characterize the reduced Mo ions. As a reference, the spectrum of partially oxidized Mo_2C (denoted as Mo_2C (oxd.)), which is calcined at 473 K for 0.5 h, is also shown in Figure 1. The energy of a first minimum peak (at 2525.7 eV) is higher than that of bare Mo_2C but lower than that of MoO_2. Because stable Mo oxy-carbide does not exist commercially, the Mo_2C (oxd.) can be applied as a reference oxy-carbide sample. Figure 2 shows the L_{III}-edge XANES spectra of MoO_3/SAH-1 and MoO_3/H-MFI (Si/Al_2=90, showed maximum activity for benzene production) catalysts before/after the reaction. For MoO_3/SAH-1, it can be presumed that octahedral Mo^{6+} ions are changed definitely to form reduced species, which has some differences from Mo_2C, by the reaction. Mo^{6+}-species on H-MFI (90) are also reduced by the reaction, but the spectrum after the reaction is similar to that of Mo_2C. It is summarized that reductive effect of Mo species on H-MFI (90) by the reaction is larger than that on SAH-1, and the difference relate to the catalytic activity. To clarify the differences, second derivatives of their spectra can be evaluated. For MoO_3/SAH-1, only shoulder peak at ca. 2525 eV can be seen, and another components of reduced ions seem to be overlapped at 2528 eV with remained Mo^{6+} ions. It is likely that partially reduced species (without deep reduction to form Mo^{2+} ions) are brought about by the reaction. The components in MoO_3/H-MFI (90) after the reaction are similar to those of Mo_2C, indicating the formation of Mo^{2+}-carbide species in major. However, coexistence of oxo-species is suggested by the results of second derivatives of XANES spectra. It is concluded that formation of dispersed Mo^{2+}-carbide species with oxo-species is a key role for generation of active species.

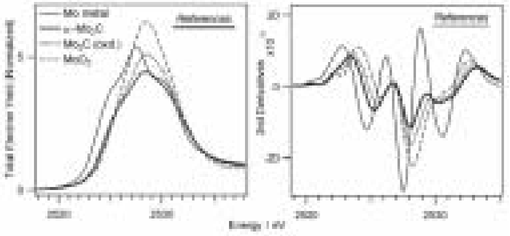

Fig. 1 Mo L_{III}-edge XANES spectra (left) and their second derivatives (right) of reference compounds: MoO_2, Mo_2C, partially oxidized Mo_2C and Mo metal.

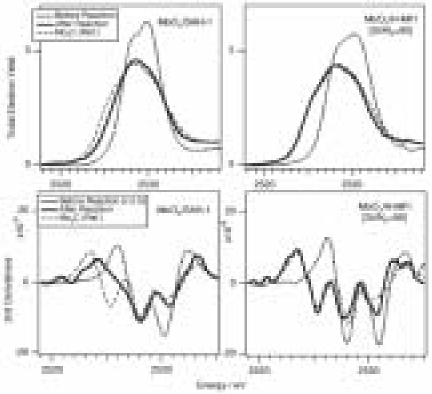

Fig. 2 Mo L_{III}-edge XANES (top) and their second derivatives (bottom) of MoO_2/SAH-1 and MoO_3/H-MFI (Si/Al_2=90) before/after dehydroaromatization of methane at 973 K.

BL1A

Analysis on Electronic Structures of the Layered and Spinel Oxides

H. Kobayashi[1], I. Teshima[2]
[1]Research Institute for Ubiquitous Energy Devices, AIST, Ikeda, Osaka, 563-8577 Japan
[2]Department of Molecular Science and Technology, Faculty of Engineering, Doshisha University, Kyotanabe, Kyoto, 610-0321 Japan

Li-containing layered and spinel oxides have been widely studied as the cathode materials of lithium secondary battery. Especially, layered oxide $LiNiO_2$ has been studied as the promising cathode material because of their large reversible capacity of 210 mAh/g in the voltage range 2.5 to 4.3 V. On the other hand, $LiNiO_2$ showed the less thermal stability compared with $LiMn_2O_4$ at high voltage of 4.3 V and decomposed to release oxygen from the structure below 200°C therefore, Al-doped $Li(Ni_{0.8}Co_{0.2})O_2$ has been reported as good candidate for cathode materials. Above mentioned, Al-doping is the effective way to improve the thermal stability of the layered and spinel materials. On the other hand, how the contribution of Al-doping to materials is still ambiguous in these systems. Detailed information on the Al *K*-edge electronic structure is very important in order to improve the thermal properties of these materials and, therefore, the electronic structures of Al-doped layered $LiNi_{0.8}Co_{0.15}Al_{0.05}O_2$, $LiNi_{0.45}Mn_{0.45}Al_{0.10}O_2$, and spinel $Li_{1.08}Mn_{1.84}Al_{0.08}O_4$ materials were investigated in this study.

Experimental

$LiNi_{0.8}Co_{0.15}Al_{0.05}O_2$ and $Li_{1.08}Mn_{1.84}Al_{0.08}O_4$ were supplied from Toda kogyou co. and Dai Nippon Toryou co.. $LiNi_{0.45}Mn_{0.45}Al_{0.10}O_2$ was synthesized in air at 1273 K for 24 h using appropriate molar ratios of $LiOH{\cdot}H_2O$, $M(CH_3COO)_2{\cdot}6H_2O$ (M=Ni and Mn), and $AlNO_3$ [1]. Al K-edge spectra were investigated by the total electron yield with KTP crystal (BL1A at UVSOR) measurements.

Results

Figure 1 shows the Al *K*-edge XANES spectra in Al-foil, α-Al_2O_3, AlF_3, and AlN. All the samples have the valence state of 3+ except for Al, but obvious different spectra were observed. This result indicated that Al *K*-edge spectra strongly depended on the anion or structure of materials. The Al *K*-edge XANES spectrum for $LiNi_{0.45}Mn_{0.45}Al_{0.10}O_2$ was observed as shown in Fig. 2, while it was difficult to obtain the spectra with the good S/N ratio for $LiNi_{0.8}Co_{0.15}Al_{0.05}O_2$ and $Li_{1.08}Mn_{1.84}Al_{0.08}O_4$ because of low content of Al in these materials. The peak position and shape of $LiNi_{0.45}Mn_{0.45}Al_{0.10}O_2$ were similar to that of α-Al_2O_3 compared with AlF_3 and AlN. $LiNi_{0.45}Mn_{0.45}Al_{0.10}O_2$ adopted the α-$NaFeO_2$ structure and the chemical composition can be expressed referring to the Wyckoff positions 3*a* and 3*b* with the space group *R3m* as $[Li_{0.92}Ni_{0.08}]_{3a}$ $[Li_{0.08}Mn_{0.45}Ni_{0.37}Al_{0.10}]_{3b}O_2$ by structural analysis. This spectra observed supported that the Al ions in $LiNi_{0.45}Mn_{0.45}Al_{0.10}O_2$ is the valence state of 3+ and occupy the octahedral site in the structure because Al $^{3+}$ ions occupied on the octahedral site in α-Al_2O_3. The TEY method using soft X-ray may give us useful information to understand the origin of battery performance of battery performance.

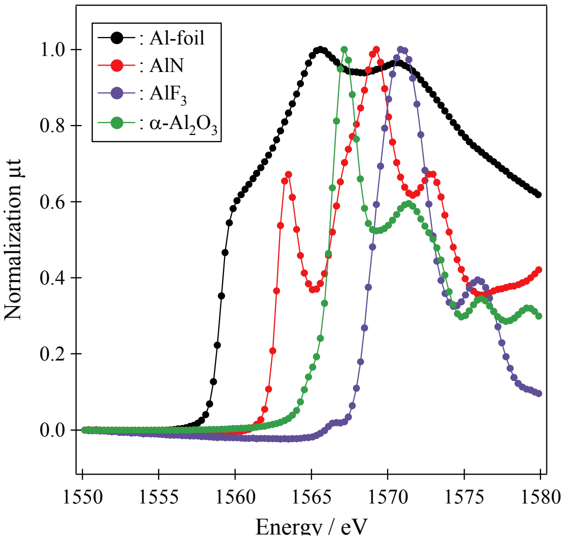

Fig. 1 Al *K*-edge XANES spectra in Al-foil, α-Al_2O_3, AlF_3, and AlN.

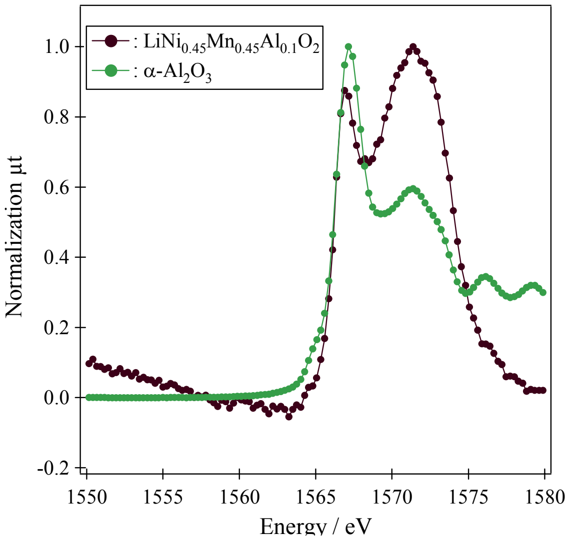

Fig. 2 Al *K*-edge XANES spectra in layered oxide $LiNi_{0.45}Mn_{0.45}Al_{0.10}O_2$ together with α-Al_2O_3.

[1] H. Kobayashi, Y. Arachi, S. Emura, and K. Tatsumi, Solid State Ionics, submitted

BL1A

Characterization of Metal Phtalocyanine by an XAFS Method

T. Kurisaki[1], M. Nasu[1], H. Yamashige[1], H. Wakita[1,2]
[1]*Department of Chemistry, Faculty of Science, Fukuoka University, Nanakuma, Jonan-ku, Fukuoka 814-0180, Japan*
[2]*Advanced Materials Institute, Fukuoka University, Nanakuma, Jonan-ku, Fukuoka 814-0180, Japan*

Phtalocyanines (PC) are synthetic analogues of porphyrins with a structure similar to that of hemoglobin and chlorophyll [1]. The molecular stacking and electronic structure of metallphthalocyanines (MPCs) attract great attention because they exhibit many remarkable capabilities e.g. as catalysts or as one-dimensional or semi-conductors in electronic or opto-electronic devices [2]. But the electronic structure of metallphthalocyanines is not well known.

In this work, we applied X-ray absorption near edge structure (XANES) spectroscopy to two type phtalocyanines, MnPC-Cl and Fe0CP-Cl. The results of the measurement indicate unoccupied and occupied electronic structure of MTPPs. The X-ray absorption spectra were measured at BL1A of the UVSOR in the Institute of Molecular Science, Okazaki [3]. The ring energy of the UVSOR storage ring was 750MeV and the stored current was 110-230 mA. Cl K-edge absorption spectra were recorded in the regions of 2533-3733eV by use of two Ge(111) crystals. The absorption was monitored by the total electron yield using a photomultiplier.

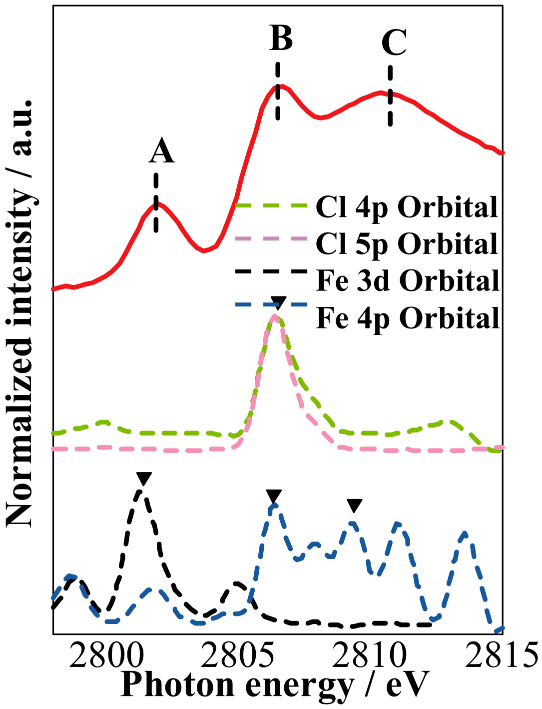

Fig. 1 Observed and calculated Cl K-edge XANES spectra of FePC-Cl.

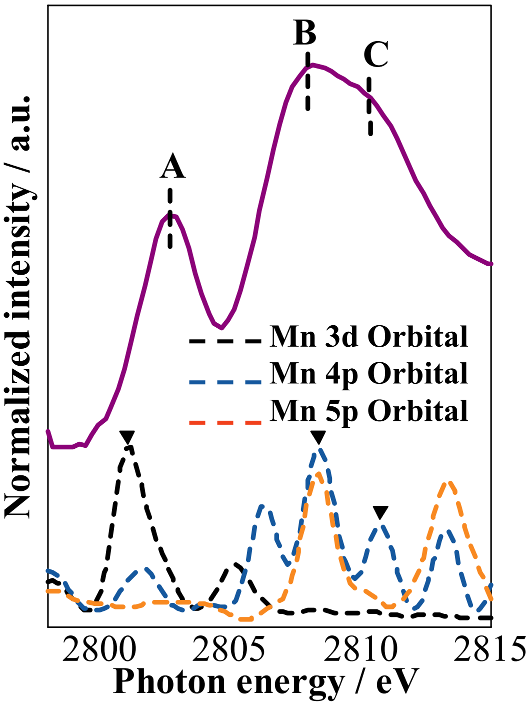

Fig. 2 Observed and calculated Cl K-edge XANES spectra of MnPC-Cl.

The Cl K-edge XANES spectra for the MPCs are shown in Figs. 1 and 2. A remarkable change of the spectral patterns was observed for the MnPC-Cl and FePC-Cl. Comparison of observed and calculated spectra revealed that metal 3d and 4p orbits contribute to peak A and B, respectively. However, MnPC-Cl did not contain contribution from the Cl4p and Cl5p orbits.

[1] F. H. Moser and A. L. Thomas, The phtalocyanines, CRC Press, Boca Raton, FL (1983).
[2] J. Simon F. Tournilhaec and J. –J. André, Nouv. J. Chim., **10** (1986) 295.
[3] S. Murata, T. Matsukawa, S. Naoè, T. Horigome, O. Matsuodo, and M. Watatabe, Rev. Sci. Instrum., **63**, (1992) 1309.

BL1A

Study of Local Structure of S-*K* Edge for Titanium Oxides Synthesized by Anodic Oxidation Treatments

A. Nakahira[1], H. Aritani[2], S. Nakamura[1], H. Nagata[1], H. Murase[1], T. Kubo[1]
[1]*Faculty of Engineering, Osaka Prefecture University, Gakuencho, Sakai 599-8531, Japan*
[2]*Faculty of Engineering, Kyoto Institute of Tech, Matsugasaki, Kyoto 605-8585, Japan*

Various attempts for synthesizing titanium oxide have been carried out by many researchers, since titanium oxide is one of very popular materials for application as a photocatalyst. Usually, the syntheses for titanium oxides have been attempted by sol-gel processings, sputtering, methods, other chemical processings, and vapor phase syntheses. On the contrary, various titanium oxides are able to be synthesize by an anodic oxidation method of titanium metal. This anodic oxidation method is a unique method for preparation of titanium oxides coating on titanium metal. At the same time, this anodic oxidation method is, in addition, considered to be applicable to prepare the high performance titanium oxides, for example, doping some anions in to titanium oxides. Nakahira et al found to be easy to perform by anodic oxidation methods. In the present experiment, titanium oxides was synthesized by anodic oxidation of titanium metal and preparation of titanium oxides doped with S ion was attempted in the mixture of H_2SO_4 solution at various temperatures ranging room temperature and upto 353 K. The evaluation of local structure of S-K edge were performed at BL1A in UVSOR for this S-doped titanium oxides prepared by the anodic oxidation method.

Experiments

In the experiments, titanium metal was used as an anode and carbon black was used as a cathode. The distance between electrodes on anodic oxidation processing was kept to be approximately 3cm. Before anodic oxidation, titanium substrates were polished using abrasive paper, washed with ethanol and finally dried in atmosphere. Ti substrate was soaked in aqueous 0.5M H_2SO_4 solution at room temperature and upto 353 K. Anodic oxidation processing in this study was carried out under a voltage of 80 to 150V supplied with direct current power. For comparison, S-doped TiO_2 were synthesized by heat-treated process at 500°C and its local structure of S was evaluated.

Results and Discussion

From the results by powder X-ray diffraction analysis, the samples obtained by anodic oxidation processing at a voltage of 350V were identified to be anatase, although they possessed relatively broad peaks due to their low crystallinity. Figure 1 shows the results of XANES of S-*K* of some titanium oxides ((a) and (b)) prepared by anodic oxidation in H_2SO_4 solution. Although also the result for S-doped TiO_2 (c) as a reference material was shown, XANES spectra of titanium oxides obtained by anodic oxidation in H_2SO_4 solution were similar to one of S-doped TiO_2 as a reference material. These results of XANES spectra at S-K edge showed that S-doped titanium oxides were successfully prepared by anodic oxidation methods.

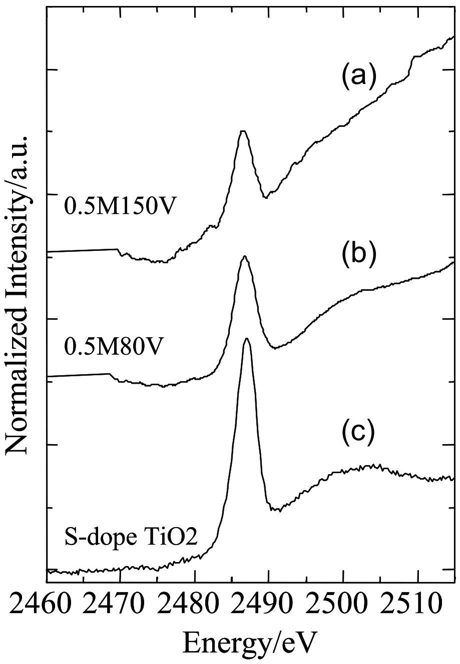

Fig. 1 XANES of S-*K* of some samples prepared by anodic oxidation method.

BL1A

Measurement of Optical Luminescence from a Silica Glass

T. Yoshida[1], S. Obata[1], T. Tanabe[2], H. Yoshida[3]
[1]Department of Materials, Physics and Energy Engineering, Nagoya University, Furo-cho, Chikusa-ku, Nagoya 464-8603
[2]Department of Advanced Energy Engineering Science, Interdisciplinary Graduate School of Engineering Science,Kyushu University6-10-1, Hakozaki, Higashi-ku, Fukuoka 812-8581
[3]EcoTopia Science Institute, Nagoya University, Furo-cho, Chikusa-ku, Nagoya 464-8603

Introduction

Radiation effects on silica glasses are one of the main concerns for their application as optical windows, insulators and optical fibers under fusion and fission environments. The present work is our trial to observe soft X-ray radiation effects on silica. Since the energy region of the soft X-ray covers the K-edges of silicon and oxygen, it is possible to study the dynamic and specific radiation effect of silica under the preferential excitation of these inner-shell electrons. In this study, we have measured the luminescence from silica glasses under the irradiation of soft X-ray near Si K-edge, and discussed the origin and the variation of the luminescence sites.

Experimental

The sample used in this work was an unirradiated low-OH fused silica glasses (T-2030, produced by Toshiba Ceramics, Japan). The diameter and thickness of the sample was 13 mm and 2 mm. The measurement of luminescence of the silica glass induced by soft X-ray irradiation (1.8-1.9 keV) was carried out on the beam line 7A and 1A at UVSOR, Institute for Molecular Science with a stored current of 100-200 mA. The luminescence was focused by a lens in the UHV chamber to the monochromator (CP-200, JOBIN YVON) and detected by a multi-channel analyser (OMA III, EG&G PRINCETON APPLIED RESEARCH). The luminescence yield spectrum was also measured using a photomultiplier (Hamamatsu Photonics R955).

Results and Discussion

Under the irradiation of soft X-rays near Si K-edge, the low-OH fused silica glass (T-2030) showed an intense emission band at around 3.1 eV. Similar luminescence spectra have been measured for silica glasses under in-reactor or UV irradiation [1], and we have concluded that the origins of the present XEOL is likely due to electron excitation of oxygen deficiencies in the silica glass by soft X-ray. Based on the photon energy of the emission bands, the 3.1 eV band should be related to the intrinsic $B_{2\beta}$ center in the low-OH silica glass (T-2030).

We also measured a photoluminescence yield (PLY) spectrum of the 3.1 eV band and showed in Fig. 1(a) together with Si K-edge XANES spectrum (Fig. 1(b)) recorded in the photocurrent mode for the same fused silica glass. One can clearly see that both PLY and XANES spectra are similar, although the former jump negatively whereas the latter positively at Si K-edge. The outline of the phenomenological theory for the shape of the PLY spectrum has been proposed previously [2,3] and is due to the competitive absorption of sites being responsible for the luminescence and those being not. Since in both cases the total absorption condition applies, the key factors that decide the direction of the edge jump are relative luminescence yield of the absorption events above and below the edge. By applying this theory to the present case, above Si K-edge, the transition of Si 1s electron to 3p orbital and/or continuum state occurs and simultaneously the relative luminescence yield reduces; therefore, the PLY spectrum may show the negative and similar feature to XANES spectrum.

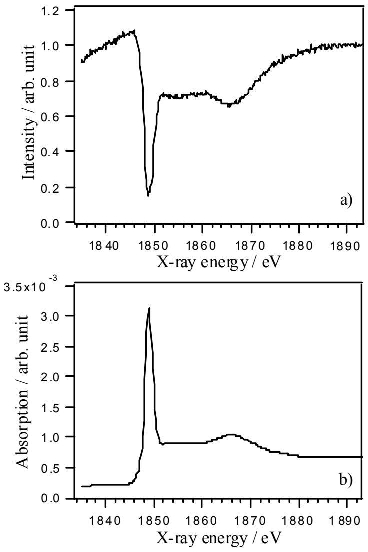

Fig. 1 The comparison between a) the luminescence yield spectrum of the 3.1 eV band and b) Si K-edge XANES spectrum of a fused silica glass.

[1] R. Tohmon *et al.*, Phys. Rev. B **55** (1989) 1337.
[2] S. Emura, H. Maeda, M. Nomura, Physica B **208-209** (1995) 108.
[3] T. Murata, D. T. Jiang, T. K. Sham, X. H. Feng, S. P. Frigo, J. Elec. Spectr. Related Phenom. **79** (1996) 155.

BL1A&8B1

Changes in Electronic Structure in $Li_3Fe_2(PO_4)_3$ upon Lithium Insertion

J. Shirakawa[1], M. Nakayama[1], M. Wakihara[1], Y. Uchimoto[2]

[1]Department of Applied Chemistry, Tokyo Institute of Technology, Tokyo 152-8552 Japan

[2]Department of Interdisciplinary Environment, Kyoto University, Kyoto 606-8501, Japan

Iron oxides with Li insertion sites are attractive for cathode material for lithium ion battery due to their low cost and abundant mine resources. However, Fe^{3+}/Fe^{2+} redox couple usually show only ~ 1.5 V vs. Li^+/Li, indicating smaller energy density than currently used $LiCoO_2$ (~ 3.8 V). In 1997, Padhi *et al.* reported cathode material, $LiFePO_4$ with sufficiently higher voltage, ~ 3.5 V[1]. In this structure, P ions reside in tetrahedral sites and form compact PO_4 polyanion units. These polyanion units form strong covalent bonding, so that the valence electrons of transition metals tend to be isolated from those of polyanions. Such an electronic structure description may relate to its relatively higher voltage.

In this study, we synthesized $Li_3Fe_2(PO_4)_3$ of iron oxide with polyanion units, PO_4, and measured X-ray absorption spectra (XAS) to understand changes in electronic structure upon electrochemical Li insertion.

Experimental

$Li_3Fe_2(PO_4)_3$ was synthesized by a citric acid complex method using $Fe(NO_3)_3{\cdot}9H_2O$, $LiNO_3$ and $NH_4H_2PO_4$ as starting materials. Each starting material with stoichiometric ratio and citric acid was solved into pure water with stirring on the hotplate. After evaporation of solvent, the precursor was sintered twice at 650 °C for 12 h, and the targert products were obtained.

X-ray absorption measurements for each element by total electron yield were performed on BL1A (P K-edge) and BL8B1 (Fe L-edge and O K-edge).

Results and Discussion

Electrochemical techniques revealed that lithium insertion took place at around 2.5 V vs Li^+/Li ($x < 1$ in $Li_{3+x}Fe_2(PO_4)_3$), showing higher voltage than conventional Fe^{2+}/Fe^{3+} redox couple. Discharge curve of $Li_{3+x}Fe_2(PO_4)_3$ monotonically varied, indicating topochemical lithium insertion proceeded in the electrochemical reaction.

Figure 1 exhibits the Fe L-edge XAS as a function of Li content in $Li_{3+x}Fe_2(PO_4)_3$. As the Li content increased, absorption peaks shifted to lower energy side, indicating Fe^{3+} reduced to Fe^{2+}. On the other hand, almost no marked change was observed in P K-edge XAS with Li insertion (Figure 2). Thus, P ions did not contribute to charge compensation. O K-edge XAS are presented in Figure 3. Two small peaks are observed at preedge region less than 532 eV, which arise from the hybridization with 3d orbital of iron. These peaks were smaller than commonly known iron oxides, such as FeO and Fe_2O_3, so that the 3d orbital of iron would isolate from the O 2p state. Whereas, the electrochemical lithium insertion led to the increase of their preedge peaks. Thus, changes in electronic structure also took place around oxide ions as well as Fe ions. In addition, this change may accompany the enhancement of hybridization between Fe 3d and O 2p as seen in Fig. 3. To understand the electronic structural change, first-principles calculations for $Li_{3+x}Fe_2(PO_4)_3$ are under progress.

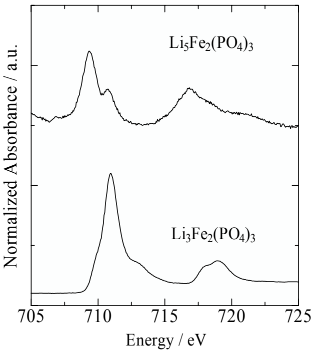

Fig. 1 Fe L-edge XAS of $Li_{3+x}Fe_2(PO_4)_3$.

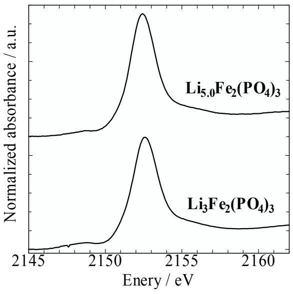

Fig. 2 P K-edge XAS of $Li_{3+x}Fe_2(PO_4)_3$.

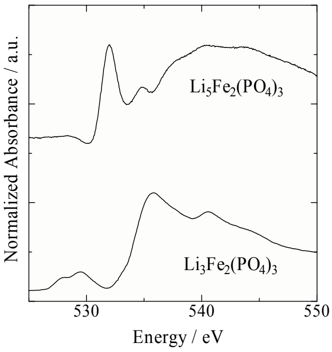

Fig. 3 O K-edge XAS of $Li_{3+x}Fe_2(PO_4)_3$.

[1] Padhi *et al.,* J. Electrochem. Soc. **144** (1997) 1188.

BL5U

Electronic Structure of CeNiGe$_{2-x}$Si$_x$: Ce 4d-4f Resonant Photoemission Spectroscopy

H.J. Im[1], T. Ito[1,2], S. Kimura[1,2], H.D. Kim[3], J.B. Hong[4], Y.S. Kwon[4]
[1]*School of Physical Sciences, The Graduate University for Advanced Studies, Okazaki 444-8585, Japan*
[2]*UVSOR Facility, Institute for Molecular Science, Okazaki 444-8585, Japan*
[3]*Pohang Accelerator Laboratory, Pohang University of Science and Technology, Pohang 790-784, Korea*
[4]*BK21 Physics Research Division and Institute of Basic Science, Sungkyunkwan University, Suwon 440-746, Korea*

Ce intermetallic compounds have attracted much attention for their various ground states, such as the magnetism, non-magnetic heavy fermion, and quantum criticality. It has been believed that the *cf* - hybridization between the local Ce 4*f* electrons and the itinerant conduction electrons plays an important role to determine these ground states. In this report, we provide a clear understanding of the *cf* - hybridization process by the systematic Ce 4*d*-4*f* resonant photoemission (RPE) study of the isostructural heavy fermion system CeNiGe$_{2-x}$Si$_x$ ($0 \le x \le 1$), where the ground state originating in Ce 4*f* character varies from an antiferromagnetic regime (AFM, $0 \le x \le 0.8$) to a quantum critical point (QCP, $x = 1$) with increasing Si concentration following a unit volume reduction by about 5 percent [1].

In figure 1 (b), the off-RPE spectra show that the Ni 3*d* peak is located at around 1.8 eV for $x = 0$ and slightly shifts to high-binding energy (around 1.95 eV for $x = 1$) with increasing x in agreement with the LSDA+U (U = 6 eV) band calculation (not shown here). In figure 1 (a), the on-RPE spectra clearly show the two peaks near the Fermi level (E$_F$): One is Ce $4f^1_{7/2}$ final state at around 0.3 eV, and the other is Ce $4f^1_{5/2}$ final state at E$_F$, the so-called tail of Kondo resonance peak. The gradual increase of the intensity ratio of Ce $4f^1_{5/2}$ to Ce $4f^1_{7/2}$ peak with increasing Si concentration indicates that the *cf* - hybridization intensity becomes stronger as the ground state of Ce 4*f* electron changes from AFM to QCP.

It is worth comparing the result of CeNiGe$_{2-x}$Si$_x$ system to that of CeNi$_{1-x}$Co$_x$Ge$_2$ system where the increase of the *cf* - hybridization comes from the lower binding energy shift of Ni/Co 3*d* state (the intense peak position : 1.8 eV for $x = 0$ and 0.8 eV for $x = 1$) with increasing Co concentration through the QCP ($x = 0.3$) [2,3]. In CeNi$_{1-x}$Co$_x$Ge$_2$ system, Co substitution gives rise to the simultaneous change of Ni/Co 3*d* density of state and the 3d state character. Therefore, it is difficult to distinguish which effect is more effective. On the other hand, in CeNiGe$_{2-x}$Si$_x$ system, the increase of hybridization strength with Si substitution is exclusively caused by the increase of chemical pressure due to the reduction of lattice constant without the change of the 3*d* state character. This means that the present system is much suitable for the detection of the *cf*-hybridization effect.

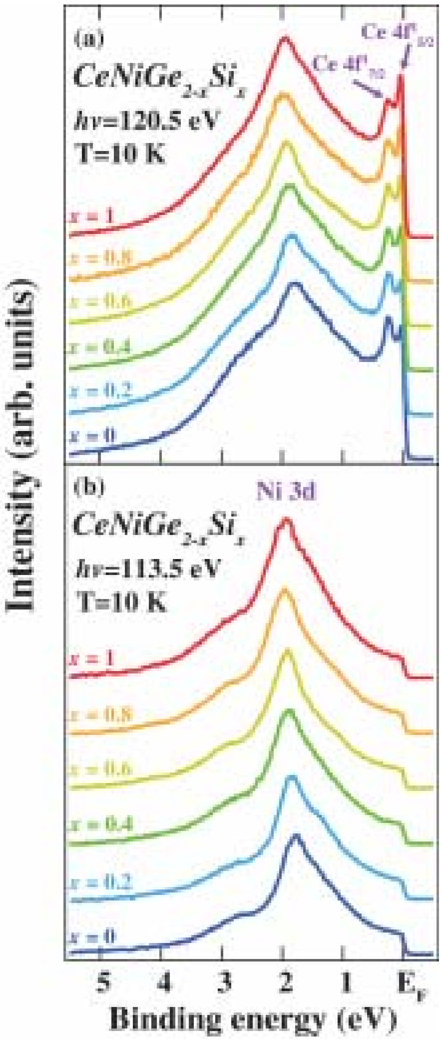

Fig. 1 Ce 4*d*-4*f* on- (a) and off- (b) RPE spectra of CeNiGe$_{2-x}$Si$_x$.

[1] D.Y. Kim *et al.*, J. Phys. Condens. Matter **16** (2004) 8323.
[2] H.J. Im *et al.*, Phys. Rev. B **72** (2005) 220405(R).
[3] H.J. Im *et al.*, UVSOR Activity Report 2004 (2005) 100.

BL5U

Three-Dimensional Angle-Resolved Photoemission Study on SmS

T. Ito[1,2], H.J. Im[2], A. Chainani[3], K. Matsubayashi[4], S. Kimura[1,2], H.-D. Kim[5], K. Imura[4],
H. Suzuki[6], N. K. Sato[4]
[1]*UVSOR Facility, Institute for Molecular Science, Okazaki 444-8585, Japan*
[2]*School of Physical Science, The Graduate University for Advanced Studies, Okazaki 444-8585, Japan*
[3]*RIKEN, SPring-8 Center, Sayo-cho, Sayo-gun, Hyogo 679-5148, Japan*
[4]*Department of Physics, Graduate School of Science, Nagoya University, Nagoya 464-8602, Japan*
[5]*Pohang Accelerator Laboratory, Pohang University of Science and Technology, Pohang 790-784, Korea*
[6]*National Institute for Material Science, Tsukuba, Ibaraki 305-0047, Japan*

SmS is a key material to clarify the physics of strongly correlated electron systems because of its characteristic insulator-metal transition with pressure (~0.7 GPa), so called “black”-“gold” phase transition. In spite of many efforts to understand the origin of its anomalous properties, there is no confidential starting point since the electronic structure has not been clarified. For example, the electrical resistivity [1] as well as the high-resolution photoemission study [2] of “black” SmS suggests the semiconducting gap of Δ~100 meV, while the angle-resolved photoemission spectroscopy (ARPES) has reported wider semiconducting-gap (Δ~400 meV) along (110) emission plane, which has been expected to be the limited tracing points in the Brillouin zone with using He discharge lamp (hν=21.2, 40.8 eV) [3].

To elucidate the intrinsic electronic structure of “black” SmS, especially to clarify the three-dimensional (3D-) electronic structure as well as the semiconducting-gap topology, we have performed 3D-ARPES on “black” SmS.

Figures 1(a) and (b) show the experimental band structures along ΓX and XW lines, respectively. From the estimation of the inner potential V=7 eV, we have mapped out the band dispersion around the exact high-symmetry points [4] with using 3D-ARPES at UVSOR-II BL5U. From the comparison with the previous ARPES, the highly dispersive bands at 3-6 eV have been attribute to S 3*p* bands, while the three non-dispersive features near E_F to Sm^{2+} multiplet structures [3]. It should be noted that the observed clear differences of the Sm-4*f*-dispersions between the Γ (> 100 meV) and X (< 20 meV) points are direct evidence for the existence of three-dimensional lattice effect on “black” SmS.

In Fig. 2, there is no feature from E_F to 400 meV, which has also been confirmed at the all points in the (100) plane (not shown). This strongly indicates the intrinsic nature of wide semiconducting gap on “black” SmS against to the previous expectation [3]. To understand the origin of contradiction between thermodynamic and ARPES experiments, further studies are intended.

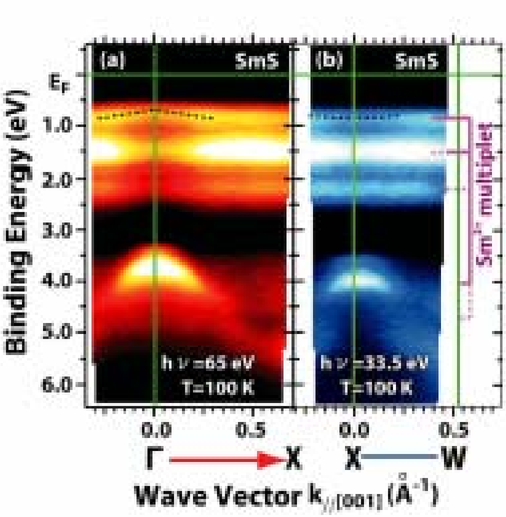

Fig. 1 Experimental band structure of “black” SmS around Γ and X points obtained by present 3D-ARPES. Bright areas correspond to energy bands. Dashed lines are dispersive features of Sm^{2+} multiplets as shown in Fig. 2.

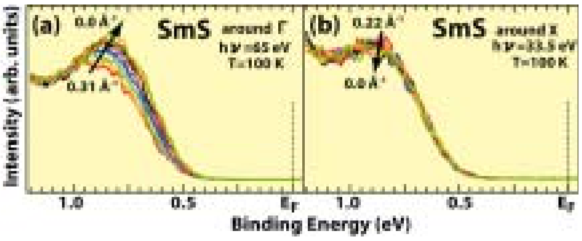

Fig. 2 3D-ARPES spectra near E_F of “black” SmS around Γ (a) and X (b) points, respectively. Arrows indicate the change of ARPES peak positions.

[1] M. Ohashi *et al.*, High Pressure Sci. Technol.**7** (1998) 611.
[2] A. Chainani *et al.*, Phys. Rev. B **65** (2002) 155201.
[3] T. Ito *et al.*, Phys. Rev. B **65** (2002) 155202.
[4] T. Ito *et al.*, Physica B (2006) in press.

BL5U

Three-Dimensional Angle-Resolved Photoemission Study on $CeTe_2$

T. Ito[1,2], H. Im[2], S. Kimura[1,2], Y. S. Kwon[3]
[1]UVSOR Facility, Institute for Molecular Science, Okazaki 444-8585, Japan
[2]School of Physical Sciences, The Graduate University for Advanced Studies, Okazaki 444-8585, Japan
[3]BK21 Physics Research Division and Institute for Basic Science, Sungkyunkwan University, Suwon 440-746, Korea

Anomalous electronic/magnetic properties, such as charge/spin density wave formation, high-Tc superconductivity, etc., have intimate relation with the anisotropic electronic/magnetic structure of materials. Thus, it is important to understand the effect of the low-dimensional electronic structure relates to the unconventional physical properties. On the other hand, the most of studies on the low-dimensional compounds persist on the standing point of ideal two- or one-dimensional case, though the sizable three-dimensionality on the real system has essential relation with its anomalous properties.

To show the importance of three-dimensionality at the electronic structure correlating with the anomalous physical properties, we have performed three-dimensional angle-resolved photoemission spectroscopy (3D-ARPES) [1] on $CeTe_2$, which crystallizes in the layered structure formed by the planar Te(1) sheet sandwiched by the corrugated CeTe(2) double layers [2].

Figure 1 shows the Fermi surface image along ΓZMR plane of $CeTe_2$ obtained by plotting the ARPES intensity integrated from the Fermi level (E_F) to 100 meV binding energies. Yellow and red areas correspond to the Fermi surface. In Fig. 1, the Brillouin zone boundaries have been estimated from the symmetry of band dispersions along ΓZ line (Fig. 2(a)) obtained by utilizing the energy vs momentum relation of $k_\perp = (2\pi/h)\sqrt{2mE_k\cos^2\theta+V}$, where E_K is kinetic energy at E_F, $\theta=0°$, and V is inner potential, which is slightly larger (V~16.4 eV) than the previous report (V~15 eV) [3], possibly due to the insufficient photon energy range on the previous estimation.

From the comparison with the band calculation [4], two Fermi surfaces around ΓZ axis (dashed lines) originating in hole-like FS with Te(1) character, whose two-dimensionality is roughly consistent with the anisotropic crystal structure as well as thermodynamic properties [2].

On the other hand, we have observed broad features (purple dashed lines in Fig. 2(a)) that indicate "band folding" along ΓZ lines. This strongly suggests the three-dimensional electronic structure on $CeTe_2$. We believe that the observed three-dimensionality can be ascribed as the existence of 3D nesting vector, which has not been reported so far [4,5]. The present results clearly show the future aspect of the 3D-ARPES as a tool for the study of the low-dimensional strongly correlated electron systems.

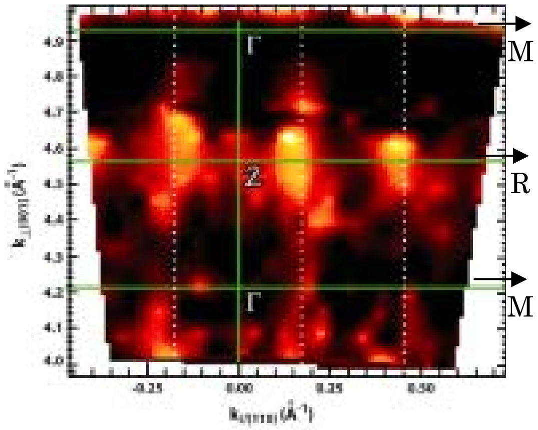

Fig. 1 Fermi surface mapping on ΓZMR plane of $CeTe_2$ obtained by 3D-ARPES. Dashed lines are guide for eyes.

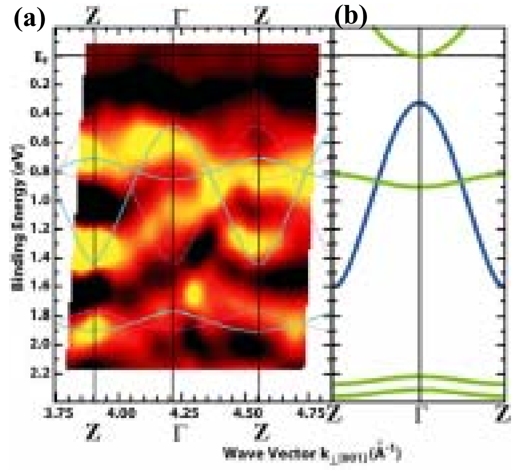

Fig. 2 (a) Band structure along ΓZ line of $CeTe_2$ obtained by 3D-ARPES. Solid and dashed lines are guide for eyes. (b) Band calculation of $CeTe_2$. Green and blue lines correspond to the bands on Te(1) and CeTe(2) layer, respectively.

[1] J. Schäfer *et al.*, Phys. Rev. B **72** (2005) 155115.
[2] M. H. Jung *et al.*, Phys. Rev. B **62** (2000) 11609.
[3] T. Ito *et al.*, UVSOR Activity Report 2004, 99; Physica B, in press.
[4] J. H. Shim *et al.*, Phys. Rev. Lett. **93** (2004) 156406.
[5] K.Y. Shin *et al.*, Phys. Rev. B **72** (2005) 085132.

BL5U

3*p*-3*d* Resonance Photoemission Spectroscopy of Heusler-Type $Fe_2VAl_{1-z}Si_z$

H. Miyazaki[1], M. Inukai[1], S. Ota[1], T. Suzuki[1], M. Kato[1], S. Yagi[1], K. Soda[1]
Y. Nishino[2], T. Ito[3], S. Kimura[3]
[1]*Graduate School of Engineering, Nagoya University, Nagoya 464-8603 Japan*
[2]*Graduate School of Engineering, Nagoya Institute of Technology, Nagoya 466-8555 Japan*
[3]*UVSOR Facility, Institute for Molecular Science, Okazaki 444-8585 Japan*

Introduction

Heusler-type Fe_2VAl and related alloys such as $Fe_2VAl_{1-z}Si_z$ have attracted much attention because of not only scientific interest in their anomalous transport properties [1] but also potential application for thermoelectric materials [2]. In order to clarify the origin of the fascinating transport and thermoelectric properties, we have investigated the electronic structure of $Fe_2VAl_{1-z}Si_z$ alloys by photoelectron spectroscopy. In this paper, we will report results of the Fe and V 3*p*-3*d* resonance photoemission study.

Experimental

Photoelectron spectra of polycrystalline specimens of $Fe_2VAl_{1-z}Si_z$ alloys were recorded under 2.7×10^{-8} Pa at 30 K with a high-resolution energy analyzer at BL5U. The origin of the binding energy E_B, the Fermi level (E_F), and the total energy resolution were determined by the measurement of the Fermi edge of an evaporated gold film. The total energy resolution was 45 meV at the excitation photon energy of 50 eV. Clean surfaces for the photoelectron measurement were prepared by in-situ fracturing the specimens.

Results and Discussion

Figures 1 and 2 show the Fe and V 3*d* states, respectively, of $Fe_2VAl_{1-z}Si_z$ estimated from the resonance photoemission spectroscopy as well as their partial densities of states theoretically calculated for Fe_2VAl. The overall features of the Fe and V 3*d* states agree considerably well with the respective partial densities of states, although there is the large intensity near E_F attributed to the surface states appearing in the pseudo-gap [3] and the V 3*d* states are located in lower binding energy than expected.

As the Si substitution z is increased from 0 to 0.05, the Fe 3*d* states show almost no change in the main peak position but the intensity decrease in the low energy side of the peak. With z increased to 0.10, the Fe 3*d* states are again enhanced between E_B of 0.5 eV and E_F. The hump around E_B = 2.5 eV seems to move to the low binding energy side. On the other hand, the V 3*d* states, in particular the V t_{2g} peak at E_B ~ 1.3 eV, are shifted gradually to the high binding energy side as z increases, but the contribution is reduced near E_F. Since it is expected that the V 3*d* t_{2g} states are not so much hybridized with the Al and Si *sp* states, the shift of the V t_{2g} states imply the increase in the electrons at the V site on the substitution, which is consistent with the observation of the V 2*p* core level shift.

The present findings indicate the non-rigid band -like change in the electronic structure induced by the Si substitution. However, the observed dependence of the thermoelectric power [2] is explainable by the observation, *i.e.* the shift of the V 3*d* states and the intensity decrease at E_F at z = 0.05 and the emergence of the Fe 3*d* states in the pseudo-gap at z = 0.10.

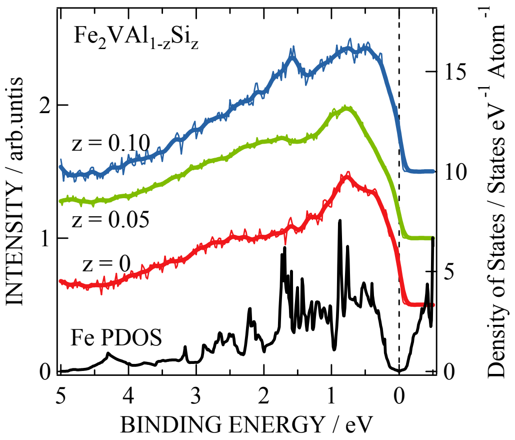

Fig. 1 Energy distribution of the Fe 3*d* states of $Fe_2VAl_{1-z}Si_z$. The theoretical density of the Fe 3*d* states (Fe PDOS) of Fe_2VAl is also shown for comparison.

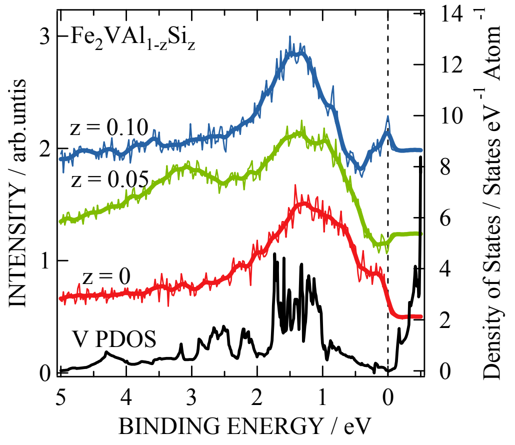

Fig. 2 Energy distribution of the V 3*d* states of $Fe_2VAl_{1-z}Si_z$. The theoretical density of the V 3*d* states (V PDOS) of Fe_2VAl is also shown for comparison.

[1] Y. Nishino *et al.*, Phys. Rev.Lett. **79** (1997) 1909.
[2] H. Kato *et al.*, J. Jpn. Inst. Metals **65** (2001) 652.
[3] K. Soda *et al.*, Phys. Rev. B **71** (2005) 245112.

Angle-Resolved Photoemission Spectroscopy of Heusler-Type Fe_2VAl

H. Miyazaki[1], M. Inukai[1], S. Ota[1], T. Suzuki[1], M. Kato[1], S. Yagi[1], K. Soda[1]
K. Fukuda[2], Y. Yamada[3], T. Ito[4], S. Kimura[4]
[1]*Graduate School of Engineering, Nagoya University, Nagoya 464-8603 Japan*
[2]*Graduate School of Science and Technology, Niigata University, Niigata 950-2181 Japan*
[3]*Department of Physics, Niigata University, Niigata 950-2181 Japan*
[4]*UVSOR Facility, Institute for Molecular Science, Okazaki 444-8585 Japan*

Introduction

A Heusler-type Fe_2VAl intermetallic compound has attracted much attention because of its unusual transport properties [1]: the semiconductor-like temperature dependence of the electric conductivity, the enhancement of the effective electron mass at low temperatures and a marginally magnetic property. Furthermore, the small deviation of its composition from the stoichiometry causes the drastic increase of the electric conductivity at low temperatures and the unexpected enhancement of the thermoelectric power. According to a band structure calculation [2], Fe_2VAl is a non-magnetic semimetal with a sharp pseudo-gap right at the Fermi level E_F. However, the origin of the unusual transport properties has not been clarified yet. Thus we have experimentally investigated the band structure of Fe_2VAl by the angle-resolved photoemission spectroscopy (ARPES).

Experimental

The ARPES measurements were carried out at BL5U under 2.7×10^{-8} Pa at 25 K. The origin of the binding energy E_B, *i.e.* E_F was determined by measuring the Fermi edge of an evaporated Au film. The total energy resolution was also estimated by the Fermi edge to be 0.13 eV at the excitation photon energy $h\nu$ of 87 eV and 0.045 eV at $h\nu$ = 47 eV. The angle resolution was set to 0.5°. Clean surfaces of single crystalline Fe_2VAl were prepared by *in situ* fracturing them in parallel to a (111) surface.

Results and Discussion

Figures 1 and 2 show the valence band structures of Fe_2VAl, which were obtained from the second derivative of the normal ARPES spectra and the off-normal ones recorded at $h\nu$ = 47 eV, respectively. We have distinguished at least five bands labeled as A to D in Fig.1 and A' to E' in Fig.2, as shown by white curves as guides for eyes. Black curves indicate the band structure calculated by the code WIEN 2K [3], which is consistent with that reported so far [2].

The A (A') and B (B') bands form small electron pockets around the Γ and L ($\overline{M}$) points, respectively. The A (A') and D (D') bands agree fairly well with the calculated ones. The C band may be attributed to a surface state, showing no dispersion along the surface normal. The present normal ARPES study also suggests that the surface state might be derived from the V $3d$ states, since $h\nu$ for the Γ point corresponds to the V $3p$ threshold region. According to the calculation and the $3p$-$3d$ resonance photoemission study for polycrystalline alloys [2,4], the main V $3d$ band is located at $E_B \sim 1.3$ eV, which may be suppressed because of the selection rules. Detailed analysis and further study for non-stoichiometric compounds $Fe_{2-x}V_{1+x}Al$ will be reported elsewhere.

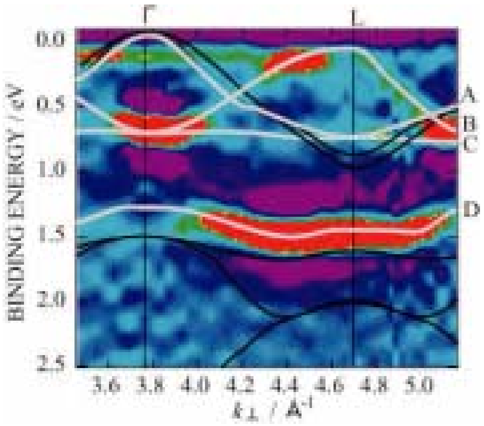

Fig. 1 Valence band structure of Fe_2VAl obtained by the normal ARPES of a (111) surface.

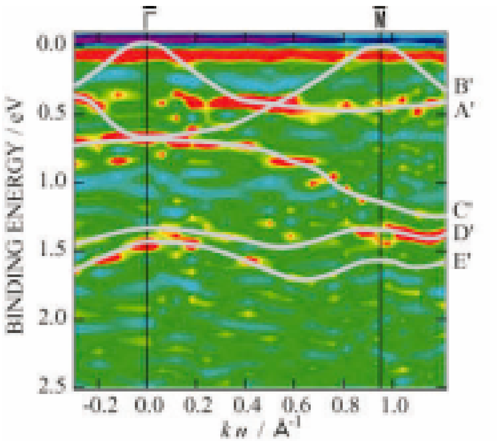

Fig. 2 Valence band structure of Fe_2VAl obtained by the off-normal ARPES of a (111) surface.

[1] Y. Nishino *et al.*, Phys. Rev. B**71** (2005) 094425.
[2] G. Y. Guo *et al.*, J. Phys.:Condens. Matter **10** (1998) 119.
[3] P. Blaha *et al.*, Compt. Phys. Commun. **59** (1990) 399.
[4] H. Miyazaki *et al.*, *in the present Activity Report.*

BL5U

Electronic Structure of Heusler-Type $(Fe_{1-x}M_x)_2VAl$ (M=Ir, Pt)

T. Mochizuki[1], H. Miyazaki[2], M. Kato[2], S. Yagi[2], K. Soda[2],
A. Miyashita[3], Y. Nishino[3], T. Ito[4], S. Kimura[4]
[1]*School of Engineering, Nagoya University, Nagoya 464-8603, Japan*
[2]*Graduate School of Engineering, Nagoya University, Nagoya 464-8603, Japan*
[3]*Graduate School of Engineering, Nagoya Institute of Technology, Nagoya 466-8555 Japan*
[3]*UVSOR, Institute for Molecular Science, Okazaki 444-8585 Japan*

Introduction

Heusler-type Fe_2VAl and its related alloys have received much attention because Fe_2VAl possesses a sharp pseudogap across the Fermi level E_F and shows the remarkable enhancement of thermoelectric properties by the partial substitution [1]. To develop new thermoelectric materials, it is important to clarify how the electronic structure is changed by the partial substitution. In this report, we will show the results of the 3*p*-3*d* resonance photoemission measurement of Heusler-type alloys $(Fe_{1-x}M_x)_2VAl$ (M=Ir, Pt).

Experimental

Samples are polycrystalline of the Heusler-type $(Fe_{0.98}Ir_{0.02})_2VAl$, $(Fe_{0.99}Pt_{0.01})_2VAl$ and Fe_2VAl in a size of 1x1x5 mm^3. Photoelectron spectra were recorded under 2.7x10^{-8} Pa at 30 K at BL5U. Clean surfaces were prepared by the in-situ fracture.

Results and Discussion

Observed valence-band spectra show three features at the binding energy E_B of 0.8, 1.4 and 3.0 eV. The overall features agree well with the bulk-sensitive soft X-ray photoelectron spectra (XPS) of Fe_2VAl [2] except for the feature around E_F. The large intensity at E_F in the present spectra for Fe_2VAl suggests the surface states appearing in the pseudogap. By the partial substitution of Ir or Pt for Fe, the intensity at E_F is reduced and the peak at E_B = 1.3 eV is shifted to the high binding energy side.

Figures 1 and 2 show partial densities of the Fe and V 3*d* states, respectively, estimated from the relevant 3*p*-3*d* resonance photoemission. With the partial substitution, the Fe 3*d* states are reduced at E_F and the hump around 2.5 eV seems to be shifted for $(Fe_{0.98}Ir_{0.02})_2VAl$ and split for $(Fe_{0.99}Pt_{0.01})_2VAl$, as shown by arrows, while the V 3*d* peak at E_B = 1.3 eV is shifted to the higher binding energy and a new peak, indicated by an arrow, appears at the low binding energy side of the peak. These changes can be explained by the large *d*-*d* interaction of Ir and Pt with Fe and V and the relative energy position of their *d* states [3], although the surface contribution is not so clear at present. The present study also suggests that the enhancement of the thermoelectric power by the substitution may be caused by the shift of the V 3*d* band and the reduction of the Fe 3*d* states near E_F.

Detailed analysis with a theoretical calculation and further study of the spectral dependence on the amount of the substitution *x* are now in progress.

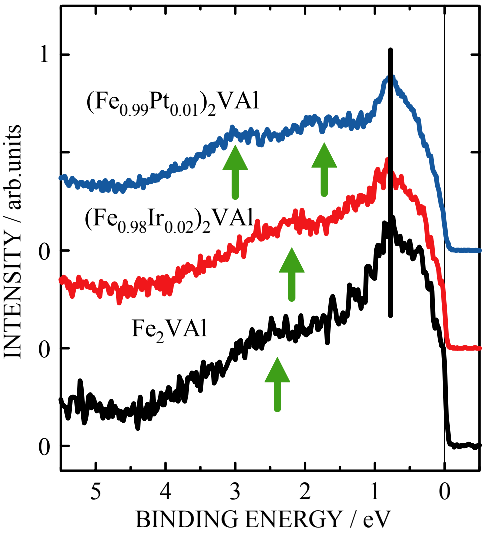

Fig. 1 Partial density of the Fe 3*d* states of $(Fe_{0.98}Ir_{0.02})_2VAl$, $(Fe_{0.99}Pt_{0.01})_2VAl$ and Fe_2VAl.

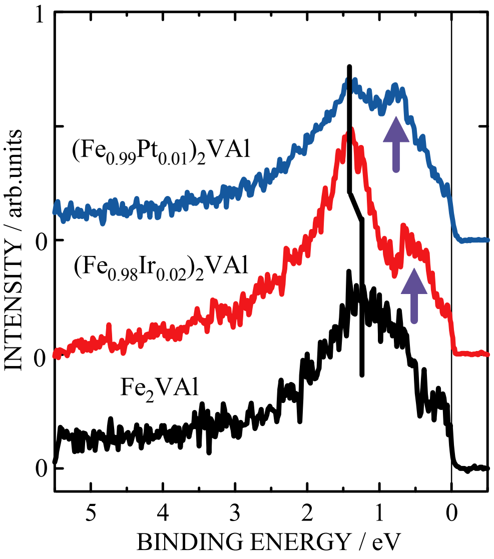

Fig. 2 Partial density of the V 3*d* states of $(Fe_{0.98}Ir_{0.02})_2VAl$, $(Fe_{0.99}Pt_{0.01})_2VAl$ and Fe_2VAl.

[1] Y. Nishino *et al.*, Mater. Sci. Forum **449-452** (2004) 909.
[2] K. Soda *et al.*, Phys. Rev. B, **71** (2005) 245112.
[3] W. A. Harrison, Electronic Structure and The Properties of Solids, (W. H. Freeman & Co., San Francisco, 1989).

BL5U

Electronic Structure of Pd-TM-P (TM = Ni, Cu) Bulk Metallic Glasses

S. Ota[1], T. Suzuki[1], H. Miyazaki[1], K. Soda[1],
T. Wada[2], M. Hasegawa[2], N. Nishiyama[3], T. Ito[4], S. Kimura[4]
[1]*Graduate School of Engineering, Nagoya University, Nagoya 464-8603 Japan*
[2]*Institute for Materials Research, Tohoku University, Sendai 980-8577 Japan*
[3]*R&D Institute of Metals and Composites for Future Industries, Sendai 980-8577 Japan*
[4]*UVSOR, Institute for Molecular Science, Okazaki 444-8585 Japan*

Introduction

Recently, the bulk metallic glasses (BMG's) have received much attention as a new material possessing excellent mechanical, physical and chemical properties. It is important for developing a new functional BMG to understand the mechanism of the BMG's phase stability from the microscopic point of view. The Pd-based BMG has the large glass formation ability and is one of promising structural materials. Here, we have studied the electronic structure of the Pd-based BMG by use of synchrotron radiation photoelectron spectroscopy (PES).

Experimental

The PES experiment was carried out at BL5U under 2 x 10^{-8} Pa at 20 K. Total energy resolution was 40 meV at the excitation photon energy $h\nu$ of 40 eV. BMG specimens were $Pd_{40}Ni_{40}P_{20}$, $Pd_{50}Cu_{30}P_{20}$ and $Pd_{42.5}Cu_{30}Ni_{7.5}P_{20}$, and their clean surfaces were prepared by in situ scraping them with a diamond file.

Result and Discussions

Figure 1 shows valence-band photoelectron spectra of $Pd_{42.5}Cu_{30}Ni_{7.5}P_{20}$ recorded with the various photon energies $h\nu$, which are indicated in the figure. They are normalized by the intensity integrated up to 11 eV. There are three structures found at the binding energies E_B of 2.3, 2.8 and 3.7 eV. The structure at E_B = 2.8 eV becomes prominent at $h\nu$ = 85 eV and those at E_B of 2.3 and 3.7 eV are distinguished at the low excitation photon energy. These are consistent with the reported results [1].

Spectra of $Pd_{50}Cu_{30}P_{20}$ and $Pd_{40}Ni_{40}P_{20}$ are shown in Fig.2. The spectra of $Pd_{50}Cu_{30}P_{20}$ reveals three structures similar to $Pd_{42.5}Cu_{30}Ni_{7.5}P_{20}$, while another band appears at E_B = 0.7 eV for $Pd_{40}Ni_{40}P_{20}$, in particular at the high excitation photon energy.

The calculated photoionization cross section of Pd 4*d* states shows a maximum at $h\nu \sim$ 35 eV and the Cooper minimum at $h\nu \sim$ 110 eV, and those of Ni and Cu 3*d* states change gradually [2]. Thus, the 0.7- and 2.8-eV bands are attributed to the Ni and Cu 3*d* states, respectively. On the other hand, the 2.3-eV band is noticeable at the low photon energy and the 3.7-eV band at $h\nu \sim$ 50 eV. This $h\nu$-dependence suggests that the 2.3- and 3.7-eV bands may be derived from the P 3*p* and Pd 4*d* states, respectively.

These assignments agree well with the results of the soft x-ray emission and hard x-ray PES measurements [3], the latter of which shows another band at $E_B \sim$ 6.3 eV, indicating the P 3*s* states. The Pd 4*d* and P 3*p* states also seems to extend from $E_B \sim$ 4 to 2 eV, which might imply a Pd-P covalent bond as in a structural unit Pd_3P reported for $Pd_{40}Ni_{40}P_{20}$ [4].

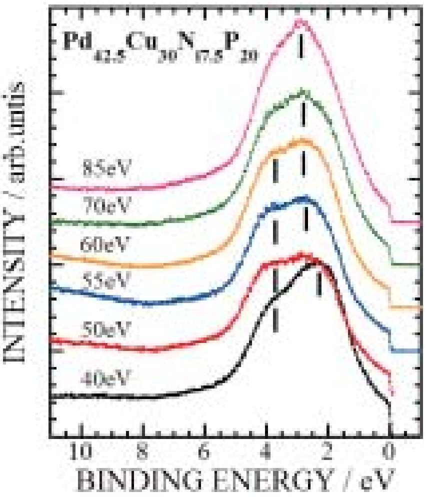

Fig. 1 Valence-band spectra of $Pd_{42.5}Cu_{30}Ni_{7.5}P_{20}$.

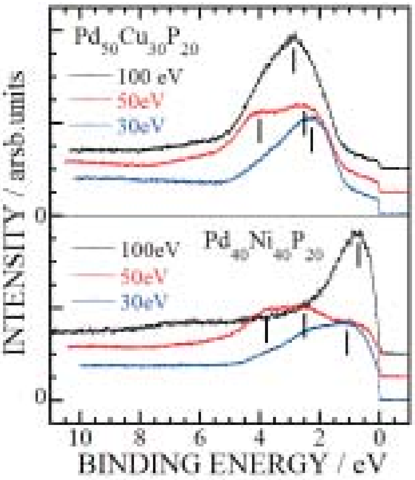

Fig. 2 Valence-band spectra of $Pd_{50}Cu_{30}P_{20}$ and $Pd_{40}Ni_{40}P_{20}$.

[1] S. Hosokawa *et al*., Mat. Trans. **46** (2005) 2803.
[2] J. J. Yeh and I. Lindau, Atomic Data and Nucl. Data Tables **32** (1985) 1.
[3] S. Ota *et al*., *unpublished*.
[4] T. Otomo *et al*., Physica B **213&214** (1995) 529.

BL5U

Electronic Structure of Zr-TM-Al (TM = Ni, Cu) Bulk Metallic Glasses II

T. Suzuki[1], H. Miyazaki[1], S. Ota[1], M. Inukai[1], M. Kato[1], S. Yagi[1], K. Soda[1]
M. Hasegawa[2], T. Takeuchi[3], H. Sato[4], U. Mizutani[5], T. Ito[6], S. Kimura[6]
[1]*Graduate School of Engineering, Nagoya University, Nagoya 464-8603, Japan*
[2]*Institute for Materials Research, Tohoku University, Sendai 980-8577, Japan*
[3]*Ecotopia Science Institute, Nagoya University, Nagoya 464-8603, Japan*
[4]*Aichi University of Education, Kariya 448-8542, Japan*
[5]*Toyota Physical and Chemical Research Institute, Nagakute-cho, Aichi-gun 480-1192, Japan*
[6]*UVSOR, Institute for Molecular Science, Okazaki 444-8585, Japan*

Introduction

Bulk metallic glasses (BMG's) show the large glass formation ability and the physical, chemical and mechanical properties which are superior to crystalline materials [1]. In order to understand the origin of their phase stability from the microscopic point of view, we have systematically studied the electronic structure of the Zr-based BMG's, Zr-TM-Al (TM = Ni, Cu), with use of photoelectron spectroscopy.

Experimental

Photoelectron spectra were recorded under 2×10^{-8} Pa at 25 K at BL5U. Total energy resolution and the origin of the binding energy E_B, *i.e.* the Fermi level E_F, were determined by the Fermi edge of an evaporated Au film.

Specimens were ternary $Zr_{66.7}Cu_{25.8}Al_{7.5}$, $Zr_{50}Cu_{35}Al_{15}$, $Zr_{65}Ni_{25}Al_{10}$, $Zr_{65}Ni_{20}Al_{15}$ and quaternary $Zr_{55}Cu_{35}Ni_5Al_{10}$ BMG's in a size of ϕ2 mm x 3 mm. Clean surfaces for the photoelectron measurement were prepared by *in situ* scraping the specimen with a diamond file.

Results and Discussions

Figure 1 shows typical valence-band spectra recorded at the excitation photon energy $h\nu$ of 40.5 eV. They are normalized by the intensity integrated up to the binding energy E_B of 10 eV. Three bands at $E_B \sim 0.6$, 2.0 and 3.5 eV are ascribed to the Zr 4*d*, Ni 3*d* and Cu 3*d* bands, respectively. For Zr-Cu-Al, the peak of the Zr 4*d* band, indicated by an arrow, is located at the higher binding energy with the supercooled liquid region $\Delta T_x = T_x - T_g$ (T_x: crystallization temperature, T_g: glass transition temperature) increased. This may suggest that the large resistance to the crystallization is induced by the formation of the Zr 4*d* chemical bond. However, Zr-Ni-Al shows almost no change in the Zr 4*d* peak.

The spectrum recorded at $h\nu$ = 21.2 eV shows the intensity reduction near E_F, *i.e.* the existence of a pseudogap [2,3], which implies the decrease in the internal energy of the electron system in the BMG. In Fig.2, the width ΔE_g of the pseudogap, estimated by the spectrum, is plotted as a function of one of the parameters representing the BMG's stability, the ratio T_g/T_l. Here, T_l is the liquidus temperature. As the ratio T_g/T_l increases, indicating that the BMG's can be made easily from the melt, ΔE_g is increased for Zr-Ni-Al but decreased for Zr-Cu-Al. This difference may be related to the fact that the maximum of ΔT_x nearly coincides with the maximum of T_g/T_l in the phase diagram for Zr-Ni-Al, while ΔT_x reveals two local maxima at the compositions of the present Zr-Cu-Al specimens.

Further systematic study is in progress for the Zr-Ni-Al and Zr-Cu-Al BMG's with different compositions.

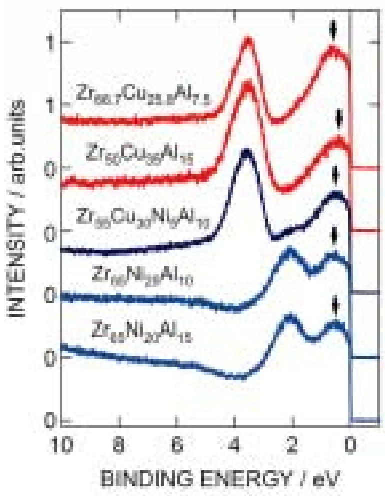

Fig. 1 Valence-band spectra of Zr-TM-Al (TM = Ni, Cu) recorded at h□ = 40.5 eV.

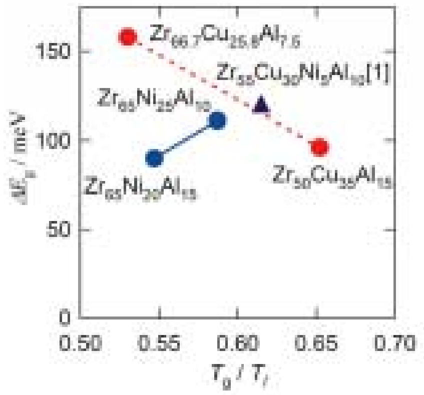

Fig. 2 Relation between the width of the pseudogap □E_g and the ratio T_g/T_l.

[1] M. Telford, Mater. Today **7** (2004) 36.
[2] T. Suzuki *et al.* J. Jpn. Soc. Powder Powder Metallurgy **53** (2006) 107.
[3] K. Soda *et al.*, J. Electron Spectrosc. Relat. Phenom. **144-147** (2005) 585.

BL5U

Pseudogap Formation in the Density of States of Relevant Crystals of the Zr-Ni-Al Bulk Metallic Glass

T. Takeuchi[1,2], S. Nakano[2], T. Kitao[2], H. Kaga[2], T. Ito[3], S. Kimura[3]
[1]*EcoTopia Science, Institute, Nagoya University, Nagoya 464-8603 Japan*
[2]*Department of Crystalline Materials Science, Nagoya University, Nagoya 464-8603 Japan*
[3]*UVSOR Facility, Institute for Molecular Science, Okazaki 444-8585 Japan*

Recent discovery of the amorphous phase capable of forming in bulk-shape has attracted a great deal of interests because of their ability in practical usage, such as mechanical parts of high strength, surface coating materials with high degree of hardness, and soft-magnetic material. These amorphous phases are widely known as the Bulk Metallic Glass (BMG). In order to utilize the BMG's as practical materials, one should gain deep insight into their stabilization mechanism.

The formation of a pseudogap at the Fermi level (E_F) has been discussed as one of the factors to reduce the internal energy of the BMG's. This effect was firstly discussed by Nagel and Tauc [1], and then studied intensively both experimentally [2] and theoretically [3][4]. Nagel and Tauc used a model with a nearly-free-electron gas and employed perturbation theory, in which structure factor $S(q)$ plays an important role in altering eigen values of the conduction electrons. A peak in $S(q)$ at particular q_p produces a pseudogap in the density of states $N(E)$ at $E_{PG} = \hbar^2 q_p^2 / (8m_e)$. If the condition $E_F = E_{PG}$ is satisfied, the population of the conduction electrons around the highest energy is effectively suppressed and the total kinetic energy of electrons is reduced to stabilize the structure.

A resonance between the conduction electrons with the local atomic arrangements would produce the experimentally observed pseudogap in the BMG. One may expect that the relevant crystals possessing the same local atomic arrangements could have the similar pseudogap in their electronic density of states at E_F. Thus it is of great importance to investigate the pseudogap formation not only of the BMG's but also of their relevant crystals to gain insight into its contribution to the BMGs' stability. In this study, therefore, we investigated electronic structure near E_F of the relevant crystals using the high-resolution ultraviolet photoemission spectroscopy.

Figure 1 shows high-resolution UPS spectra near E_F of the Zr_6NiAl_2, ZrNiAl, Zr_5Ni_4Al, and ZrNi. All the intermetallic compounds except for the Zr_5Ni_4Al were already confirmed to possess the local atomic clusters constituting the BMG. [5] Only the structure of Zr_5Ni_4Al has not been determined yet, and therefore, we were not able to know its local atomic arrangements. We employed it in the present UPS measurements because the Zr_5Ni_4Al is stabilized in the vicinity of the composition area of the BMG's and may have the similar local atomic arrangements as those in the BMG's.

Obviously the UPS spectra of all relevant crystals possess a pseudogap of a few hundred meV in width. [6] The energy width of these pseudogaps is comparable with that reported for the Zr-Ni-Cu-Al BMG.[4] Thus it is argued from the present UPS measurements that the characteristic local atomic arrangements could produce the pseudogap formation, and that the resulting pseudogap does effectively reduce the internal energy of the BMG's and their relevant crystals.

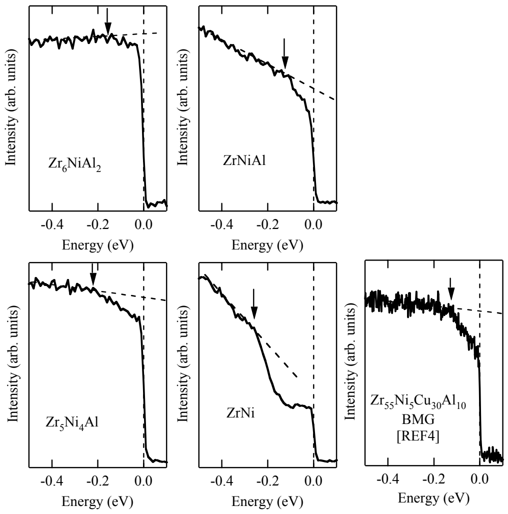

Fig. 1 (a)-(d) High-resolution UPS spectra near E_F of the relevant crystals. UPS spectrum of the corresponding BMG is also shown in the panel (e).

[1] S. R. Nagel, J. Tauc, Phys. Rev. Lett. **35** (1975) 380.
[2] For example, U. Mizutani, K. T. Hartwig, T. B. Massalski, Phys. Rev. Lett. **41** (1978) 661.
[3] For example, D. Nicholson, L. Schwartz, Phys. Rev. Lett. **49** (1982) 1050-1053., J. Hafner, Phys. Rev. B **21** (1980) 406.
[4] K. Soda, K. Shimba, S. Yagi, M. Kato, T. Takeuchi, U. Mizutani, T. Zhang, M. Hasegawa, A. Inoue, T. Ito, S. Kimura, J. Elec. Spec. Relat. Phenom. **144-147** (2005) 585.
[5] T. Takeuchi, S. Nakano, K. Soda, H. Sato, M. Hasegawa, U. Mizutani, K. Itoh, T. Fukunaga, Mat. Trans **46** (2005) 2791.
[6] T. Takeuchi, S. Nakano, K. Soda, H. Sato, M. Hasegawa, U. Mizutani, K. Itoh, T. Fukunaga, submitted to Materials Science and Engineering A (2005) August.

BL5U

Synchrotron-Radiation Photoemission Study of Alkyl-Passivated Si Nanoparticle

A. Tanaka[1, 2, 3], R. Saito[2, 4], T. Kamikake[2], M. Imamura[3]
[1]*Department of Mechanical Engineering, Faculty of Engineering, Kobe University, Kobe 657-8501, Japan*
[2]*Department of Mechanical Engineering, Graduate School of Science and Technology, Kobe University, Kobe 657-8501, Japan*
[3]*Department of Mechanical and Systems Engineering, Graduate School of Science and Technology, Kobe University, Kobe 657-8501, Japan*
[4]*Department of Physics, Graduate School of Science, Tohoku University, Sendai 980-8578, Japan*

Semiconductor nanoparticles are attracting much interest from the viewpoint of both fundamental and device physics, since they show the distinctive physical and chemical properties found in neither bulk nor molecular/atomic systems. Especially, the various Si nanostructures have a great interest, since it has been reported that they show a strong photoluminescence [1]. However, their optical properties depend on the samples in the literatures. In order to understand the intrinsic properties of these Si-based nanostructured materials, it is indispensable to prepare the well- defined samples and investigate their intrinsic electronic structures. In this work, we have carried out a systematic synthesis and the various spectroscopic studies of alkyl-passivated Si nanoparticles in order to characterize their intrinsic optical properties and electronic structures.

The synthesis procedure of alkyl-passivated Si nanoparticles used in this work is described elsewhere [2]. Photoemission measurements of alkyl-passivated Si nanoparticles on the HOPG substrates were performed at BL5U of UVSOR II Facility. The optical spectroscopic measurements of these alkyl-passivated Si nanoparticles were also performed at Kobe University.

The photoluminescence (PL) spectrum of butyl-passivated Si nanoparticle with mean diameter less than 3 nm exhibits a strong emission around 3.7 eV in photon energy. Moreover, the optical extinction spectrum exhibits an absorption edge around 4 eV in photon energy, and the PL excitation (PLE) spectrum also exhibits a distinct resonance around 4 eV in photon energy. In order to investigate the detailed electronic structure of this butyl-passivated Si nanoparticles and clarify the physical origin of its strong photoluminescence, we have performed the valence-band photoemission measurements with photon energy of 184.1 eV as shown in Fig. 1. In Fig. 1, the spectral features around 3.5, 9, and 11 eV in binding energy originate from the Si 3*p*- and 3*s*-derived states, and those around 5.5 and 7 eV in binding energy originate from the C 2*p*-derived states in Si-C σ bonds and butyl passivants. Other features originate from the uncovered region of HOPG substrate. In the inset of Fig. 1, we plot the photoemission spectrum in the vicinity of Fermi level. As shown in the inset of Fig. 1, we have taken into account the contributions from Si nanoparticles and the uncovered region of semimetallic HOPG substrate and have estimated the valence-band maximum of about 2 eV below the Fermi level. Therefore, the energy gap of the present butyl-passivated Si nanoparticles is considered to be about 4 eV, which is modified by the quantum confinement effect. This value corresponds to the absorption edge in extinction spectrum and resonance in PLE spectrum, and therefore, the present photoluminescence is considered to originate from the electron-hole pair recombination between the modified valence-band and conduction-band due to the quantum size effect.

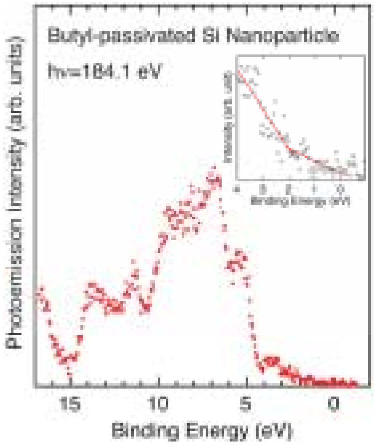

Fig. 1 Valence-band photoemission spectrum of butyl-passivated Si nanoparticle with mean diameter less than 3 nm on the HOPG substrate at room temperature measured with $h\nu$=184.1 eV. The inset shows the photoemission spectrum in the vicinity of Fermi level.

[1] *For example*, L. T. Canham, Appl. Phys. Lett **57** (1990) 1046.
[2] R. Saito, T. Kamikake, A. Tanaka, and H, Yasuda, Trans. Mat. Res. Soc. Jpn. (2006) in press.

BL8B1

Characterization of Lithium in Metal Oxide by an XAFS Method

T. Kurisaki[1], Y. Inoue[1], H. Tsutsumi[1], H. Yamashige[1], H. Wakita[1,2]
[1]Department of Chemistry, Faculty of Science, Fukuoka University, Nanakuma, Jonan-ku, Fukuoka 814-0180, Japan
[2]Advanced Materials Institute, Fukuoka University, Nanakuma, Jonan-ku, Fukuoka 814-0180, Japan

Lithium compounds are generally used in lithium batteries, lithium glasses and other materials. However, there are a few reports about Li-K absorption spectra [1]. Therefore, it is very interesting to investigate the chemical bonding condition of lithium compounds by comparing the experimental and theoretical spectra.

In this work, we applied the X-ray absorption near edge structure (XANES) spectroscopy to lithium compounds. X-ray absorption spectra of near Li K absorption edges were (XAFS) measured at BL8B1 of the UV-SOR in the Institute of Molecular Science, Okazaki [2]. The energy of the UVSOR storage ring was 750MeV and the stored current was 110-230 mA. The absorption was monitored by the total electron yield using a photomultiplier. We employed the discrete variational (DV)-Xα molecular orbital (MO) method to perform calculated spectra, and compared observed spectra with calculated spectra.

The Li *K* XANES spectra for six lithium compounds are shown in Fig. 1. A remarkable change of the spectral patterns was observed for the lithium hardies and other lithium compounds.

The observed and calculated Li K XANES spectra for lithium chloride are shown in Fig. 2. The peaks that appear at approximately 65, 66, 67.5 and 68.5 eV on experimental spectrum are labeled A, B, C and D in the order of increasing energy, respectively. The peaks A and B are estimated to the electron transition (mainly Li 1s to unoccupied mixed orbital consisting of Li 2s, Li2p Cl 3p and Cl 4s).

[1] J. Tsuji, K. Kojima, S. Ikeda, H. Nakamatsu, T. Mukoyama and K. Taniguchi, J. Synchrotron Rad. **8** (2001) 554.
[2] S. Murata, T. Matsukawa, S. Naoe, T. Horigome, O. Matsuodo, and M. Watanabe, Rev. Sci. Instrum. **63** (1992) 1309.

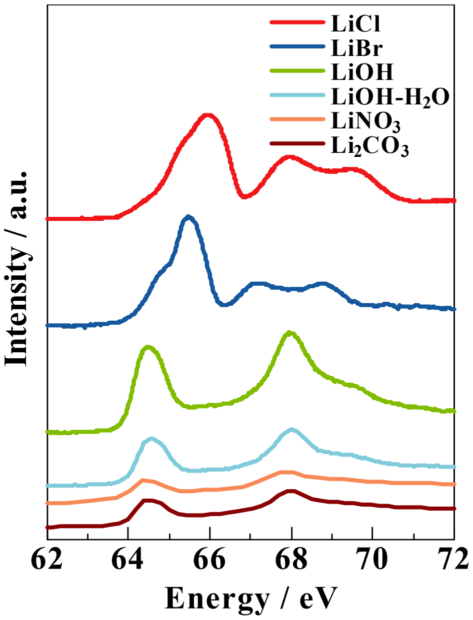

Fig. 1 Li K-edge XANES Spectra of Lithium Compounds.

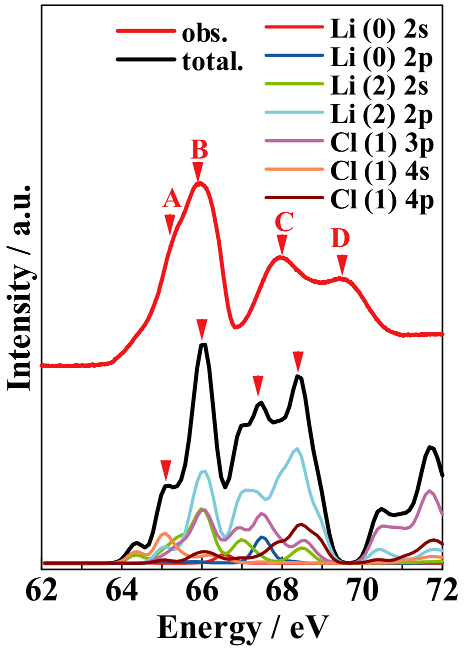

Fig. 2 Observed and Calculated Li K-edge XANES Spectra of Lithium Chloride.

BL8B1

The Study on the Local Structural Change of FIB–CVD DLC by Annealing

A. Saikubo, Y. Kato, K. Kanda, S. Matsui
Graduate School of Science, Laboratory of Advanced Science and Technology for Industry, University of Hyogo, 3–1–2 Kouto, Kamigori–cho, Ako–gun, Hyogo 678–1205, Japan

Introduction

It is known that focused ion beam–chemical vapor deposition (FIB–CVD) is useful to fabricate three dimensional nano structures. The fundamental structure of carbon thin film formed by FIB–CVD has been reported to be diamond like carbon (DLC) from the measurement of Raman spectrum and near edge x–ray absorption fine structure (NEXAFS) of K absorption edge of carbon [1,2]. It was known that the gallium using as an ion source remained in the FIB–CVD DLC. Moreover, it was recognized that the gallium located at the center of the FIB–CVD DLC moved toward the surface of DLC by annealing [3]. In the present work, we investigated the relation between the movement of gallium in the FIB–CVD DLC and the annealing at the temperature of 200°C and 600°C. The NEXAFS spectrum for K edge absorption of carbon was measured with the change of the incident angle of synchrotron radiation x–ray beam in order to obtain the information on the local structure along depth direction.

Experiment

The measurement of NEXAFS spectra for FIB–CVD DLC were performed at BL8B1 of UVSOR in Institute for Molecular Science, which was synchrotron radiation facility with 0.75 MeV electron storage ring. The beamline provides the photons with the desired energy in the energy range of 30–800 eV by using the monochromator with three gratings. The energy range of 275–320 eV, which is the energy range near K edge absorption for carbon, was extracted by using 540 lines/mm laminar grating which had a 15 m radius. The energy resolution was estimated to be approximately 0.5 eV in full width at half maximum. The reading of monochromator was calibrated by making use of the peak of the resonance transition from 1s orbital to π^* orbital observed at 285.3 eV in the spectrum of graphite. The detection of photocurrent coming from the sample was performed in the total electron yield. The intensity of incident x–ray was measured by detecting the photocurrent coming from gold film using as a sample for the measurement of incident x–ray intensity. The absorption intensity was measured by detecting the photocurrent coming from the sample. In this measurement, the NEXAFS spectra of FIB–CVD DLC were measured for the incident angle of the synchrotron radiation x–ray beam from 0° to 60° by 15° step.

Result and Discussion

The NEXAFS spectra of measured at incident angle of 60° for each annealing temperature of 200°C, 400°C and 600°C are shown in Fig. 1. The sharp peak located at 285.3 eV and the broad peak located on the high energy side of ~293 eV is assignable to the resonance transition from 1s orbital to π^* orbital originating from sp^2 sites and σ^* orbital originating from sp^2 and sp^3 sites, respectively. Moreover, in the NEXAFS spectrum of FIB–CVD DLC, the peak which is assignable to the resonance transition from 1s orbital to σ^* orbital originating from carbon bonding to gallium appears at 289.0 eV [2]. For the FIB–CVD DLC annealed at 400°C, the peak intensity observed at 289.0 eV increases remarkably. This indicates that the gallium distributed inside FIB–CVD DLC moves to the vicinity of surface. On the other hand, the peak intensity located at 285.3 eV decreases. Considering these experimental results, the gallium moved from the inside of FIB–CVD DLC to the vicinity of surface is considered to couple to the carbon atom by decoupling the carbon double bonding. For the FIB–CVD DLC annealed at 600°C, it is considered that the carbon double bonding is generated because the gallium in the FIB–CVD DLC departs from that.

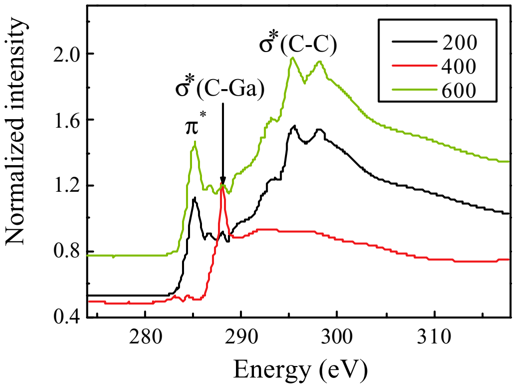

Fig. 1 NEXAFS spectra of FIB–CVD DLC measured at incident angle of 60° for each annealing temperature of 200°C, 400°C and 600°C.

[1] S. Matsui *et al.*, J. Vac. Sci. Tech. B **18** (2000) 3181.
[2] K. Kanda *et al.*, to be published in Rad. Phys. Chem.
[3] J. Fujita *et al.*, Jpn. J. Appl. Phys. **41** (2002) 4423.

BL8B2

Impacts of Intermolecular Scattering on Photoelectron Angular Distribution for Well-Ordered Phthalocyanine Doublelayer

S. Kera[1], T. Hanatani[1], H. Fukagawa[1],
S. Nagamatsu[1], R. Sumii[2], H. Yamane[2], K.K. Okudaira[1], N. Ueno[1]
[1]*Faculty of Engineering, Chiba University, Chiba 263-8522 Japan*
[2]*Graduate School of Science, Nagoya University, Nagoya University, Nagoya 464-8602 Japan*

Angle-resolved ultraviolet photoelectron spectroscopy (ARUPS) has been known as a powerful technique to obtain crucial information on an electronic band structure for various kinds of materials. Moreover, for organic thin films, information on the geometrical structure of the thin films can be also discussed in accordance with a qualitative analysis according to the selection rule with polarization dependence. However, it is believed that the quantitative analysis of the ARUPS intensity to obtain structural information is difficult due to a lack of a standard/simple theoretical model.

The observed take-off angle (θ) dependences of HOMO bands in ARUPS spectra of well-ordered OTi- (or OV-) phthalocyanine (Pc) monolayer and doublelayer were compared with calculated results to clarify the intermolecular effects on the angular distribution.

Experiments

ARUPS spectra were measured at photon incidence angle $\alpha=70^{\circ}$, $h\nu=20\text{-}40$ eV, and $T=295$ K. θ dependence of ARUPS spectra was analyzed using the single-scattering approximation combined with molecular orbital calculation (SS/MO) [1]. The purified Pc molecules were carefully evaporated onto the HOPG. Characterization of the monolayer and doublelayer formation as well as the molecular orientation has been carried out for Pc/graphite systems [2,3]. Coverage of the film can be estimated from the work function as discussed in the previous paper [3].

Results and Discussion

Figure 1(a) shows θ dependence of ARUPS of annealed-OTiPc doublelayer on HOPG. The intensity is normalized to the incidence photon flux and the background is subtracted. The HOMO band is assigned to a single π MO as in CuPc [4] (inset of Fig.1). For the doublelayer, HOMO band is observed as two prominent peaks (labeled A and B). Peak A is related to photoemission from the underlying 1st layer, in which molecules are oriented flat with O-atom protruding vacuum side. Peak B is assigned as photoemission from the 2nd layer, where molecules are oriented reversely. Figure 1(b) shows the comparison between observed and calculated θ dependences of the HOMO-band intensities. In this fitting, the observed θ pattern of the peak B is well reproduced by the SS/MO calculation. However, peak A shows marked disagreement with the SS/MO. The disagreement suggests there is a strong scattering effect of photoelectron from the underlying layer, since for the oriented monolayer the HOMO-band angular distribution is well reproduced by the calculation as for peak B in Fig.1(b). Now we are trying to get a calculated pattern of peak A by taking into account the intermolecular effects between 1st and 2nd layer in various molecular arrangement and orientations.

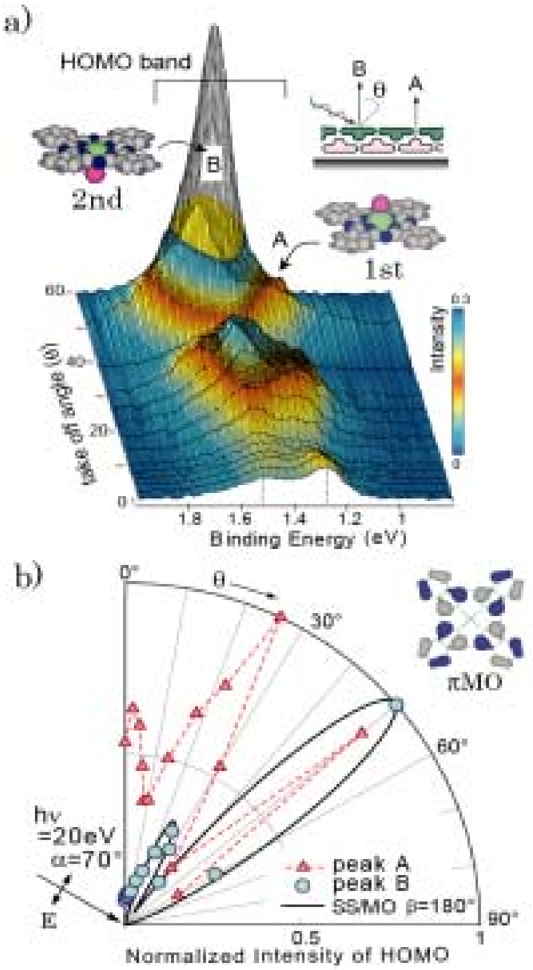

Fig. 1 (a) θ dependence of ARUPS of 2-ML-OTiPc on HOPG. (b) Comparison with the observed and calculated θ patterns of the HOMO-band A and B. β is tilt angle of a molecular plane.

[1] N. Ueno *et al.*, J. Chem. Phys. **107** (1997) 2079.
[2] H. Yamane *et al.*, J. Elec. Spec. Relat. Phenom. **137-140** (2004) 223.
[3] H. Fukagawa *et al.*, Phys. Rev. B **73** (2006) 14302(R).
[4] S. Kera *et al.*, Chem. Phys. Lett. **364** (2002) 93.

BL8B2

Electronic Structure of $LiNi_{1-x}M_xO_2$ Mixed Oxides (II)

T. Miyazaki[1], Y. Komatsu[1], D. Yoshimura[2], R. Sumii[2], T. Yamaguchi[1]
[1]Department of Applied Chemistry, Faculty of Engneering, Ehime University, Matsuyama 790-8577 Japan
[2]Research Center for Materials Science, Nagoya University, Nagoya 464-8602, Japan

Lithium and nickel mixed oxide ($LiNiO_2$) has a two-dimensional triangular lattice in lamellar structure in which lithium and nickel are alternately and regularly arranged to oxygen layers. The surface lattice oxygen progresses as a reduction/oxidation (redox) catalyst for the oxidative coupling of methane (OCM). The top valence band structures usually determine the electronic properties and surface catalysis of the materials. Therefore, it should be carefully investigated that the electronic structure led to intense experimental approach to the Ni3d and O2p states. Ultraviolet photoelectron spectroscopy (UPS) was surface sensitive technique and effective for the top valence band structures which determined the activities of the selective oxidation. In this study the comparison of $LiNiO_2$ and $LiNi_{1-x}M_xO_2$ (M = Mn, Ti, Al, Fe, Co, Te; $0 \leq x < 0.2$) which replaced the part of Ni with other transition metal element. Also, Ar^+ bombardment was done in order to imitate dynamic redox surface and remove the contamination such as carbonates.

$LiNi_{1-x}M_xO_2$ (M = Mn, Ti, Al, Fe, Co, Te; $0 \leq x < 0.2$) were prepared from $LiNO_3$, $Ni(OH)_2$ and $M(NO_3)_n$ by the solid-state reaction. UPS spectra were measured for the incident photon energy ($h\upsilon$=30~75eV) using photoelectron spectroscopy equipment (BL8B2) of UVSOR facility in IMS. The Fermi energy of the UPS system was determined by using the Fermi edge of gold films. The total resolution was found to be about 0.3eV in the photon energy region of $30 \leq h\upsilon \leq 75$eV by measuring the Fermi edge of gold. A sample surface processing by Ar^+ bombardment or heating of infrared radiation was carried out as a pretreatment.

Figure 1 exemplified the UPS spectra of $LiNiO_2$, $LiNi_{0.9}Mn_{0.1}O_2$ and $LiNi_{0.9}Ti_{0.1}O_2$ with reference to E_F as the zero of the energy scale and the Gaussian curve fitted data. The overall features in the spectra of NiO were similar as far as the peak positions were concerned. There were at least five structures on the top valence region. These curve made up from five individual bands consistently matched with the observed spectra. The peak position of $LiNiO_2$, denoted by the characters A-E, appears in the binding energy which left at E_b = 1.6eV, 2.8eV, 5.1eV, 7.0eV and 9.8eV from the Fermi level, respectively. The band structures at E_b = 1.6 and 2.8eV should be contribution from these t_{2g} and e_g states, respectively. The bands of C and D at E_b = 5.1 and 7.0 eV should be contributed to O2p bands. The C-band of $LiNi_{0.9}Mn_{0.1}O_2$ occupied about 80% for area intensity of total O2p bands, and it was almost equivalent to 79% in case of $LiNiO_2$. The C-band area intensity of of $LiNi_{0.9}Ti_{0.1}O_2$ meanwhile increased to 87%. The C_2-selectivity was $LiNi_{0.9}Mn_{0.1}O_2$ (61%) $\leq$ $LiNiO_2$ (63%) < $LiNi_{0.9}Ti_{0.1}O_2$ (70%), and it was possible to conclude a direct relation in electronic structures of the metal oxide surface and the selective oxidation.

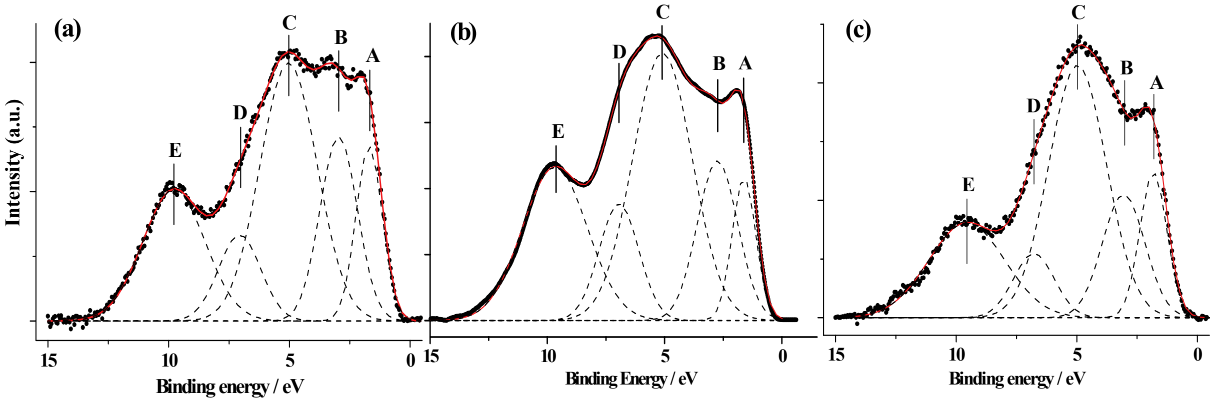

Fig.1. UPS spectra and the Gaussian fitted curves of a) $LiNi_{0.9}Mn_{0.1}O_2$, b) $LiNiO_2$ and c) $LiNi_{0.9}Ti_{0.1}O_2$.

BL8B2

Photoemission Spectroscopy Study of Bathocuproine Insertion Effect to Au/Zn-phthalocyanine Interface

S. Tanaka[1,2], Y. Yoshida[3], M. Nonomura[3], K. Yoshino[2], I. Hiromitsu[3]

[1] *Center of Integrated Research in Science, Shimane University, Matsue 690-8504 Japan*
[2] *Research Project Promotion Institute, Shimane University, Matsue 690-8504 Japan*
[3] *Faculty of Science and Engineering, Shimane University, Matsue 690-8504 Japan*

An insertion of a thin layer in the organic -material/metal-electrode interfaces is a well known technique to improve the performance of organic semiconductor devices. [1,2] We have recently observed that the hole transport from Au to Zn-phthalocyanine (ZnPc) is enhanced substantially under the forward bias condition by an insertion of a thin bathocpuroine (BCP) layer to the Au/ZnPc interface. [3] In this study, we measured the electronic energy level structures of Au/ZnPc and Au/BCP interfaces by photoemission spectroscopy in order to understand the insertion effect of a thin BCP layer.

Experimental

ZnPc and BCP were purchased from Aldrich, and were purified by vacuum sublimation. All the photoemission measurements were carried out in ultrahigh-vacuum at room temperature. The base pressure of the main chamber and the preparation chamber were about 2×10^{-8} Pa and about 2×10^{-7} Pa, respectively. Evaporation of organic molecules was performed using a glass-cell evaporator after careful outgassing, keeping the pressure of the preparation chamber at less than 4×10^{-6} Pa. The substrates were Si (100) wafers precoated with Au *in situ*. The deposition rates of the organic molecules were monitored with a quartz microbalance, using the bulk densities of 1.55 g/cm^3 for ZnPc, 1.3 g/cm^3 for BCP.

Results and Discussion

Figure 1 shows photoemission spectra of ZnPc (5nm) on Au and BCP (5nm) on Au around the Fermi level. The photoemission spectrum of Au was also shown for comparison. The thickness of 5nm was chosen for making the same structural condition using in ref. 3.

In the ZnPc spectrum, the signal from Au substrate still appeared. The 5nm thickness of ZnPc was not enough for a complete covering of the Au substrate or Au atoms were diffused from the substrate to the ZnPc layer. On the other hand, in the BCP spectrum, no signal of Au was shown. The Au substrate was completely covered by the 5nm BCP layer. This result suggests that the interaction between Au and ZnPc is more active than that between Au and BCP.

The edge energy of the highest occupied molecular orbital of ZnPc and BCP was observed at about 1.0 eV and 3.0 eV respectively from the Fermi edge of Au. This result suggests that the barrier height of the hole injection from Au to BCP is larger than that from Au to ZnPc. These result seem to be inconsistent with the increase of the dark current density, J_{dark}, from Au by the insertion of BCP layer: the J_{dark} of the Au/BCP/ZnPc/In/Al cell was larger than that of the Au/ZnPc/In/Al cell.[3] If the barrier height of the hole injection at the Au/ZnPc interface is the only factor that determines the J_{dark} of the systems (the majority carrier is the hole in this case because of the ZnPc property), the Au/BCP/ZnPc/In/Al cell should show lower J_{dark} than the Au/ZnPc/In/Al cell.

These facts can probably be explained as follows: the effect of insertion of the BCP layer is not to lower the barrier height for the hole injection at Au/ZnPc interface but to prevent an interaction between Au and ZnPc. The interaction of Au and ZnPc may increase the concentration of trapped states at the interface region of the Au/ZnPc and decrease the conductivity.

The present study suggests that the control of the interaction between an organic material and an electrode, as well as the injection barrier height from the electrode to the organic materials, is important for the control of the operation of the organic semiconductor devices.

[1] L. S. Hung, C. W. Tang, M. G. Mason, Appl. Phys. Lett., **70** (1997) 1233.
[2] F. Li, H. Tang, J. Andregg, J. Shinar, Appl. Phys. Lett., **73** (1998) 2763.
[3] M. Nonomura, I. Hirmoitsu, S. Tanaka, Appl. Phys. Lett., **88** (2006) 042111.

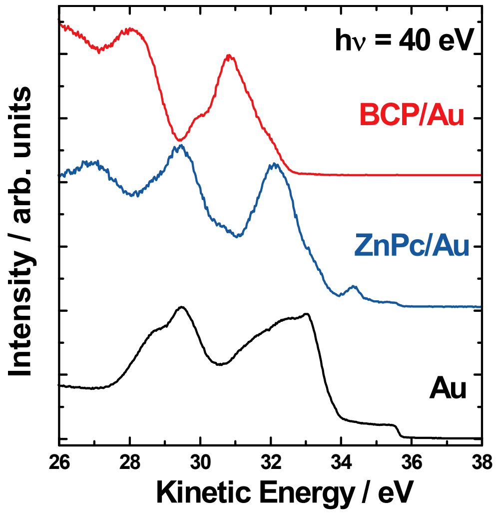

Fig. 1 Photoemission spectra of Au, ZnPc (5nm) on Au and BCP (5nm) on Au around the Fermi level.

BL8B2

Energy-Band Dispersion in Highly Ordered Thin Films of Pentacene Prepared on Cu(110)

H. Yamane [1], D. Yoshimura [2], R. Sumii [3], K. Kanai [1], Y. Ouchi [1], K. Seki [1,3]
[1] *Department of Chemistry, Nagoya University, Nagoya 464-8602, Japan*
[2] *SAGA light source, Kyushu Synchrotron Light Research Center, Saga 841-0005, Japan*
[3] *Research Center for Materials Science, Nagoya University, Nagoya 464-8602, Japan*

Introduction

Pentacene, a high hole mobility material, is one of the important organic semiconductors in realizing efficient organic devices, in particular organic field-effect transistors. Therefore, the film growth, the film structure, and the electronic structure of pentacene thin films have been studied by many research groups. Recent experimental data reflecting the progress in experimental techniques such as high energy resolution and the preparation of high quality samples point towards the necessity of using polaronic concepts to rationalize the electrical properties of organic-semiconductor films. The charge-vibration coupling and the energy-band dispersion of the highest occupied molecular orbital (HOMO) plays crucial roles in the hopping- and band-like hole transport in organic solids, respectively. In this work, in order to study the hole transport mechanism in pentacene thin films, angle-resolved ultraviolet photoemission spectroscopy (ARUPS) experiments were performed for highly ordered thin films of pentacene prepared on Cu(110).

Experiments

The take-off angle (θ) dependence of ARUPS spectra were measured at the photon energy ($h\nu$) of 20 and 30 eV, the photon incidence angle (α) of 60°, and the specimen temperature of 300 K.

The purified pentacene was carefully evaporated onto a clean Cu(110) surface heated at about 450 K. This enabled the preparation of the highly ordered monolayer.[1]

Results and Discussion

According to ref.[1], pentacene molecules deposited on Cu(110) in the monolayer regime form a highly ordered structure with a planar adsorption geometry, where the molecular long axis is parallel to the [1-10] substrate direction. We confirmed these by measuring the ARUPS spectra as a function of the azimuthal angle, using symmetry selection rule (not shown). For thick multilayers, subsequent growth proceeds with an upright molecular orientation and leads to the formation of crystalline films which are epitaxially oriented with respect to the substrate. [1]

Figure 1 shows the θ dependence of the ARUPS spectra of the pentacene monolayer on Cu(110), where the substrate electronic states are colored by yellow. The binding-energy (E_B) position is measured from the Fermi level of the substrate (E_F^{sub}) and the intensity is normalized to the incident photon flux. The feature near E_F^{sub} colored by blue can be ascribed to the charge-transfer (CT) state due to the molecule-substrate chemical interaction, which induces the large vacuum-level shift of about -1.0 eV (not shown). The HOMO appears at E_B of 0.9 eV at $\theta = 43°$. With increasing θ, the HOMO shifts to the high-E_B side, and turns back at $\theta = 45°$. Also, at $\theta = 50°$ and 58°, similar turn back of the peak is seen. The total shift of the HOMO is about 0.25 eV. Such a cyclic shift can also be seen for the HOMO-1. We can attribute these shifts to the energy-band dispersion of the pentacene monolayer along the [1-10] substrate direction. Analyses using the tight-binding model gave a lattice constant of about 1.6 nm, which agrees well with the lateral lattice constant of the pentacene monolayer formed on Cu(110) [1], with the estimated transfer integral of 63 meV for the HOMO band and the effective mass of the HOMO hole of 0.24 m_0.

By using the density-functional-theory method, the transfer integral for the σ-σ interaction in the pristine pentacene monolayer is calculated to be a few meV, which is much smaller than that of the experimental value of 63 meV. The observed energy-band dispersion may originate from the intermolecular interaction via the substrate due to the hybridization of the molecular orbital and the substrate.

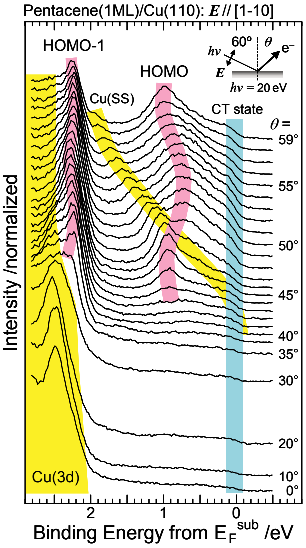

Fig. 1 ARUPS spectra of the pentacene monolayer on Cu(110). The inset shows the measurement geometry.

[1] S. Söhnchen *et al.*, J. Chem. Phys. **121** (2004) 525.

BL4B

Effect of Surface Chemisorption on the Spin Reorientation Transition in Magnetic Ultrathin Fe Film on Ag(001)

X.D. Ma[1], T. Nakagawa [1,2], T. Yokoyama [1,2]

[1]*Department of Structural Molecular Science, The Graduate University for Advanced Studies (Sokendai), Okazaki, Aichi 444-8585, Japan*

[2]*Department of Molecular Structure, Institute for Molecular Science (IMS), Okazaki, Aichi 444-8585, Japan*

We have investigated the effect of surface chemsiorption of O_2, NO and H_2 on the spin reorientation transitions in magnetic ultrathin Fe films on Ag(001) by means of the polar and longitudinal magneto-optical Kerr effect (MOKE) and X-ray magnetic circular dichroism (XMCD) measurements. Fe was deposited on clean and ordered Ag(001) in ultrahigh vacuum at ~100 K, and the surfaces were dosed with gases at the same temperature. Fe $L_{\mathrm{III,II}}$-edge XMCD was taken at BL4B.

Figure 1 shows the remanence magnetization and coercive field of Fe/Ag(001) along the surface normal before and after each gas adsorption, examined by polar MOKE. It is found that adsorption of O_2 and NO induces the shift of the critical thickness for the spin reorientation transitions to a thinner side from 3.5 ML to 2.2-2.5 ML, together with the suppression of the remanent magnetization and the coercive field of the Fe film. This implies destabilization of the perpendicular magnetic anisotropy. On the other hand, H_2 adsorption is found not to change the magnetic anisotropy as shown in Fig. 1, though the enhancement of the coercive field is observed.

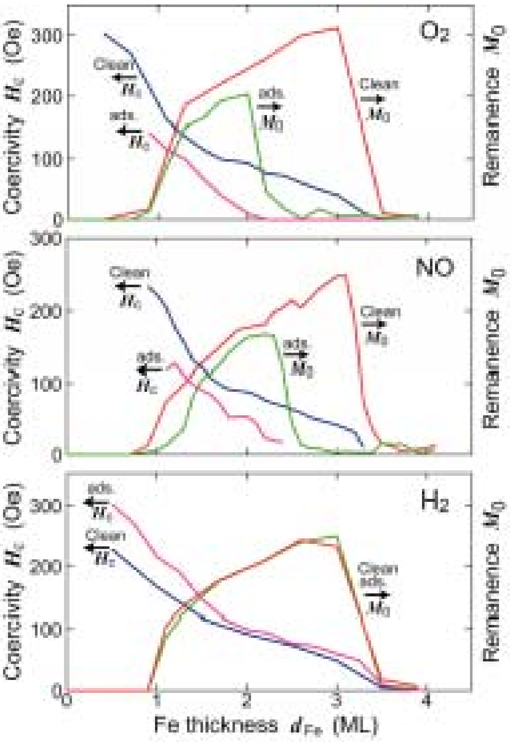

Fig. 1 Remanent magnetization (right axis) and coercive field (left) of 1.2 ML Fe films on Ag(001) before and after gas adsorption, examined by polar MOKE at 100 K.

The sum-rule analysis of Fe $L_{\mathrm{III,II}}$-edge XMCD shown in Fig. 2 reveals that although both the spin and orbital magnetic moments along the surface normal are noticeably reduced upon O_2 and NO adsorption, the reduction of the orbital magnetic moments are more significant. This indicates that the destabilization of the perpendicular magnetic anisotropy upon chemisorption of O_2 and NO originates from the change of the spin-orbit interaction at the surface.

The present finding that perpendicular magnetic anisotropy is destabilized by O and NO adsorption is in good contrast to the other systems of CO,NO/Co/Pd(111) and CO,NO,H,O/Ni/Cu(001), where perpendicular magnetic anisotropy is stabilized. These differences can be ascribed to different adsorption fashions; on Fe/Ag(001) the O and NO adsorbates are rather embedded on the topmost Fe layer, while on Co/Pd(111) and Ni/Cu(001) the adsorbates are located above the topmost metal layers. The latter case cannot induce a noticeable reduction of the out-of-plane orbital magnetic moments.

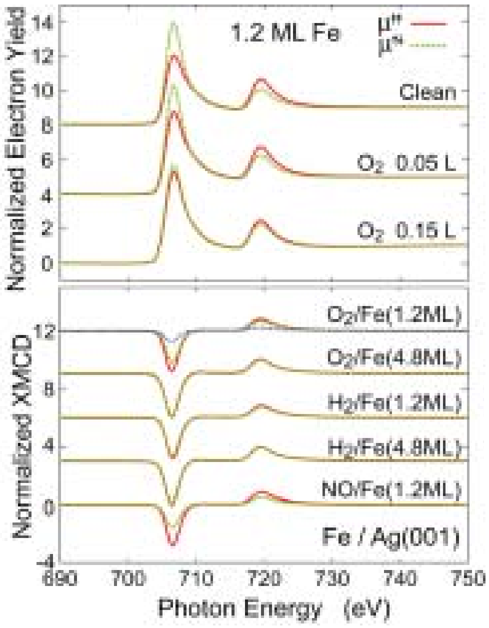

Fig. 2 Fe $L_{\mathrm{III,II}}$-edge x-ray absorption and XMCD spectra at 100 K.

BL4B

X-Ray Magnetic Circular Dichroism of Co Nanowires Grown on Cu(110)-(2×3)N Surface

X.D. Ma[1], T. Nakagawa [1,2], T. Yokoyama[1,2]
[1]Department of Structural Molecular Science, The Graduate University for Advanced Studies (Sokendai), Okazaki, Aichi 444-8585, Japan
[2]Department of Molecular Structure, Institute for Molecular Science (IMS), Okazaki, Aichi 444-8585, Japan

Magnetic properties of nanowires are hot subjects in recent years. There have been reported several nanowire systems grown on well-defined single crystal surfaces. Due to their easy aggregation, however, most of them can only be obtained with very small amount of deposited magnetic metal atoms and the thickness of the nanowires along the surface normal direction is usually 1 atomic layer. York *et al.* [1] discovered Co nanowires grown on Cu(110)-(2×3)N that are well separated with each other up to as much as ~2 ML (monolayer) in a nominal coverage. This implies that both the vertical thickness and the lateral width of the nanowire should be 3-4 atomic layers. In the present work, we have tried to detect the magnetization of the Co nanowires by means of the x-ray magnetic circular dichroism (XMCD) technique using a simple electromagnet.

The experiments were performed using an ultrahigh vacuum chamber with a base pressure of ~1×10^{-10} Torr). A Cu(110) single crystal was cleaned by repeated cycles of Ar$^+$ sputtering and annealing at ~900 K. The (2×3)N surface was prepared by N$^+$ sputtering (500 V) and subsequent annealing at ~600 K. A very clear (2×3) LEED (low energy electron diffraction) was observed. Co was deposited on the Cu(110)-(2×3)N surface with a commercial evaporator. The nominal thicknesses prepared were 1.5 and 2.0 ML. The Co nanowire is grown along the [1-10] direction. For comparison, Co on clean Cu(110) was also prepared. On clean Cu(110), rectangular islands are known to be formed with a longer side aligned along the [1-10] direction.

We have at first investigated the magneto-optical Kerr effect (MOKE) of Co on clean and N-terminated Cu(110) surfaces. Although the experiment is still in progress, we have obtained some preliminary information. A blue plot in Fig. 1 is the hysteresis loop of 2 ML Co on clean Cu(110) with the magnetic field parallel to [1-10], a longer side of the rectangular island. On clean Cu(110), the magnetic easy axis always seems be [1-10] at least up to ~10 ML. On the N-terminated surface, it was found that above 3 ML the easy axis is [001] perpendicular to the nanowire axis, as seen in the red plot in Fig. 1. This may indicate that coalescence of the nanowires occurs at 3 ML. We have not yet obtained good data for 2 ML due to a little too high temperature of 100 K, but suppose that the 2 ML.

The Co *L*-edge XMCD spectra were taken with the total electron yield (measurement of drain current from the sample) with the circular polarization factor of ~0.70 under the flipped magnetic field of ±1500 Oe at ~100 K. The magnetic field was parallel to the x-ray propagation direction, which is perpendicular to the [001] axis. The angle between the nanowire axis and the x-ray helicity is 30° (grazing x-ray incidence). Figure 2 shows the XMCD results. The 2 ML Co on clean Cu(110) exhibits large XMCD signals compared to the reference, in good accordance with the MOKE results in Fig. 1. The Co nanowires of 1.5 and 2 ML Co on N-terminated Cu(110) also show some XMCD signals even at 100 K. The XMCD measurements using a new superconducting magnet and at lower temperature as ~10 K will be conducted in a next beamtime.

[1] S.M York *et al.*, Phy. Rev. B**64** (2001) 033411.

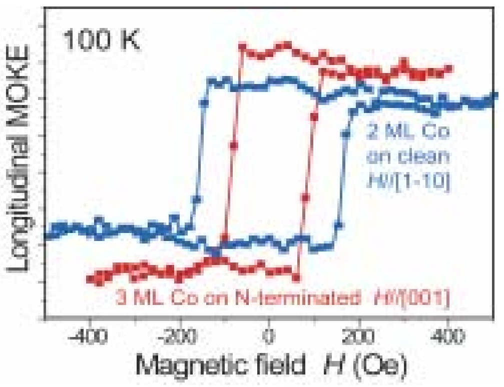

Fig. 1 Longitudinal MOKE of Co on clean and N-terminated Cu(110).

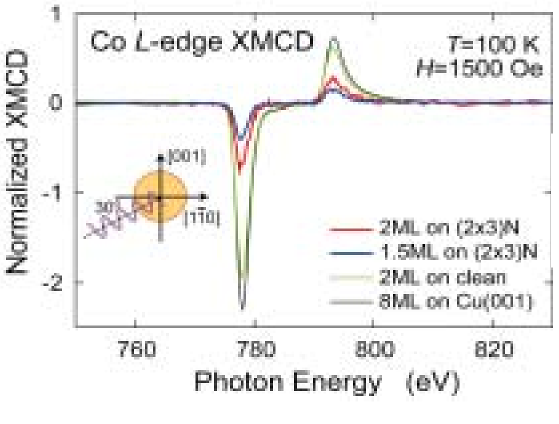

Fig. 2 Co $L_{III,II}$-edge XMCD.

BL4B

X-Ray Magnetic Circular Dichroism Study on Fe/Ni(6 ML)/Cu(001)

T. Nakagawa, T. Yokoyama

Department of Molecular Structure, Institute for Molecular Science, Okazaki 444-8585 Japan

Introduction

Magnetism in thin films sometimes much differ from that in bulk because of different structure, the presense of surface and interface. Especially Fe shows variety of magnetism in thin films. For example, Fe on Cu(001) has a fcc-like structure and shows a much reduced magnetic moments, which comes from a partial antiferromagnetic coupling in the films or a formation of spin-density waves. Fe on Ni(7 ML)/Cu(001) also shows a unique magnetism [1], where the total magnetic moment is not proportional to the thickness.

Experiment

The experiment was performed in a ultra-high vacumm chamber at BL4B. The magnetic hysteresis curves were taken by magneto-optical Kerr effect (MOKE), and the x-ray magnetic circular dichroism (XMCD) was taken at BL4B. As shown in Fig. 1, we measured the magnetic moments not only parallel, but also perpendicular to the magnetic field applied using cross-configured magnets or rotating the asimuthal angle of the sample in remanence magnetization.

Result

Figure 2 shows MOKE intensity in an in-plane magnetized Fe/Ni(6 ML)/Cu(001), which is proportional to the magnetization. Note that the contribution of Ni to the MOKE intensity is negligible and that Fe magnetization dominates the MOKE intensity. The MOKE intensity increase around 2-3 ML with the increase of the Fe thickness. However above 3 ML the MOKE intensity decreases with the increase of the Fe thickness. This broken of the magnetization shows that the Fe/Ni/Cu(001) is not magnetized in a single direction, indicating that the Fe has non-colinear coupling such as a antiferroganetic one. However the antiferromagnetic coupling is ruled out since the magnetic moment does not goes to zero every two layers.

We performed XMCD measurement to evaluate the direction and magnitude of the magnetism. Figure 3(a) shows Fe XMCD spectra on 3 ML Fe/Ni(6 ML)/Cu(001). This shows the Fe magnetization is completely parallel to the magnetic field, in agreement with the MOKE result. Figure 3(b) shows Fe XMCD spectra on 7 ML Fe/Ni(6 ML)/Cu(001). The Fe XMCD is observed in the both directions perpendicular to and parallel to the magnetic field. This shows that the coupling in Fe is 4th-order. Such a coupling comes from a coupling between adjacent interlayers or microscopic domains.

We will adapt a microscopic method such as photoelectron emission microscope to distinguish between the interlayer coupling and the microscopic domain coupling.

[1] X. Liu *et al.*, Phys. Rev. B**64** (2001) 104408, K. Amemiya *et al.*, Phys. Rev. B**70** (2004) 195405.

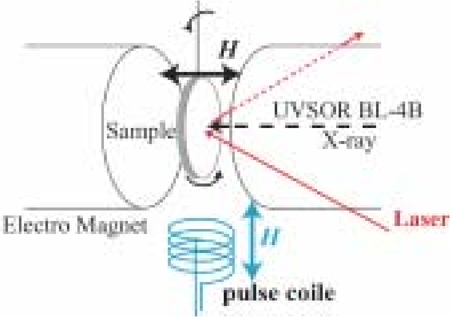

Fig. 1 Experimental setup at BL4B.

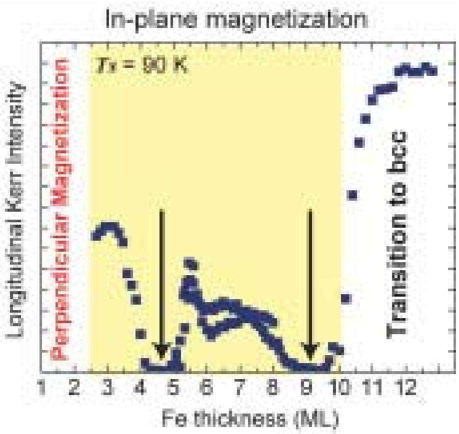

Fig. 2 Longitudinal MOKE intensity on a wedge shaped Fe(1-13 ML)/Ni(6 ML)/Cu(001) as a function of Fe thickness.

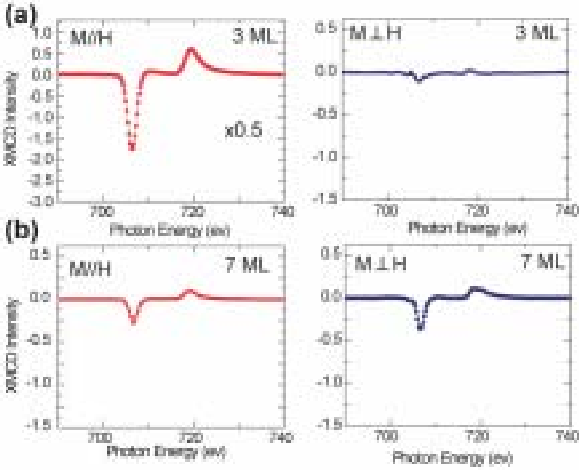

Fig. 3 Fe *L* edge XMCD spectra parallel and perpendicular to the magnetic field. (a) Fe(3 ML)/Ni(6ML)/Cu(001).(b)Fe(7ML)/Ni(6ML)/Cu(001).

BL5U(FEL)

Absolute Asymmetric Synthesis of *rac*-Leucine by Circularly Polarized Radiation from UVSOR II-FEL

H. Nishino[1], M. Hosaka[2], M. Katoh[2], Y. Inoue[1]
[1]Entropy Control Project, ICORP, JST, Toyonaka 560-0085, Japan
[2]UVSOR Facility, Institute for Molecular Science, Okazaki 444-8585, Japan

The origin of homochirality in biomolecules has been one of the most intriguing issues with severe scientific debates since the early last century. Many hypotheses have been proposed to explain the mechanisms and conditions that led to the terrestrial homochirality. Of these hypotheses, the enantioselective photodecomposition of racemic amino acids by circularly polarized light (CPL) or elliptically polarized light, radiated from a neutron star or a star-forming region, in outer space is believed to be the most plausible mechanisms. Such an asymmetric photoreaction is called "absolute asymmetric synthesis (AAS)," has been demonstrated to occur with a variety of compounds [1]. Recently, it was reported that a variety of amino acids found in Murchison and Lake Murray Meteorites are consistently enantiomerically enriched in the L-form [2]. Furthermore, it was found that the infrared radiation from the star-forming region is highly polarized indeed, reinforcing the idea that the terrestrial homochirality was triggered by the extraterrestrial photochemical event, i.e. AAS [2]

The principle of AAS is that asymmetric photoreactions are brought about through the preferential excitation and subsequent reaction of one enantiomer over the other, via either left- or right-handed CPL (*l*- and *r*-CPL) irradiation. The factor that determines the degree of preferential excitation is called the anisotropy (*g*) factor, and is defined as the relative difference in molar extinction coefficient (ε) of each enantiomer towards *l*- and *r*-CPL at a given wavelength: $g = (\varepsilon_\lambda - \varepsilon_\rho)/\varepsilon = \Delta\varepsilon/\varepsilon$, where $\varepsilon = (\varepsilon_\lambda + \varepsilon_\rho)/2$ and $0 \le g < 2$ [1].

The determination of accurate *g* factor of the target compound is essential in examining the efficiency of AAS. L-Amino acids exhibit a positive circular dichroism (CD) peak around 210 nm and an extremely weak negative CD peak around 250 nm in acidic solutions.[3] The nature of the both CD bands has long been discussed, but the assignment of the CD band around 255 nm has not yet been done. The □ at the corresponding wavelength is extreme small, and hence the *g* factor has not been determined for this tiny negative CD peak. Also, the irradiation by CPL at this wavelength has not been examined. However, if the *g* factor of this negative CD peak is appreciable and CPL irradiation leads to photoreaction, the amino acid obtained at this wavelength is opposite in sign from that obtained upon irradiation at shorter wavelengths (e.g. 215 nm). In this aspect, it should be emphasized that the Kuhn-Condon's zero-sum rule, which claims that the CD bands of a chiral molecule alternate in sign and sum to zero over the whole spectrum [2], is not applicable to the photoreaction of amino acids in water or ice, as the H_2O absorbs the radiation shorter than ca. 200 nm.

The negative CD peak around 254 nm in acidic solutions [4,5] has been assigned by some researcher to the n,π^* transition of the carboxylic chromophore without considering the contribution of minor conformers. On the other hand, some believe that the negative CD around 254 nm originates from the n,π^* transition of the less stable rotamer(s)[3]. Yet other idea is that the negative CD around 254 nm arises from the coupling of heteroatom's non-bonding orbital with the chromophoric transition of the carbonyl group [6]. Thus, there still exist the controversial ideas and interpretations about the negative CD bands of L-amino acids at longer wavelengths.

In this research, we will examine the *rac*-Leu samples irradiated at several wavelengths by using the tunable FEL, the full-width at half-maximum (fwhm) of which is extreme narrow and best suitable for the investigation of the present case, where the precise wavelength tuning is essential to exploit the optimum *g* factor for executing the AAS of amino acids. We are now trying to optimize the chemical and physical conditions for irradiation of amino acids by intense FEL.

[1] H. Rau, in Chiral Photochemistry **11** (Eds.: Y. Inoue, V. Ramamurthy), Marcel Dekker, New York, (2004) 1.
[2] J. Alain, C. Corinne, Origins Life Evol. Biosphere **32** (2002) 129.
[3] R. Håkansson, in Chem. Acid Deriv. **2** (Ed.: S. Patai), Wiley, Chichester, UK. (1992) Issue Pt. 1.
[4] C. Toniolo, J. Phys. Chem. **74** (1970) 1390.
[5] M. Legrand, R. Viennet, Bull. Soc. Chim. Fr. (1965) 679.
[6] J. Cymerman Craig, J. Pereira, Tetrahedron **26** (1970) 3457.

Fabrication of Compound Semiconductor Array Using PTFE Templates

Q.X. Guo, Y. Kume, Y. Mitsuishi, T. Tanaka, M. Nishio, H. Ogawa
Department of Electrical and Electronic Engineering, Saga University, Saga 840-8502, Japan

Zinc oxide (ZnO), one of the II-VI compound semiconductors with a wurtzite crystalline structure, is technologically an important material due to its wide range of optical and electrical properties. It has been investigated as functional material for electronic and optoelectronic devices such as transparent conductors, varistors, solar cell windows, and bulk acoustic wave devices. Recently, ZnO has attracted tremendous attention for applications in blue and UV light-emitting diodes, which can be an alternative to those based on III-nitride due to its large exciton binding energy and abundant mineral sources of Zn. Demonstration of ultraviolet lasing from vertically aligned arrays of ZnO rods initiated a great interest in fabrication of ZnO and their applications in various optoelectronic devices. Here, we report a success in achieving periodic arrays of ZnO using polytetrafluoroethylene (PTFE) temples which was patterned by synchrotron radiation (SR) light irradiation.

The irradiation experiments were carried at a beam line, BL8A, in UVSOR facility at Institute for Molecular Science. The critical energy of the SR from the bending magnet field of the 0.75 GeV electron storage ring is 425 eV. The SR light was irradiated perpendicularly to the surface of commercially available PTFE substrates through Ni mesh masks. The proximity distance between the Ni mesh masks and the substrates surface is zero, i.e. the masks were placed on the PTFE substrates directly. ZnO were then grown on the patterned PTFE substrates by metal organic decomposition (MOD) [1]. A commercially available precursor solution for ZnO was used for the MOD deposition. The solution was deposited onto the substrate by spin coating and then thermally annealed in air ambient. Figure 1 and 2 show the scanning electron microscopy (SEM) image and the energy-dispersive X-ray (EDX) spertroscopy, respectively, for the obtained sample. The Zn, F, and O peaks are clearly observed in the EDX spectrum. The cathodoluminescence (CL) spectrum at room temperature under excitation by an electron beam from the sample, is shown in Fig. 3, where exhibits a strong UV emission band at 3.2 eV. Figure 4 shows elemental mapping of Zn for the sample. It is clear that the presence of Zn is uniform within the patterns. Based on these results, we believe that highly ordered ZnO array can be obtained by using PTFE template.

[1] Q.X. Guo, Y. Kume, T. Tanaka, M. Nishio, H. Ogawa, and A. Yoshida, Jpn. J. Appl. Phys. **44** (2005) 8451.

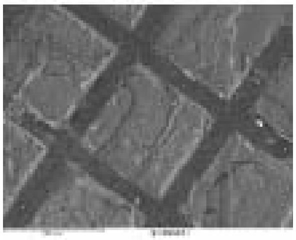

Fig. 1 SEM image of the sample.

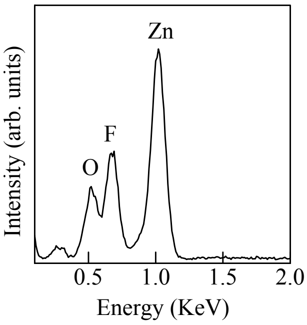

Fig. 2 EDX spectroscopy profile of the sample.

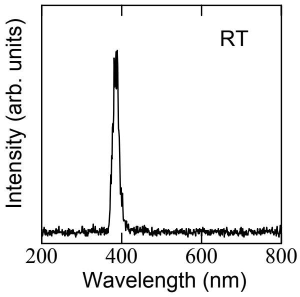

Fig. 3 CL spectrum of the sample.

Fig. 4 Elemental mapping of Zn for the sample

List of Publication 2005

H. Aritani, S. Shinohara, S. Koyama, K. Otsuki, T. Kubo and A. Nakahira
Mo L_{III}-Edge XANES Study of Catalytically Active Mo Species on Silica-Alumina Supports for Methane Dehydroaromatization
Chem. Lett. **35** (2006) 416.

L. Chen, M. Matsunami, T. Nanba, T. Matsumoto, S. Nagata, Y. Ikemoto, T. Moriwaki, T. Hirono and H. Kimura
Far-Infrared Spectroscopy of Electronic States of $CuIr_2Se_4$ at High Pressure
J. Phys. Soc. Jpn. **74** (2005) 1099.

L. Chen, M.Matsunami and T. Nanba
Infrared Spectroscopy on the Electronic State of Transition Metal Compounds Under High Pressure
Physica B **359-361** (2005) 1186.

T. Fuyuki, K. Sasaki and N. Ohno
Time-Resolved Photoluminescence of Hydrogen-Bonded Ferroelectrics $PbHPO_4$
J. Lumin. **112** (2005) 250.

T. Gejo, E. Nakamura and E. Shigemasa
Development of Symmetry-Resolved Zero-Kinetic-Energy Photoelectron Spectroscopy for Probing Multielectron Processes
Rev. Sci. Instrum. **77** (2006) 036112.

Q. X. Guo, J. Ding, T. Tanaka, M. Nishio and H. Ogawa
X-ray Absorption Near-Edge Fine Structure Study of AlInN Semiconductors
Appl. Phys. Lett. **86** (2005) 111911.

Q. X. Guo, Y. Hachiya, T. Tanaka, M. Nishio and H. Ogawa
Cathodoluminescence Study of Anodic Nanochannel Alumina
J. Lumin. **119-120** (2006) 253.

T. Hatsui, H. Setoyama, N. Kosugi, B. Wassermann, I. L. Bradeanu and E. Rühl
Photoionization of Small Krypton Clusters in the Kr 3d Regime: Evidence for Site-Specific Photoemission
J. Chem. Phys. **123** (2005) 154304.

E. Hayashi, K. Ito, S. Yabashi, M. Yamaga, N. Kodama, S. Ono and N. Sarukura
Vacuum Ultraviolet and Ultraviolet Spectroscopy of $BaMgF_4$ Codoped with Ce^{3+} and Na^+
J. Lumin. **119-120** (2006) 69.

E. Hayashi, K. Ito, S. Yabashi, M. Yamaga, N. Kodama, S. Ono and N. Sarukura
Ultraviolet Irradiation Effect of Ce^{3+}-Doped $BaMgF_4$ Crystals
J. Alloys Compd. **408-412** (2006) 883.

Y. Hikosaka, P. Lablanquie and E. Shigemasa
Efficient Production of Metastable Fragments around the 1s Ionization Threshold in N_2
J. Phys. B **38** (2005) 3597.

Y. Hikosaka, E. Shigemasa
Anisotropic Fragment Emission on Valence Photoionization of CF_4
J. Electron Spectrosc. Relat. Phenom. **152** (2006) 29.

S. Hino, N. Wanita, K. Iwasaki, D. Yoshimura, T. Akachi, T. Inoue, Y. Ito, T. Sugai and H. Shinohara
Ultraviolet Photoelectron Spectra of $(YC)_2$ @ C_{82} and Y_2 @ C_{82}
Phys. Rev. B **72** (2005) 195424.

S. Hino, N. Wanita, K. Iwasaki, D. Yoshimura, N. Ozawa, T. Kodama, K. Sakaguchi, H. Nishikawa, I. Ikemoto and K. Kikudhi
Electronic Structure of Metallofillerene, Tm@C_{82}(II)
Synthetic Metals **152** (2005) 357.

S. Hino, N. Wanita, M. Kato, K. Iwasaki, D. Yoshimura, T. Inoue, Y. Okazaki and H. Shinohara
Ultraviolet Photoelectron Spectrascopy of Multiple Atoms Encaqsulated Fullerenes
J. Electron Spectrosc. Relat. Phenom. **144-147** (2005) 239.

T. Hirai, N. Ohno, S. Hashimoto and S. Sakuragi
Luminescence of $NaGdF_4$:Tb^{3+}, Eu^{3+} under Vacuum Ultraviolet Excitation
J. Alloys Compd. **408-412** (2006) 894.

H. J. Im, T. Ito, J. B. Hong, S. Kimura and Y. S. Kwon
Continuity of Ce 4*f* Electronic Structure Across the Quantum Critical Point: A Resonant Photoemission Study on $CeNi_{1-x}Co_xGe_2$
Phys. Rev. B **72** (2005) 220405.

H. Ishikawa, T. Hirano, Y. Nagasaka, K. Kawakami, H. Ohta, T. Nanba, A. Hirano and R. Kanno
Reflectivity Measurements of Superionic Conductors for Li Ion Secondary Battery Materials
J. Phys. Chem. Solids **66** (2005) 2065.

M. Itoh, J. Azuma, T. Shimizu, M. Kamada, M. Kobayashi and Y. Usuki
Laser-induced Infrared Absorption in Lead Tungstate Observed by Laser-SR Combined Spectroscopy
J. Lumin. **119-120** (2006) 590.

T. Ito, M. Maeda, K. Nakamura, H. Kato and Y. Ohki
Similarities in Photoluminescence in Hafnia and Zirconia Induced by Ultraviolet Photons
J. Appl. Phys. **97** (2005) 054104.

K. Kanda, J. Igaki, Y. Kato, R. Kometani and S. Matsui
Characterization of Amorphous Carbon Nitride Films Formed by Plasma-Enhanced Chemical Vapor Deposition of CN Radicals Using C K-Edge X-Ray Absorption Fine Structure Spectroscopy
New Diamond and Frontier Carbon Technology **15** (2005) 123.

K. Kanda, M. Kono, K. Shobatake and T. Ibuki
Photodissociation Spectroscopy of Cyanogen Halides in the Extreme Vacuum Ultraviolet Region
J. Electron Spectrosc. Relat. Phenom. **144-147** (2005) 139.

H. S. Kato, M. Furukawa, M. Kawai, M. Taniguchi, T. Kawai, T. Hatsui and N. Kosugi
Electronic Structure of Bases in DNA Duplexes Characterized by Resonant Photoemission Spectroscopy Near the Fermi Level
Phys. Rev. Lett. **93** (2004) 086403.

H. Kobayashi, Y. Arachi, S. Emura, H. Kageyama, K. Tatsumi and T. Kamiyama
Investigation on Lithium De-Intercalation Mechanism for $Li_{1-y}Ni_{1/3}Mn_{1/3}Co_{1/3}O_2$
J. Power Sources **146** (2005) 640.

M. Matsunami, L. Chen, M. Takimoto, H. Okamura, T. Nanba, C. Sekine and I. Shirotani
Metal-Insulator Transition in $PrRu_4P_{12}$ and $SmRu_4P_{12}$ Investigated by Optical Spectroscopy
Phys. Rev. B **72** (2005) 073105.

M. Matsunami, M. Takimoto, H. Okamura, T. Nanba, C. Sekine and I. Shirotani
Optical Response of a Filled Skutterudite Compound $GdRu_4P_{12}$ due to Magnetic Ordering
Physica B **359-361** (2005) 844.

M. Mogi, T. Yamamoto, T. Mizoguchi, K. Tatsumi, S. Yoshioka, S. Kameyama, I. Tanaka and H. Adachi
Theoretical Investigation of Al K-Rdge X-Ray Absorption Spectra of Al, AlN and Al_2O_3
Mat. Trans. **45** (7) (2004) 2031.

S. Nagaoka and K. Mase
Ion Desorption Caused by Nls Core-Level Photoexcitation of N_2O on Si(100) Surface
Surface Science **593** (2005) 276.

A. Nakahira, K. Konishi, K. Yokota, T. Honma, H. Aritani and K. Tanaka
Synthesis and Characterization of TiO_2 Doped with P Ions by Anodic Oxidation of Titanium in Acid Solution
J. Ceramic. Soc. Jpn. **114** (2006) 46.

T. Nishi, S. Kimura, T. Takahashi, Y. Mori, Y.S. Kwon, H. J. Im and H. Kitazawa
Infrared Spectroscopy under Multiextreme Conditions: Direct Observation of Pseudogap Formation and Collapse in CeSb
Phys. Rev. B **71** (2005) 220401.

T. Nishi, S. Kimura, T. Takahashi, T. Ito, H. J. Im, Y.S. Kwon, K. Miyagawa, H. Taniguchi,
A. Kawamoto and K. Kanoda
The Origin of the Phase Separation in Partially Deuterated κ-$(ET)_2Cu[N(CN)_2]Br$ Studied by Infrared Magneto-Optical Imaging Spectroscopy
Solid State Commun. **134** (2005) 189.

H. Okamura, M. Matsubara, K. Tanaka, K. Fukui, M. Terakami, H. Nakagawa, Y. Ikemoto,
T. Moriwaki, H. Kimura and T. Nanba
Photogenerated Carriers in $SrTiO_3$ Probed by Mid-Infrared Absorption
J. Phys. Soc. Jpn. **76** (2006) 023703.

H. Okamura, T. Michizawa, T. Nanba, S. Kimura, F. Iga and T. Takabatake
Indirect and Direct Energy Gaps in Kondo Semiconductor YbB_{12}
J. Phys. Soc. Jpn. **74** (2005) 1954 .

K. Saito, M. Igeta, T. Ejima, T. Hatano, A. Arai, M. Watanabe
Magnetic Rotation Spectra of Co/Pt and Co/Cu Multilayers in 50-90 eV Region
J. Electro Spectrosc. Relat. Phenom. **144-147** (2005) 757.

Y. Shibata, A. Motogaito, H. Miyake, K. Hiramatsu, Y. Ohuchi, H. Okagawa,
K. Tadatomo, T. Nomura, Y. Hamamura and K. Fukui
Fabrication and Characterization of UV Schottky Detectors by Using a Freestanding GaN Substrate
Mater. Res. Soc. Symp. Proc. **831** (2005) E3.12.1.

J. Sichelshmidt, V. Voevodin, V. Pacheco, Yu. Grin, F. Steglich, T. Nishi and S. Kimura
Optical Investigations of the Clathrate α-$Eu_8Ga_{16}Ge_{30}$
Eur. Phys. J. B **46** (2005) 363.

J. Sichelschmidt, V. Voevodin, H. J. Im, S. Kimura, H. Rosner, A. Leithe-Jasper, W. Schnelle, U. Burkhardt, J. A. Mydosh, Yu. Grin and F. Steglich

Optical Pseudogap from Iron States in Filled Skutterudites $A\mathrm{Fe_4Sb_{12}}$(A=Yb,Ca,Ba)

Phys. Rev. Lett. **96** (2006) 037406.

T. Suga, T. Mizoguchi, M. Kunisu, K. Tatsumi, T. Yamamoto, I. Tanaka and T. Sekine

X-Ray Absorption Near Edge Structures of Silicon Nitride Thin Film by Pulsed Laser Deposition

Mat. Trans. **45** (2004) 2039.

K. Takarabe, H. Doi, Y. Mori, K. Fukui, Y. Shim, N. Yamamoto, T. Yoshitake and K. Nagayama

Optical Properties of Nanocrystalline $FeSi_2$ and the Effects of Hydrogenation

Appl. Phys. Lett. **88** (2006) 061911.

Y. Takashima, M. Katoh, M. Hosaka, A. Mochihashi, S. Kimura and T. Takahashi

Observation of Intense Bursts of Terahertz Synchrotron Radiation at UVSOR-II

Jpn. J. Appl. Phys. **44** (2005) L1131.

T. Takeuchi, S. Nakano, K. Soda, H. Sato, M. Hasegawa, U. Mizutani, K. Itoh and T. Fukunaga

Free-Energy Estimation of the Zr-Ni-Al Bulk Metallic Glass from the Local Atomic Arragements of the Relevant Crystals

Mat. Trans. **46** (2005) 2791.

I. Tanaka, T. Mizoguchi and T. Yamamoto

XANES and ELNES in Ceramic Science

J. Am. Ceram. Soc. **88** (2005) 2013.

T. Tsujibayashi, M. Itoh, J. Azuma, M. Watanabe, O. Arimoto, K. Toyoda, S. Nakanishi, H. Itoh and M. Kamada

Time-Resolved Study of Auger-Free Luminescence in Two-Photon Excited BaF_2 with Use of Synchrotron Radiation and Laser

Phys. Stat. Sol. **2** (2005) 228.

T. Tsujibayashi, M. Itoh, J. Azuma, M. Watanabe, O. Arimoto, S. Nakanishi, H. Itoh and M. Kamada

Two-Photon Spectroscopy of Core Excitons in Barium Fluoride Using Synchrotron Radiation and Laser Light

Phys. Rev. Lett. **94** (2005) 076401.

K. Watamnabe, A. Kokalj, H. Horino, I. Rzeznicka, K. Takahashi, N. Nishi and T. Matsushima
Scanning-Tunneling Microscopy, Near-Edge X-Ray-Absorption Fine Structure, and Density-Functional Theory Studies of N_2O Orientation on Pd(110)
Jpn. J. Appl. Phys. **45** (2006) 2290.

M. Yamaga and N. Kodama
Fluorescence of Ce^{3+} in Fluorides and Long-lasting Phosphorescence of Ce^{3+} in Oxides
J. Alloys Compd. **408-412** (2006) 706.

I. Zerec, W. Carrillo-Cabrera, V. Voevodin, J. Sichelschmidt, F. Steglich, Y. Grin, A. Yaresko and S. Kimura
Influence of Cage Distortions on the Electronic Structure and Optical Properties of Ba_6Ge_{25}
Phys. Rev. B **72** (2005) 045122.

S. Nakano, T. Takeuchi, K. Soda, M. Hasegawa, U. Mizutani, H. Sato, K. Itoh and T. Fukunaga
Investigation of Stability of Zr-Ni-Al Bulk Amorphous Phase from Local Atomic Arrangements of the Relevant Crystals
J. Jpn. Soc. Powder Powder Metallurgy **53** (2006) 100. (in Japanese)

T. Suzuki, H. Miyazaki, K. Soda, T. Takeuchi, M. Hasegawa, H. Sato and U. Mizutani
Electronic Structure of Zr-TM-Al (TM=Ni, Cu) Bulk Metallic Glasses
J. Jpn. Soc. Powder Powder Metallurgy **53** (2006) 107. (in Japanese)

1st Joint Workshop on Beamline Technology

February 27 and 28, 2006

Feb. 27 (Mon) 13:30 – 18:00 (coffee break included)

Coordinator: E. Shigemasa (UVSOR)

13:30 – 13:40	Preface	E. Shigemasa (UVSOR)
13:40 – 14:40	Fundamental aspect of high heat-load frontend components	N. Takahashi (JASRI)
14:40 – 15:40	Basic concept on double crystal monochromators as a high heat load component	T. Goto (JASRI)
15:40 – 16:00	Coffee break	
16:00 – 17:00	Design concept on a new generation monochromator for soft X-ray emission spectroscopy and related basic technology	T. Hatsui (IMS)
17:00 – 18:00	Principium of soft X-ray monochromator ~ Challenge towards realizing the ultimate performance monochromator ~	K. Amemiya (Univ. Tokyo)
18:00 – 18:30	Short tour to UVSOR	
18:30 –	Banquet	

Feb. 28 (Tue) 9:30 – 15:00 (coffee break included)

<First session> Coordinator: H. Ohashi (JASRI)

9:30 – 10:15	Manufacture of a transmission grating soft X-ray monochromator	T. Horigome (UVSOR)
10:15 – 11:00	Current situation against heat load problems at UVSOR	E. Nakamura (UVSOR)
11:00 – 11:15	Coffee break	
11:15 – 12:00	Cooling systems for double crystal monochromators at KEK-PF	Y. Uchida (KEK-PF)
12:00 – 13:00	Lunch	

<Second session> Coordinator: H. Ohashi (JASRI)

13:00 – 13:45	Countermeasure against high heat-load to double crystal monochromators	H. Yamazaki (JASRI)
13:45 – 14:30	Development of a surface profile measuring instrument for optical elements	Y. Higashi (KEK-PF)
14:30 – 15:00	Summary & perspective (panel discussion)	H. Ohashi (JASRI) & E. Shigemasa (UVSOR)
15:00 – 15:10	Closing remarks	N. Kosugi (UVSOR)

2nd *JSSRR Wakate Workshop on Next Generation Light Sources*
~ Future Science Developed by New Light Source ~

Place: Okazaki Conference Center

August 8, 2005

[Chairperson : S. Kimura]

14:00-	Preface	S. Kimura (UVSOR)
14:10-	Interim report of the next generation light sources committee	Y. Amemiya (Univ. Tokyo)
14:40-	Possibility of X-FEL and SCSS project	T. Ishikawa (RIKEN)
15:15-	ARC-EN-CIEL, the present FEL activity and the scientific case	M.E. Couprie (CEA)
15:50-	Coffee break	

[Chairperson : K. Mase]

16:10-	Present status of plasma x-ray laser and expectation to X-FEL	K. Nagashima (JAERI)
16:45-	Possibility of the use of X-FEL extended from the present SR	M. Yabashi (JASRI)
17:15-	Applications of X-FEL (Examples of LCLS)	K. Hirano (KEK-PF)
17:30-	Discussion: Future science with X-FEL	T. Ishikawa (RIKEN)
18:30-	Banquet	

August 9, 2005

[Chairperson: K. Harada]

8:30-	Limit of present SR and requests to next generation light sources	H. Tanaka (JASRI)
8:55-	Possibility of ERL for ring-type light source	R. Hajima (JAERI)
9:20-	Next generation ring-type and ERL light sources	S. Sakanaka (KEK-PF)
9:45-	Coffee break	

[Chairperson: K. Amamiya]

10:00-	Present and future of photoemission spectroscopy of solids	K. Shimada (Hiroshima Univ.)
10:25-	Present and future of structural physics	H. Sawa (KEK-PF)
10:50-	Future of structural biology using SR	S. Wakatsuki (KEK-PF)
11:15-	Present and future of spectroscopy of atoms and molecules	E. Shigamasa (UVSOR)
11:40-	Present and future of x-ray imaging	Y. Kagoshima (Univ. Hyogo)
12:05-	Discussion chair: M. Takata (JASRI), Panelist: T. Kinoshita (JASRI) & H. Kawata (KEK-PF)	

The workshop was organized by The Japanese Society for Synchrotron Radiation Research and was sponsored by UVSOR.

UVSOR User's Union (UUU) Users Meetings

OCC
(Oral:2F conference room, Poster & Get-together Party:1F conference room)

27 Feb. 2006 (Mon)

13:00 - 13:30	reception		
		chariman	K. Soda (Nagoya Univ.)
13:30 - 13:35	Opening remarks	UUU president	K. Soda
13:35 - 13:50	Current status of UVSOR	facility head	N. Kosugi
13:50 - 14:20	Present Status of UVSOR-II Accelerators	UVSOR	M. Kato
	coffee break		
		chairman	S. Hino (Chiba Univ.)
14:40 - 15:10	Present status of the undulator beamline BL3U	IMS	T. Hatsui
15:10 - 15:40	Light source developments at UVSOR-II	UVSOR	M. Kato
15:40 - 16:10	IR absorption reflection spectroscopy at BL6B	UVSOR	Y. Sakurai
	coffee break		
		chariman	K. Soda (Nagoya Univ.)
16:30 - 17:00	Quantitative evaluation of electron transport properties by use of high-resolution angle-resolved photoemission spectroscopy	Nagoya Univ.	T. Takeuchi
17:00 - 17:30	Recent development of photoelectron spectroscopy of metallofullerenes	Chiba Univ.	S. Hino
17:30 - 18:00	Various spin reorientation transitions induced by molecular adsorption on magnetic thin films	IMS	T. Yokoyama
	coffee break (Poster session)		
18:30 - 20:30	Get-together Party		

28 Feb. 2006 (Tue)

		chairman	K. Hayashi (Gifu Univ.)
9:00 - 9:30	Structural Analysis on the Amorphous Carbon Thin Films Using C K-Edge NEXAFS	Hyougo Pref. Univ.	K. Kanda
9:30 - 10:00	Development of quantitative structural analysis by using XANES and an attempt to micro component detection	Nagoya Univ.	T. Yoshida
10:00 - 10:30	Core exciton measurements using synchrotron radiation and laser light	Osaka Dent. Univ.	T. Tsujibayashi
	coffee break		
10:40 - 12:30	Poster session		
	lunch		
		chariman	K. Fukui (Univ. of Fukui)
13:30 - 14:00	Phase observation of reflection multilayer using reflection and total electron yield spectra	Tohoku Univ.	T. Ejima
14:00 - 14:30	Synchrotron radiation spectroscopy of biomolecules	Kobe Univ.	K. Nakagawa
14:30 - 15:00	discussion		

Poster session

No.	Author	Affiliation	BL	Title
P1	K. Kanda	Hyogo Pref. Univ.	8B1	Structural Analysis on the Amorphous Carbon Thin Films Using C K-Edge NEXAFS
P2	Y. Izumi	Kobe Univ.	5B	Silicon K-edge XANES measurement of left- and right-handed quartz crystals
P3	K. Soda	Nagoya Univ.	5U	3p-3d Resonant Photoemission of Heusler-type $Fe_2VAl_{1-x}Si_x$
P4	H. Miyazaki	Nagoya Univ.	5U	Angle resolved photoemission of Fe_2VAl Heusler-type alloy
P5	T. Mochizuki	Nagoya Univ.	5U	3p-3d Resonant Photoemission of Heusler-type $(Fe_{1-x}M_x)_2VAl$(M=Ir,Pt)
P6	T. Suzuki	Nagoya Univ.	5U	SR photoemission of Zr bulk metal glasses
P7	S. Ohta	Nagoya Univ.	5U	Photoelectron Spectroscopy of Pd-based Bulk Metallic Glasses with use of Synchrotron Light
P8	M. Imamura	Kobe Univ.	5U	Photoemission study of organic-metal hybrid nanoparticles : Prospect of research for the fluorescent Au nanoclusters encapsulated within dendrimer templates
P9	T. Kamikake	Kobe Univ.	5U	Photoemission study of alkyl-passivated Si nanoparticles
P10	M. Kitaura	Fukui Nat. Col. Tech.	7B	Excitation processes of long lasting afterglow in $SrAl_2O_4$:Eu,Dy phosphors
P11	K. Hayashi	Gifu Univ.	5B	Photoinduced phenomena in amorphous chalcogenide semiconductors
P12	K. Mitsuke	IMS	2B2	Pulsed ZEKE spectroscopy of fullerenes: setup and performance
P13	T. Yokoyama	IMS	4B	Various spin reorientation transitions induced by molecular adsorption on magnetic thin films
P14	T. Nakagawa	IMS	4B	Possibility of UV MCD Photoelectron Microscope
P15	T. Miyazaki	Ehime Univ.	8B2	Valence band structure and selective oxidation of Li-Ni complex oxide system
P16	Y. Nakajima	Univ. of Fukui	7B	Luminescence properties of YPO_4:Mn codoped with Zr
P17	N. Nakagawa	Univ. of Fukui	1A,8B1,7B	Excitonic Emisson Spectra and Time Resolved Decay Curves of AlGaN Alloys
P18	N. Nakagawa	Univ. of Fukui	5B,8B1,7B	Visible - UV Emission Spectra in Ⅲ - Ⅴ Nitride Semiconductors by Using High Energy Excitation and Excitation Energy Dependence

P19	M. Ohta	Niigata Univ.	1B	Photoluminescence Property of Hydroxyapatite
P20	T. Yokoyama	Chiba Univ.	8B2	Electronic structure of 6P monolyer on Cu(110)
P21	T. Matsui	Kobe Univ.	7B	Vacuum ultraviolet absorption spectra of amino acid films
P22	M. Ono	Chiba Univ.	8B2	SR-damaged doping of organic thin films: UPS study of PTFE film
P23	N. Ohno	Osaka Elec Commun. Univ.	1B	Superfluorescence from fluoride crystals
P24	N. Ohno	Osaka Elec Commun. Univ.	2B	VUV excitation luminescence properties of fluoride phosphors
P25	S. Kimura	UVSOR	7U	Design og the Wadsworth-type normal incident monochromator at UVSOR-II
P26	S. Kimura	UVSOR	6B	Present status of IR-THz beamline at UVSOR-II
P27	T. Ito	UVSOR	5U	Study of $CeTe_2$ electronic states using high resolution 3D angle resolved photoemission spectroscopy
P28	T. Ito	UVSOR	5U	Ce 4d-4f resonant photoemission of $CeNiGe_{2-x}Si_x$
P29	J. Yamazaki	UVSOR	M	Present Status of UVSOR-II Accelerators
P30	M. Hosaka	UVSOR	M	Present Status of UVSOR-II FEL
P31	K. Takashima	Nagoya Univ.	M	Correlation between high intensity THz SR burst and electron bunch motion
P32	H. Hayashi	UVSOR	M	Closed Orbit Distortion at UVSOR-II
P33	A. Mochihash	UVSOR	M	Present status of upgraded RF accelerating system in UVSOR-II
P34	J. Azuma	Saga Univ.	5U	Surface photo induced EMF effect of Cr/p-GaAs(100)
P35	K. Fukui	Univ. of Fukui	5B	Manufacturing and VUV-SX region optical properties of self standing metal thin films
P36	Y. Sakurai	UVSOR	6B	IR absorption reflection spectroscopy at BL6B
P37	M. Kato	Chiba Univ.	8B2	Recent development of photoelectron spectroscopy of metallofullerenes
P38	T. Ejima	Tohoku Univ.	5B	Phase observation of reflection multilayer using reflection and total electron yield spectra

UVSOR Lunch Seminar

FY2005

May 18	Dr. M. Ono, Graduate School of Science and Technology, Chiba University Investigation of doping in organic thin film by using synchrotron radiation damage
May 25	Dr. K. HOTTA, R&D Center Technology & Engineering Division Lamp Company, Ushio INC. EUV lithography and DPP EUV sources
July 12	Drs. M. Labat & G. Lambert, CEA, France FEL saturation in case of UVSOR-II Seeding a free electron laser in "High Gain Harmonic Generation" configuration with laser harmonics produced in gases
July 14	Prof. V.G. Stankevich, Russian Research Centre Kurchatov Institute, Russia and UVSOR Optical investigations ferroelectric ordering $C_{60}F_{18}$ single crystals
July 27	Prof. H. Xu, NSRL, University of Science and Technology of China Present status and future plan of Hefei light source
Sept. 7	Dr. H.-D. Kim, Beamline Division, Pohang Accelerator Laboratory, South Korea Present status and activities at Pohang Light Source
Dec. 20	Drs. S. Bielawski & C. Szwaj, Phlam/CERLA, France Introduction to mode-locked lasers Recent results obtained on the UVSOR FEL
Dec. 21	Dr. T. Nishi, Graduate University for Advanced Studies (SOKENDAI) Electronic structure of a quasi-two-dimensional organic superconductor and development of infrared spectroscopy under multiextreme conditions
Mar. 22	Prof. L. Sheng, NSRL,University of Science and Technology of China Introduce of the Hefei Light Source (HLS) and some experiments.